Modeling of Welding-Induced Distortion Effects on Fatigue Behaviors of Lightweight Shipboard Structures

by

Wenqing Zhou

A dissertation submitted in partial fulfillment
of the requirements for the degree of
Doctor of Philosophy
(Naval Architecture and Marine Engineering)
in the University of Michigan
2021

Doctoral Committee:

Professor Pingsha Dong, Chair
Associate Professor Matthew D. Collette
Associate Professor Dale G. Karr
Professor Wei Lu

Wenqing Zhou

wqzhou@umich.edu

ORCID iD: 0000-0003-4997-6138

Dedication

This dissertation is dedicated to my wife Mengqi, who has offered me unwavering love, support, and encouragement during my doctoral journey.

Acknowledgements

Foremost, I would like to express the most profound appreciation to my advisor and committee chair, Professor Pingsha Dong, who has the attitude and the substance of a genius, for his continuous support of my Ph.D. study and research, his patience, motivation, and immense knowledge. Without his guidance and persistent help, this dissertation would not have been possible.

I would also like to thank all my dissertation committee members, Professor Dale G. Karr, Professor Matthew D. Collette, and Professor Wei Lu, for their insightful comments and encouragements.

In addition, a thank you to Professor Heikki Remes and Dr. Ingrit Lillemäe-Avi of Aalto University for providing me valuable test data for my research. I would like to thank the Welding Research Council (WRC), Lightweight Innovations for Tomorrow (LIFT), and National Research Foundation of Korea (NRF) for providing funding during my doctoral studies.

My sincere thanks also go to my colleagues in our lab, Dr. Shaopin Song, Dr. Shizhu Xing, Dr. Jifa Mei, Dr. Xianjun Pei, Sandipp Krishnan, and Lunyu Zhang for the stimulating discussions, their support and encouragement.

Finally, I would like to thank my parents for their support. They gave me the strength to overcome difficulties in my life over the years. Special thanks to my wife, Mengqi, for her love and for accompanying me throughout my doctoral journey.

Table of Contents

List of Tables

List of Figures

List of Appendices

List of Symbols

e	Axial misalignment
E	Young's Modulus
F_0	Notional force
I	Area moment of inertia
k_b	Bending stress concentration factor
l	Beam length
l_i	Beam length of Member i
m_0	Notional moment
M	Total bending moment
$M^{(i)}$	Total bending moment in Member i
M_0	Bending moment caused by notional loads
$M_0^{(i)}$	Bending moment caused by notional loads in Member i
M_1	Secondary bending moment caused by axial load P
$M_1^{(i)}$	Secondary bending moment caused by axial load P in Member i
n	Number of distortion measurements
P	Axial load
t	Plate thickness

t_i Plate thickness of Member *i*

v_0 Initial distortion, in terms of displacement in *y*-direction

$v_0^{(i)}$ Initial distortion of Member i, in terms of displacement in *y*-direction

$v_{0,i}$ Initial distortion, in terms of displacement in *y*-direction at knot *i*

$v'_{0,i}$ Initial distortion, rotation at knot *i*

v_1 Deflection caused by axial load P

$v_1^{(i)}$ Deflection of Member i caused by axial load P

v Total deflection, $v = v_0 + v_1$

$v^{(i)}$ Total deflection of Member i, $v^{(i)} = v_0^{(i)} + v_1^{(i)}$

V Total shear force

$V^{(i)}$ Total shear force in Member *i*

V_0 Shear force caused by notional loads

$V_0^{(i)}$ Shear force caused by notional loads in Member *i*

V_1 Secondary shear force caused by axial load P

$V_1^{(i)}$ Secondary shear force caused by axial load P in Member *i*

$\mathbf{y}$ Vector of observed distortion measurements

α_{G} Relative global angular distortion angle/angular misalignment angle between two members of a joint

$\alpha_{\mathrm{L},1}$ Relative local angular distortion angle between two members of a joint

$\alpha_{L,2}$ Local angular distortion angle measured at the gripped end with respect to the baseline

δ_0 Peak distortion value of buckling distortion and cosine angular distortion

θ_1 Total angular distortion angle at Position 1 with respect to the baseline

θ_2 Total angular distortion angle at Position 2 with respect to the baseline

θ_G Global angular distortion angle with respect to the baseline

θ_{iG} Global angular distortion angle of Member *i* with respect to the baseline

θ_1' Local angular distortion angle at Position 1

θ_2' Local angular distortion angle at Position 2

θ_{ij}' Local angular distortion angle of Member *i* at Position *j*

Abstract

In the design and construction of modern lightweight shipboard structures, wide-spread welding-induced distortions have become a major structural producibility issue and an increasing structural integrity concern over secondary bending stresses caused by interactions of distortions with cyclic service loads. The goal of this dissertation is to develop an effective methodology for evaluating the secondary bending effects caused by complex welding-induced distortions on fatigue behaviors of lightweight structures. A novel analytical approach based on a divide-and-conquer approach is taken to obtain the solutions to complex distortion problems in closed-forms through an assembly of its solution parts achievable through a decomposition technique.

A notional load method for providing analytical treatment of distortion curvature effects on fatigue behaviors of lightweight shipboard structures within the context of beam theory is first presented. Using this method, closed-form analytical formulae can be developed for analyzing secondary bending stresses caused by nonlinear interactions between several common distortion types and remotely applied load.

Then, an analytical method for computing the secondary bending stresses at weld locations caused by both axial and angular misalignments without curvatures. The model enables a consistent definition of each type of misalignment commonly observed in practice. As such, the secondary bending stresses caused by misalignments at each weld toe location can be appropriately combined for fatigue evaluation purposes.

All closed-form analytical solutions derived are validated by direct finite element computations in various cases. Moreover, the developed analytical solutions are used for

interpreting fatigue test data of welded components with misalignments and distortion curvatures. An excellent agreement is achieved not only between thin plate lab specimens and full-scale stiffened panels but also with the traction structural stress-based master S-N curve scatter band adopted by ASME Div. 2 since 2007, further validating their effectiveness in fatigue evaluation of welded structures exhibiting general forms of misalignments and distortion curvatures.

These new closed-form solutions offer some significant insights not only on what types of distortions are more detrimental to fatigue performance than others but also on the validity limits of the empirical equations stipulated in current Codes and Standards. In addition, parameterized limits can now be clearly stated on conditions when straightening effects should be considered based on the closed-form solutions.

Finally, a general distortion mode decomposition-and-assembly procedure is presented. By introducing a consistent reference framework, complex distortions regarding both butt-welded joints and fillet-welded joints in panel structures can be readily decomposed into various elementary distortion modes studied in this dissertation. The final assembly of the constituent secondary stress solutions is accomplished through superposition. To facilitate real-world engineering applications and support future adoptions of Codes and Standards, the closed-form formulae are presented in tabular form for following the workflow of the proposed decomposition-assembly procedure. Two examples are provided for illustrating how the procedure and closed-form solutions are used in real engineering applications.

In summary, this dissertation presents a series of novel analytical treatments for computing secondary bending stresses caused by various elementary distortion modes, accompanied by a comprehensive distortion decomposition-and-assembly procedure based on a consistent framework. These new solutions offer a comprehensive suite of tools to engineers and researchers

for a consistent and effective treatment of secondary stresses caused by distortion types unique to lightweight shipboard structures in performing fatigue evaluations.

Chapter 1

Introduction

1.1 Background

In recent years, the demand for structural lightweighting for transportation vehicles has become more intensified as the industry strives for further improved fuel economy and reduced environmental emissions [1]. Furthermore, an effective structural lightweighting can help achieve an improved weight balance for maneuverability under dynamic conditions, even with increased payloads [2–4]. For instance, in the automotive industry, numerous name-brand vehicles have recently been replaced by newer models with significantly lighter weight components [5]. For example, the new Ford F-150 achieved a 300 kg (14% decrease) weight reduction over its 2014 model by adopting an aluminum car body structure over an advanced high-strength steel frame [2]. In a Department of Energy project, researchers managed to shave off over 600kg of weight from the original 2013 Fusion design by adapting a mixed-material Mach-II structure design [6] (see Fig. 1.1). In the railroad industry, engineers are also seeking innovative weight reduction solutions like using aluminum, sandwich structures, and recently Carbon Fiber-reinforced Plastics (CFRP) (see Fig. 1.2) in rail vehicle structures [3,7,8]. In the shipbuilding industry, there is also an increasing interest in using high-strength low-density alloys such as aluminum alloys and titanium alloys [9,10] or using thinner plate thicknesses in the design [11] (Fig. 1.3) to achieve effective lightweighting.

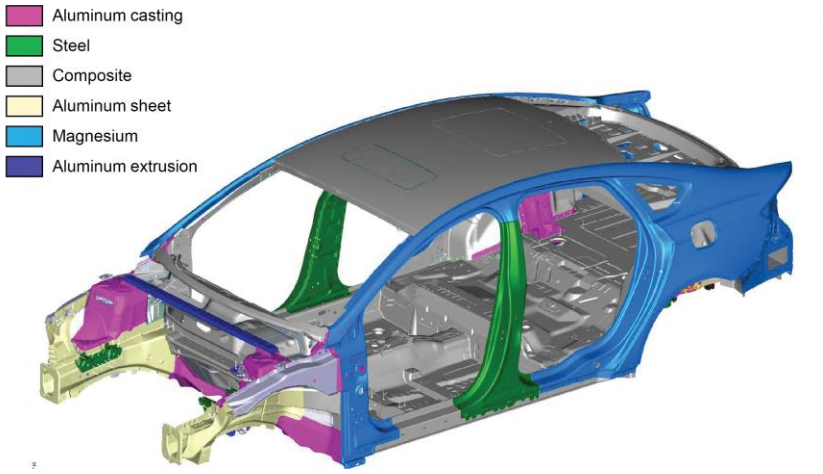

Fig. 1.1 Mixed-material lightweight vehicle Mach-II design material distribution [6].

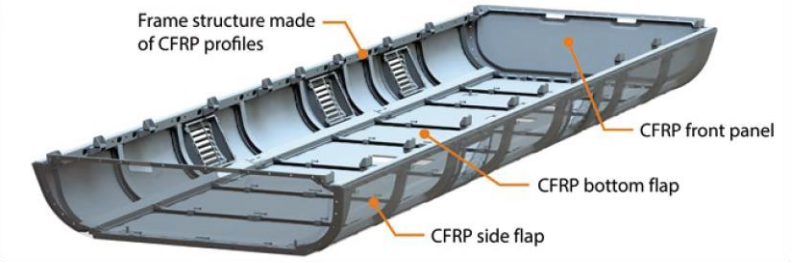

Fig. 1.2 Load-bearing structure of a rail vehicle subfloor cladding with heavy use of CFRP [3].

Despite these novel lightweighting concepts, their use in actual structural designs is still limited due to cost considerations [12] or challenges in joining dissimilar materials [13] in today's production environment. As a result, one of the simplest and most cost-effective ways of achieving structural lightweighting today is the use of high strength thin gauge steel plates or sheets. As reported by Huang et al. [9,14], plates with thicknesses equal to or less than 10 mm have become increasingly dominant in lightweight shipboard structures in surface combatants (see Fig. 1.4). As such, significant challenges in distortion control during construction have been reported [15–17] due to the following reasons. First, since the residual stress developed after welding could easily reach the material's yield strength magnitude [15,18], a higher yield strength means higher residual stresses. Second, thin plate sections have significantly lower flexural rigidity, which leads to lower

buckling strength and larger deformations under the same residual stress level. Therefore, high-strength thin gauge steel sheets are much more prone to distortions (see. Fig. 1.5).

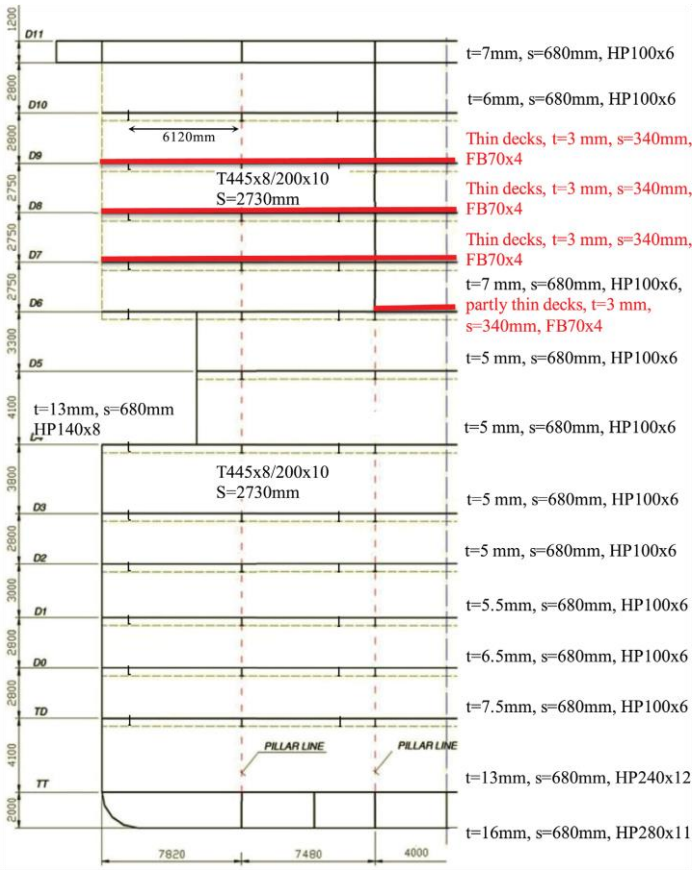

Fig. 1.3 Midship cross-section of a case passenger ship with thin deck design [11].

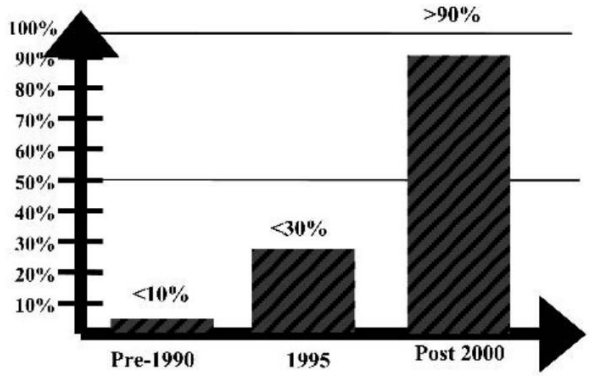

Fig. 1.4 Percentage of thin steel plate (less than 10 mm) ordered by vessels at NGSS/Avondale Shipyards [9].

Such rampant distortions can cause serious issues in both construction and structural performance. The first issue is dimensional accuracy control in modular assembly. Severe

distortions at part and component levels cause poor fit-up conditions for subsequent welding assembly, often require costly distortion corrections. The second problem is that large distortions could negatively affect the performance of the structure in service. For example, the distortion may affect the buckling strengths of stiffened panels [19]. More importantly, the distortion would also introduce additional stress concentration when the structure is loaded and could cause problems like stress corrosion cracking, reduced structural strength, and shortened fatigue life at welded joints. These problems could lead to a significant reduction of structural life and need to be addressed properly, especially their impact on fatigue performance since it is less likely to be noticed until severe damage has been done. Therefore, it is necessary to understand how such distortions would affect the structure's fatigue performance in order to establish a concrete mechanics basis for facilitating the development of distortion allowance criteria for ensuring the operational safety of these new lightweight structures in service.

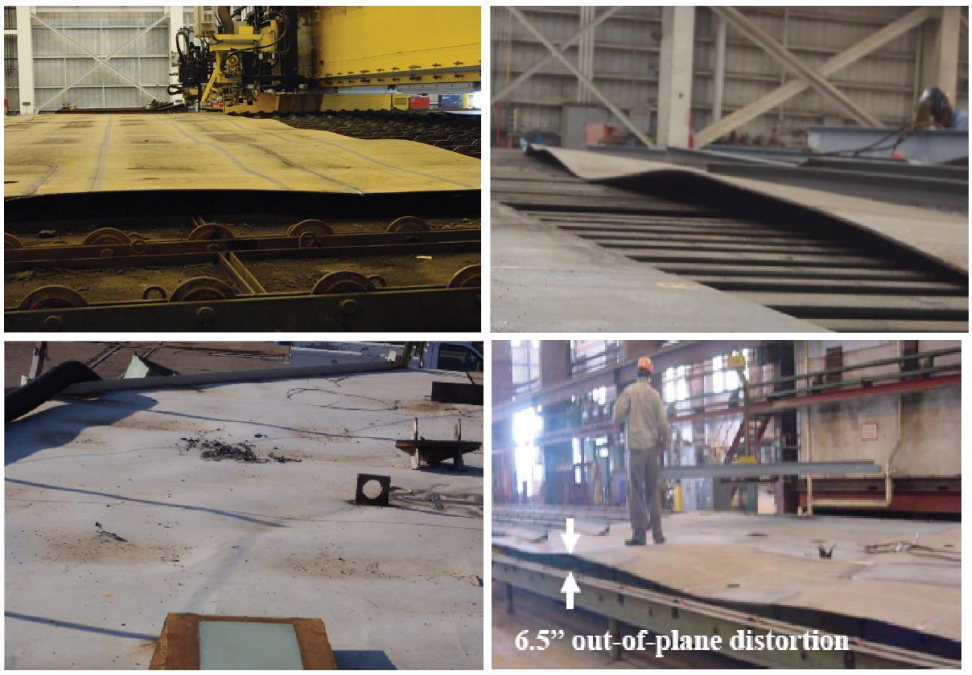

Fig. 1.5 Severe distortions associated with thin plates observed in shipyards [20].

1.2 Representative Research Efforts on Distortion Effects on Fatigue Performance

In this section, the state-of-the-art fatigue evaluation approaches relevant to welded components, and recent research efforts on distortion effects on fatigue will be reviewed to establish areas of further research needs

1.2.1 Fatigue Evaluation Methods

It is estimated that 50-90% of the failures which occur in engineering components can be related to fatigue [21,22], and welded components show much lower fatigue strengths than those of unwelded components, as shown in Fig. 1.6. In welded structures, fatigue failures usually happen at welded joints due to stress concentration caused by weld shape and discontinuities [23]. Many approaches have been developed for the fatigue assessment of welded joints. These include the nominal stress method [24,25], the hot spot stress method [26], the local notch stress method [27–29], and the traction structural stress method [30–32].

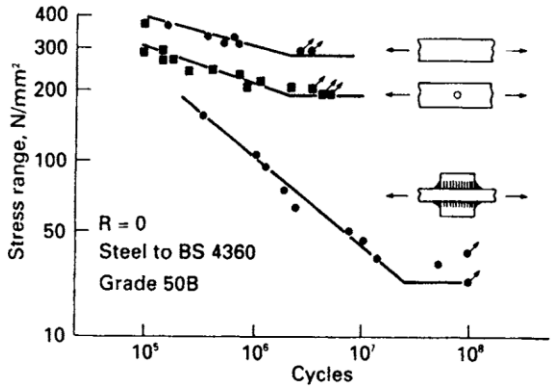

Fig. 1.6 Comparison of fatigue strengths between steel plate, notched steel plate, and plate with welded attachments [23].

(a) Nominal stress method

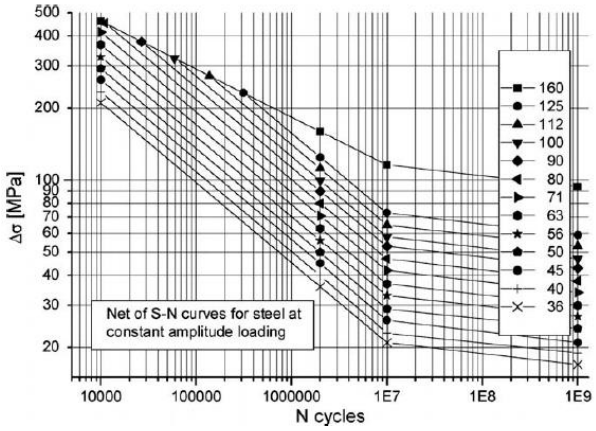

Fig. 1.7 Net of S-N Woehler curves at constant stress amplitude (steel) [26].

Nominal stress is a simple stress state that would exist at a weld location without considering geometric discontinuity (local stress concentration), of which strength of materials formulae are applicable. It is a stress definition widely adopted by well-recognized national and international Codes and Standards [24,25,33]. Since the nominal stress definition cannot differentiate variations in stress concentration behaviors resulted from joint types, joint dimensions, etc., each unique structural detail is assigned a different S-N curve based on limited testing and experience (i.e., one out of many as shown in Fig. 1.7) for fatigue life estimation. Although the current codes and standards provide various weld joint detail classifications (e.g., BS7608 [24], IIW Recommendations [25]), it is often difficult to determine a proper classification for a welded joint in design. Furthermore, the nominal stress could not be clearly defined in complex structures, as well as the stress component caused by misalignment and distortions.

(b) Hot spot stress method

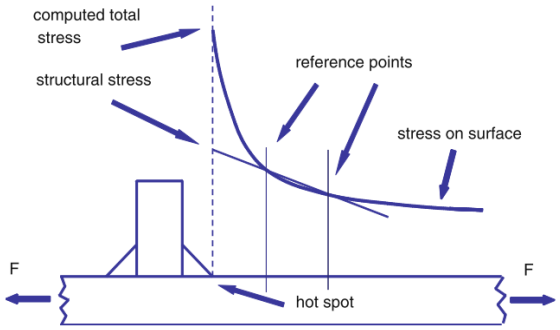

Fig. 1.8 Definition of hot spot stress [25].

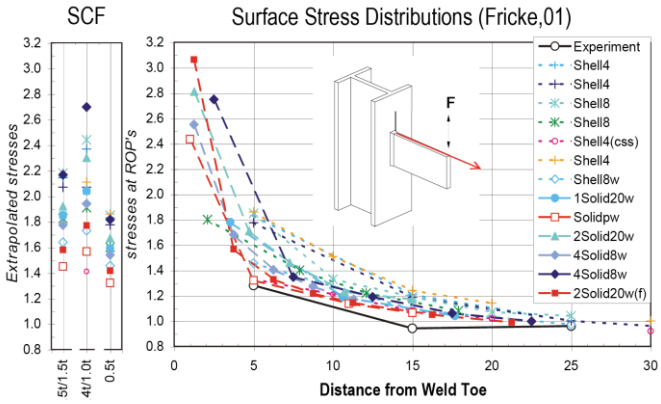

Fig. 1.9 Hot spot stress using different extrapolation methods [34].

The hot spot stress refers to the stress that includes the stress riser effects of structural details but without that from the local weld profile itself [25]. The hot spot stress is determined by extrapolating from surface stresses at reference points to the weld toe, as shown in Fig. 1.8, so that the stress singularity due to geometry discontinuity is excluded. There are different reference point positions and extrapolation methods recommended [25], based on either finite element analysis (FEA) results or test measurements (strain gauge readings). However, based on a study by Fricke [34], the hot spot stresses obtained using different extrapolation method show a great variation and is highly mesh sensitive (as illustrated in Fig. 1.9). This increases the uncertainties of the hot spot stress result and is the main drawback of this method. Also, the application of the hot spot stress method is limited to weld toe failure since it requires surface stresses.

(c) Local notch stress method

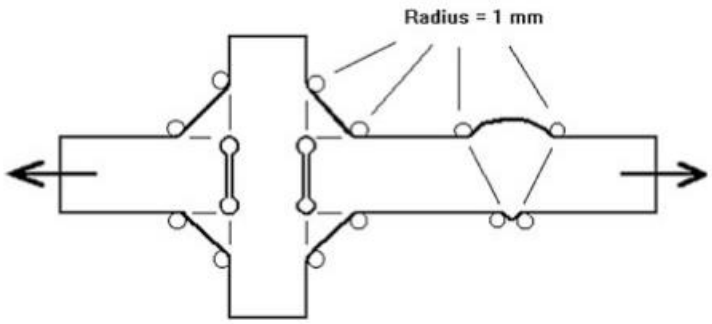

Fig. 1.10 Effective notch root radius [26]**.**

The notch stress is the total stress at the root of a notch, obtained assuming linear-elastic material behavior [25]. Due to the irregularity of the weld toe and the root configuration, there is no well-defined notch radius at welded joints; therefore, an effective notch root radius of 1.0 mm was used [26,27] for steel and aluminum alloys, as shown in Fig. 1.10. However, the local notch stress method requires extra fine mesh around the notch root (minimum element size about 0.05 mm, see Fig. 1.11), making it computational expensive and challenging to implement in complex engineering structure models. Moreover, the notch stress method is limited to thicknesses $t \geq 5$ mm, granting it limited applicability in lightweight structures.

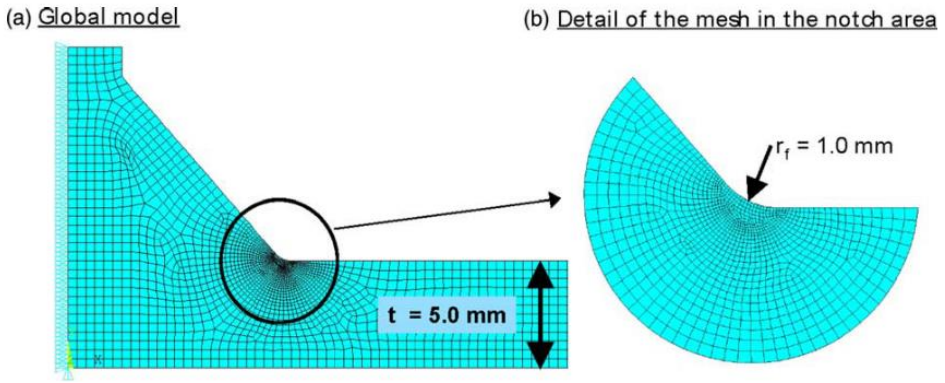

Fig. 1.11 Finite element (FE) mesh of the weld toe with effective notch root radius of 1 mm [27].

(d) Traction structural stress and the Master S-N curve method

The traction structural stress definition and the Master S-N curve method were originally developed by Dong et al. [30–32,35] and have been used in a number of recent studies [36–40] for dealing with both weld toe and weld root cracking fatigue failure modes.

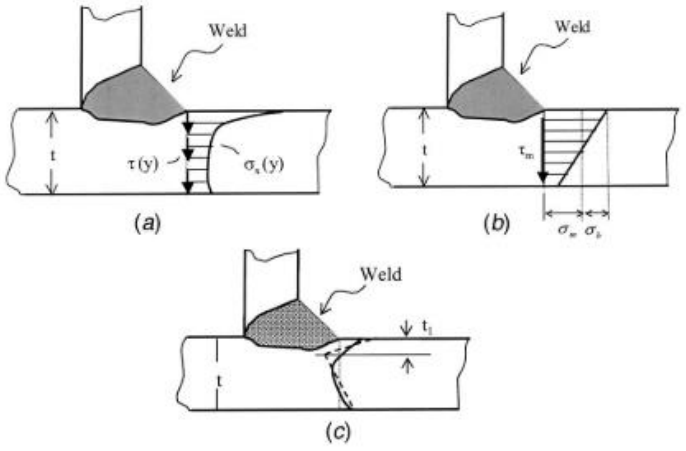

Fig. 1.12 Through-thickness structural stresses definition: (a) local stresses from FE model; (b) traction structural stress or far-field stress; (c) self-equilibrating notch stress [31].

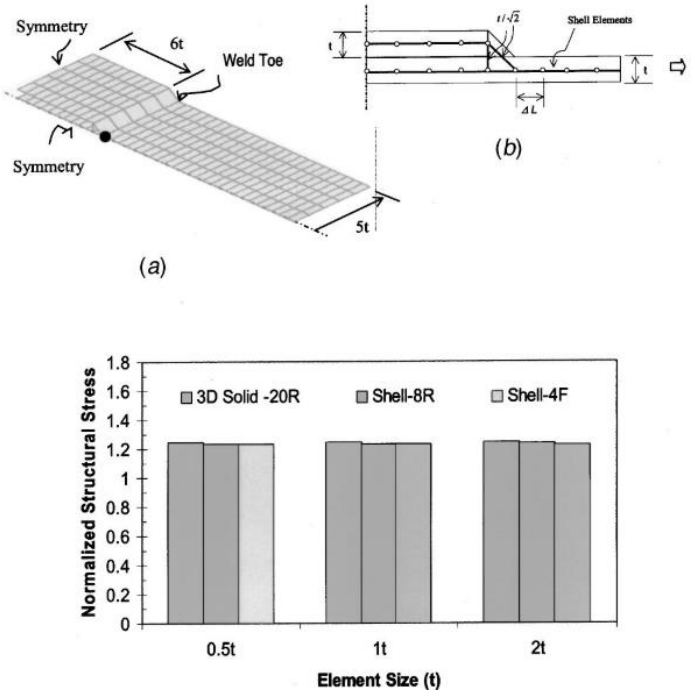

Fig. 1.13 Comparison of the traction structural stress results for a cover plate fillet weld: (a) shell element model; (b) 2D cross-section showing weld geometry; (c) comparison of traction structural stress at the weld toe with different element sizes and types [31].

It can be assumed that the stress at a fatigue prone location, such as the weld toe in Fig. 1.12a, can be represented by the simple equilibrium-equivalent stress, referred to as the traction structural stress (or far-field stress in fracture mechanics, Fig. 1.12b), and self-equilibrating notch stress (Fig. 1.12c), both affects the fatigue life of a welded joint. Based on the underlying force equilibrium condition of the traction structural stress, nodal forces from FEA output are used to calculate the traction structural stress. The calculation procedure has been demonstrated to be rather mesh-insensitive (see Fig. 1.13) because the equilibrium of nodal forces is always satisfied at nodes [31], unlike the stress output.

Based on the traction structural stress, Dong et al. further derived an equivalent structural stress range parameter [32,35] using fracture mechanics that cover the contribution from the self-equilibrating notch stress. This parameter can correlate a large amount of S-N data from various joint types, thicknesses, loading modes, and forms a narrow scatter band [31,32], which is the basis of the master S-N curve, proving its effectiveness in characterizing essential fatigue failure mechanisms. This method has been adopted by ASME Div.2 Code since 2007. With the equivalent structural stress range parameter, only the master S-N curve is needed for the fatigue assessment of various welded joints.

The above four fatigue evaluation methodologies can all be used for assessing distortion effects on fatigue. Nevertheless, the nominal stress method requires much testing with carefully controlled distortion (for classification purposes), which is very difficult. The hot spot stress method and the local notch stress method rely fully on FE models with explicitly modeled distortions; due to their empirical assumptions, the analytical stress solution derived in this research cannot be used in these methods. The traction structural stress, however, is based on force equilibrium, and thus the analytical solution can be directly added to the traction structural stress.

Therefore, the traction structural stress and the master S-N curve is used for fatigue performance assessment in this research.

1.2.2 Distortions in Welded Structures

It has been well recognized that welding-induced shrinkage is responsible for distortions in welded structures [9,15]. Based on their underlying mechanisms, there are two major types of welding-induced distortion, i.e., stable distortions and unstable distortions. Stable distortions can be directly related to a given residual stress field after welding, often in a strongly nonlinear manner. Examples along this line include angular distortions observed around a fillet weld (Fig. 1.14a) or a butt weld (Fig. 1.14b). Unstable distortions are caused by structural instability, or buckling, triggered by compressive residual stresses caused by welding-induced shrinkage. Such unstable distortions in thin-walled structures often result in some distinct waveforms, as shown in Fig. 1.15. In actual structures, the distortions around welded joints could be much more complicated, such as those observed by Lillemäe et al. [41] (Fig. 1.16), because the aforementioned two types of distortions may coexist.

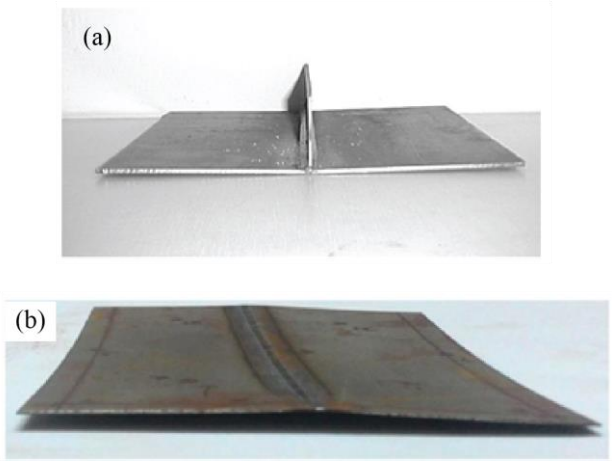

Fig. 1.14 Angular distortion: (a) around a fillet weld [42]; (b) around a butt weld [43].

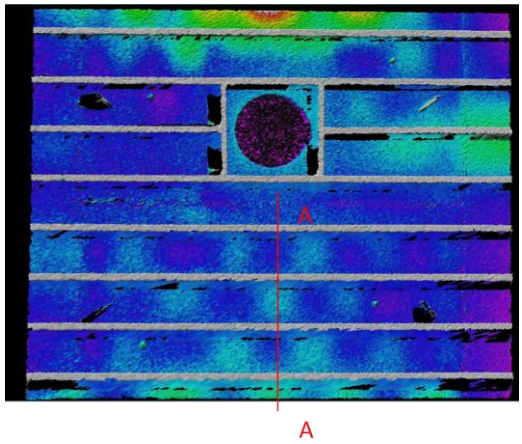

Fig. 1.15 Unstable distortions caused by buckling in a panel structure [9].

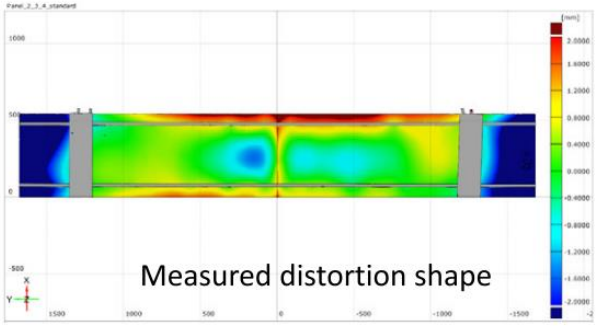

Fig. 1.16 Measured distortion in a structure-level specimen [41].

There have been numerous studies on detailed modeling of various types of distortions induced by welding [44–48]. As for modeling distortion effects on fatigue [49,50], a systematic approach is still not available. For instance, some of these investigations were focused on a specific type of distortions (e.g., angular distortions or half sinusoidal wave) observed in lab specimens and investigating their effects on fatigue by performing fatigue testing and finite element based stress concentration analysis. The findings developed are specific to the distortion types studied and difficult to be generalized for applications for actual components that often exhibit rather complex distortions. As such, there is a need for a more general approach for characterizing typical distortion modes or shapes associated with lightweight shipboard structures such that a consistent

stress concentration computational procedure can be developed for each type of distortions, and their combined contributions to a weld location can be properly accounted for.

1.2.3 Distortion Effects on Fatigue Performance

There have been a number of noted research efforts carried out over the recent years on the effects of the welding-induced residual stresses on the structural integrity in the literature, e.g., by Dong and Brust [18], Dong et al. [51], and their co-workers [15,52,53], and others [54–56] in the context of pressure vessels and piping components. In contrast, discussions on the effects of welding-induced distortions on the structural integrity of lightweight shipboard structures have been rather limited. For instance, Antoniou [57] and Carlsen and Czujko [58] studied experimental observations on some specific types of distortions observed in the ship construction environment. These studies mainly focused on structural buckling strength under compressive loading applied on plates with thicknesses greater than 10mm and did not address how distortions influence fatigue behaviors of welded structures. In current fatigue assessment and fitness-for-service (FFS) procedures, there is essentially no procedure for assessing complex distortion effects on structural integrity except for some limited provisions given in BS 7910 [59] and DNV-RP-C203 [33] for treating both simple axial and angular misalignments in butt-welded joints. Distortion curvature effects on fatigue, which may generate significant secondary bending stresses (the stresses associated with remote in-plane loading) in thin-section structures, have not been considered in any recognized Codes and Standards or recommended practices. Furthermore, the existing distortion tolerances in current code and standards stipulated by Class Societies and other Codes and Standards are mostly carried over from legacy requirements which were based on data and experiences associated with thick-section structures (e.g. [60]) or decades-old (e.g., MIL-STD-1689A [61]), and may require revisiting for their application in modern lightweight structures. For

example, Dong et al. [62] examined the fairness tolerance criteria in MIL-STD-1689A using a simple linear beam model and found that the criteria for thin plate could have significant difference with those for thick plates, as shown in Fig. 1.17.

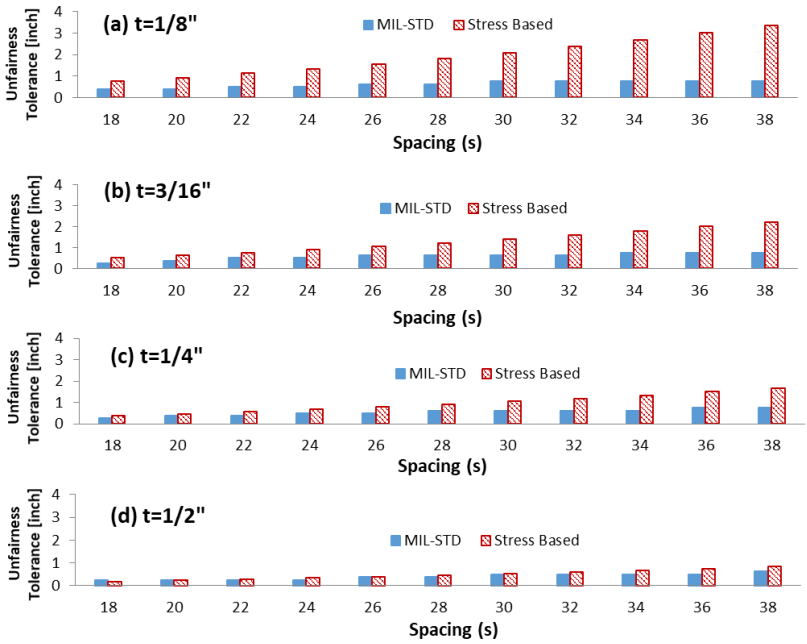

Fig. 1.17 Comparison of distortion tolerances for different thicknesses from MIL-STD-1689A and from [62].

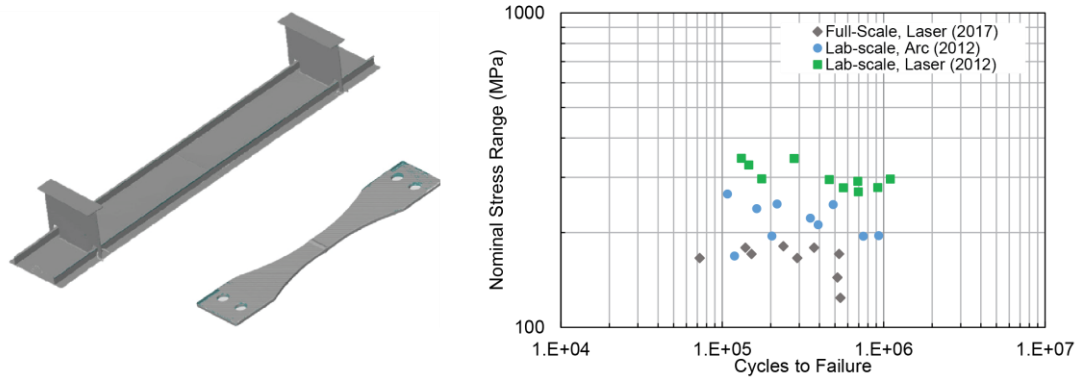

Fig. 1.18 Test study conducted by Lillemäe et al. [41,49]: (a) thin plate butt-welded full- and lab-scale specimens; (b) fatigue test data correlation using nominal stress range.

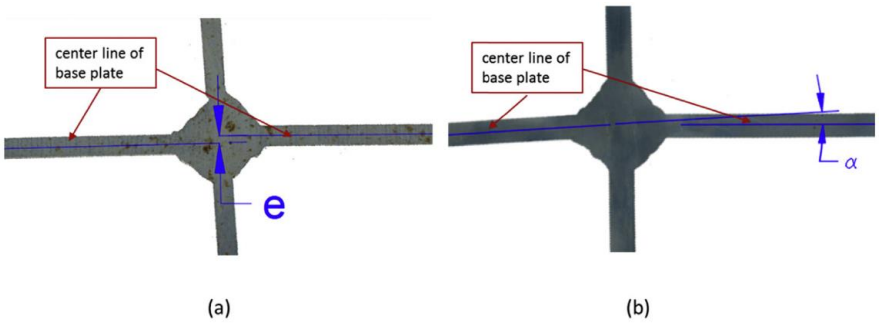

Fig. 1.19 Illustration of two joint misalignments: (a) axial misalignment; (b) angular misalignment (or global angular distortion) [63].

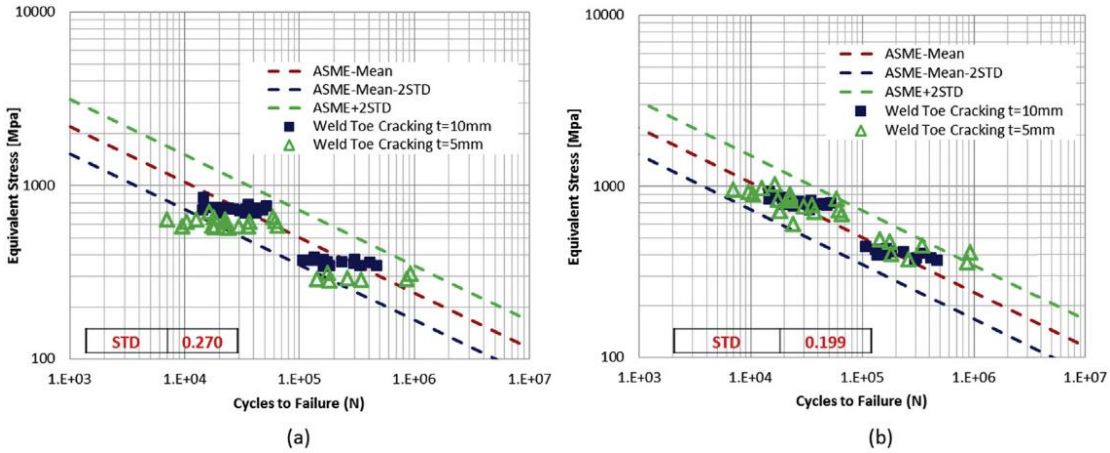

Fig. 1.20 Fatigue test data correlation in [63] using equivalent structural stress: (a) without considering misalignments; (b) with considering misalignments.

To address such a need, Lillemäe et al. [41,49] conducted a detailed investigation into how complex distortions could impact fatigue behaviors in butt-welded thin plate specimens (see Fig. 1.18a). The test data plotted in the nominal stress range (Fig. 1.18b) shows a significant level of scatter (within each type of specimen) despite the specimens having identical nominal geometry. Xing et al. [36,63,64] also studied the effects of joint misalignments (Fig. 1.19) on fatigue failure mode transition behaviors in thin plate cruciform joints by performing both experimental and finite element studies. The comparison of data correlation without (Fig. 1.20a) and with considering the misalignment effects (Fig. 1.20b) demonstrated that joint misalignments, if not properly accounted for, can cause a significant data scatter in S-N test data correlation when dealing with thin plate joints. Their studies have concluded that both axial and angular joint misalignments (the former

caused by poor fit-ups and the latter caused by welding-induced angular distortions) must be treated properly for their interaction effects at a weld location.

The most significant finding from the studies to date on distortion effects on the fatigue of welded lightweight components is that fatigue behaviors in thin plate structures tend to show a great deal of scattering, much more so than thick plate joints, regardless of stress definitions used for data interpretation, e.g., hot spot stress, local notch stress, and structural stress methods, etc. Without properly addressing this issue, the existing fatigue design procedures stipulated in Codes and Standards cannot be used with confidence, and the applicability of legacy distortion tolerance (or fairness) requirements becomes questionable.

1.2.4 Limitations in Past Studies and Existing Methods

Based on the above discussions, as far as distortion effects on fatigue are concerned, both the existing research efforts and available analysis procedures available today have the following limitations:

(a) Lack of a clearly defined procedure on how to treat complex distortions for computing secondary stresses at a joint location of interest, such as the one shown in Fig. 1.21, which often represent a combined effect of multiple types of distortions.

(b) Lack of a more generalizable method, e.g., expressed in a close form, for treating various forms of distortions or misalignments without relying on complex FE computations for fatigue evaluation of lightweight structures by taking into account actual measured distortions, which often introduce additional.

(c) Lack of an effective means for determining what types of distortions are more important than others to fatigue under the same distortion magnitude so that distortion tolerance limits in Codes and Standards can be properly defined for cost-effectiveness.

To address the above issues, a more fundamental approach is required for identifying and decomposing a given distortion shape into a series of basic distortion modes on which the secondary stresses generated under a given weld location can be more readily solved in closed forms and then assembled to represent the combined stress concentration effects of actual distortion shape.

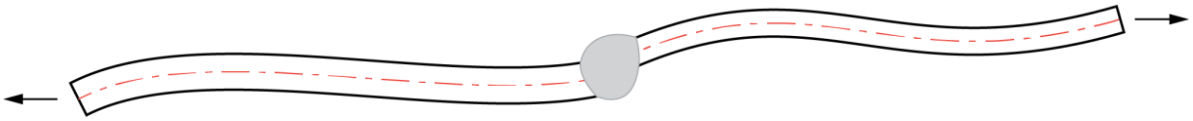

Fig. 1.21 Complex distortion condition with respect to a welded joint.

1.3 Research Objective and Approach

The major objective of this research is to develop an effective methodology for evaluating the secondary bending effects caused by welding-induced distortions on fatigue behaviors of modern lightweight structures. To ensure broad applicability of the method developed, we take a novel analytical approach which can be characterized as a "divide-and-conquer" strategy to attain the final closed-form solution to a given complex distortion problem through an assembly of its solution parts, as described below:

1. Decompose a given complex distortion problem into a series of sub-set problems corresponding to elementary distortion modes.
2. Develop analytical solutions of secondary bending stresses caused by the resulting elementary distortion modes by means of strip beam theory.
3. Introduce a consistent reference framework for facilitating the final assembly of secondary stress solutions corresponding to various elementary distortion modes involved, e.g., deformation sign definitions and position references, etc.
4. Validate the resulting closed-form solutions at both the elementary distortion mode level and the final assembled level.

5. Further validate the developed approach by examining its ability in effectively correlating available fatigue test data under various welding-induced distortion conditions with well-established traction structural stress-based master S-N curve recently adopted by ASME B&PV Div. 2 Code.

1.4 Dissertation Structure and Topic Outline

This dissertation is prepared in a multi-manuscript format. **Chapter 1** serves as an integrated introduction on the state of the art of research in welding-induced distortions in lightweight shipboard structures and the importance of addressing their effects on fatigue performance of modern lightweight structures. As such, the need for a more rigorous, consistent, and general treatment of distortion effects on fatigue is demonstrated, leading to our proposed "divide-and-conquer" approach.

Chapter 2 mainly focuses on the analytical modeling of the distortion curvatures' effects on fatigue. The notional load method is presented for providing analytical treatment of complex distortion effects on fatigue behaviors of lightweight shipboard structures together with a distortion decomposition technique. Two sets of lab-scale specimens and nine full-scale stiffened panel fatigue tests involving complex distortion shapes are also analyzed using the closed-form analytical solutions developed and achieved an excellent agreement in fatigue test data not only between butt-welded thin plate lab specimens and full-scale stiffened panels but also with the traction structural stress-based master S-N curve scatter band adopted by ASME Div. 2 since 2007.

Chapter 3 investigates the effects of axial and angular misalignment. An analytical method for computing the secondary bending actions caused by both axial and angular joint misalignments is presented with consideration of the joint representation. The closed-form analytical solutions presented have been validated by finite element analysis with joint geometry explicitly modeled.

In addition, the validity and effectiveness of the analytical solutions have been further proven by correlating some well-known fatigue test data of welded components with controlled misalignments into a single narrow band.

Chapter 4 aims to develop a general distortion mode decomposition and assembly procedure for the analytical treatment of misalignment and distortion curvature effect. The local angular distortion model is first extended to a more general extent to enable the superposition of the analytical solutions. Then, a general distortion mode decomposition and assembly procedure is established, whose objective is to provide a consistent procedure to reliably divide the complicated distortion effect on a welded joint into several sub-problems and combine the result from each sub-problem together.

Chapter 5 summarizes the analytical solutions developed in each chapter and categorizes them based on engineering application scenarios. A step by step distortion mode decomposition and assembly procedure is provided. Finally, several application examples are provided to illustrate how the analytical solutions developed can be used in real engineering problems.

Chapter 6 concludes the dissertation with key findings and the broach implications of the developed analytical approach both for understanding distortion effects on fatigue and supporting engineering applications in structural life evaluation involving various forms of distortions. Future research areas are also discussed in light of the findings from this investigation.

1.5 Publications

The following is a list of publications that have resulted from the work described in this dissertation to date.

- Zhou, W., Dong, P. "An Analytical Method for Modeling Combined Effects of Axial and Angular Misalignments on Fatigue of Welded Joints" (Submitted, 2020)

- Zhou, W., Dong, P., Lillemae, I. and Remes, H. "Analytical Treatment of Distortion Effects on Fatigue Behaviors of Lightweight Shipboard Structures." International Journal of Fatigue (2019): 105286.
- Zhou, W., Dong, P., Lillemae, I. and Remes, H. "A 2nd− order SCF solution for modeling distortion effects on fatigue of lightweight structures." Welding in the World (2019): 1-11.
- Dong, P., W. Zhou, and S. Xing. "An analytical method for interpreting distortion effects on fatigue test results of thin plate panel specimens." Welding in the World (2019): 1-8.
- Dong, P., Zhou, W., Xing, S., "Analytical treatment of welding distortion effects on fatigue in thin panels: Part II—applications in test data analysis", The 11th International Congress of the Maritime Association of the Mediterranean, 2017.
- Dong, P., Xing, S., Zhou, W., "Analytical treatment of welding distortion effects on fatigue in thin panels: Part I—closed-form solutions and implications", The 11th International Congress of the Maritime Association of the Mediterranean, 2017.
- Zhou, Wenqing, Pingsha Dong, Xianjun Pei, Özler Karakas, and Xiangwei Li. "Evaluation of magnesium weldment fatigue data using traction and notch stress methods." International Journal of Fatigue 138 (2020): 105695.

Chapter 2

Analytical Treatment of Distortion Curvature Effects on Fatigue

2.1 Chapter Introduction

There are several factors that can cause secondary bending at a welded joint in lightweight shipboard structures with distortions. Based on [49,63,65], two major factors that would affect the stress concentrations at the welded joint are the curved distortion shapes and misalignments. This chapter mainly focuses on the analytical modeling of the distortion curvatures' effects on fatigue.

The stress concentration caused by initial distortions or geometric imperfections observed in thin plate shipboard structures under fatigue loading was recently studied by several researchers. Eggert et al. [66] and Lillemäe et al. [67] performed finite element (FE) analyses using FE models incorporating detailed distortion measurements of test specimens and found that both the shape and magnitude of distortions can have significant effects on stress concentration factors calculated. However, a generalized stress concentration analysis method for incorporating various distortion modes or types remains to be found. It is worth noting that Chan et al. [68,69] and Gu et al. [70] presented a series of analytical solutions based on beam theory with presumed simple geometric imperfections described in the form of a half sine wave or a parabolic function. Even though these solutions cannot be directly applied for distortion problems of interest here, the analytical approach should be of interest for the present applications. Further along this line of analytical approach, Liew [71] introduced a notional load approach in which equivalent loads were applied against a nominally perfect geometry of a beam or a frame member to re-produce initial imperfections of interest for studying nonlinear deformation problems of beams. In a rather similar manner, Dong

et and Zhou [62,72] recently presented an analytical treatment of distortion effects on secondary stress concentration development in stiffened panel structures in which notional loads were used to model nonlinear interactions between a lateral load and out-of-plane distortions. They used their analytically calculated stress concentration factors (SCF) and achieved a very good correlation of some available fatigue test data on thin-plate butt-welded specimens exhibiting severe distortions [41,49].

In this chapter, we present a more general analytical method for computing SCF caused by various common forms of welding-induced distortions and their interactions with a lateral load (perpendicular to weld direction). Starting with some of the typical distortion shapes presented in [62,72], we introduce a classic Euler-Bernoulli beam model with notional loads that are used to re-produce various distortion modes. Then, an imperfect beam based on Timoshenko beam-column theory is introduced and solved by taking advantage of the notional loads for modeling nonlinear interactions between a distortion mode and lateral load applied. A series of analytical SCF solutions are then presented for studying fatigue behaviors observed in thin plate fatigue test specimens both at lab-scale and full-scale levels. Finally, for the treatment of complex distortions such as those observed in full-scale shipboard components, a general distortion data interpretation procedure is also presented for taking advantage of the analytical SCF solutions developed. It is found that the analytical SCF solutions developed in this study are effectively for interpreting fatigue test data available for both thin plate lab-scale and full-scale components.

2.2 Analytical Treatment of Distortion Curvatures

2.2.1 Assumptions

The analytical developments presented in this section are based on the following assumptions, which will be further validated by FE analysis at the end of this section:

a) A transverse section of a butt-seam welded or stiffened shipboard panel follows a beam theory (consistent with strip beam theory often used for analyzing ship structures)

b) Beam material is assumed to follow linear material behaviors within the loading range of concern while beam deflection and lateral load interactions can be nonlinear or in the regime of nonlinear deformation.

c) The magnitude of pre-existing beam distortions or imperfections is small compared to beam length.

d) Transverse shear deformation is negligible.

2.2.2 Method of Notional Loads

Consider the interactions between a pre-existing distortion mode $v_0(x)$ of a beam and its axial load P, as depicted in Fig. 2.1a, where P is considered positive when it generates tensile stress in the beam, and $v_1(x)$ represents an unknown beam deflection of the beam caused by P. The classic governing differential equation of such a beam with imperfections described by $v_0(x)$, incorporating geometric nonlinearity, is given as [73],

$$EI\frac{d^4v_1}{dx^4} - P\frac{d^2\left(v_0+v_1\right)}{dx^2} = 0 \tag{2.1}$$

in which E is material Young's Modulus and I represents the moment of inertia. And the secondary bending moment M_1 can be expressed as:

$$M_1 = EI\frac{d^2v_1}{dx^2} \tag{2.2}$$

Eqn. (2.1) can be solved directly with a prescribed simple initial distortion shape function $v_0(x)$, e.g., a simple one-half sine wave [69,70] or a parabolic shape [68]. For more complex distortion shapes, however, Eqn. (2.1) often becomes difficult to solve in closed form. This difficulty can be overcome if the concept of notional loads [71] is introduced. As such, consider

that an initial distortion $v_0(x)$ is caused by a set of notional loads acting on a linear Euler-Bernoulli beam, (e.g., Fig. 2.1b). The resulting $v_0(x)$ shall satisfy:

$$EI\frac{d^4v_0}{dx^4}=0. \tag{2.3}$$

Note that displacement boundary conditions on the linear beam can be imposed in a manner that best represents a pre-existing distortion shape of interest and are independent of the ones prescribed for the imperfect beam (Fig. 2.1a). To enable the superposition between the imperfect beam problem and the linear beam problem, we can add or release boundary restraints of the linear beam by replacing them with statically equivalent notional loads. As such, the constrained displacements or rotations are consistent between the linear beam and the imperfect beam, as illustrated in Fig. 2.1c.

Then, through a superposition of the two problems described in Fig. 2.1a governed by Eqn. (2.1) and Fig. 2.1c governed by Eqn. (2.3), the resulting governing equation becomes:

$$EI\frac{d^4\left(v_0+v_1\right)}{dx^4}-P\frac{d^2\left(v_0+v_1\right)}{dx^2}=0. \tag{2.4}$$

By denoting $v=v_0+v_1$, Eqn. (2.4) becomes

$$EI\frac{d^4v}{dx^4}-P\frac{d^2v}{dx^2}=0, \tag{2.5}$$

which is the governing equation of a geometrically nonlinear beam with perfect nominal geometry (Fig. 2.1d) subjected to the notional loads on the nominally perfect beam (Fig. 2.1c) and the axial force P applied to the imperfect beam (Fig. 2.1a).

Hence, the imperfect beam problem in Fig. 2.1a can be solved by first determining the loading pattern of notional loads on a linear beam (Fig. 2.1b and Fig. 2.1c) and their values, then solving the nonlinear perfect beam problem in Fig. 2.1d, which allows the determination of $v_1=$

$v - v_0$ sought. With such a procedure, we can either solve the problem by obtaining the solution to the homogeneous equation Eqn. (2.5) or use existing solutions to corresponding nonlinear perfect beam problems, avoiding solving the nonhomogeneous equation Eqn. (2.1) for every possible distortion shape of concern.

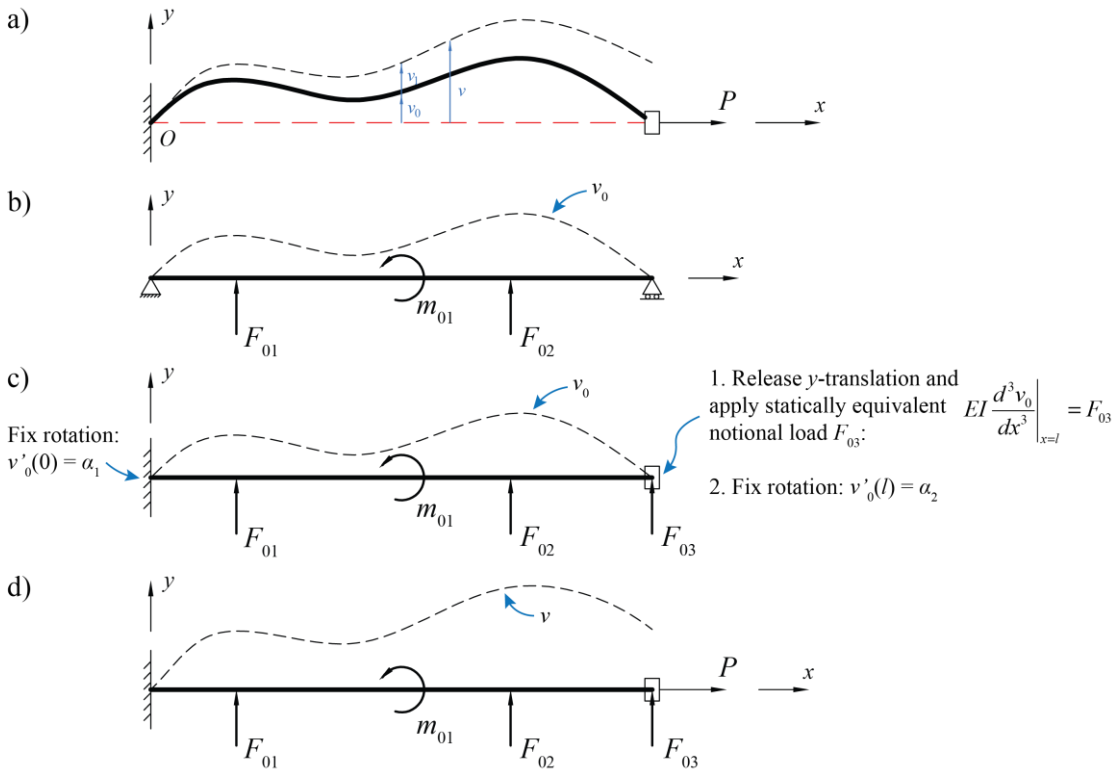

Fig. 2.1 Procedure for solving imperfect beam problems using the method of notional loads: (a) imperfect beam; (b) linear beam subjected to notional loads; (c) linear beam with adjusted boundary conditions; (d) nonlinear perfect beam with notional loads.

2.3 Analytical Solutions to Common Distortion Types

2.3.1 Distortions in Stiffened Panels

According to the detailed distortion investigations by Dong [31,53] and Yang and Dong [17], two typical distortion modes are dominant in lightweight shipboard structures, as illustrated in Fig. 2.2. One is referred to as buckling type, resulted from structural instability behaviors triggered by compressive residual stresses. Fig. 2.2a shows a LIDAR (LIght Detection and Ranging) image of a 16'×20' (4.877m×6.096m) stiffened panel, which clearly exhibits well-

defined checker-board pattern shown at the lower half of the image. The other type is referred to as cosine angular distortion, which is depicted in a sketch for clarity as shown in Fig. 2.2b. If a transverse cross-section, say along Section A-A, is considered, the two types of distortions can be depicted in Fig. 2.2c and Fig. 2.2d, respectively. Within one stiffener spacing l, the buckling distortion is defined as one-half sinusoidal waveform, while the cosine angular distortion has one-half cosine shape with no rotation at stiffener locations. For both distortion types, the stiffeners are horizontally aligned (i.e., $v_0 = 0$ at stiffener locations). The amplitude or peak distortion values for both cases are given as δ_0. In this study, strip beam theory is assumed to be applicable for simplicity, and the beams mentioned in this dissertation are all in unit width.

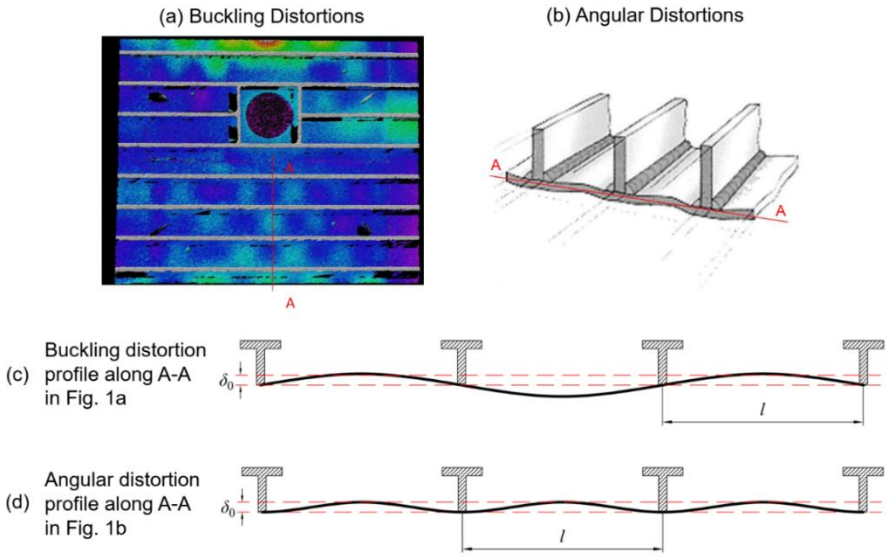

Fig. 2.2 Two major distortion types in thin plate structures [72].

2.3.1.1 Cosine Angular Distortion

According to Fig. 2.1d, an imperfect beam model representing a typical angular distortion within one stiffening spacing of l is depicted in Fig. 2.3a, in which two beam ends are restrained under embedded conditions. Such an initial distortion shape, as discussed in Sec. 2.2.2, can be represented by a linear beam subjected to a concentrated notional force F_0 at beam mid-span, as

shown in Fig. 2.3b. The magnitude of F_0 can be obtained through classic beam theory by setting beam mid-span deflection δ_0. The distortion field $v_0(x)$ can then be obtained from the linear beam theory.

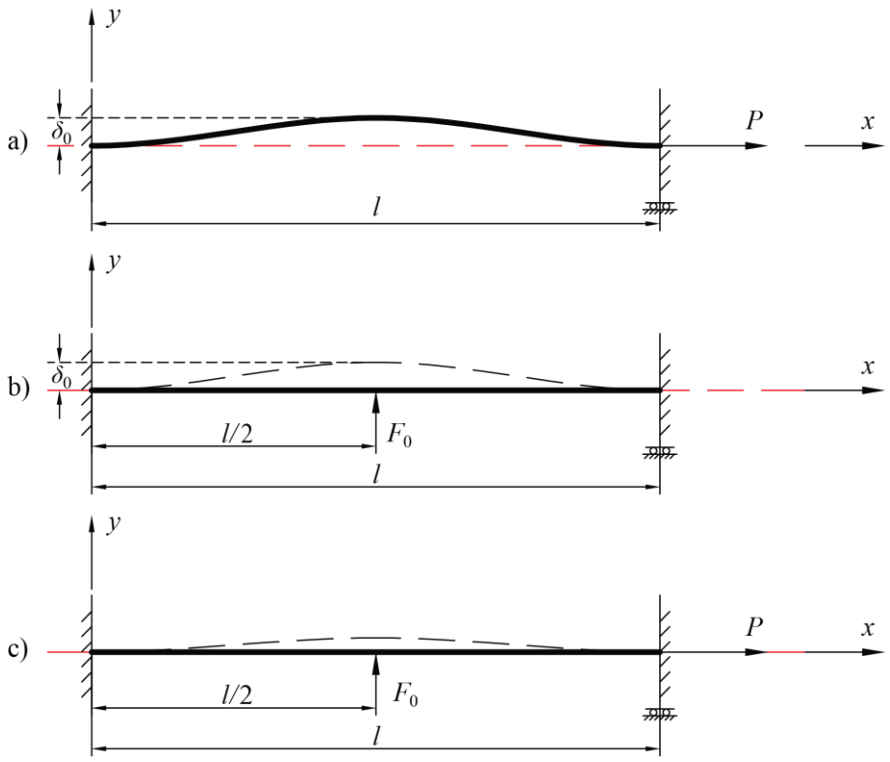

Fig. 2.3 Beam models used for modeling interactions of angular distortion with load *P*: (a) imperfect beam; (b) linear beam; (c) nonlinear perfect beam.

Using the procedure presented in Sec. 2.2.2, the secondary bending stress induced by the angular distortion as a result of lateral load P can be expressed as the bending stress concentration factor k_{b} (see Appendix A.1 for detailed solution process) at the stiffener location (i.e., $x = 0, y = t/2$):

$$k_{\mathrm{b}}=\begin{cases}-\dfrac{144}{(\lambda l)^2}\dfrac{\delta_0}{t}\left(\dfrac{4}{\lambda l}\dfrac{\cosh\dfrac{\lambda l}{2}-1}{\sinh\dfrac{\lambda l}{2}}-1\right) & P>0\\ -\dfrac{144}{(\lambda l)^2}\dfrac{\delta_0}{t}\left(\dfrac{4}{\lambda l}\dfrac{\cos\dfrac{\lambda l}{2}-1}{\sin\dfrac{\lambda l}{2}}+1\right) & P<0\end{cases}, \tag{2.6}$$

where λ is an auxiliary variable defined as

$$\lambda=\sqrt{\frac{|P|}{EI}}. \tag{2.7}$$

Note that, unless otherwise stated, all k_{b} solutions refer to the top surface (i.e., $y=t/2$) in the rest of the dissertation and that the second equations given in all k_{b} expressions are valid before the compressive axial loading magnitude reaches the model's Euler's critical load beyond which buckling occurs.

2.3.1.2 Buckling Distortions

Similarly, the buckling distortion shape illustrated in Fig. 2.2c can be represented as the deflection of a beam with two pinned ends and a concentrated notional force in the middle, as illustrated in Fig. 2.4b. The corresponding imperfect beam problem is illustrated in Fig. 2.4a, and the corresponding nonlinear perfect beam model is given in Fig. 2.4c. Then, k_{b} due to secondary bending resulted from the buckling distortion mode with respect to the stiffener ($x=0$) can be then obtained as

$$k_b = \begin{cases} 18\dfrac{\delta_0}{t}\left[\dfrac{\cosh\dfrac{\lambda l}{2}}{\lambda l \sinh\dfrac{\lambda l}{2}} - \dfrac{8}{(\lambda l)^2}\left(\dfrac{\cosh\dfrac{\lambda l}{2}-1}{\lambda l \sinh\dfrac{\lambda l}{2}}\right)\right] & P>0 \\ -18\dfrac{\delta_0}{t}\left[\dfrac{\cos\dfrac{\lambda l}{2}}{\lambda l \sin\dfrac{\lambda l}{2}} + \dfrac{8}{(\lambda l)^2}\left(\dfrac{\cos\dfrac{\lambda l}{2}-1}{\lambda l \sin\dfrac{\lambda l}{2}}\right)\right] & P<0 \end{cases} . \quad (2.8)$$

The detailed solution process is provided in Appendix A.2.

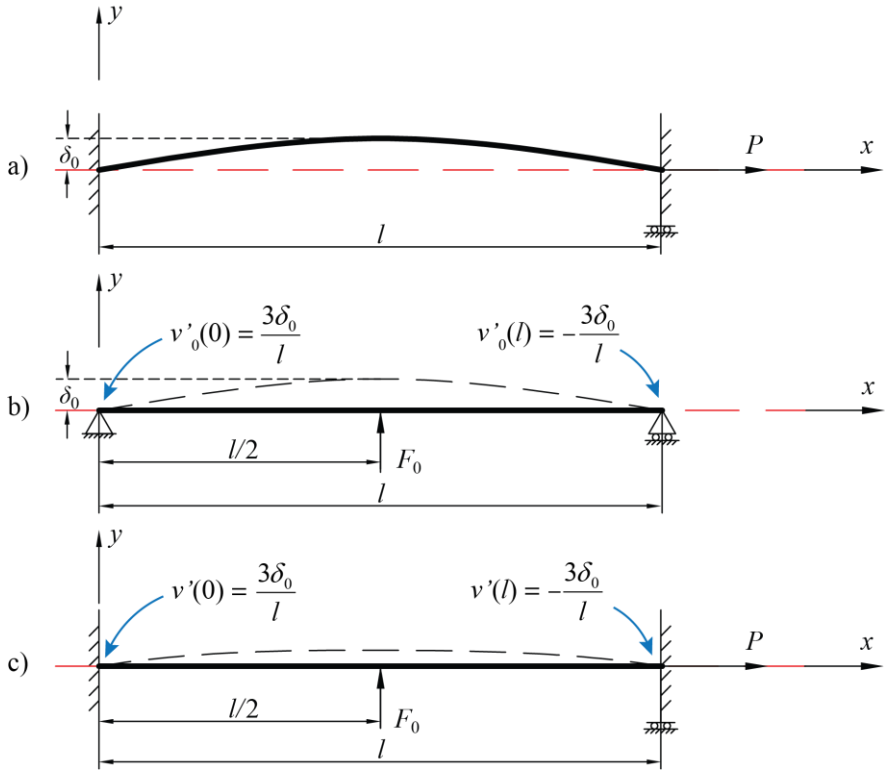

Fig. 2.4 Beam models used for modeling interactions of buckling distortion with load *P*: (a) imperfect beam; (b) linear beam; (c) nonlinear perfect beam.

2.3.2 Distortions in Butt-Welded Plates

Lillemäe et al. [49] reported some interesting fatigue tests on lab-scale butt-welded specimens with distortions characterized as shown in Fig. 2.5. Detailed axial misalignments e, angular distortions measurements in terms of $\alpha_{L,1}$ and α_G, as defined in Fig. 2.5, are also given in [49]. As a part of this study, $\alpha_{L,2}$ is also measured and used for test data analysis.

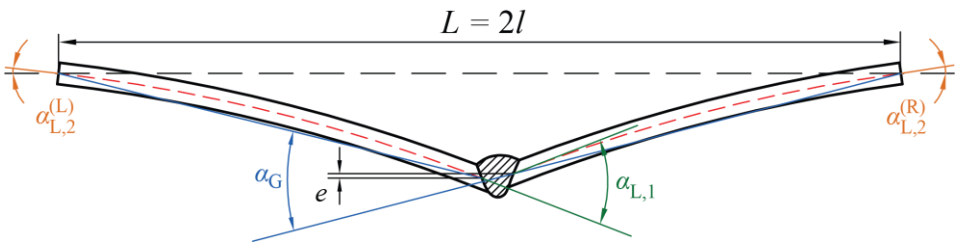

Fig. 2.5 Angular distortion definitions for butt-welded thin plate specimens [49].

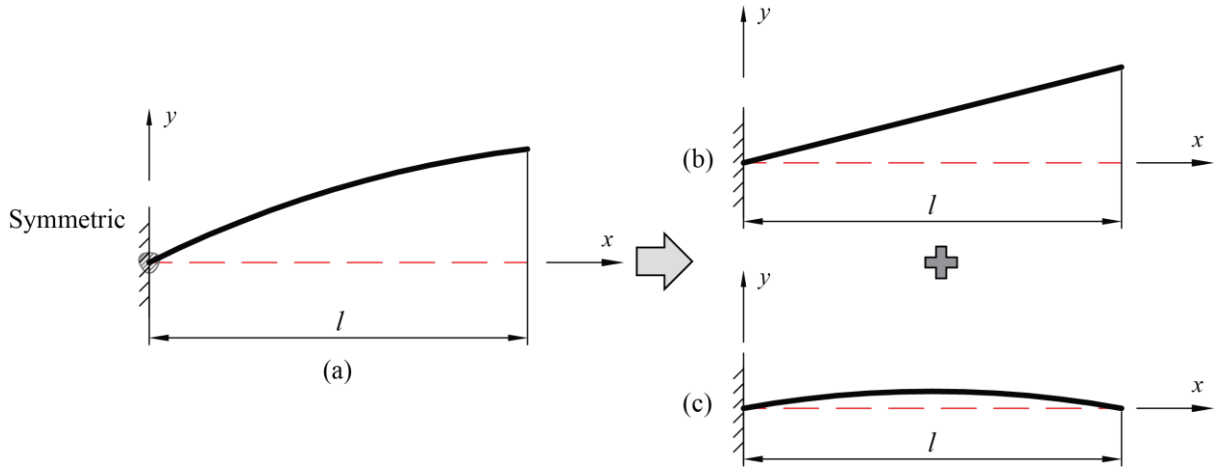

Fig. 2.6 Decomposition of complex angular distortions in butt-welded plate shown in Fig. 2.5: (a) a general distortion shape; (b) global angular distortion; (c) local angular distortion.

To demonstrate how the analytical procedure described in Sec. 2.2.2 can be used for characterizing the distortion types shown in Fig. 2.5, axial misalignment e is not discussed in this chapter since the solutions under various conditions can be found from the recent work by Xing and Dong [63] and the solution under nonlinear geometry will be further studied in Chapter 3. As far as the angular distortions shown in Fig. 2.5 are concerned, they can be assumed to be symmetric about the weld centerline and thus only one half of the specimen needs to be considered, as depicted in Fig. 2.6a. Furthermore, the distortions involved in Fig. 2.5 can be decomposed into two simple distortion modes: global angular distortion (Fig. 2.6b), which is typically referred to as angular misalignment, e.g., in BS 7910 [59], and local angular distortion (Fig. 2.6c).

2.3.2.1 Global Angular Distortion

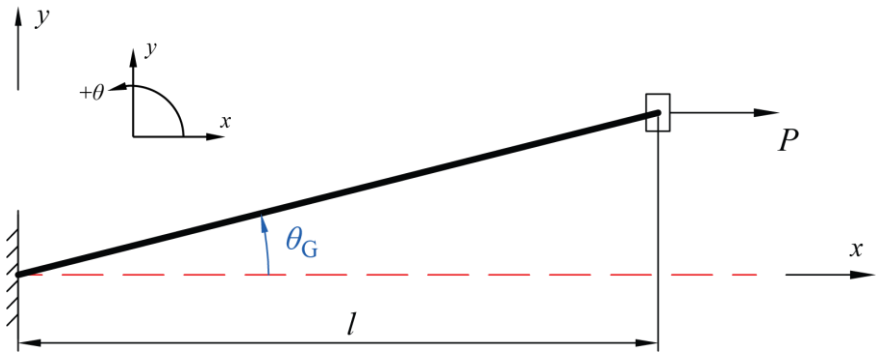

Fig. 2.7 Nonlinear beam model: global angular distortion.

The global angular distortion shown in Fig. 2.6b does not involve any curvature as pre-existing distortion. Therefore, no notional load needs to be considered when examining its interaction with a beam axial load P, according to the method described in Sec. 2.2.2. The equivalent nonlinear beam model corresponding to the clamped-end condition is given in Fig. 2.7 with the global angular distortion defined as θ_{G}. Note that the sign conventions for the rotations throughout the rest of this dissertation follows the right-hand rule, which is also given in Fig. 2.7. It then can be shown that stress concentration factor k_{b} with respect to the weld location ($x = 0$) can be solved as:

$$k_{\mathrm{b}} = \begin{cases} 6\theta_{\mathrm{G}} \dfrac{l}{t}\left(\dfrac{\cosh \lambda l - 1}{\lambda l \sinh \lambda l}\right) & P > 0 \\ -6\theta_{\mathrm{G}} \dfrac{l}{t}\left(\dfrac{\cos \lambda l - 1}{\lambda l \sin \lambda l}\right) & P < 0 \end{cases} . \tag{2.9}$$

The detailed solution process lead to Eqn. (2.9) is given in Appendix A.3. It is worth pointing out that Eqn. (2.9) is exactly the same as the one given in BS 7910 [59] for computing secondary stress caused by angular misalignment with fixed-end conditions. However, the source of this solution is not given in BS 7910 [59]. This confirms the validity of our approach as described in Sec. 2.2.2.

2.3.2.2 Local Angular Distortion

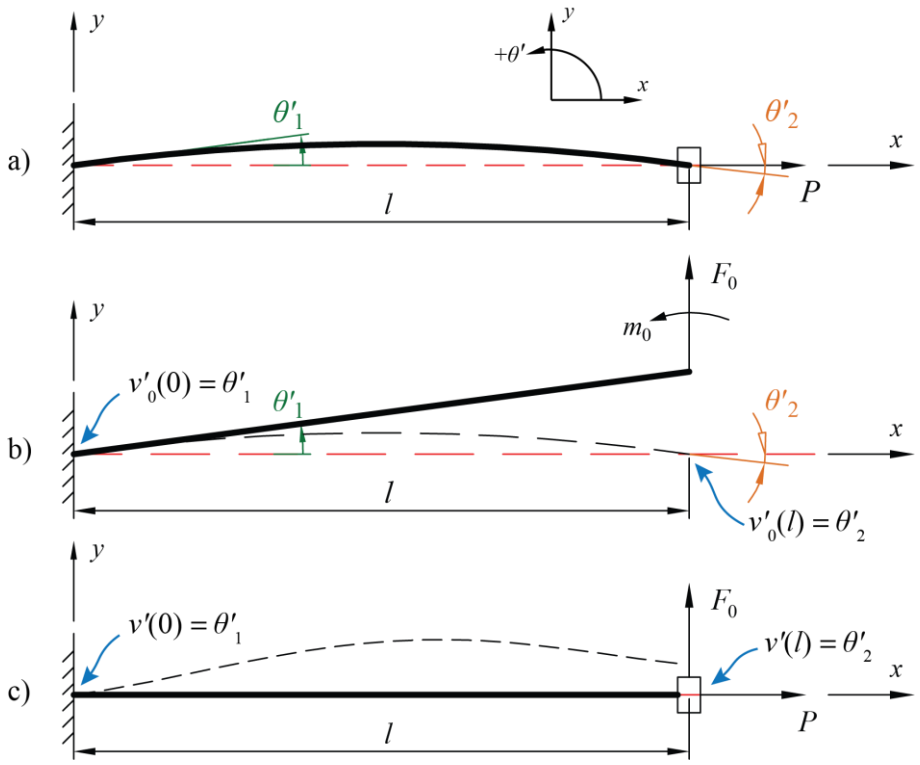

Fig. 2.8 Beam models used for local angular distortion of butt-welds: (a) imperfect beam; (b) linear beam; (c) nonlinear perfect beam.

The treatment of local angular distortion depicted in Fig. 2.6b is shown in Fig. 2.8, assuming that the distortion curvature is simple and can be fully described by the rotations at both ends θ'_1 and θ'_2 (Note: based on the coordinate definition, θ'_1 is positive and θ'_2 is negative in Fig. 2.8). Then, this type of local angular distortion can be modeled by a tilted cantilever beam loaded with a notional force and a notional moment at the free end, as shown in Fig. 2.8b. The relationships between the initial rotations θ'_1, θ'_2 and the notional loads can be determined by classic beam theory as

$$F_0 = -\frac{6EI}{l^2}\left(\theta'_1 + \theta'_2\right)$$
$$m_0 = \frac{2EI}{l}\left(\theta'_1 + 2\theta'_2\right) \tag{2.10}$$

Following the procedure described in Sec. 2.2.2, one can show that, for the nonlinear perfect beam shown in Fig. 2.8c, k_b at weld location ($x = 0$) can be expressed as

$$k_{\mathrm{b}}=\begin{cases} 6\dfrac{l}{t}\left\{\theta_1'\left[\dfrac{6}{(\lambda l)^2}\dfrac{\cosh\lambda l-1}{\lambda l\sinh\lambda l}+\dfrac{\cosh\lambda l}{\lambda l\sinh\lambda l}-\dfrac{4}{(\lambda l)^2}\right]\right. & \\ \left.\quad+\theta_2'\left[\dfrac{6}{(\lambda l)^2}\dfrac{\cosh\lambda l-1}{\lambda l\sinh\lambda l}-\dfrac{1}{\lambda l\sinh\lambda l}-\dfrac{2}{(\lambda l)^2}\right]\right\} & P>0 \\ 6\dfrac{l}{t}\left\{\theta_1'\left[\dfrac{6}{(\lambda l)^2}\dfrac{\cos\lambda l-1}{\lambda l\sin\lambda l}-\dfrac{\cos\lambda l}{\lambda l\sin\lambda l}+\dfrac{4}{(\lambda l)^2}\right]\right. & \\ \left.\quad+\theta_2'\left[\dfrac{6}{(\lambda l)^2}\dfrac{\cos\lambda l-1}{\lambda l\sin\lambda l}+\dfrac{1}{\lambda l\sin\lambda l}+\dfrac{2}{(\lambda l)^2}\right]\right\} & P<0 \end{cases} \tag{2.11}$$

2.3.3 Validation Using Finite Element Solutions

To validate the solutions developed in Secs. 2.3.1-2.3.2, including the assumptions introduced, four finite element imperfect beam models incorporating the distortion shapes considered in the previous sections are shown in Fig. 2.9. Nonlinear geometry effects are considered in all these models. All these beam models have a unit width and the same Young's modulus ($E = 210000\mathrm{MPa}$). The axial load for the models in Fig. 2.9a and Fig. 2.9b varies from $P = -317.5\mathrm{N}$ ($\sigma_n = -50\mathrm{MPa}$) to $P = 1587.5\mathrm{N}$ ($\sigma_n = 250\mathrm{MPa}$), while the minimum axial load for the models in Fig. 2.9c and Fig. 2.9d is set as $P = -114.3\mathrm{N}$ ($\sigma_n = -18\mathrm{MPa}$). The FE-based k_{b} at weld location ($x = 0$) are calculated and compared with analytical solutions in Fig. 2.10, demonstrating an excellent agreement between the analytical and FE methods for the entire axial load range.

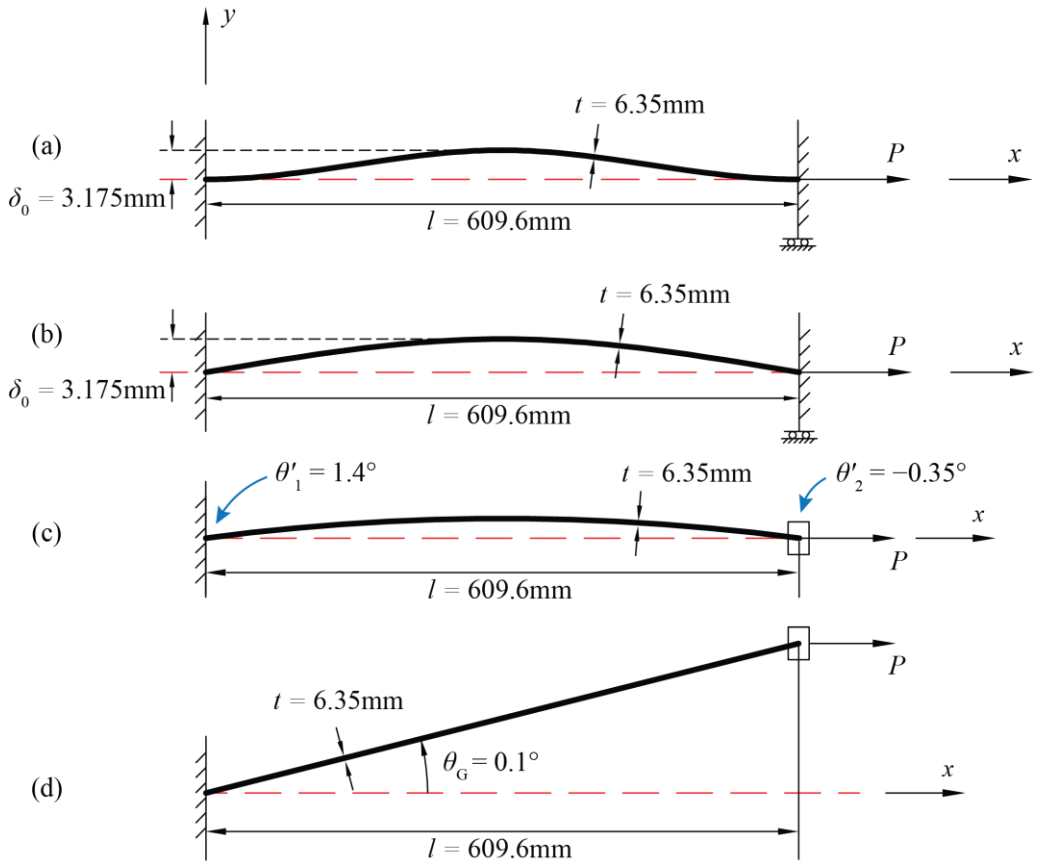

Fig. 2.9 FE beam models used for validating the analytical solutions: (a) cosine angular distortion; (b) buckling distortion; (c) local and (d) global angular distortion of butt-welds.

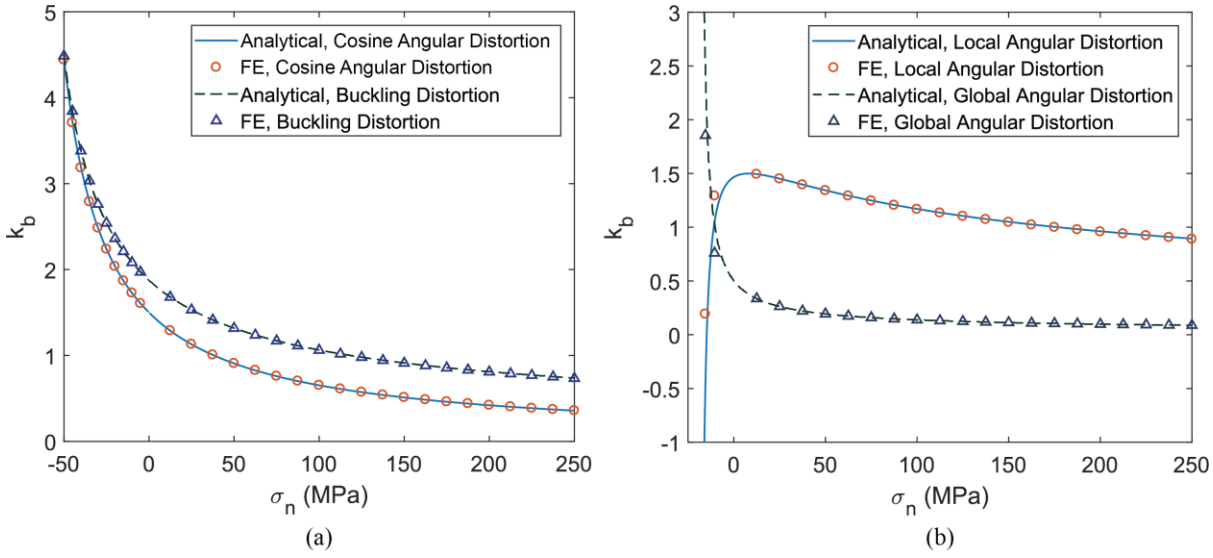

Fig. 2.10 Comparison of stress concentration factors (k_b) results between FE and analytical solutions: (a) cosine angular distortion and buckling distortion; (b) local and global angular distortions of butt-welded plate specimens.

2.4 Applications in Fatigue Test Data Analysis

2.4.1 Lab-Scale Butt-Welded Specimens

Some fatigue test results on lab-scale butt welded specimens (3 mm in thickness) were reported in [49], in which detailed geometric nonlinear finite element analysis of these specimens with measured distortions was also performed. In these cyclic tensile fatigue tests, rotations at grip positions were fixed during testing and special clamping system was used to avoid additional bending from clamping. They evaluated the feasibility of using either surface extrapolated hot spot stress or local notch stress method recommended by IIW (Hobbacher, [26]) based on the assumption of distortion shapes being simple arcs and the results are shown in Fig. 2.11. The data using either the hot spot stress (Fig. 2.11a) or local notch stress (Fig. 2.11b) spread within a factor of 10 in fatigue lives at a rather similar stress range level, especially for arc-welded specimens which are prone to larger distortions, suggesting that neither method could provide a satisfactory correlation of the test data with their assumption on distortion shape.

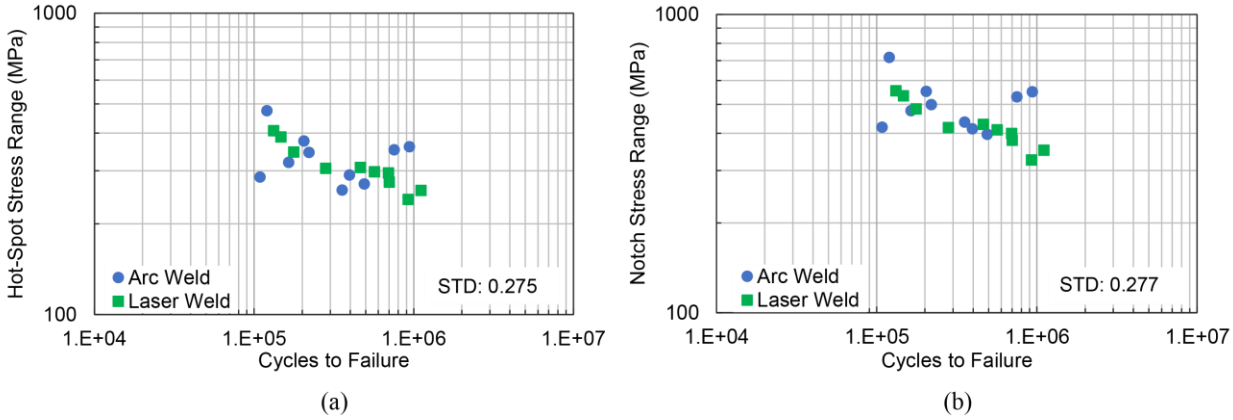

Fig. 2.11 Test data correlation using nonlinear geometry FEA calculated stress (taken from [49]): (a) IIW's surface extrapolation based hot-spot stress method; (b) IIW's effective notch stress method.

By considering the test clamping conditions as well as the distortions involved, these lab-scale specimens can be modeled as the imperfect beam illustrated in Fig. 2.12. Through a comparison between Fig. 2.5 and Fig. 2.12, the butt weld is located at $x = 0$, and the beam end angles are $\theta_1 = \alpha_{L,1}/2$, and $\theta_G = \alpha_G/2$, where α_G and $\alpha_{L,1}$ are defined in Fig. 2.5 and given in

[49]. Note that simplified distortion shapes were assumed in [49] and $\theta_2 = \alpha_{L,2}$ values were not given, thus a modified local angular distortion model is introduced to accommodate such assumption.

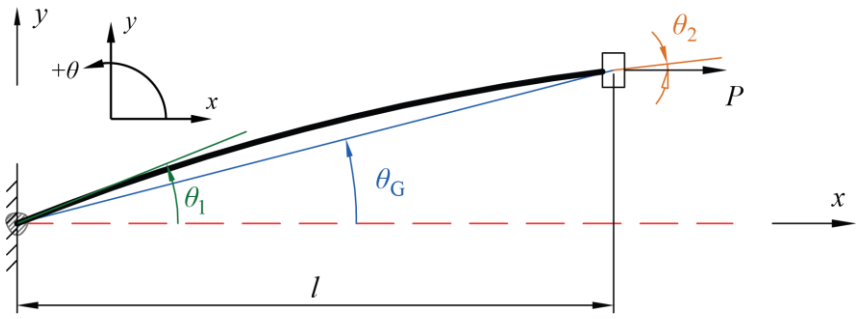

Fig. 2.12 Imperfect beam model for modeling lab-scale specimens.

Based on the development in Sec. 2.3.2, such distortions are first decomposed into global angular distortion and local angular distortion as in Fig. 2.6; thus, the global angular distortion is θ_G and the initial rotations in the local angular distortion θ'_1 and θ'_2 is obtained by $\theta'_1 = \theta_1 - \theta_G$ and $\theta'_2 = \theta_2 - \theta_G$. Since the θ_2 values are not available, we adjust the model by setting $m_0 = 0$ in the linear beam model shown in Fig. 2.8a, leading to $\theta'_2 = -\theta'_1/2$. Then, the distortion induced stress concentration factors $k_{b,global}$ and $k_{b,local}$ can be obtained through Eqns. (2.9) and (2.11), respectively. However, through a close examination of the specimens' pictures, we found that the distortion shape of several arc-welded specimens cannot be well represented by the adjusted model and thus their $\alpha_{L,2}$values are measured specifically in this study, as summarized in Table 2.1. These specimens are then treated using the approach in Sec. 2.3.2 without the adjustment discussed above.

Based upon Eqn. (2.5), we can see that the method of superposition is applicable for geometric-nonlinear beams as long as the beams have the same length l, same bending rigidity EI, and are subjected to the same axial load P, resulting in $k_b = k_{b,global} + k_{b,local}$ for each specimen. The bending stress concentration caused by axial misalignment (e) is calculated separately using

$k_e = 3e/t$ according to [63] using detailed e measurements given in [49]. The equivalent structural stress range parameter adopted by ASME Div. 2 Code since 2007 (see Dong [30–32]) can then calculated as:

$$\Delta S_s = \frac{\Delta\sigma_s}{t^{\frac{2-m}{2m}} I(r)^{\frac{1}{m}}} \tag{2.12}$$

where σ_s is calculated by

$$\sigma_s = \left(1 + k_e + k_b\right) \times \sigma_n \tag{2.13}$$

in which σ_n is the nominal stress. In Eqn. (2.12), t is the actual thickness of the specimen at the crack location, m is given as 3.6, and $I(r)$ is a dimensional polynomial function of bending ratio $r = (k_e + k_b)\sigma_n/\sigma_s$. And the structural stress range $\Delta\sigma_s$ in Eqn. (2.12) becomes simply $\Delta\sigma_s = \sigma_{s,\max} - \sigma_{s,\min}$.

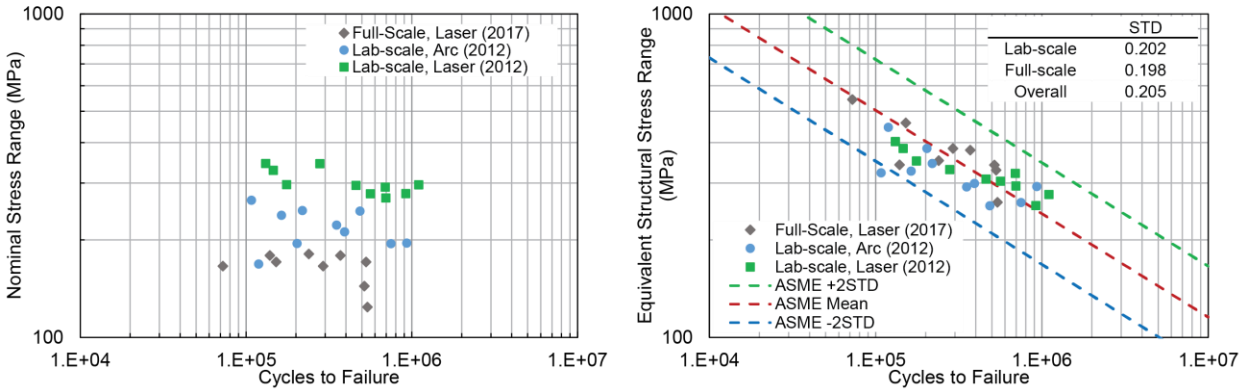

Fig. 2.13 Data correlation using: (a) nominal stress range; (b) equivalent structural stress range given in 2007 ASME master S-N curve incorporating analytically calculated k_b due to global and local angular distortions and k_e caused by axial misalignments.

Table 2.1 Measured $\alpha_{L,2}$ values for lab-scale specimens

Specimen no.	$\alpha_{L,2}$ deg
Arc 7	-1.71
Arc 9	-0.69
Arc 10	-1.90
Arc 11	-1.89

With the equivalent structural stress range in Eqn. (2.12), the same fatigue test results given in Fig. 2.11 are replotted in Fig. 2.13b, labeled as "lab-scale" specimens. It can be seen that the same test data not only show a significantly improved correlation with a standard deviation of 0.202, but also exhibit a clearly defined slope. For comparison purpose, the nominal stress range-based plot of the same test data is also given in Fig. 2.13a and the master S-N curve scatter band from ASME [74] as dashed lines in Fig. 2.13b. It is interesting to note that in Fig. 2.13b that the butt-welded lab-scale specimen data fall within 2007 ASME's master S-N curve scatter band which represents about 1000 large scale fatigue tests with plate thickness varying from 5mm up to over 100mm.

2.4.2 Full-Scale Stiffened Panels

Lillemäe et al. [41] also conducted detailed distortion measurements and fatigue tests of full-scale stiffened specimens (see Fig. 2.14). Prior to fatigue testing, the distortion profiles were measured and documented for a total of nine specimens (Fig. 2.14b) along mid-width, as summarized in Fig. 2.15. The fatigue tests were conducted at a load ratio of $R = 0.1$. In what follows, a procedure for taking advantage of the analytical approach given in Sec. 2.2.2 will be discussed.

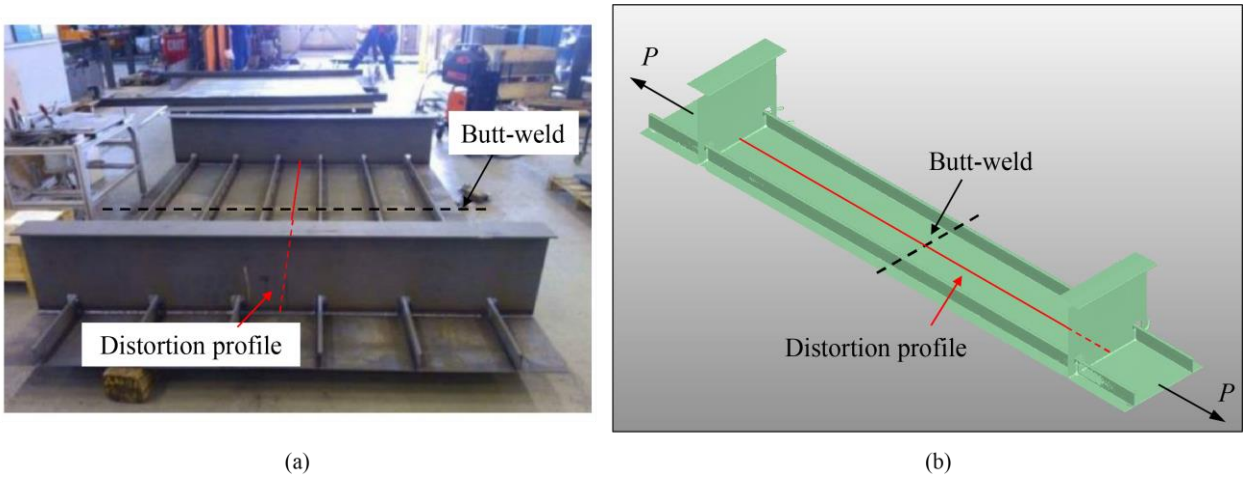

Fig. 2.14 Full-scale stiffened panel (4-mm thick base plate) and full-scale fatigue test specimen containing a hybrid laser butt-weld [41]: (a) Full scale stiffened panel; (b) Illustration of full-scale fatigue test specimen extracted from (a) for distortion measurements and fatigue testing.

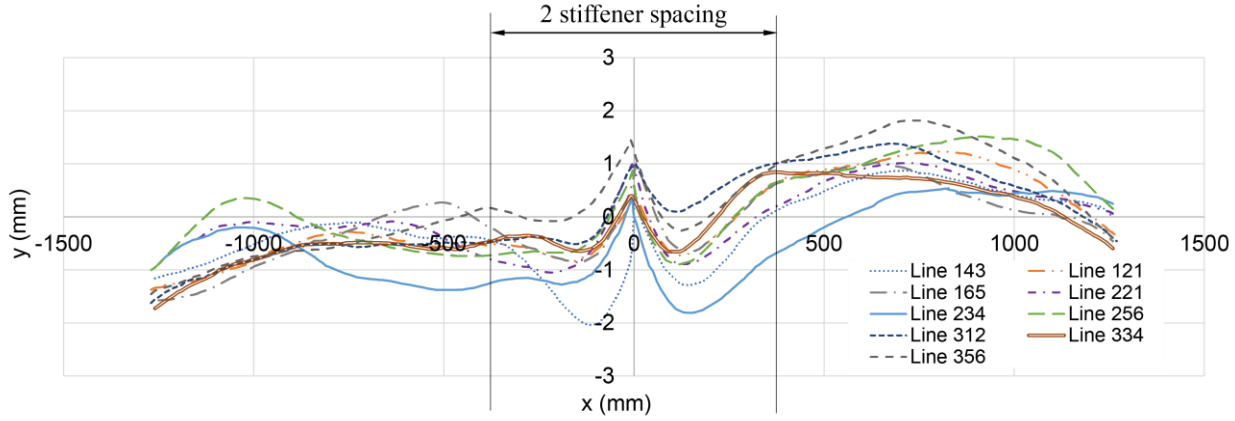

Fig. 2.15 Out-of-plane distortion profiles measured along mid-width line of nine full-scale fatigue specimens prior to fatigue testing [41] **(The transverse butt weld is located at $x = 0$).**

2.4.2.1 Distortion Profile Characterization

As illustrated in Fig. 2.2, there exists a characteristic length scale in terms of stiffener spacing (l) for characterizing welding-induced distortions in stiffened shipboard panels. With this consideration, a characteristic distance of two stiffening spacing of two-stiffener spacing ($2l$) or one spacing (l) on one side of the butt weld is considered as shown in Fig. 2.15. As a result, distortion profiles on one side of the butt weld are considered for further analysis.

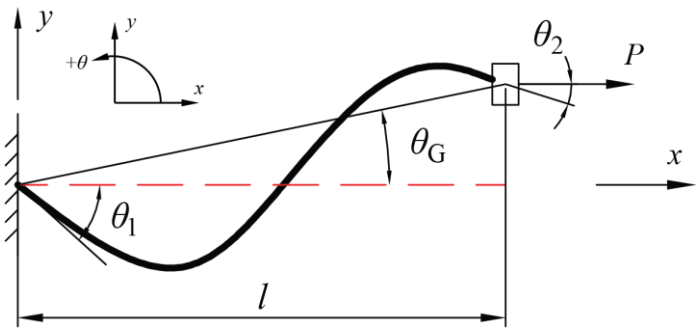

Fig. 2.16 Characteristic distortion profile serving as initial beam imperfections for treatment of distortions in full-scale fatigue specimens

Upon further inspection, the distortion profiles within one characteristic length l from the welded joint (Fig. 2.15) can be represented by a characteristic profile illustrated in Fig. 2.16, which is used as the initial imperfections of a beam, as discussed in Sec. 2.2.2, with the left end (weld location) embedded and the rotation fixed at the right end. As such, θ_1, θ_2 and θ_G are parameters that can be adjusted to provide the best fit of the distortion profiles shown in Fig. 2.15. It is worth noting that the initial distortion profile described in Fig. 2.16 is, in fact, the same as the one shown in Fig. 2.12. Thus, the local and global angular distortion modes discussed in Sec. 2.3.2 can also be used to model such distortion.

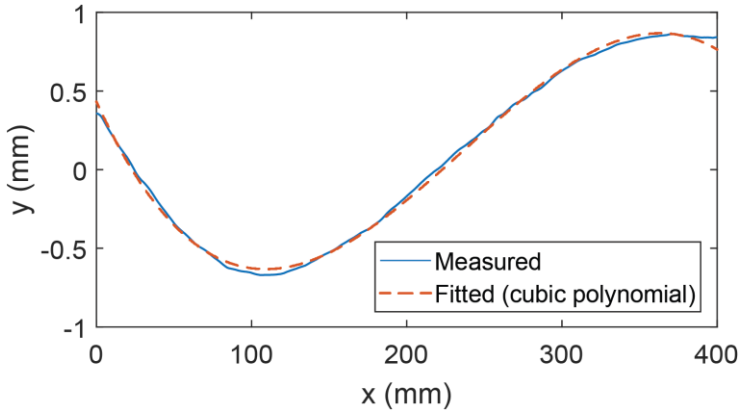

Fig. 2.17 Cubic polynomial fitting of measured distortions (Specimen 334, right side).

Without losing generality, consider the distortion profile corresponding to Specimen 334 (see Fig. 2.15); the corresponding measured distortion profile (the solid line in Fig. 2.17) can be

reasonably fitted into a third order polynomial model, i.e., $v_0(x) = a_0 + a_1 x + a_2 x^2 + a_3 x^3$ (see the dashed lines in Fig. 2.17). Because the beam deflection curve corresponding to the model in Fig. 2.16 is also a cubic polynomial function based on the classical beam theory, the good agreement shown in Fig. 2.17 should not be surprising at all. In the same manner, a cubic polynomial representation for all other distortion profiles in Fig. 2.15 can be established for further analytical treatment in secondary bending stress calculations.

2.4.2.2 SCF Calculation and FE Validation

With the distortion function $v_0(x)$ given by the third order polynomial (see Fig. 2.17), beam end rotations θ_1, θ_2 can then be obtained by $\theta_1 = v'_0(0)$ and $\theta_2 = v'_0(l)$. The corresponding global angular distortion is given by $\theta_{\mathrm{G}} = [v_0(l) - v_0(0)]/l$. Similar to the procedure discussed in Sec. 2.4.1, the local angular distortions θ'_1, θ'_2 are obtained by $\theta'_1 = \theta_1 - \theta_{\mathrm{G}}$ and $\theta'_2 = \theta_2 - \theta_{\mathrm{G}}$. Then, stress concentration factors corresponding to the global and local angular distortions can be directly obtained using Eqns. (2.9) and (2.11) in Sec 2.3.2, referred to as $k_{\mathrm{b}} = k_{\mathrm{b,global}} + k_{\mathrm{b,local}}$.

For validation purpose, two shell element models are used here. One is a full-scale specimen model shown in Fig. 2.18a and the other is a local model with only one stiffener spacing on each side of the transverse butt weld (or "$2l$" model in Fig. 2.18b). In both cases, the actually measured distortion fields provided in [41] were mapped onto these models as coordinate changes in z-axis before remote tension loading was applied. The k_{b} values were calculated using the mesh-insensitive method [75] by means of a matrix equation that transforms nodal forces/moments from an FE calculation to nodal line force/moments at a specified remote tension load level or nominal stress (σ_n) level.

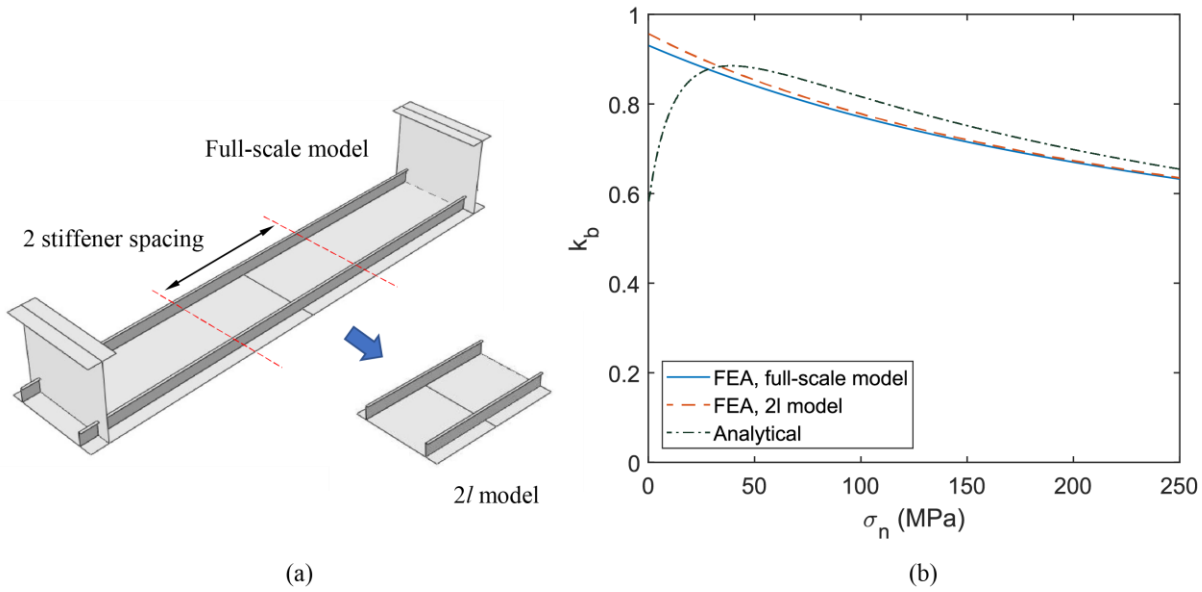

Fig. 2.18 Validation of analytically calculated k_b using FE models incorporating actual measured distortions: (a) Full-scale and characteristic length based FE models used; (b) Comparison of k_b results at weld toe at mid weld length.

Both FE and analytical results of k_b are compared in Fig. 2.18b. The two FE solutions are consistent with each other over the entire remote load (i.e.,σ_n) range evaluated, suggesting the use of a characteristic length of $2l$ is a reasonable assumption. When the applied nominal stress is greater than 50MPa, the analytical results are consistent with the FE results, being slightly higher (about 5%). In a rather low nominal stress region, say below about 30MPa, the strip beam model seems too flexible, resulting in an under-estimated k_b. It should be noted that such an under-estimation in low nominal stress regime tends to have a limited impact on the structural stress range calculated since an error in $\sigma_{s,\min}$ is also scaled by a small $\sigma_{n,\min}$ value. Therefore, the results in Fig. 2.18b further justifies the approach proposed here by considering a strip beam model representing a given longitudinal panel through-thickness section.

2.4.2.3 Fatigue Data Correlation

With analytically calculated k_b values for all nine full-scale fatigue test specimens under loading ranges documented in [41], and k_e which is computed in the same manner as in Sec. 2.4.1

based on the axial misalignment measured from Fig. 2.15, the test data can be represented using the equivalent structural stress range given in Eqn. (2.12)corresponding to fatigue crack locations (see [41]) for data correlation purpose. The results are given in Fig. 2.13b, labeled as "full-scale" specimens. The nine full-scale test data surprisingly correlate well with one another, forming a narrow scatter band near the ASME master S-N curve mean line. The standard deviation (STD) of the nine data is calculated as 0.198. In contrast, the nominal stress range based plot in Fig. 2.13b for the same set of the data shows no clearly defined trend. Furthermore, both full-scale and lab-scale tests in Fig. 2.13b fall within the ASME master S-N curve's mean$\pm$2STD scatter band [32], suggesting the validity of both sets of test data and applicability of the ASME master S-N curve for fatigue evaluation of lightweight shipboard panel structures.

2.5 Chapter Conclusions

In this chapter, a notional load method is presented for providing analytical treatment of complex distortion effects on fatigue behaviors of lightweight shipboard structures through a distortion decomposition technique. Its applications for analyzing secondary bending stresses caused by nonlinear interactions between four common distortion types induced by welding and remotely applied load are discussed in detail. In addition, two sets of lab-scale specimens and nine full-scale stiffened panel fatigue tests involving complex distortion shapes are also analyzed using the closed form analytical solutions developed. The analytically calculated stress concentration factor results are validated by direct finite element computations in all cases. Furthermore, an excellent agreement in fatigue test data is achieved not only between butt-welded thin plate lab specimens and full-scale stiffened panels but also with the traction structural stress based master S-N curve scatter band adopted by ASME Div. 2 since 2007. Some of the specific findings are worth noting, including:

(a) With the proposed method of notional loads, the imperfect beam problem is converted into a nonlinear perfect beam problem. As a result, existing nonlinear perfect beam solutions with a specified loading pattern can be used for deriving closed-form analytical k_{b} solutions for typical distortion modes of interest.

(b) With such an analytical approach, only a few distortion measurements are needed for evaluating fatigue performance of weld joints in lightweight structures, significantly reducing the needs for full-field distortion measurements and their mapping onto a structural FE model.

(c) Welding-induced distortions are shown to have significant effects on fatigue behaviors in welded thin-plate structures. Without appropriate treatment for secondary bending stresses, available test data cannot be correlated with existing data that support existing Codes and Standards (see Figs. 11 and 13a). The analytical approach presented in this paper proves effective for interpreting fatigue test data obtained in welded thin plate components.

(d) The very fact that thin-plate test data (lab-scale and full-scale specimens) fall into the scatter band of the master S-N curve adopted by ASME Div. 2 suggests not only their relationship to existing thick plate fatigue test data, but also the applicability of the master S-N curve method for fatigue evaluation of lightweight structures.

Chapter 3

Analytical Treatment of Modeling Combined Effects of Axial and Angular Misalignments on Fatigue of Welded Joints

3.1 Chapter Introduction

The demands for structural lightweighting of transportation systems have intensified over the last decade or so, largely driven by environmental sustainability concerns [1]. One major trend along this line is a significant increase in the use of high strength thin plates in marine structures, as recently discussed by Huang et al. [9,14], Xing et al. [36,64], and Lu et al. [38]. The construction of these lightweight structures can be particularly challenging since they are prone to various forms of welding-induced distortions [15,17,53]. Two common forms of distortions are typically referred to as axial and angular misalignments with respect to the load-carrying member (i.e., the horizontal member Fig. 3.1). Note that the definition of axial misalignments here also includes the conditions corresponding to butt-welded joints between two plates of different thicknesses [76], as illustrated in Fig. 3.2, which have become increasingly common in structural lightweighting [9,14], referred to as thick "insert" plate into the thin base plate in marine structures or "tailor-welded blanks" in automotive structures [77]. These misalignments can cause additional secondary bending stress or stress concentration at the weld location and significantly degrade the fatigue performance of welded joints subjected to time-varying service loading conditions.

There have been numerous investigations on both some specific effects of the two types of joint misalignments on fatigue performance and how to effectively model the resulting secondary bending stresses. Some noted efforts include: analytical and experimental studies such as those on

load-carrying fillet-welded cruciform joints by Berge and Myhre [78], Andrews [79], Jakubczak et al. [80] and those on butt joints by Wylde and Maddox [81], Iwata et al. [82]; numerical studies by Pachoud et al. [83], Ottersböck et al. [84] using local approaches; Lotsberg [85] and Liu et al. [86] on the plate thickness mismatch-induced misalignment (see Fig. 3.2) effects on fatigue. These studies have shown that seemingly acceptable misalignments can still introduce a rather high stress concentration at welded joints, causing significant fatigue performance degradation both in laboratory testing and service loading conditions. More recently, fatigue tests done by Xing et al. [63,64] have further demonstrated that misalignments have more pronounced effects on thinner plate joints, particularly on the weld toe fatigue failure mode in fillet-welded load-carry cruciform specimens. These studies have highlighted the importance of determining stress concentration factors (SCF) caused by various forms of joint misalignments, particularly in the form of closed-form solutions for supporting reliable fatigue evaluation of lightweight welded structures.

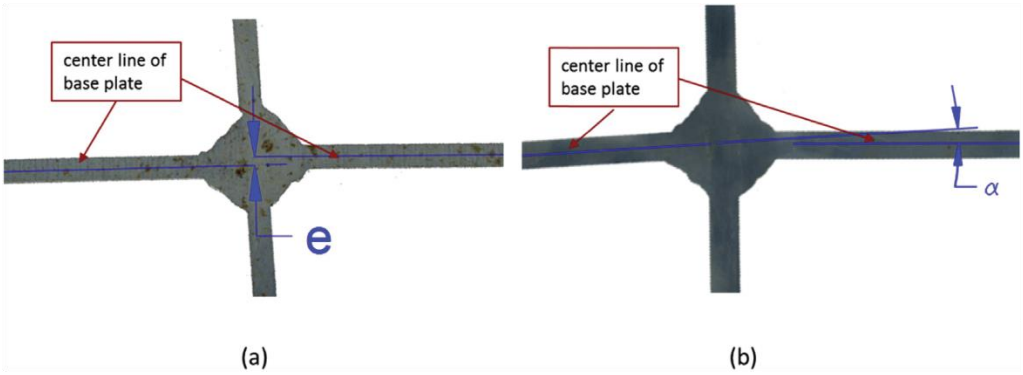

Fig. 3.1 Two types of joint misalignments [63]: (a) axial misalignment; (b) angular misalignment.

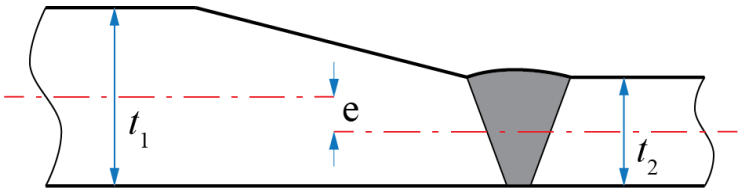

Fig. 3.2 Axial misalignment caused by thickness mismatch across a joint [33].

There exist numerous closed-form equations for calculating SCF caused by joint misalignments in the literature. Some of the earlier classical SCF equations can be traced back to the original work by Berge and Myhre [78] and further evaluated experimentally by conducting fatigue testing on welded joints with controlled misalignments [81,87]. Some of these equations have been adopted by existing Codes and Standards, such as BS 7910 [59], DNV-RP-C203 [33], and IIW Recommendations [25]. Most of the SCF formulae were developed based on either test data or FE results, and their validity can only be assured within the confinement of common joint configurations considered in their studies. To provide a more general SCF solution to cover more cases, particularly on thin-plate joints, Xing et al. [63] analytically derived an SCF solution based on beam theory under various boundary conditions and achieved a significantly improved fatigue test data correlation. Zhou et al. [88,89] have recently introduced an analytical method for incorporating curvature effects into the SCF caused by axial and angular joint misalignments. Their studies have demonstrated that the secondary bending effects due to both distortion curvature and misalignments can be effectively modeled with a notional load approach, leading to a set of closed-form solutions.

However, a critical assessment of the existing SCF formulae in the literature as discussed above reveals the following limitations: 1) most of the classical solutions used in current Codes and Standards [25,33,59] rely on empirical data or limited finite element solutions, resulting in limited applicability, particularly for thin section lightweight components; 2) in constructing these existing SCF expressions, the analytical models used all ignored the physical presence of a welded joint which could have significant effects on stress concentration behaviors, e.g., actual positions of the weld toe or stiffness change, even in beam-based models; 3) when both the axial and angular misalignments are present at a joint, there lacks a consistent procedure for defining joint

misalignments so that the resulting SCFs can be superimposed properly at a weld toe position of interest; 4) nonlinear geometry effects were only considered for limited conditions, which can have significant effects on thin-section structures.

In this chapter, we present an analytical method for systematically computing the secondary bending stresses caused by misalignments by incorporating the presence of a welded joint upon which the interactions between angular and axial misalignments can be explicitly captured. We first introduce an analytical model containing a fillet-welded joint for which both and angular misalignments are assumed to be present and consistently defined. After establishing the governing equations in the context of beam bending theory and imposing relevant boundary conditions, we then show that both geometrically linear and nonlinear solutions can be found in closed forms. For selected cases, finite element solutions are then used for validating the analytical developments. Finally, we show that the new analytical solutions can be used to effectively interpret fatigue test data of welded components containing both axial and angular misalignments.

3.2 Analytical Model

3.2.1 Assumptions

The following assumptions are made to facilitate the development of the close-form solutions:

a) The material is assumed to follow linear elastic behavior.

b) The magnitude of axial misalignment is small compared with the structural members' length, and the angle of angular misalignment is small ($\leq 5°$)

c) Transverse shear effects are negligible.

3.2.2 Joint and Misalignment Definitions

Fig. 3.3 shows a typical load-carrying fillet-welded connection that contains both axial and angular misalignment. The joint is represented by the shaded region between Sections A-B and C-D. Positions A, B, C, D are the four weld toes of interest for SCF evaluations. The base plate on the left is referred to as Member 1, which has a thickness of t_1 and a length of l_{1b}, and the member on the right as Member 2, which has a thickness of t_2 and a length of l_{2b}, respectively. Either member is modeled as a beam section with a unit width into the paper. The length of each member is measured from the weld toe to the end of that member. In this context, the joint size is defined as $l_{joint} = 2l_t$ in terms of its horizontal span or the distance between Sections A-B and C-D. In order to facilitate the analytical derivation process in the next section, a global coordinate system (x, y, θ) and some local x-coordinates (x_1, x'_1, x_2) for each member are also given in Fig. 3.3.

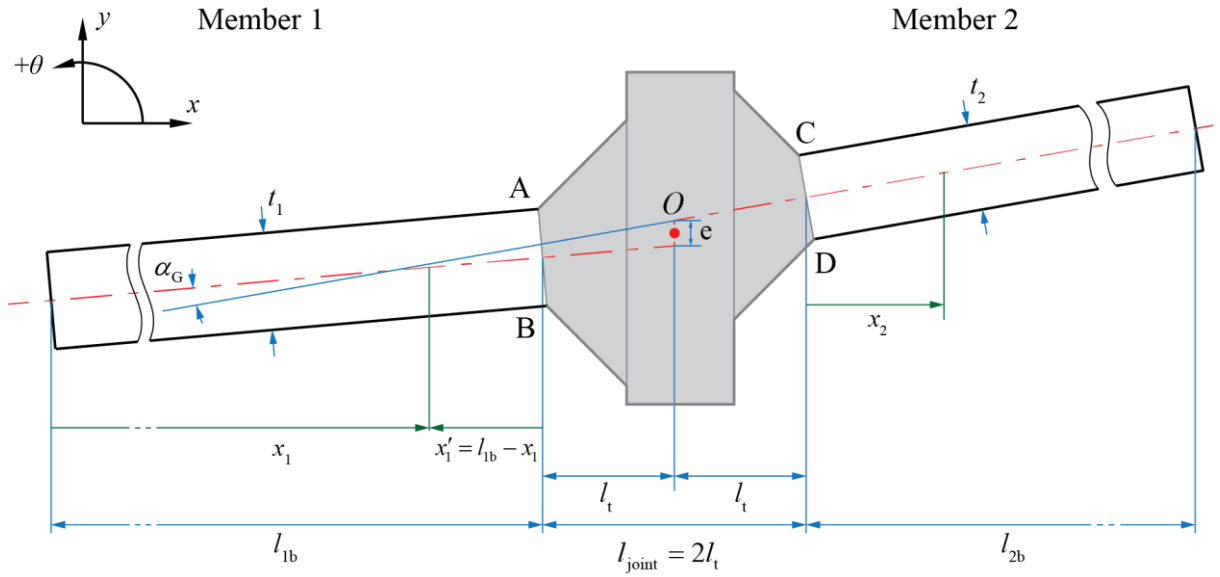

Fig. 3.3 Representation of the joint in analytical model and definitions of axial and angular misalignment.

Axial misalignment e is defined as the vertical distance between the center lines of Member 1 and that of Member 2 at the joint center position (Position *O*), as shown in Fig. 3.3. Angular misalignment α_G is defined as the angle formed between the centerlines of the two members. The sign of the axial misalignment is positive if the centerline of Member 2 is above

that of Member 1 at the joint center and vice versa, as shown in Fig. 3.4a. The sign of the angular misalignment is positive when the "arrow" formed by the two center lines points downward and vice versa, as illustrated in Fig. 3.4b. The sign of an angular misalignment can also be quantitatively determined based on the slope of each member, θ_{1G} and θ_{2G}, as discussed later in Sec. 0.

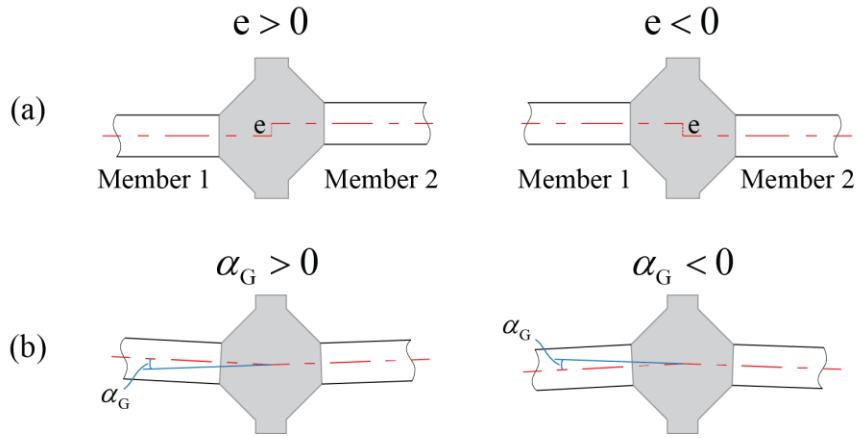

Fig. 3.4 Sign conventions of (a) axial misalignment; (b) angular misalignment.

3.2.3 Analytical Formulation and Solutions

In welded structures, joint areas typically have a complex geometric profile, as illustrated in Fig. 3.3. The resulting bending stiffness can be treated approximately as a rigid section for computing traction structural stresses without losing noticeable accuracy [31]. As such, we denote $v^{(1)}$, $M^{(1)}$, $V^{(1)}$ and $v^{(2)}$, $M^{(2)}$, $V^{(2)}$ as the final displacement, bending moment, and shear force of Member 1 and Member 2, respectively. The slope of each member at weld toe position (i.e. $x_1 = l_{1b}$ and $x_2 = 0$) are θ_{1G} and θ_{2G}, as shown in Fig. 3.5. The angular misalignment can be represented by $\alpha_G = \theta_{2G} - \theta_{1G}$. It is also assumed that an axial tension load P load is applied as shown.

3.2.3.1 Small Deformation Conditions

The analytical model defined in Fig. 3.3 is analyzed under small deformation conditions (i.e., without geometric nonlinearity) first. The axial load *P* acting on each member is assumed to follow the centerline direction of that member to model its interaction with the angular misalignment explicitly.

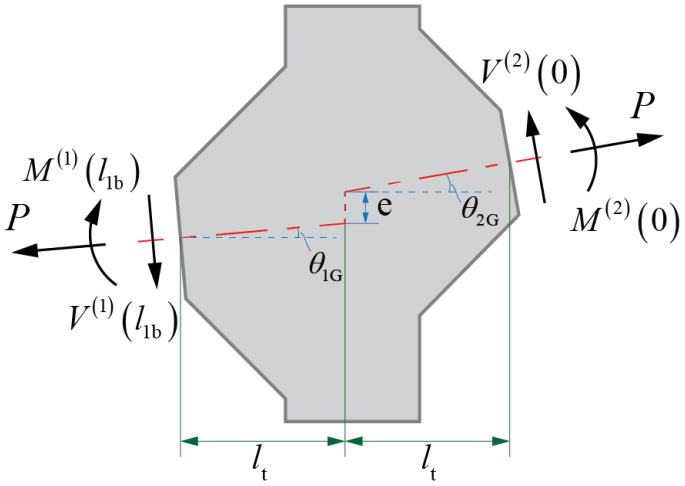

Fig. 3.5 Free body diagram of the joint based on rigid joint behavior.

Based on the free body diagram of the joint section shown in Fig. 3.5 and the assumption of small-angles (θ_{1G}, θ_{2G}), we can write the following equilibrium equations:

$$\begin{aligned} &\sum M = 0: \\ &M^{(1)}(l_{1b}) + P\mathrm{e} = V^{(1)}(l_{1b})l_t + V^{(2)}(0)l_t + M^{(2)}(0) \\ &\sum F_y = 0: \\ &V^{(1)}(l_{1b}) + P\theta_{1G} = V^{(2)}(0) + P\theta_{2G} \end{aligned} \tag{3.1}$$

Since the joint is assumed to act as a rigid body, the following geometry relationship can be imposed:

$$\begin{aligned} &v^{(1)}(l_{1b}) + l_t\theta_{1G} + l_t\theta_{2G} + \mathrm{e} = v^{(2)}(0) \\ &v'^{(1)}(l_{1b}) = v'^{(2)}(0) - (\theta_{2G} - \theta_{1G}) \end{aligned} \tag{3.2}$$

both of which need to be combined with other boundary conditions at the end of each member, e.g., clamped conditions without losing generality. Then, we have:

$$
\begin{aligned}
v^{(1)}(0) &= 0 \\
v'^{(1)}(0) &= \theta_{1\mathrm{G}} \\
v^{(2)}(l_{2\mathrm{b}}) &= (l_{1\mathrm{b}} + l_{\mathrm{t}})\theta_{1\mathrm{G}} + (l_{2\mathrm{b}} + l_{\mathrm{t}})\theta_{2\mathrm{G}} + \mathrm{e} \\
v'^{(2)}(l_{2\mathrm{b}}) &= \theta_{2\mathrm{G}}
\end{aligned}
\tag{3.3}
$$

The governing differential equations for both beam sections can be written as:

$$
\begin{aligned}
EI_1 \frac{d^4 v^{(1)}}{dx_1^4} &= 0 \\
EI_2 \frac{d^4 v^{(2)}}{dx_2^4} &= 0
\end{aligned}
\tag{3.4}
$$

where $I_1 = t_1^3/12$, $I_2 = t_2^3/12$ are the area moment of inertia of Member 1 and Member 2, respectively. The bending moment in Member 1 can be then obtained as follows, noting that $x'_1 = l_{1\mathrm{b}} - x_1$ is the distance from the weld toe position of Member 1, as shown in Fig. 3.3, and the angular misalignment angle α_{G} is in radius.

$$
M^{(1)}(x'_1) = P\mathrm{e}\left(x'_1 \mathcal{G}_{\mathrm{e}}^{(1)} + \mathcal{F}_{\mathrm{e}}^{(1)}\right) + P\alpha_{\mathrm{G}}\left(x'_1 \mathcal{G}_{\alpha_{\mathrm{G}}}^{(1)} + \mathcal{F}_{\alpha_{\mathrm{G}}}^{(1)}\right) \tag{3.5}
$$

where

$$
\begin{aligned}
\mathcal{F}_{\mathrm{e}}^{(1)} &= -\frac{t_1^3 l_{2\mathrm{b}}}{\mathcal{L}}\left(4l_{1\mathrm{b}}^3 t_2^3 + 3l_{1\mathrm{b}}^2 l_{2\mathrm{b}} t_2^3 + l_{2\mathrm{b}}^3 t_1^3\right) \\
\mathcal{G}_{\mathrm{e}}^{(1)} &= \frac{t_1^3 l_{2\mathrm{b}}}{\mathcal{L}}\left(6l_{1\mathrm{b}}^2 t_2^3 + 6l_{1\mathrm{b}} l_{2\mathrm{b}} t_2^3\right) \\
\mathcal{F}_{\alpha_{\mathrm{G}}}^{(1)} &= -\frac{t_1^3 l_{2\mathrm{b}}}{\mathcal{L}}\left(4l_{1\mathrm{b}}^3 l_{\mathrm{t}} t_2^3 + 2l_{1\mathrm{b}}^3 l_{2\mathrm{b}} t_2^3 + 3l_{1\mathrm{b}}^2 l_{\mathrm{t}} l_{2\mathrm{b}} t_2^3 + 2l_{1\mathrm{b}}^2 l_{2\mathrm{b}}^2 t_2^3 - l_{\mathrm{t}} l_{2\mathrm{b}}^3 t_1^3\right) \\
\mathcal{G}_{\alpha_{\mathrm{G}}}^{(1)} &= \frac{t_1^3 l_{2\mathrm{b}}}{\mathcal{L}}\left(3l_{1\mathrm{b}}^2 l_{2\mathrm{b}} t_2^3 + 6l_{1\mathrm{b}}^2 l_{\mathrm{t}} t_2^3 + 6l_{1\mathrm{b}} l_{2\mathrm{b}} l_{\mathrm{t}} t_2^3 + 4l_{1\mathrm{b}} l_{2\mathrm{b}}^2 t_2^3 + l_{2\mathrm{b}}^3 t_1^3\right)
\end{aligned}
\tag{3.6}
$$

and

$$
\mathcal{L} = l_{1\mathrm{b}}^4 t_2^6 + 4l_{1\mathrm{b}}^3 l_{2\mathrm{b}} t_1^3 t_2^3 + 12l_{1\mathrm{b}}^2 l_{\mathrm{t}} l_{2\mathrm{b}} t_1^3 t_2^3 + 6l_{1\mathrm{b}}^2 l_{2\mathrm{b}}^2 t_1^3 t_2^3 + 12l_{1\mathrm{b}} l_{\mathrm{t}} l_{2\mathrm{b}}^2 t_1^3 t_2^3 + 4l_{1\mathrm{b}} l_{2\mathrm{b}}^3 t_1^3 t_2^3 + l_{2\mathrm{b}}^4 t_1^6 \tag{3.7}
$$

Similarly, the bending moment in Member 2 can be expressed as:

$$M^{(2)}(x_2) = P\mathrm{e}\left(x_2\mathcal{G}_{\mathrm{e}}^{(2)} + \mathcal{F}_{\mathrm{e}}^{(2)}\right) + P\alpha_{\mathrm{G}}\left(x_2\mathcal{G}_{\alpha_{\mathrm{G}}}^{(2)} + \mathcal{F}_{\alpha_{\mathrm{G}}}^{(2)}\right) \tag{3.8}$$

where

$$\begin{aligned}
\mathcal{F}_{\mathrm{e}}^{(2)} &= \frac{t_2^3 l_{1\mathrm{b}}}{\mathcal{L}}\left(4l_{2\mathrm{b}}^3 t_1^3 + 3l_{2\mathrm{b}}^2 l_{1\mathrm{b}} t_1^3 + l_{1\mathrm{b}}^3 t_2^3\right) \\
\mathcal{G}_{\mathrm{e}}^{(2)} &= -\frac{t_2^3 l_{1\mathrm{b}}}{\mathcal{L}}\left(6l_{2\mathrm{b}}^2 t_1^3 + 6l_{2\mathrm{b}} l_{1\mathrm{b}} t_1^3\right) \\
\mathcal{F}_{\alpha_{\mathrm{G}}}^{(2)} &= -\frac{t_2^3 l_{1\mathrm{b}}}{\mathcal{L}}\left(4l_{2\mathrm{b}}^3 l_{\mathrm{t}} t_1^3 + 2l_{2\mathrm{b}}^3 l_{1\mathrm{b}} t_1^3 + 3l_{2\mathrm{b}}^2 l_{\mathrm{t}} l_{1\mathrm{b}} t_1^3 + 2l_{2\mathrm{b}}^2 l_{1\mathrm{b}}^2 t_1^3 - l_{\mathrm{t}} l_{1\mathrm{b}}^3 t_2^3\right) \\
\mathcal{G}_{\alpha_{\mathrm{G}}}^{(2)} &= \frac{t_2^3 l_{1\mathrm{b}}}{\mathcal{L}}\left(3l_{2\mathrm{b}}^2 l_{1\mathrm{b}} t_1^3 + 6l_{2\mathrm{b}}^2 l_{\mathrm{t}} t_1^3 + 6l_{2\mathrm{b}} l_{1\mathrm{b}} l_{\mathrm{t}} t_1^3 + 4l_{2\mathrm{b}} l_{1\mathrm{b}}^2 t_1^3 + l_{1\mathrm{b}}^3 t_2^3\right)
\end{aligned} \tag{3.9}$$

The bending moments at the two weld toe sections (i.e., Sections A-B and C-D in Fig. 3.3) can be obtained by plugging $x'_1 = 0$ into Eqn. (3.5) and $x_2 = 0$ into Eqn. (3.8), resulting in:

$$\begin{aligned}
M_{\text{A-B}} &= M^{(1)}(0) = P\left(\mathcal{F}_{\mathrm{e}}^{(1)}\mathrm{e} + \mathcal{F}_{\alpha_{\mathrm{G}}}^{(1)}\alpha_{\mathrm{G}}\right) \\
M_{\text{C-D}} &= M^{(2)}(0) = P\left(\mathcal{F}_{\mathrm{e}}^{(2)}\mathrm{e} + \mathcal{F}_{\alpha_{\mathrm{G}}}^{(2)}\alpha_{\mathrm{G}}\right)
\end{aligned} \tag{3.10}$$

The bending stresses at the four weld toe positions (A, B, C, D in Fig. 3.3) can then be obtained as:

$$\begin{aligned}
\sigma_{\mathrm{b,A}} &= -\sigma_{\mathrm{b,B}} = -\frac{6M_{\text{A-B}}}{t_1^2} \\
\sigma_{\mathrm{b,C}} &= -\sigma_{\mathrm{b,D}} = -\frac{6M_{\text{C-D}}}{t_2^2}
\end{aligned} \tag{3.11}$$

Finally, the secondary bending induced stress concentration factor, k_{b}, at the four weld toe positions can be calculated as:

$$k_{\mathrm{b},i} = \frac{\sigma_{\mathrm{b},i}}{\sigma_{\mathrm{n}}} \quad i \in \{\mathrm{A, B, C, D}\} \tag{3.12}$$

in which the beam section nominal stress σ_{n} is expressed as P/t_1 by definition, corresponding to the average stress in Member 1 or P/t_2 corresponding to the average stress in Member 2.

3.2.3.2 Solutions to Some Common Misalignment Cases

In the previous section, we derived the analytical solutions that can accommodate general misalignment scenarios in which Member 1 and Member 2 can have different thicknesses and lengths. It would be useful to examine their specific solution forms corresponding to some common misalignment configurations for illustrating the applications and implications of the new solutions described in the previous section.

Case 1: Consider a joint containing misalignments between two plates of the same thickness. By setting $t_1 = t_2 = t$ in Eqn. (3.10), we have:

$$\begin{aligned} M_{\text{A-B}} &= -\frac{Pl_{2\text{b}}\left(4l_{1\text{b}}^3 + 3l_{1\text{b}}^2 l_{2\text{b}} + l_{2\text{b}}^3\right)}{l_{1\text{b}}^4 + 4l_{1\text{b}}^3 l_{2\text{b}} + 12l_{1\text{b}}^2 l_{\text{t}} l_{2\text{b}} + 6l_{1\text{b}}^2 l_{2\text{b}}^2 + 12l_{1\text{b}} l_{\text{t}} l_{2\text{b}}^2 + 4l_{1\text{b}} l_{2\text{b}}^3 + l_{2\text{b}}^4}\text{e} \\ &\quad -\frac{Pl_{2\text{b}}\left(4l_{1\text{b}}^3 l_{\text{t}} + 2l_{1\text{b}}^3 l_{2\text{b}} + 3l_{1\text{b}}^2 l_{\text{t}} l_{2\text{b}} + 2l_{1\text{b}}^2 l_{2\text{b}}^2 - l_{\text{t}} l_{2\text{b}}^3\right)}{l_{1\text{b}}^4 + 4l_{1\text{b}}^3 l_{2\text{b}} + 12l_{1\text{b}}^2 l_{\text{t}} l_{2\text{b}} + 6l_{1\text{b}}^2 l_{2\text{b}}^2 + 12l_{1\text{b}} l_{\text{t}} l_{2\text{b}}^2 + 4l_{1\text{b}} l_{2\text{b}}^3 + l_{2\text{b}}^4}\alpha_{\text{G}} \\ M_{\text{C-D}} &= \frac{Pl_{1\text{b}}\left(4l_{2\text{b}}^3 + 3l_{2\text{b}}^2 l_{1\text{b}} + l_{1\text{b}}^3\right)}{l_{1\text{b}}^4 + 4l_{1\text{b}}^3 l_{2\text{b}} + 12l_{1\text{b}}^2 l_{\text{t}} l_{2\text{b}} + 6l_{1\text{b}}^2 l_{2\text{b}}^2 + 12l_{1\text{b}} l_{\text{t}} l_{2\text{b}}^2 + 4l_{1\text{b}} l_{2\text{b}}^3 + l_{2\text{b}}^4}\text{e} \\ &\quad -\frac{Pl_{1\text{b}}\left(4l_{2\text{b}}^3 l_{\text{t}} + 2l_{2\text{b}}^3 l_{1\text{b}} + 3l_{2\text{b}}^2 l_{\text{t}} l_{1\text{b}} + 2l_{2\text{b}}^2 l_{1\text{b}}^2 - l_{\text{t}} l_{1\text{b}}^3\right)}{l_{1\text{b}}^4 + 4l_{1\text{b}}^3 l_{2\text{b}} + 12l_{1\text{b}}^2 l_{\text{t}} l_{2\text{b}} + 6l_{1\text{b}}^2 l_{2\text{b}}^2 + 12l_{1\text{b}} l_{\text{t}} l_{2\text{b}}^2 + 4l_{1\text{b}} l_{2\text{b}}^3 + l_{2\text{b}}^4}\alpha_{\text{G}} \end{aligned} \tag{3.13}$$

Case 2: Consider a joint containing misalignments between two plates of the same length. By setting $l_{1\text{b}} = l_{2\text{b}} = l_{\text{b}}$ in Eqn. (3.10), we have:

$$\begin{aligned} M_{\text{A-B}} &= -\frac{Pt_1^3 l_{\text{b}}\left(7t_2^3 + t_1^3\right)}{l_{\text{b}} t_2^6 + 14l_{\text{b}} t_1^3 t_2^3 + 24l_{\text{t}} t_1^3 t_2^3 + l_{\text{b}} t_1^6}\text{e} - \frac{Pt_1^3 l_{\text{b}}\left(7l_{\text{t}} t_2^3 + 4l_{\text{b}} t_2^3 - l_{\text{t}} t_1^3\right)}{l_{\text{b}} t_2^6 + 14l_{\text{b}} t_1^3 t_2^3 + 24l_{\text{t}} t_1^3 t_2^3 + l_{\text{b}} t_1^6}\alpha_{\text{G}} \\ M_{\text{C-D}} &= \frac{Pt_2^3 l_{\text{b}}\left(7t_1^3 + t_2^3\right)}{l_{\text{b}} t_2^6 + 14l_{\text{b}} t_1^3 t_2^3 + 24l_{\text{t}} t_1^3 t_2^3 + l_{\text{b}} t_1^6}\text{e} - \frac{Pt_2^3 l_{\text{b}}\left(7l_{\text{t}} t_1^3 + 4l_{\text{b}} t_1^3 - l_{\text{t}} t_2^3\right)}{l_{\text{b}} t_2^6 + 14l_{\text{b}} t_1^3 t_2^3 + 24l_{\text{t}} t_1^3 t_2^3 + l_{\text{b}} t_1^6}\alpha_{\text{G}} \end{aligned} \tag{3.14}$$

Case 3: Consider a joint containing misalignments between two plates of the same thickness and length. As a result, Eqn. (3.10) can be further simplified to:

$$M_{\text{A-B}} = -\frac{Pl_{\text{b}}}{2l_{\text{b}} + 3l_{\text{t}}}\text{e} - \frac{Pl_{\text{b}}}{4}\alpha_{\text{G}}$$
$$M_{\text{C-D}} = \frac{Pl_{\text{b}}}{2l_{\text{b}} + 3l_{\text{t}}}\text{e} - \frac{Pl_{\text{b}}}{4}\alpha_{\text{G}} \tag{3.15}$$

It is worth noting that if the analytical model does not consider joint representation, i.e., setting $l_{\text{t}} = 0$, $l_{1\text{b}} = l_1$, and $l_{2\text{b}} = l_2$ in Eqn. (3.10) (also see Fig. 3.6), the resulting stress concentration k_{b} from Eqns. (3.11) and then (3.12) can be expressed as:

$$\begin{aligned}
k_{\text{b,A}} = -k_{\text{b,B}} = \frac{6}{t_1}\Bigg[& \frac{t_1^3 l_2\left(4l_1^3t_2^3 + 3l_1^2l_2t_2^3 + l_2^3t_1^3\right)}{l_1^4t_2^6 + 4l_1^3l_2t_1^3t_2^3 + 6l_1^2l_2^2t_1^3t_2^3 + 4l_1l_2^3t_1^3t_2^3 + l_2^4t_1^6}\text{e} \\
& + \frac{t_1^3 l_2\left(2l_1^3l_2t_2^3 + 2l_1^2l_2^2t_2^3\right)}{l_1^4t_2^6 + 4l_1^3l_2t_1^3t_2^3 + 6l_1^2l_2^2t_1^3t_2^3 + 4l_1l_2^3t_1^3t_2^3 + l_2^4t_1^6}\alpha_{\text{G}}\Bigg] \\
k_{\text{b,C}} = -k_{\text{b,D}} = \frac{6}{t_2}\frac{t_1}{t_2}\Bigg[& -\frac{t_2^3 l_1\left(4l_2^3t_1^3 + 3l_2^2l_1t_1^3 + l_1^3t_2^3\right)}{l_1^4t_2^6 + 4l_1^3l_2t_1^3t_2^3 + 6l_1^2l_2^2t_1^3t_2^3 + 4l_1l_2^3t_1^3t_2^3 + l_2^4t_1^6}\text{e} \\
& + \frac{t_2^3 l_1\left(2l_2^3l_1t_1^3 + 2l_2^2l_1^2t_1^3\right)}{l_1^4t_2^6 + 4l_1^3l_2t_1^3t_2^3 + 6l_1^2l_2^2t_1^3t_2^3 + 4l_1l_2^3t_1^3t_2^3 + l_2^4t_1^6}\alpha_{\text{G}}\Bigg]
\end{aligned} \tag{3.16}$$

recovering the same expressions given in [63]. The stress concentration factors given in Eqn. (3.16) refer to k_{b} values defined with respect to Position *O* in Fig. 3.3, i.e., the idealized intersection point between two misaligned beam sections. Although still providing an overall stress concentration measure caused by the misalignments, they cannot differentiate joints with different sizes, nor do they provide any specific weld toe position information for a consistent treatment of axial and angular misalignments when both are present.

3.2.4 Nonlinear Geometry Effects

Nonlinear geometry effects are expected to become increasingly important in welded joints as plate thickness decreases in lightweight structures. With respect to the model definitions given

in Fig. 6, it can be shown that the governing equations incorporating nonlinear geometry effects can be written as [73]:

$$EI_1 \frac{d^4 v^{(1)}}{dx_1^4} - P \frac{d^2 v^{(1)}}{dx_1^2} = 0$$
$$EI_2 \frac{d^4 v^{(2)}}{dx_2^4} - P \frac{d^2 v^{(2)}}{dx_2^2} = 0 \tag{3.17}$$

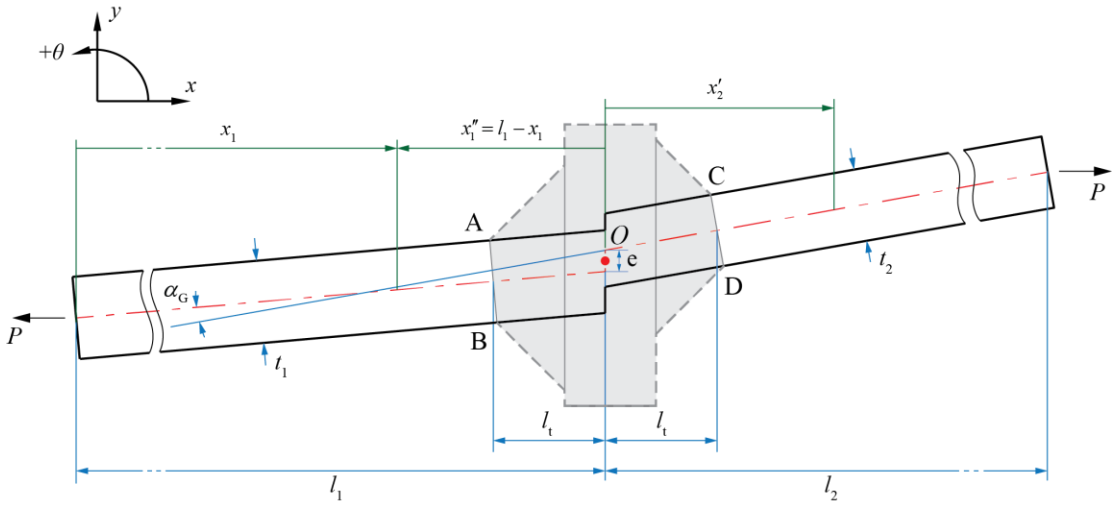

Fig. 3.6 Model definition for incorporating nonlinear geometry effects.

Different from those in Eqn. (3.4) under small deformation conditions (i.e., linear geometry), Eqn. (3.17) now contains the interaction of the horizontal axial load *P* with the beam deformation, and the rigid body assumption of the joint area has to be removed. Instead, the joint area can be treated as an extended part of a beam section, as shown in Fig. 3.6. Note that the length of each beam member now extends to the center of the joint (Position *O*), denoted as $l_1 = l_{1b} + l_t$ and $l_2 = l_{2b} + l_t$, respectively. The local coordinate definitions of the two beam members are now given as x''_1 and x'_2, as shown in Fig. 3.6. Although the joint representation is not explicitly modeled as a rigid body as used in Sec. 3.2.3, it can be implicitly considered by taking the bending moment of the beam at the exact same location as where Sections A-B and C-D are located, i.e.,

$x''_1 = l_t$ and $x'_2 = l_t$. Considering this difference, we can write the force equilibrium and geometric relationships with respect to the joint center (Position *O* in Fig. 3.6) as

$$\begin{aligned} &\sum M = 0: \\ &M^{(1)}(l_1) + Pe = M^{(2)}(0) \\ &\sum F_y = 0: \\ &V^{(1)}(l_1) = V^{(2)}(0) \end{aligned} \tag{3.18}$$

and

$$\begin{aligned} &v^{(1)}(l_1) + e = v^{(2)}(0) \\ &v'^{(1)}(l_1) = v'^{(2)}(0) - (\theta_{2G} - \theta_{1G}) \end{aligned} \tag{3.19}$$

Together with the boundary conditions given in Eqn. (3.3), Eqn. (3.17) can be solved, leading to the following bending moment expressions for each beam member for $P > 0$:

$$\begin{aligned} M^{(1)}(x_1'') = &Pe\left(\phi_e^{(1)} \sinh \lambda_1 x_1'' + \psi_e^{(1)} \cosh \lambda_1 x_1''\right) \\ &+ P\alpha_G \left(\phi_{\alpha_G}^{(1)} \sinh \lambda_1 x_1'' + \psi_{\alpha_G}^{(1)} \cosh \lambda_1 x_1''\right) \\ M^{(2)}(x_2') = &Pe\left(\phi_e^{(2)} \sinh \lambda_2 x_2' + \psi_e^{(2)} \cosh \lambda_2 x_2'\right) \\ &+ P\alpha_G \left(\phi_{\alpha_G}^{(2)} \sinh \lambda_2 x_2' + \psi_{\alpha_G}^{(2)} \cosh \lambda_2 x_2'\right) \end{aligned} \tag{3.20}$$

where λ_1, λ_2 are defined as

$$\lambda_i = \sqrt{\frac{|P|}{EI_i}} \quad i \in \{1, 2\} \tag{3.21}$$

The detailed expressions of the coefficients $\phi_e^{(1)}, \phi_{\alpha_G}^{(1)}, \psi_e^{(2)}, \psi_{\alpha_G}^{(2)}$ in Eqn. (3.20) are given in Appendices C.2 and C.3. The solutions corresponding to $P < 0$ can also be found in Appendices C.2 and C.3. With the above developments, the bending moments at the weld toe positions can be obtained by setting $x''_1 = l_t$ and $x_2 = l_t$ in Eqn. (3.20) and the corresponding k_b can be then calculated through Eqns. (3.11) and then (3.12).

3.3 Validation using Finite Element Method

In this section, we will use the finite element method to validate the solutions derived previously. The commercial software ABAQUS is used for all finite element computations in this section.

3.3.1 Traction Structural Stress Method

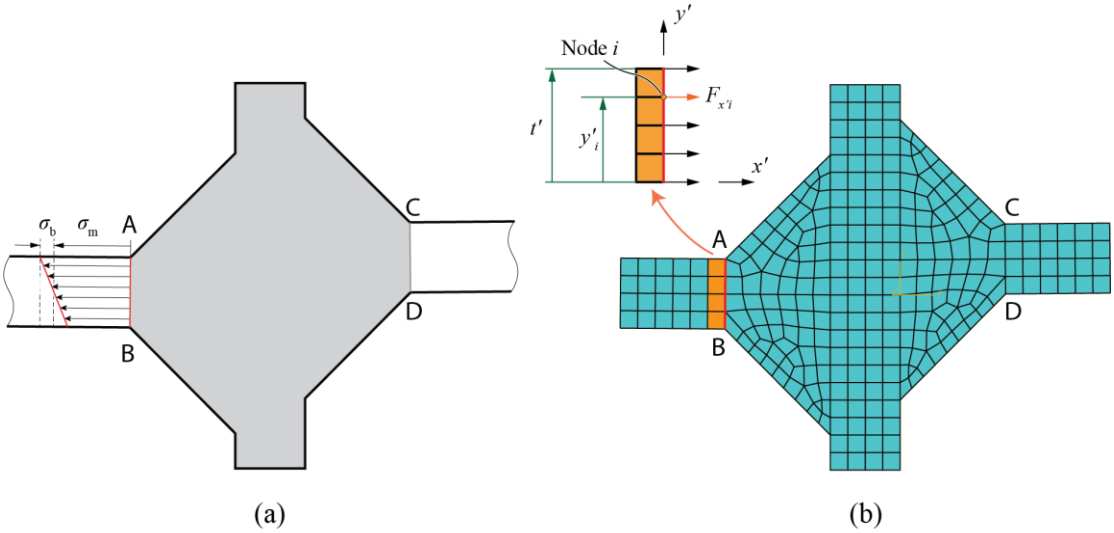

Fig. 3.7 Finite element model and traction structural stress implementation: (a) traction structure stress definition along a weld toe section (Section A-B); (b) implementation in 2D finite element analysis.

The bending stress consistent with the traction-based structural stress at a weld toe position can be directly calculated using a mesh-insensitive method developed by Dong et al. [30–32]. The method's effectiveness in achieving mesh-insensitivity and fatigue test data correlation has been demonstrated in a number of studies [30–32,36,37]. Given the simple joint configurations and loading conditions, only 2D structural stress definition and implementation are needed in this study. Further details of the traction stress method and its implementation in 3D analysis for complex structures can be found in previous publications [30,31].

The normal traction structural stress at a weld toe can be expressed as the sum of a statically equivalent membrane component (σ_m) and bending component (σ_b) as defined in Fig. 3.7a, as

$$\sigma_s = \sigma_m + \sigma_b \tag{3.22}$$

Each of the above two components can be calculated using the nodal forces acting on a hypothetical crack path (for example, Path A-B in Fig. 3.7b) from the element set (see the highlighted elements in Fig. 3.7b). As shown in Fig. 3.7b, we define $x' - y'$ as the local coordinate system of Path A-B with x' being normal to A-B, t' as the length of path A-B, $F_{x'i}$ as the total nodal force in x' direction on Node i of the output element set, and set $\mathcal{N} = \{i|$Node i being on path A-B$\}$. Then, σ_m and σ_b with respect to Path A-B can be calculated by

$$\begin{aligned} \sigma_m &= \frac{1}{t'} \sum_{i \in \mathcal{N}} F_{x'i} \\ \sigma_b &= \frac{6}{t'^2} \sum_{i \in \mathcal{N}} F_{x'i} \left(y'_i - \frac{t'}{2} \right) \end{aligned} \tag{3.23}$$

In ABAQUS, the nodal force output is obtained through the extraction of the "NFORC" output parameter.

3.3.2 Finite Element Models and Results

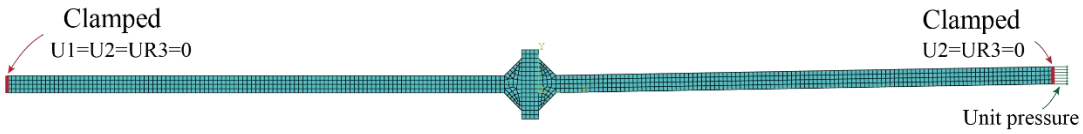

Fig. 3.8 A representative FE model used for validation.

In the finite element analysis, ABAQUS "CPS4" plane stress elements were used, and the material properties used are $E = 206000$ MPa (Young's modulus) and $\nu = 0.3$ (Poisson's ratio). Linear geometry was used for the validation of the solutions given by Eqns. (3.10)-(3.12). A joint area profile was modeled to be consistent with that seen in a typical cruciform fillet welded connection in the FE model, as shown in Fig. 3.8. The left end of the model was fixed for all degrees of freedom, while the right end was only allowed to move in x direction for

accommodating the axial load, which were modeled as an edge pressure. Table 3.1 summarizes the detailed dimensions of all eight models analyzed with the definitions given in Fig. 3.3.

The traction structural stresses at weld toes were calculated using Eqn. (3.23) in terms of their membrane and bending components and then presented in the form of SCF, i.e., $k_{\mathrm{m}} = \sigma_{\mathrm{m}}/\sigma_{\mathrm{n}}$ and $k_{\mathrm{b}} = \sigma_{\mathrm{b}}/\sigma_{\mathrm{n}}$, respectively. For convenience, the nominal stress with respect to Member 1, i.e., $\sigma_{\mathrm{n}} = P/t_1$ will be used hereafter for comparing both computational and analytical results under various thickness combinations. Then, we have:

$$\begin{aligned} k_{\mathrm{m}} &= 1 \quad \text{in Member 1} \\ k_{\mathrm{m}} &= \frac{t_1}{t_2} \quad \text{in Member 2} \end{aligned} \tag{3.24}$$

Both the FE and analytical SCF (k_{b}) results at the weld toe exhibiting the maximum SCF value among the four weld toes are compared in Fig. 3.9 in which the analytical results were directly calculated using Eqns. (3.10)-(3.12)). The k_{b} values calculated without considering the joint representation (as given in [63]) are also provided in Fig. 3.9 for comparison purpose (also see Table 3.2). The SCFs calculated using the analytical solutions derived in this study are in excellent agreement with the FE results (with errors $< 2\%$), as depicted in Fig. 3.9.

Table 3.1 Dimension details of FE models used

Case no.	Misalignments		Member 1		Member 2		Joint
	e/mm	α_{G}/deg	$l_{1\mathrm{b}}$/mm	t_1/mm	$l_{2\mathrm{b}}$/mm	t_2/mm	l_{joint}/mm
1	6.25	0	287	12.5	287	12.5	38.5
2	6.25	0	280.5	12.5	280.5	12.5	51.5
3	6.25	0	187	12.5	287	10	38.5
4	0	1	290	10	290	10	30
5	0	1	290	10	290	10	34
6	-0.0873	1	290	10	290	10	30
7	5	1	190	10	290	10	30
8	5	1	190	10	290	8	30

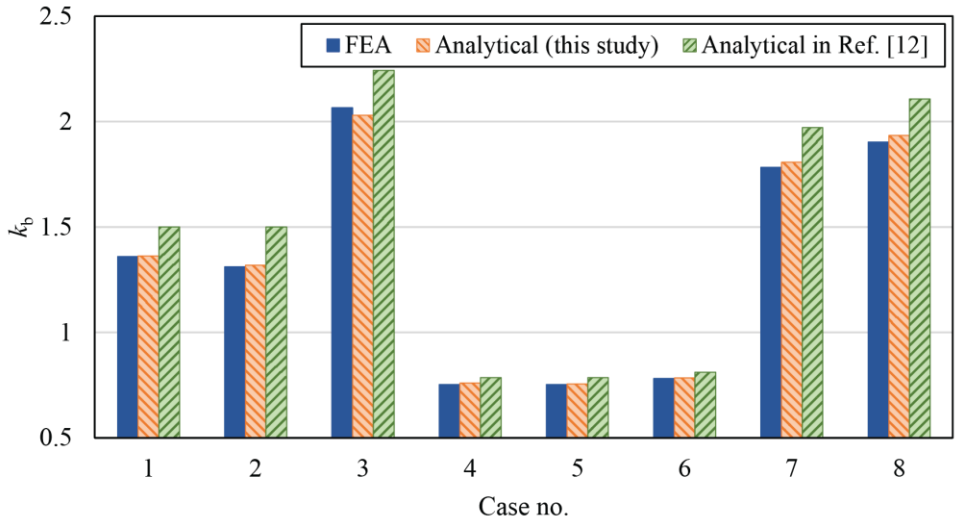

Fig. 3.9. Comparison of k_b values under small deformation conditions among FEA, new analytical solution with joint representation from this study, and the analytical solution without joint representation [63].

Table 3.2. Detailed comparison of calculated k_b values for all cases based on linear geometry

Case no.	FEA	Analytical (this study)	Analytical in Ref. [63]
1	1.3594	1.3629	1.5000
2	1.3115	1.3184	1.5000
3	2.0657	2.0301	2.2425
4	0.7528	0.7592	0.7854
5	0.7526	0.7553	0.7854
6	0.7854	0.7835	0.8116
7	1.7835	1.8066	1.9712
8	1.9030	1.9338	2.1077

For the validation of the analytical solutions developed in Sec. 3.2.4, as described in Eqn. (3.20), two representative cases (e.g., Case 1 and Case 8 in Table 3.1) were further considered by performing the corresponding finite element analysis under nonlinear geometry conditions, with the edge pressure applied on the end of Member 2 varies from 0 to $t_1/t_2 \times 200$ MPa such that the nominal stress (with respect to Member 1) is 0 to 200 MPa. The results of k_b as a function of applied nominal stress using both FEA and the analytical solution according to Eqn. (3.20) are given in Fig. 3.10. The error between the analytical solution and the FE results is less than 1.5%.

It clearly shows that the analytical results from Eqn. (3.20) accurately capture the nonlinear geometry (or beam straightening) effects.

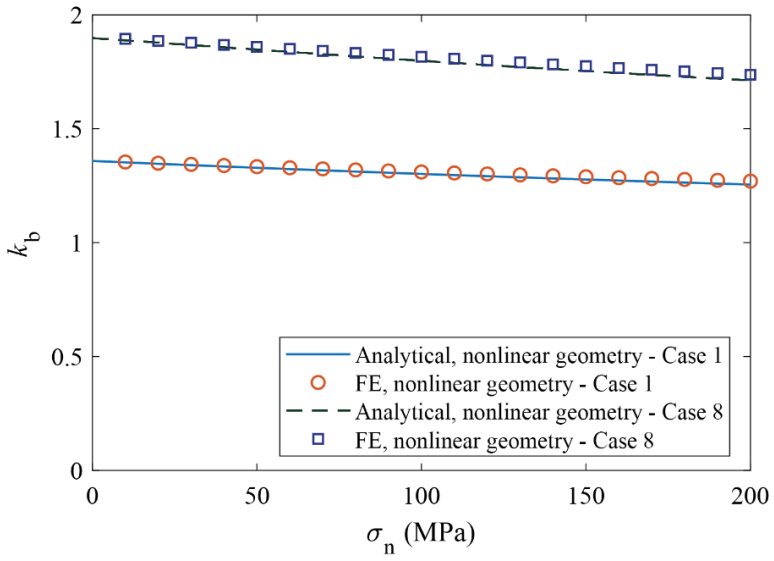

Fig. 3.10. Comparison of k_b between FEA and the analytical results of Case 1 and Case 8 under geometric nonlinear conditions.

3.4 Effectiveness in Fatigue Test Data Interpretation

The validity of the analytical solutions developed in this study can be further demonstrated by its effectiveness in correlating fatigue test data available. Andrew [79] performed a series of fatigue tests on fillet-welded load-carrying cruciform specimens with controlled axial misalignments. The specimens have the thickness $t = 12.5$ mm. The length of each member in these test specimens is 300 mm.

The test data plotted using the nominal stress range (Fig. 3.11a) clearly shows a strong misalignment effect, resulting in a wide scatter band with a standard deviation (STD) of 0.3215. Next, the test data are plotted in Fig. 3.11b in terms of the traction structural stress range

$$\Delta\sigma_s = \left(k_m + k_b\right)\Delta\sigma_n \tag{3.25}$$

where $k_m = 1$ and k_b were calculated using the analytical solutions given by Eqns. (3.11), (3.12) , and (3.15), as both Members 1 and 2 in these specimens have the same thickness and length. As

to be discussed in the next section, nonlinear geometry effects need not be considered due to the relatively large plate thickness, i.e., $t = 12.5$ mm. The data correlation shows a significant improvement (see Fig. 3.11b) with a standard deviation of 0.1584 versus 0.3215 in Fig. 3.11a.

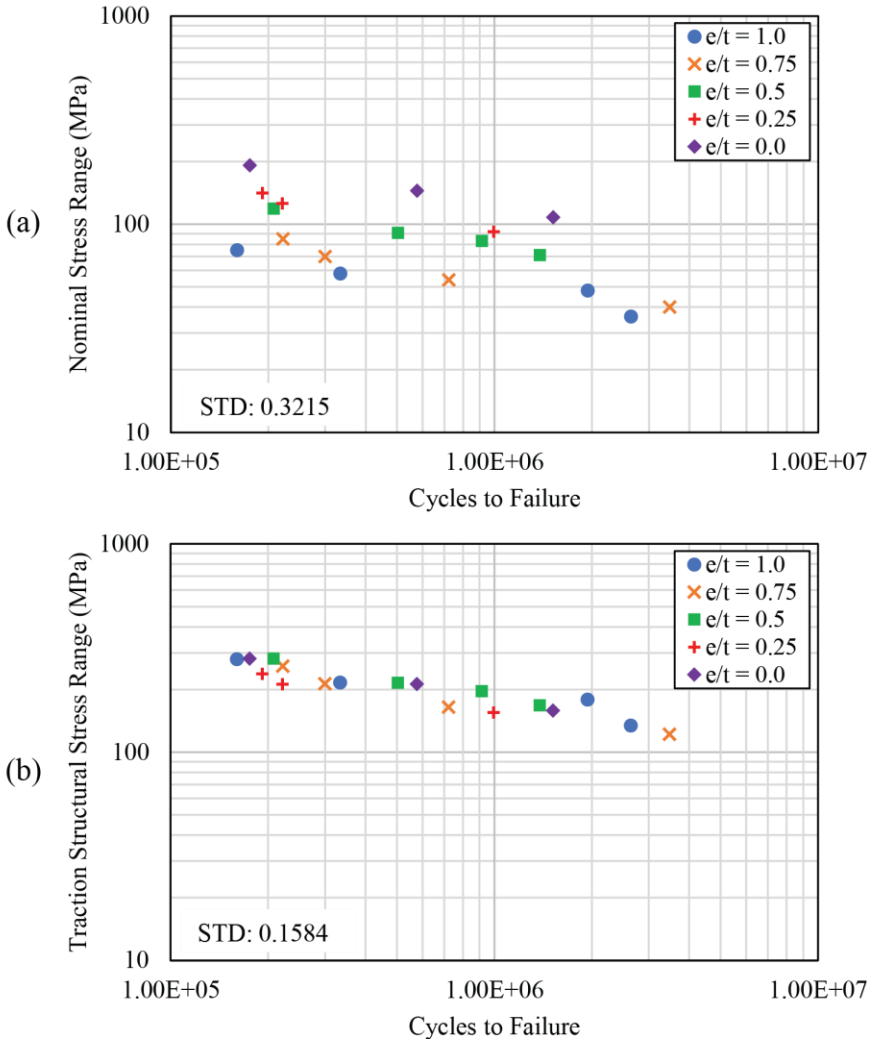

Fig. 3.11. Test data in [79] plotted using (a) nominal stress range; (b) traction structural stress range.

To further evaluate the validity of the test data correlation shown in Fig. 3.11a, it would be useful to compare the data trend with the master S-N curve scatter band adopted by ASME Div. 2 Code [30,31,74]. To do so, the structural stress range computed by the analytical solution by the means of k_{b} in Eqn. (3.25) can be converted to the equivalent structural stress range parameter given as [74]:

$$\Delta S_s = \frac{\Delta\sigma_s}{t^{*\frac{2-m}{2m}} I(r)^{\frac{1}{m}}} \tag{3.26}$$

where $\Delta\sigma_s$ is calculated using Eqn. (3.25), $t^* = t'/(1\,mm)$ is the dimensionless length of the hypothetical crack path, m takes the value of 3.6 (obtained from a unified representation of both short and long fatigue crack growth data [74]), $I(r)^{1/m}$, given in [74], is a dimensionless polynomial function of the bending ratio $r = k_b/(k_m + k_b)$.

The same set of the fatigue test data in Fig. 3.11b are re-plotted in Fig. 3.12 using the equivalent structural stress range parameter in Eqn. (3.26). The master S-N curve scatter band lines from ASME [74], which represents about 1000 large scale fatigue tests, are also given in Fig. 3.12 for comparison purposes. The same fatigue test data are all situated well within the master S-N curve scatter band, further confirming both the validity and effectiveness of the developed analytical solution in interpreting fatigue test data.

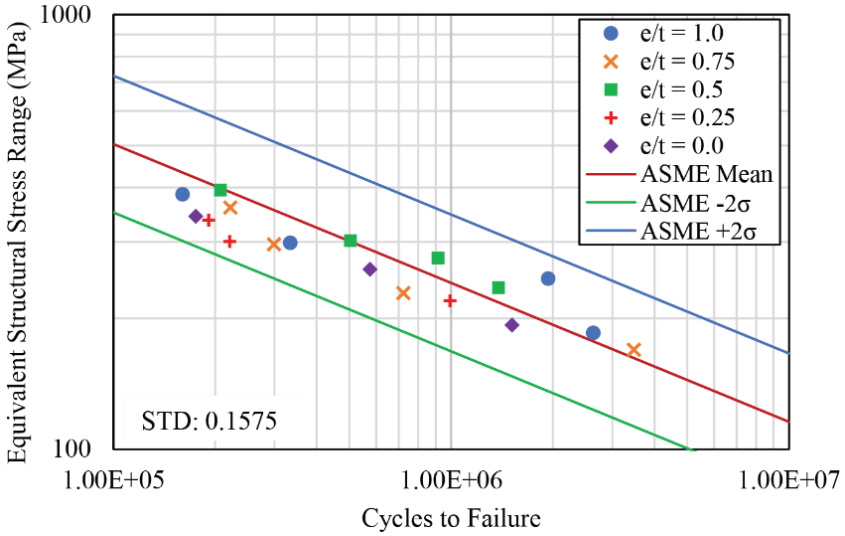

Fig. 3.12. Test data correlation using equivalent structural stress range.

3.5 Discussions

3.5.1 Effect of Joint Representation

Fig. 3.9 shows that the present analytical solutions incorporating a joint representation are in good agreement with the finite element solutions while the analytical solutions without a joint presentation [63] seem consistently over-estimate secondary bending stress-induced k_b, particularly when the joint area size (i.e., l_{joint} in Table 3.1) are larger, e.g., comparing Cases 1 and 2, or there exist an increased degree of asymmetry, e.g., Cases 3, and 7-8. This is because in [63], the joint misalignment effects were considered with idealized analytical models containing two beams only, and the bending moment calculated is defined with respect to Position *O* in Fig. 3.3 instead of weld toe positions. Therefore, the solutions provided in [63] are only able to reflect the overall misalignment effect on the secondary stress at the center of a joint location without being able to capture joint size effects or distinguish specific weld toe position of interest. The solutions based on linear geometry (Eqn. (3.10)) and nonlinear geometry (Eqn. (3.20)) can both effectively estimate the secondary bending stress at weld toe positions and reflect the joint size effects.

In terms of fatigue test data interpretation, the analytical solutions developed in this study have been shown effective in correlating the plate fatigue test data in [79] (Fig. 3.11a) into a narrow band (see Fig. 3.11b) for establishing data transferability. The validity of the data correlation shown in Fig. 3.11b can be further proven by the fact that the narrow data scatter band is consistent with independent data in the form of the master S-N curve scatter band adopted by ASME Div. 2 (Fig. 3.12). This suggests that the analytical model, along with its assumptions introduced in this study, is reasonable.

In this study, the geometric joint profile is assumed to be approximately symmetrical with respect to the horizontal axis. For unsymmetrical weld profiles, such as single-sided butt joint, the additional secondary bending can be readily calculated using FEA-based the traction structural

stress method without modeling misalignments. Then, the misalignment induced secondary bending stresses calculated from the analytical solutions can be directly superimposed with the FEA results.

Although only the clamped conditions are considered in this paper, the approach presented for joint representation can be readily extended to any other boundary conditions of interest by replacing Eqn. (3.3) with a specific set of displacement boundary conditions. Additional members (i.e., vertical members in a cruciform joint) can also be added to the model. These specific applications will be presented in a separate publication at a later date.

3.5.2 Combined Effects of Axial and Angular Misalignments

It is common that axial and angular misalignments simultaneously exist in a welded joint, which introduce two new issues that have not been clarified in the literature to our best knowledge: 1) how to define an axial misalignment so that its resulting secondary stresses can be properly combined with those caused by an angular misalignment; 2) which weld toe out of the four (e.g., as shown in Fig. 3.3) is subjected to the highest k_b and their signs.

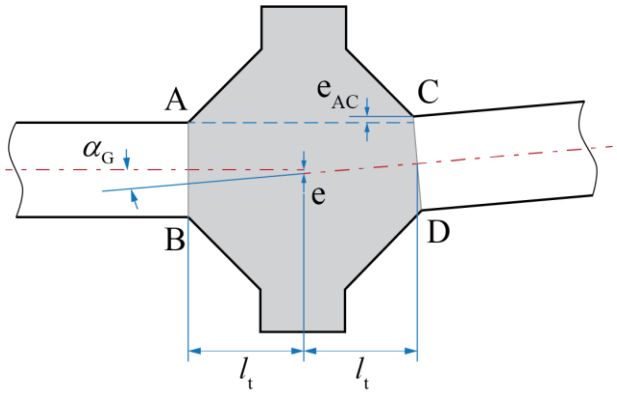

Fig. 3.13. Definitions of axial and angular misalignments in Case 6.

The first issue is resolved in this study by introducing the misalignment definitions based on the centerlines of plate members and Position *O*, as given in Fig. 3.3. It can be shown that, without a proper and consistent definition, the misalignments considered can yield significantly

different results in determining which weld toe positions is subjected to the highest k_b. For instance, consider the joint geometric details corresponding to Case 6, as shown in Fig. 3.13. The effects of angular misalignment, say at $\alpha_{\mathrm{G}} = 1°$, will not be affected by its specific definition, but the effects of an axial misalignment will. One definition of axial misalignment is the vertical distance between weld toe A and weld toe C (i.e., e_{AC} in Fig. 3.13), and the resulting axial misalignment will be $\mathrm{e}_{\mathrm{AC}} = 0.175$ mm. According to the definitions introduced in Sec. 3.2.2 (Fig. 3.3), the axial misalignment should be $\mathrm{e} = -0.0873$ mm. Using Eqn. (3.15) (due to the same length on both sides and uniform plate thickness), the maximum k_{b} calculated based on e_{AC} would be 0.8078 at weld toe A, while the maximum k_{b} calculated using the proposed axial misalignment definition is 0.7835 at weld toe C. In fact, the FE result shows that $k_{\mathrm{b}} = 0.7854$ at weld toe C, and $k_{\mathrm{b}} = 0.7245$ at weld toe A. Using the proposed axial misalignment (e) definition, we can obtain the correct k_{b} and determine which weld toe is subjected to the maximum secondary bending stress.

The second issue is also related to how to properly define misalignments in the analytical model, for which a joint presentation is essential, as discussed above. Based on Eqn. (3.10) corresponding to linear geometry (or small deformation) conditions or Eqn. (3.20) incorporating nonlinear geometry effects, we can clearly see that they represent a linear superposition of axial and angular misalignments. With the joint representation considered, we can evaluate the sign of the stress at each weld toe location with respect to each of the two types of misalignments and then determine which weld toe is subject to tension under both misalignments. Generally, based on the coefficients in Eqns. (3.5)-(3.9) and $l_{1\mathrm{b}}, l_{2\mathrm{b}} \gg l_{\mathrm{t}}$, the sign of stress at all four weld toes with respect to each misalignment type when $P > 0$ can be summarized in Fig. 3.14. Moreover, the

analytical solutions provided in this study enables the estimation of misalignment-induced stress at all four weld toes.

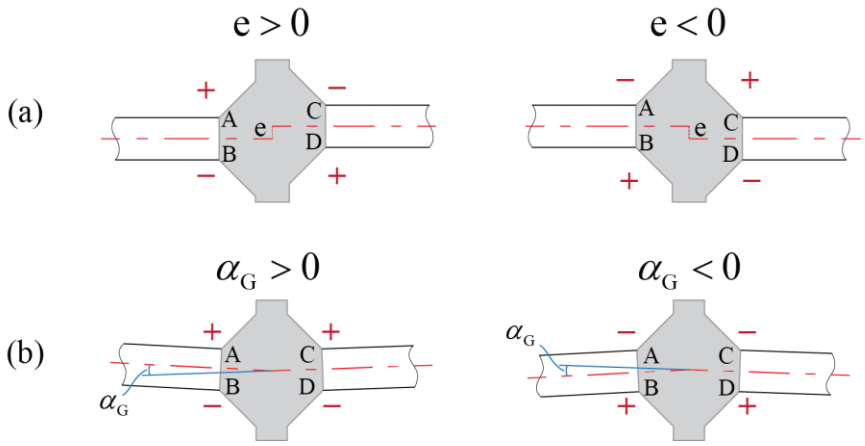

Fig. 3.14. Sign of secondary bending stress at each weld toe under tensile axial load *P* with respect to (a) axial misalignment; (b) angular misalignment.

3.5.3 Misalignment-induced Bending Stress Formulae in BS 7910

In BS 7910:2013 [59], the following formulas are provided for calculating bending stress (in terms of SCF) caused by axial and angular misalignment (with both members (1 and 2) having the same thickness):

$$k_{b,axial} = \kappa \frac{e}{t} \frac{l_1}{l_1 + l_2}$$
$$k_{b,angular} = \kappa \frac{\alpha_G}{t} \frac{l_1 l_2}{l_1 + l_2} \quad (3.27)$$

which is derived from a simply supported condition, and κ is an empirical factor dependent on the end restraints, which was determined using stress measurement data or FE results in [78]. However, these equations do not contain the consideration of joint size effects and can only represent the secondary stress in the middle of an idealized joint (Position *O* in Fig. 3.3) instead of the stress at the weld toe position. Also, there is no information given with Eqn. (3.27) about which of the weld toes of this joint have tensile bending stress, whereas Eqn. (3.13) in this study can be used to derive the misalignment-induced bending stress at each weld toe position.

It has also been shown in [63] that the empirical κ factor provided in BS 7910 cannot adequately represent boundary conditions other than the simply supported condition because the solution form would be rather different if other boundary conditions were considered. To demonstrate this point, we can compare the expression without considering the joint representation to Eqn. (3.27). By taking advantage of the solutions corresponding to Case 2 ($t_1 = t_2 = t$) and ignoring the joint representation (by setting $l_t = 0$, $l_{1\mathrm{b}} = l_1$, $l_{2\mathrm{b}} = l_2$), as discussed in Sec. 3.2.3.2, we can rewrite Eqn. (3.13) and obtain the stress concentration factor (at weld toe A in Fig. 3.3) as:

$$k_{\mathrm{b,A}} = 6\frac{\mathrm{e}}{t}\left[1-4\left(\frac{l_1}{l_1+l_2}\right)+9\left(\frac{l_1}{l_1+l_2}\right)^2-6\left(\frac{l_1}{l_1+l_2}\right)^3\right] + 6\frac{\alpha_{\mathrm{G}} l_1}{t}\left[2\left(\frac{l_1}{l_1+l_2}\right)-4\left(\frac{l_1}{l_1+l_2}\right)^2+2\left(\frac{l_1}{l_1+l_2}\right)^3\right] \tag{3.28}$$

Eqn. (3.28) shows that the secondary bending caused by misalignments under clamped condition is a third-order polynomial function of $l_1/(l_1 + l_2)$, while Eqn. (3.27) is only a linear function of $l_1/(l_1 + l_2)$. Obviously, the use of κ in Eqn. (3.27) cannot adequately represent the difference between Eqn. (3.27) and Eqn. (3.28) for all $l_1/(l_1 + l_2)$.

3.5.4 Importance of Nonlinear Geometry Effect

In Fig. 3.10, we can see the straightening effect under axial load (i.e., k_{b} drops when σ_{n} increases) by considering nonlinear geometry effects. Since the model used in the test cases are relatively thick, the straightening effect is not significant. However, as thin plates are increasingly used for lightweight purposes, nonlinear geometry effects could become more important.

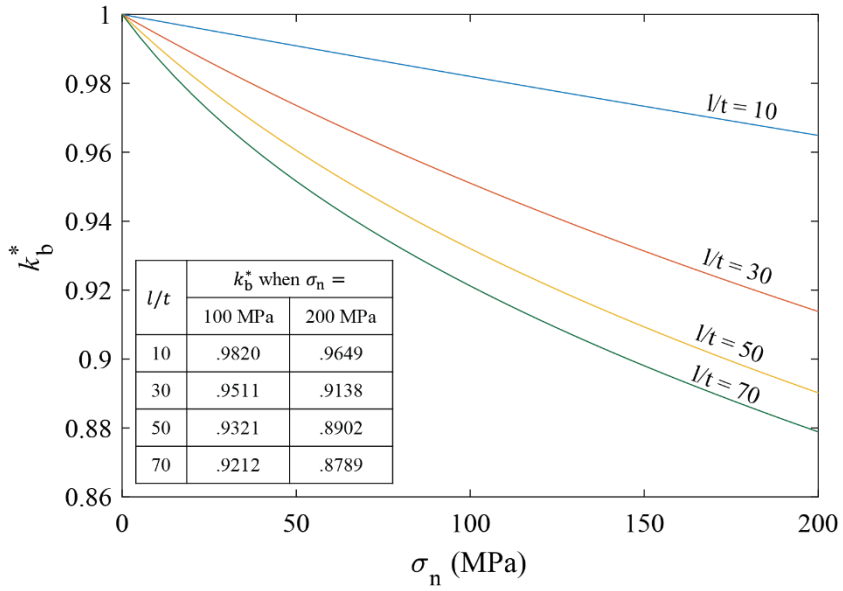

l/t	k_b^* when σ_n =	
	100 MPa	200 MPa
10	.9820	.9649
30	.9511	.9138
50	.9321	.8902
70	.9212	.8789

Fig. 3.15. Normalized k_b^* under different l/t ratio.

To examine under what conditions nonlinear geometry effects should be considered, the relationship between general structural dimensions and the importance of the nonlinear geometry effects is investigated here by using the analytical model by setting $l_{1b} = l_{2b} = l$ and $t_1 = t_2 = t$. The joint size is assumed to be l_t=1.5t, and the axial misalignment is assumed to be e = 0.5t. Based on the analytical solutions given in [88,89], the slenderness ratio l/t should have a strong effect on the straightening behaviors. Therefore, we would compare the k_b over different σ_n calculated based on Eqn. (3.20) under different l/t ratios, as shown in Fig. 3.15. To gauge nonlinear geometry effects, the following normalized k_b^* is used.

$$k_b^* = \frac{k_{b,nonlinear}}{k_{b,linear}} \tag{3.29}$$

where $k_{b,nonlinear}$ is the k_b considering nonlinear geometry; $k_{b,linear}$ is the k_b considering linear geometry, which is independent of σ_n. It can be seen from Fig. 3.15 that structures with a larger slenderness ratio l/t have more significant nonlinear geometry effects. For example, at $\sigma_n = 200$ MPa, $k_b^* \approx 0.91$ corresponding to $l/t = 30$ while $k_b^* \approx 0.88$ corresponding to $l/t = 70$. This

means that the nonlinear geometry effect, compared to the linear geometry-based solution, causes a 9% drop in k_b when $l/t = 30$, and causes a 12% drop in k_b when $l/t = 70$. An approximate threshold for considering nonlinear geometry effects may be introduced by considering both the load level and the slenderness ratio l/t. For instance, if we choose $k_b^* = 0.95$ at $\sigma_n = 100$ MPa as the threshold, then for cases where $l/t > 30$, we would have $k_b^* < 0.95$ when $\sigma_n > 100$ MPa and the nonlinear geometry effect needs to be considered.

3.6 Chapter Conclusions

In this chapter, an analytical method for computing the secondary bending actions caused by both axial and angular joint misalignments is presented with consideration of the joint representation. Both linear and nonlinear geometry effects are considered. The closed-form analytical solutions presented have been validated by finite element analysis with joint geometry explicitly modeled. In addition, the validity and effectiveness of the analytical solutions have been further proven by correlating some well-known fatigue test data of welded components with controlled misalignments into a single narrow band. Furthermore, the resulting test data scatter is shown to fall within the master S-N curve scatter band adopted by ASME Div. 2 since 2007, again confirming the effectiveness of the analytical solutions developed in this study. The following specific findings are worth noting:

(1) By introducing a rigid body-based joint representation in the analytical model, the force equilibrium and geometry relationships about the joint can be established in such a way that enables the development of the closed-form analytical solution.

(2) With the joint definition and the resulting analytical solutions derived in this study, the interactions between axial and angular misalignment can be properly combined for determining specific secondary bending stress at each of all four weld toe positions.

(3) With the analytical solution incorporating nonlinear geometry effects, the joint straightening effects on secondary stress development can be clearly captured. It is shown that the slenderness ratio l/t can be related to the severity of the nonlinear geometry effect: the higher the l/t becomes, the stronger the nonlinear effect can be seen.

Chapter 4

An Analytical Framework for Treatment of Combined Misalignment and Distortion Curvature Effects on Fatigue of Welded Joints

4.1 Chapter Introduction

In previous chapters, we have studied common distortion modes' effects on welded joints individually, including axial misalignment, global angular distortion (also referred to as angular misalignment), and local angular distortion (also called distortion curvature). We realized all these distortion modes could make a significant contribution to the secondary bending in the welded joint. Furthermore, in the processing of the distortion measurement data of actual welded structures such as those in [41], it is shown that all distortion modes may simultaneously exist with respect to a welded joint, causing high complexity in the determination of the secondary bending stress.

In this chapter, we first bring the analytical treatments of local angular distortions to a consistent analytical framework with that of the axial and angular misalignments developed in Chapter 3 to enable the superposition of the analytical solutions. Then, we develop a general distortion mode decomposition and assembly procedure, whose objective is to provide a consistent procedure to reliably divide the complicated distortion effect on a welded joint into several sub-problems and combine the result from each sub-problem together.

4.2 Assumptions

The analytical modeling, decomposition and assembly procedure developed in this chapter are all based on the following assumptions:

a) A transverse section of a butt-seam welded or stiffened shipboard panel follows the beam

theory (consistent with strip beam theory often used for analyzing ship structures)

b) The beam material is assumed to follow linear elastic material behaviors within the loading range of concern, while the beam deflection and lateral load interactions can be nonlinear or in the regime of nonlinear deformation.

c) The axial misalignment at the joint is small compared with beam length, and the angular distortion angles are small (i.e., $\leq 5°$).

d) Transverse shear deformation is negligible.

4.3 Analytical Treatment of Unsymmetric Local Angular Distortion

In Sec. 2.3.2.2, we used the method of notional loads to model the local angular distortion (or distortion curvature) in butt-welded plates based on symmetric structure dimensions (i.e., both beam members have the same length and thickness) and distortion shape assumption. Chapter 3 studied the axial misalignment and the global angular misalignment with respect to unsymmetric structure dimensions. To formulate a general analytical modeling procedure of the misalignment and distortion's effect on welded joints, we need to extend the local angular distortion model to cover general unsymmetric structure dimensions and distortion shapes. With such extension, the local angular distortion solution can then be properly superimposed onto the solution developed in Sec. 3.2.

4.3.1 Notional Loads Model

The local angular distortion, or distortion curvature, refers to the curved part of the distortion shape, excluding the global angular distortion or the angular misalignment defined in Sec. 3.2.2. A general local angular distortion shape with respect to a butt-welded joint is shown in Fig. 4.1. The thicknesses of Member 1 (the base plate on the left) and Member 2 (the base plate on the right) are t_1 and t_2, and the lengths of both members are l_1 and l_2, measured from the center

of the joint (Position *O*, which is the joint center, as shown in Fig. 4.1), respectively. The horizontal dashed line in Fig. 4.1 is the baseline. $v_0(x)$ is the initial distortion shape function with respect to the baseline. Specifically, $v_0^{(1)}(x_1)$ and $v_0^{(2)}(x_2)$ are the initial distortion shape of Member 1 and Member 2, where x_1 and x_2 are local x-coordinates of each beam member, as defined in Fig. 4.1. The local angular distortion angles (or the slopes) at the ends of each member are given as $\theta'_{11}, \theta'_{12}, \theta'_{21}$, and θ'_{22}, and the ends of each member beam is aligned with the baseline (i.e., $v_0^{(1)}(0) = v_0^{(1)}(l_1) = v_0^{(2)}(0) = v_0^{(2)}(l_2) = 0$), as depicted in Fig. 4.1. We assume the distortion shape can be well approximated by the above four local angular distortion angles. The local angular distortions in Fig. 4.1 are plotted in such a way that all local angular distortion angles are positive to provide clear definitions.

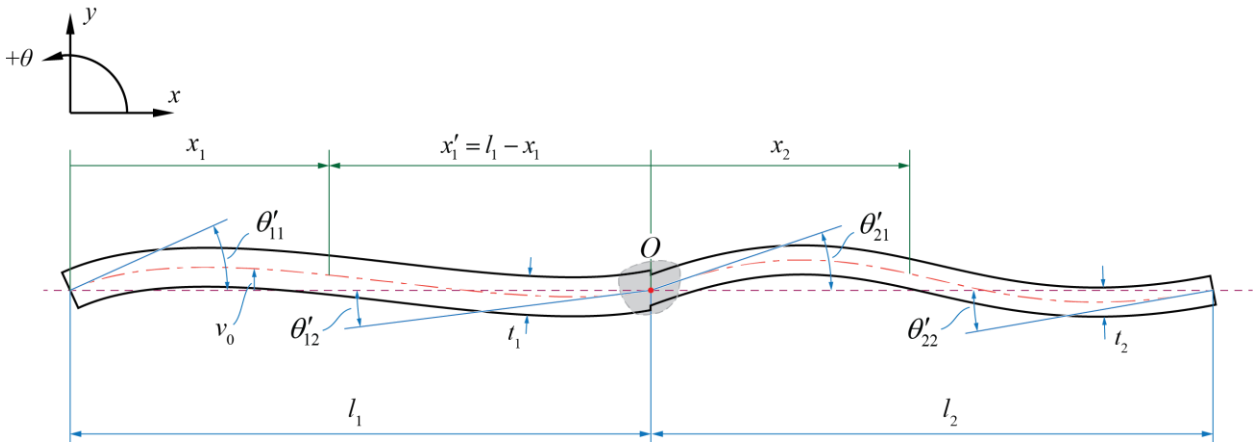

Fig. 4.1 Illustration of a general local angular distortion.

The imperfect beam problem of the general local angular distortion is given in Fig. 4.2a, which corresponds to a butt-welded joint condition. While the restraints on the model can vary depending on the application scenario, we focus on the clamped boundary condition here to illustrate the methodology. The translational and rotational degrees of freedom are restrained at both ends ($x_1 = 0$ and $x'_2 = l_2$), and the joint is free to move.

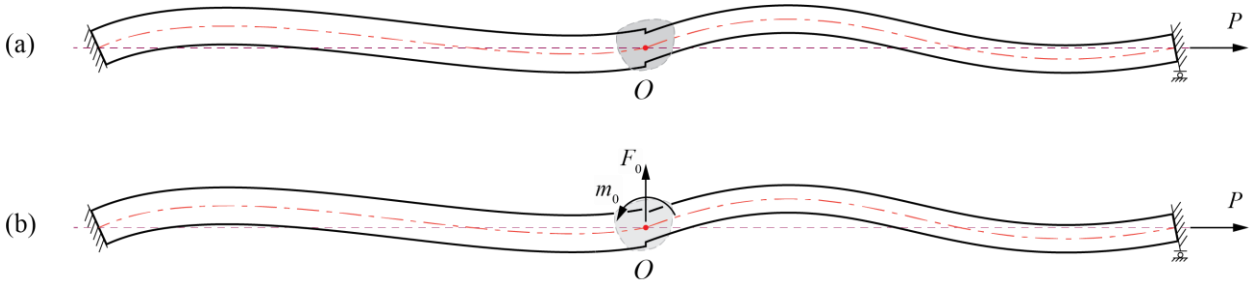

Fig. 4.2 Beam models used for general local angular distortion: (a) imperfect beam; (b) nonlinear beam.

As discussed in Sec. 2.2.2, we first apply notional loads onto an initially straight linear beam to obtain the distortion shape. We can also apply displacements on the beam since they can always be replaced by equivalent notional loads. To simplify the notional load model, we can split the model into two individual cantilever beams by fixating the joint position and apply notional loads (in this case, we apply displacements) on the free ends, as shown in Fig. 4.3.

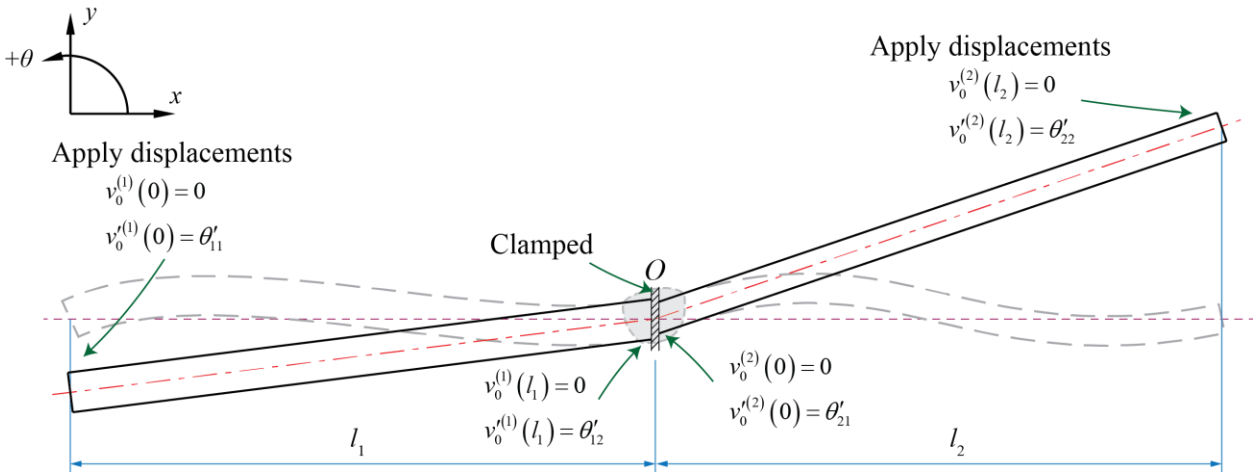

Fig. 4.3 Notional load model used for achieving the general local angular distortion shape.

After the initial distortion shape is achieved, we then adjust the restraints on the notional load model to match those on the imperfect beam model (Fig. 4.2a) by adding or replacing constraints with corresponding notional loads. The general principle for modifying the notional load model constraints is discussed in Appendix A.6 in detail. In this model, we constrain the translational and rotational degrees of freedom at both free ends, release the restraints on the joint position (Position O) and apply a notional force F_0 and a notional moment m_0 which would

maintain the force equilibrium. F_0 and m_0 can be obtained using the following force equilibrium along with the reaction forces at Position *O*, as shown in Fig. 4.4a:

$$\begin{aligned} &\sum M = 0: \\ &M_0^{(1)}(l_1) = M_0^{(2)}(0) + m_0 \\ &\sum F_y = 0: \\ &V_0^{(1)}(l_1) = V_0^{(2)}(0) + F_0 \end{aligned} \tag{4.1}$$

where $M_0^{(i)}$, $V_0^{(i)}$ ($i \in \{1,2\}$) are the bending moment and shear force caused by notional loads in Member i. The resulting F_0 and m_0 is given by

$$\begin{aligned} m_0 &= M_0^{(1)}(l_1) - M_0^{(2)}(0) \\ F_0 &= V_0^{(1)}(l_1) - V_0^{(2)}(0) \end{aligned} \tag{4.2}$$

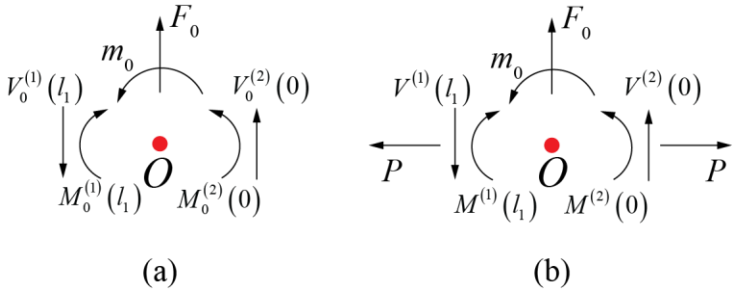

Fig. 4.4 Force equilibrium at position *O* in: (a) notional load model; (b) nonlinear beam model.

With the above notional load model, we can formulate the nonlinear beam problem (Fig. 4.2b) by superimposing the imperfect beam problem onto the linear beam model used for notional loads modeling [88,89]. The imperfect beam problem is governed by

$$EI_i \frac{d^4 v_1^{(i)}}{dx_i^4} - P \frac{d^2\left(v_0^{(i)} + v_1^{(i)}\right)}{dx_i^2} = 0 \tag{4.3}$$

where $i \in \{1,2\}$ indicates the member number, I_i is the area moment of inertia of Member i, $v_1^{(i)}$ is the unknown deflection caused by the axial load P. The linear beam model is governed by the following classic differential equation:

$$EI_i \frac{d^4 v_0^{(i)}}{dx_i^4} = 0 \tag{4.4}$$

The superposition of Eqn. (4.3) and (4.4) yields the governing equation for a nonlinear beam problem, given as

$$EI_i \frac{d^4 v^{(i)}}{dx_i^4} - P \frac{d^2 v^{(i)}}{dx_i^2} = 0 \tag{4.5}$$

where $v^{(i)} = v_0^{(i)} + v_1^{(i)}$ is the total displacement of Member i from the baseline. We need a total of 8 equations to solve Eqn. (4.5) for the displacement of both members. For this model, we have four boundary condition equations from the clamped condition, and we can write the rest four equations based on the force equilibrium and geometry relationships at position *O* where the two members connect.

After superposition, the force equilibrium about position O of the nonlinear beam model (see Fig. 4.4b) can be written as

$$\begin{aligned} &\sum M = 0: \\ &M^{(1)}(l_1) = M^{(2)}(0) + m_0 \\ &\sum F_y = 0: \\ &V^{(1)}(l_1) = V^{(2)}(0) + F_0 \end{aligned} \tag{4.6}$$

where $M^{(i)}$, $V^{(i)}$ are the total bending moment and shear force in Member i. The geometry relationships between the two members are simply

$$\begin{aligned} &v^{(1)}(l_1) = v^{(2)}(0) \\ &v'^{(1)}(l_1) = v'^{(2)}(0) - (\theta'_{21} - \theta'_{12}) \end{aligned} \tag{4.7}$$

where $v'^{(i)}$ is the slope of Member i. Using Eqns. (4.6) and (4.7) with the clamped boundary conditions at both ends, we can solve Eqn. (4.5) and obtain the total deflection for both members. Finally, we can derive the bending moment induced by distortion in Member i, $M_1^{(i)}$, given as

$$M_1^{(i)} = M^{(i)} - M_0^{(i)} = EI_i \frac{d^2 v^{(i)}}{dx_i^{\,2}} - EI_i \frac{d^2 v_0^{(i)}}{dx_i^{\,2}} \tag{4.8}$$

The solutions are given in the next section, and more details of the solution procedure is provided in Appendix A.5.

4.3.2 Analytical Solution

4.3.2.1 Notional Loads

Based on the model given in Fig. 4.3, the bending moment caused by notional loads in each member is (note that $x'_1 = l_x - x_1$)

$$\begin{aligned} M_0^{(1)}\left(x_1'\right) &= \frac{2EI_1}{l_1^2}\left[\left(l_1 - 3x_1'\right)\theta_{11}' + \left(2l_1 - 3x_1'\right)\theta_{12}'\right] \\ M_0^{(2)}\left(x_2\right) &= \frac{2EI_2}{l_2^2}\left[\left(-2l_2 + 3x_2\right)\theta_{21}' + \left(-l_2 + 3x_2\right)\theta_{22}'\right] \end{aligned} \tag{4.9}$$

The shear force in each member is

$$\begin{aligned} V_0^{(1)}\left(x_1'\right) &= -\frac{6EI_1}{l_1^2}\left(\theta_{11}' + \theta_{12}'\right) \\ V_0^{(2)}\left(x_2\right) &= -\frac{6EI_2}{l_2^2}\left(\theta_{21}' + \theta_{22}'\right) \end{aligned} \tag{4.10}$$

The notional loads applied on the nonlinear beam (Fig. 4.2b) is then obtained using Eqn. (4.2) as

$$\begin{aligned} m_0 &= \frac{2EI_1\left(\theta_{11}' + 2\theta_{12}'\right)}{l_1} + \frac{2EI_2\left(2\theta_{21}' + \theta_{22}'\right)}{l_2} \\ F_0 &= -\frac{6EI_1\left(\theta_{11}' + \theta_{12}'\right)}{l_1^2} + \frac{6EI_2\left(\theta_{21}' + \theta_{22}'\right)}{l_2^2} \end{aligned} \tag{4.11}$$

4.3.2.2 Local Angular Distortion-Induced Bending Moment

The bending moment induced by the local angular distortion in Fig. 4.1 under the clamped condition when $P > 0$ takes the form of

$$
\begin{aligned}
M_1^{(1)}(x_1') &= P\left(\phi_{\theta_{11}'}^{(1)}\sinh\lambda_1 x_1' + \psi_{\theta_{11}'}^{(1)}\cosh\lambda_1 x_1'\right)\theta_{11}' + P\left(\phi_{\theta_{12}'}^{(1)}\sinh\lambda_1 x_1' + \psi_{\theta_{12}'}^{(1)}\cosh\lambda_1 x_1'\right)\theta_{12}' \\
&+P\left(\phi_{\theta_{21}'}^{(1)}\sinh\lambda_1 x_1' + \psi_{\theta_{21}'}^{(1)}\cosh\lambda_1 x_1'\right)\theta_{21}' + P\left(\phi_{\theta_{22}'}^{(1)}\sinh\lambda_1 x_1' + \psi_{\theta_{22}'}^{(1)}\cosh\lambda_1 x_1'\right)\theta_{22}' \\
&-P\left(\zeta_{\theta_{11}'}^{(1)} + \kappa_{\theta_{11}'}^{(1)} x_1'\right)\theta_{11}' - P\left(\zeta_{\theta_{12}'}^{(1)} + \kappa_{\theta_{12}'}^{(1)} x_1'\right)\theta_{12}' \\
M_1^{(2)}(x_2) &= P\left(\phi_{\theta_{11}'}^{(2)}\sinh\lambda_2 x_2 + \psi_{\theta_{11}'}^{(2)}\cosh\lambda_2 x_2\right)\theta_{11}' + P\left(\phi_{\theta_{12}'}^{(2)}\sinh\lambda_2 x_2 + \psi_{\theta_{12}'}^{(2)}\cosh\lambda_2 x_2\right)\theta_{12}' \\
&+P\left(\phi_{\theta_{21}'}^{(2)}\sinh\lambda_2 x_2 + \psi_{\theta_{21}'}^{(2)}\cosh\lambda_2 x_2\right)\theta_{21}' + P\left(\phi_{\theta_{22}'}^{(2)}\sinh\lambda_2 x_{21} + \psi_{\theta_{22}'}^{(2)}\cosh\lambda_2 x_2\right)\theta_{22}' \\
&-P\left(\zeta_{\theta_{21}'}^{(2)} + \kappa_{\theta_{21}'}^{(2)} x_2\right)\theta_{21}' - P\left(\zeta_{\theta_{22}'}^{(2)} + \kappa_{\theta_{22}'}^{(2)} x_2\right)\theta_{22}'
\end{aligned}
\tag{4.12}
$$

where λ_i is defined as

$$
\lambda_i = \sqrt{\frac{|P|}{EI_i}} \tag{4.13}
$$

and $\phi_{\theta'_{11}}^{(1)}, \psi_{\theta'_{11}}^{(1)}, \phi_{\theta'_{12}}^{(1)}, \psi_{\theta'_{12}}^{(1)}, \phi_{\theta'_{21}}^{(1)}, \psi_{\theta'_{21}}^{(1)}, \phi_{\theta'_{22}}^{(1)}, \psi_{\theta'_{22}}^{(1)}, \zeta_{\theta'_{11}}^{(1)}, \kappa_{\theta'_{11}}^{(1)}, \zeta_{\theta'_{12}}^{(1)}, \kappa_{\theta'_{12}}^{(1)}$ are coefficients associated with Member 1, and $\phi_{\theta'_{11}}^{(2)}, \psi_{\theta'_{11}}^{(2)}, \phi_{\theta'_{12}}^{(2)}, \psi_{\theta'_{12}}^{(2)}, \phi_{\theta'_{21}}^{(2)}, \psi_{\theta'_{21}}^{(2)}, \phi_{\theta'_{22}}^{(2)}, \psi_{\theta'_{22}}^{(2)}, \zeta_{\theta'_{21}}^{(2)}, \kappa_{\theta'_{22}}^{(2)}$, $\zeta_{\theta'_{21}}^{(1)}, \kappa_{\theta'_{22}}^{(1)}$ are coefficients associated with Member 2. All coefficients are the function of l_1, l_2, t_1, t_2, and P. Detailed expressions of these coefficients and the solution corresponding to $P < 0$ are given in Appendix C.4. Eqn. (4.12) provides the bending moment of the entire beam model. The local angular distortion's (or distortion curvature's) effect on the joint can be evaluated by setting $x'_1 = 0$, $x_2 = 0$ in Eqn. (4.12). If joint representation needs to be considered, the bending moment at weld toe position is obtained by setting $x'_1 = l_\mathrm{t}$, $x_2 = l_\mathrm{t}$ in Eqn. (4.12) where l_t is the distance from Position *O* to the weld toe. The subsequent secondary bending stress and bending stress concentration factor corresponds to the top surface ($y = t_i/2$) can be obtained by

$$
\begin{aligned}
\sigma_\mathrm{b}^{(i)} &= -\frac{M_1^{(i)}}{I_i}y = -\frac{6M_1^{(i)}}{t_i^2} \\
k_\mathrm{b}^{(i)} &= \frac{\sigma_\mathrm{b}^{(i)}}{\sigma_\mathrm{n}}
\end{aligned}
\tag{4.14}
$$

where σ_{n} is the nominal stress which is expressed as P/t_1 by definition, corresponding to the average stress in Member 1 or P/t_2 corresponding to the average stress in Member 2. Note that Eqn. (4.12) are valid before the compressive axial loading magnitude reaches the model's Euler's critical load beyond which buckling occurs.

4.3.3 Linear Geometry Approximation

It is difficult to directly obtain the secondary bending moment induced by distortion curvatures without considering nonlinear geometry. However, when $P \to 0$, the secondary bending in Eqn. (4.12) should approach that acquired with respect to linear geometry. As such, a closed-form analytical solution for the distortion curvature effect under linear geometry can be derived from Eqn. (4.12), if the joint size effect is ignored, i.e., $x'_1 = 0, x_2 = 0$, as

$$\begin{aligned} M^{(1)}_{1,\text{linear}} &= \lim_{P\to 0} P\left[\left(\psi^{(1)}_{\theta'_{11}} - \zeta^{(1)}_{\theta'_{11}}\right)\theta'_{11} + \left(\psi^{(1)}_{\theta'_{12}} - \zeta^{(1)}_{\theta'_{12}}\right)\theta'_{12} + \psi^{(1)}_{\theta'_{21}}\theta'_{21} + \psi^{(1)}_{\theta'_{22}}\theta'_{22}\right] \\ &= P\left[\mathcal{F}^{(1)}_{\theta'_{11}}\theta'_{11} + \mathcal{F}^{(1)}_{\theta'_{12}}\theta'_{12} + \mathcal{F}^{(1)}_{\theta'_{21}}\theta'_{21} + \mathcal{F}^{(1)}_{\theta'_{22}}\theta'_{22}\right] \\ M^{(2)}_{1,\text{linear}} &= \lim_{P\to 0} P\left[\psi^{(2)}_{\theta'_{11}}\theta'_{11} + \psi^{(2)}_{\theta'_{12}}\theta'_{12} + \left(\psi^{(2)}_{\theta'_{21}} - \zeta^{(2)}_{\theta'_{21}}\right)\theta'_{21} + \left(\psi^{(2)}_{\theta'_{22}} - \zeta^{(2)}_{\theta'_{22}}\right)\theta'_{22}\right] \\ &= P\left[\mathcal{F}^{(2)}_{\theta'_{11}}\theta'_{11} + \mathcal{F}^{(2)}_{\theta'_{12}}\theta'_{12} + \mathcal{F}^{(2)}_{\theta'_{21}}\theta'_{21} + \mathcal{F}^{(2)}_{\theta'_{22}}\theta'_{22}\right] \end{aligned} \tag{4.15}$$

where

$$\begin{aligned} \mathcal{F}^{(1)}_{\theta'_{11}} &= \mathcal{F}^{(2)}_{\theta'_{11}} = -\frac{l_1^2 t_2^3}{30\mathcal{L}}\left(l_1^3 t_2^3 + 9 l_1 l_2^2 t_1^3 + 10 l_2^3 t_1^3\right) \\ \mathcal{F}^{(1)}_{\theta'_{12}} &= \mathcal{F}^{(2)}_{\theta'_{12}} = \frac{l_1^2 t_2^3}{15\mathcal{L}}\left(2 l_1^3 t_2^3 + 3 l_1 l_2^2 t_1^3 + 5 l_2^3 t_1^3\right) \\ \mathcal{F}^{(1)}_{\theta'_{21}} &= \mathcal{F}^{(2)}_{\theta'_{21}} = -\frac{l_2^2 t_1^3}{15\mathcal{L}}\left(2 l_2^3 t_1^3 + 3 l_2 l_1^2 t_2^3 + 5 l_1^3 t_2^3\right) \\ \mathcal{F}^{(1)}_{\theta'_{22}} &= \mathcal{F}^{(2)}_{\theta'_{22}} = \frac{l_2^2 t_1^3}{30\mathcal{L}}\left(l_2^3 t_1^3 + 9 l_2 l_1^2 t_2^3 + 10 l_1^3 t_2^3\right) \end{aligned} \tag{4.16}$$

and

$$\mathcal{L} = l_1^4 t_2^6 + 4 l_1^3 l_2 t_1^3 t_2^3 + 6 l_1^2 l_2^2 t_1^3 t_2^3 + 4 l_1 l_2^3 t_1^3 t_2^3 + l_2^4 t_1^6 \tag{4.17}$$

When the beam members in the joint are less slender and the straightening effect is small, as discussed in Sec. 3.5.4, Eqn. (4.15) can be used to approximate the secondary bending induced by the local angular distortion or distortion curvatures.

4.3.4 Simplification Based on Symmetric Nominal Structure

The solution given in Eqn. (4.12) can be greatly simplified by considering symmetric nominal structure, i.e., $l_1 = l_2 = l$ and $t_1 = t_2 = t$, which is common in application. The solution can be further simplified if the effect from the position of the weld toe is neglected ($x'_1 = x_2 = 0$). Since we have a uniform thickness t, we can unambiguously define the secondary bending stress concentration factor as

$$k_{\mathrm{b,s}} = -\frac{6M_1^{(i)}(0)}{t^2 \cdot P/t} = \begin{cases} 6\dfrac{l}{t}\left[\left(\dfrac{\lambda^2 l^2 \cosh \lambda l - 4\lambda l \sinh \lambda l + 6\cosh \lambda l - 6}{2\lambda^3 l^3 \sinh \lambda l}\right)\left(\theta'_{21} - \theta'_{12}\right) \right. \\ \qquad \left. + \left(\dfrac{-\lambda^2 l^2 - 2\lambda l \sinh \lambda l + 6\cosh \lambda l - 6}{2\lambda^3 l^3 \sinh \lambda l}\right)\left(\theta'_{22} - \theta'_{11}\right)\right] & P > 0 \\ 6\dfrac{l}{t}\left[\left(\dfrac{-\lambda^2 l^2 \cos \lambda l + 4\lambda l \sin \lambda l + 6\cos \lambda l - 6}{2\lambda^3 l^3 \sin \lambda l}\right)\left(\theta'_{21} - \theta'_{12}\right) \right. \\ \qquad \left. + \left(\dfrac{\lambda^2 l^2 + 2\lambda l \sin \lambda l + 6\cos \lambda l - 6}{2\lambda^3 l^3 \sin \lambda l}\right)\left(\theta'_{22} - \theta'_{11}\right)\right] & P < 0 \end{cases} \tag{4.18}$$

$k_{\mathrm{b,s}}$ in both members are the same because of the symmetric structure. From Eqn. (4.18), we recognize that the secondary bending SCF induced by a general local angular distortion under symmetric structure condition is a linear combination of $\theta'_{21} - \theta'_{12}$ and $\theta'_{22} - \theta'_{11}$. By setting $\theta'_{21} = -\theta'_{12} = \theta'_1$ and $\theta'_{22} = -\theta'_{11} = \theta'_2$, we can recover the analytical solution given by Eqn. (2.11) for symmetric distortion.

The secondary bending SCF with respect to linear geometry under the same simplification assumption can be derived based on Eqn. (4.15), which leads to

$$k_{\mathrm{b,s,linear}} = \lim_{P\to 0} k_{\mathrm{b,s}} = \frac{1}{4}\frac{l}{t}\left[\left(\theta'_{21} - \theta'_{12}\right) - \left(\theta'_{22} - \theta'_{11}\right)\right] \tag{4.19}$$

4.3.5 Validation by Finite Element Method

This section will use the commercial software ABAQUS to perform finite element (FE) calculation for validating the solutions derived previously. In the finite element model, ABAQUS "B21" beam elements were used, and all beam models have a unit width. The Young's modulus of the material is $E = 207000$ MPa, and the Poisson's ratio is $\nu = 0.3$. Nonlinear geometry was considered in the finite element calculation. For convenience, the nominal stress with respect to Member 1, i.e., $\sigma_{\mathrm{n}} = P/t_1$ will be used hereafter for comparing both computational and analytical results under various thickness combinations.

Fig. 4.5 Illustration of a representative FE beam model used for validation.

The initial local angular distortion shape is explicitly modeled in the FE model, as shown in Fig. 4.5. The initial distortion shape of Member 1 follows a 3rd-order polynomial based on the local angular distortion angles θ'_{11} and θ'_{12}, and the initial distortion shape of Member 2 follows a 3rd-order polynomial based on the local angular distortion angles θ'_{21} and θ'_{22}. The left end of the model was fixed for all degrees of freedom, while the right end was only allowed to move in x direction for accommodating the axial load, which were modeled as a concentrated force, as shown in Fig. 4.5. The axial load P applied in the analysis is from 0 to 1000 N, such that the nominal stress is $\sigma_{\mathrm{n}} = 0$ to 200 MPa. Table 4.1 summarizes the detailed dimensions of all three models analyzed with the definitions given in Fig. 4.1.

Table 4.1 Dimension details of FE models used

Case no.	Member 1				Member 2			
	l_1/mm	t_1/mm	θ'_{11}/deg	θ'_{12}/deg	l_2/mm	t_2/mm	θ'_{21}/deg	θ'_{22}/deg
1	200	5	1	-1	200	5	1	-1
2	200	5	1	-1	300	4	1	-1
3	200	5	1	-1	300	4	1.5	-1

The analytical k_b at the weld location of interest (top surface of Member 2 at $x_2 = 0$) for the cases listed in Table 4.1 are computed based on Eqn. (4.12) for $\sigma_n > 0$, and Eqn. (4.15) for $\sigma_n = 0$. The FE-based k_b with respect to the same weld location of interest are calculated and compared with analytical solutions in Fig. 4.6, which clearly exhibits an excellent agreement between the analytical and FE results over the entire axial load range with the error being less than 0.5%.

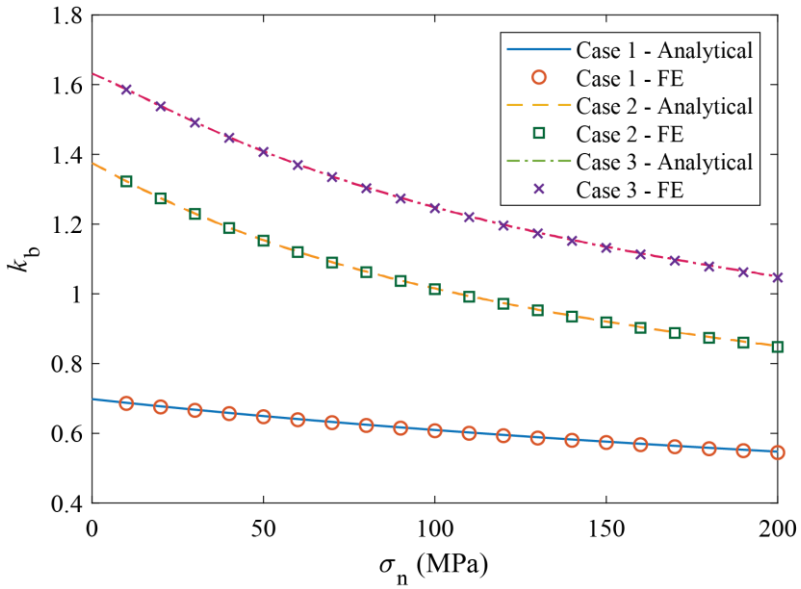

Fig. 4.6 Comparison of k_b between FE and the analytical results.

4.4 General Distortion Mode Decomposition and Assembly Procedure

The overall procedure to evaluate the complicated distortion effect on a welded joint can be described as a divide and conquer procedure, as shown in Fig. 4.7. First, the distortion's effect on a welded joint goes through a decomposition procedure and is split into three parts (referred to as basic distortion modes): 1) axial misalignment; 2) global angular distortion (angular misalignment); 3) local angular distortion (distortion curvature). Then, the secondary bending moment at the location of interest with respect to each distortion mode can be calculated using the analytical solutions developed in 3.2 and Sec. 4.3.2.2. Finally, the obtained secondary bending moments are assembled and finally yields the secondary bending caused by the complicated distortion effect. This section will first focus on developing a clear and reliable decomposition procedure and then derive the formula for the assembly based on the principle of superposition.

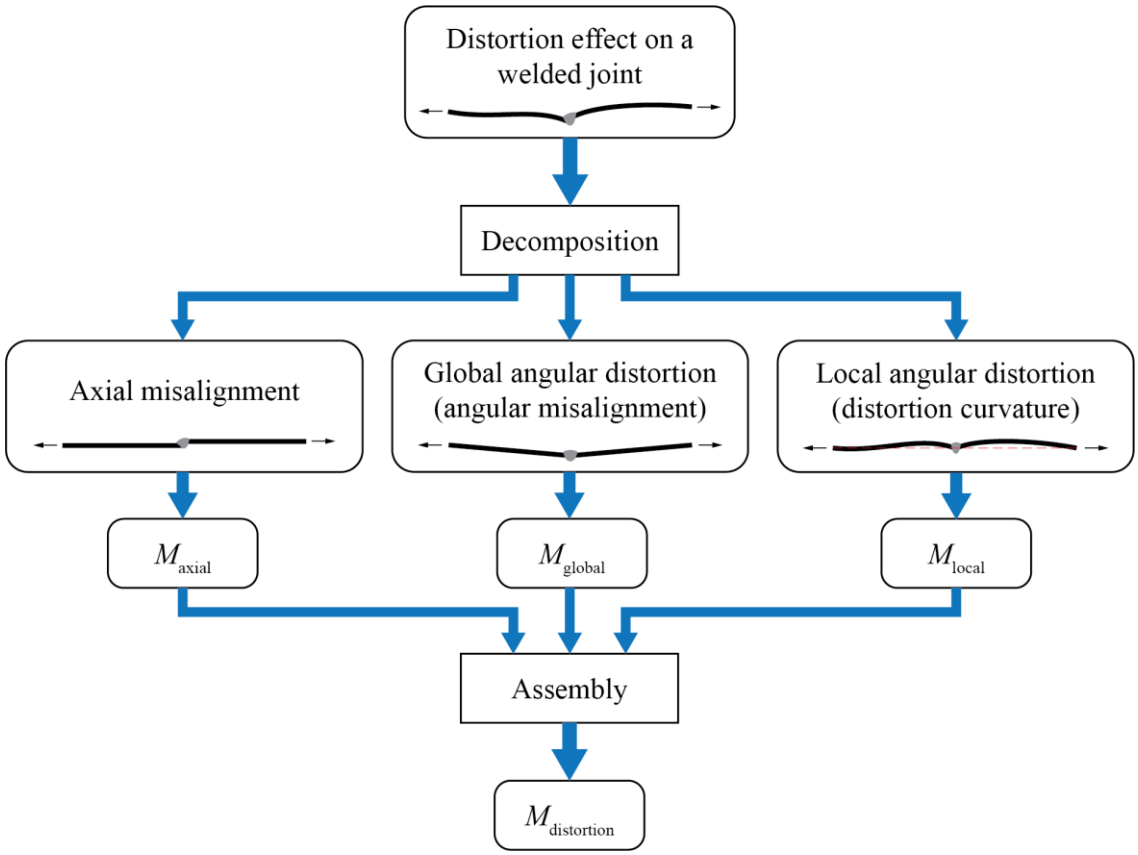

Fig. 4.7 Divide and conquer procedure for evaluating the complex distortion effect on a welded joint.

4.4.1 Distortion Mode Decomposition

Suppose a complicated distortion shape around a butt joint in terms of the centerline of the beam members (red dash-dot line in Fig. 4.8a) is given after measurement data treatment (e.g., curve fitting based on Appendix B.2), with the initial deflection of Member i from the baseline being $v_0^{(i)}(x)$. The structure is subject an axial load of P.

The first mode to be extracted is the axial misalignment. Based on 3.2.2, the axial misalignment contained in this distortion shape is defined as the vertical distance between the two centerlines at Position *O*, also shown in Fig. 3.3 and Fig. 4.8a. It can be obtained by

$$\mathrm{e} = v_0^{(2)}(0) - v_0^{(1)}(l_1) \tag{4.20}$$

The model for the axial misalignment can be then established as Fig. 4.8b; its shape function can be described as

$$\begin{aligned} v_{0,\mathrm{axial}}^{(1)}(x_1) &= 0 \\ v_{0,\mathrm{axial}}^{(2)}(x_2) &= \mathrm{e} \end{aligned} \tag{4.21}$$

where x_1 and x_2 are member-wise x-coordinate as defined in Fig. 4.1. After the extraction of axial misalignment, the remaining distortion shape of Member i becomes $v_0^{(i)} - v_{0,\mathrm{axial}}^{(i)}$, as illustrated in Fig. 4.8c.

The next step is to separate the global angular distortion and the local angular distortion. By connecting Point *O* (red dot in Fig. 4.8c) and the ends of the beam, we can obtain two angles $\theta_{1\mathrm{G}}, \theta_{2\mathrm{G}}$ using

$$\begin{aligned} \theta_{1\mathrm{G}} &= \frac{v_0^{(1)}(l_1) - v_0^{(1)}(0)}{l_1} \\ \theta_{2\mathrm{G}} &= \frac{v_0^{(2)}(l_2) - v_0^{(2)}(0)}{l_2} \end{aligned} \tag{4.22}$$

which is used to define the global angular distortion angle

$$\alpha_{\mathrm{G}} = \theta_{2\mathrm{G}} - \theta_{1\mathrm{G}} \tag{4.23}$$

The shape functions for the global angular distortion (Fig. 4.8d) are

$$\begin{aligned} v_{0,\mathrm{global}}^{(1)}\left(x_1\right) &= \theta_{1\mathrm{G}} x_1 \\ v_{0,\mathrm{global}}^{(2)}\left(x_2\right) &= \theta_{2\mathrm{G}} x_2 + \theta_{1\mathrm{G}} l_1 \end{aligned} \tag{4.24}$$

After subtracting the global angular distortion from Fig. 4.8c, the remaining distortion is the local angular distortion, given in Fig. 4.8e. Its shape functions can be expressed as

$$\begin{aligned} v_{0,\mathrm{local}}^{(1)} &= v_0^{(1)} - v_{0,\mathrm{axial}}^{(1)} - v_{0,\mathrm{global}}^{(1)} \\ v_{0,\mathrm{local}}^{(2)} &= v_0^{(2)} - v_{0,\mathrm{axial}}^{(2)} - v_{0,\mathrm{global}}^{(2)} \end{aligned} \tag{4.25}$$

The local angular distortion parameters are obtained by

$$\begin{aligned} \theta_{11}' &= v_{0,\mathrm{local}}'^{(1)}\left(0\right) \\ \theta_{12}' &= v_{0,\mathrm{local}}'^{(1)}\left(l_1\right) \\ \theta_{21}' &= v_{0,\mathrm{local}}'^{(2)}\left(0\right) \\ \theta_{22}' &= v_{0,\mathrm{local}}'^{(2)}\left(l_2\right) \end{aligned} \tag{4.26}$$

As such, the complicated distortion is decomposed into three simple basic distortion modes (Fig. 4.8b, d, and e). Note that the axial load in all basis distortion modes are still P. The secondary bending moment caused by the axial misalignment e and global angular distortion α_{G} can be acquired using the analytical solution developed in 3.2, and the secondary bending moment by the local angular distortion can be calculated using the solution derived in Sec. 4.3.2.2.

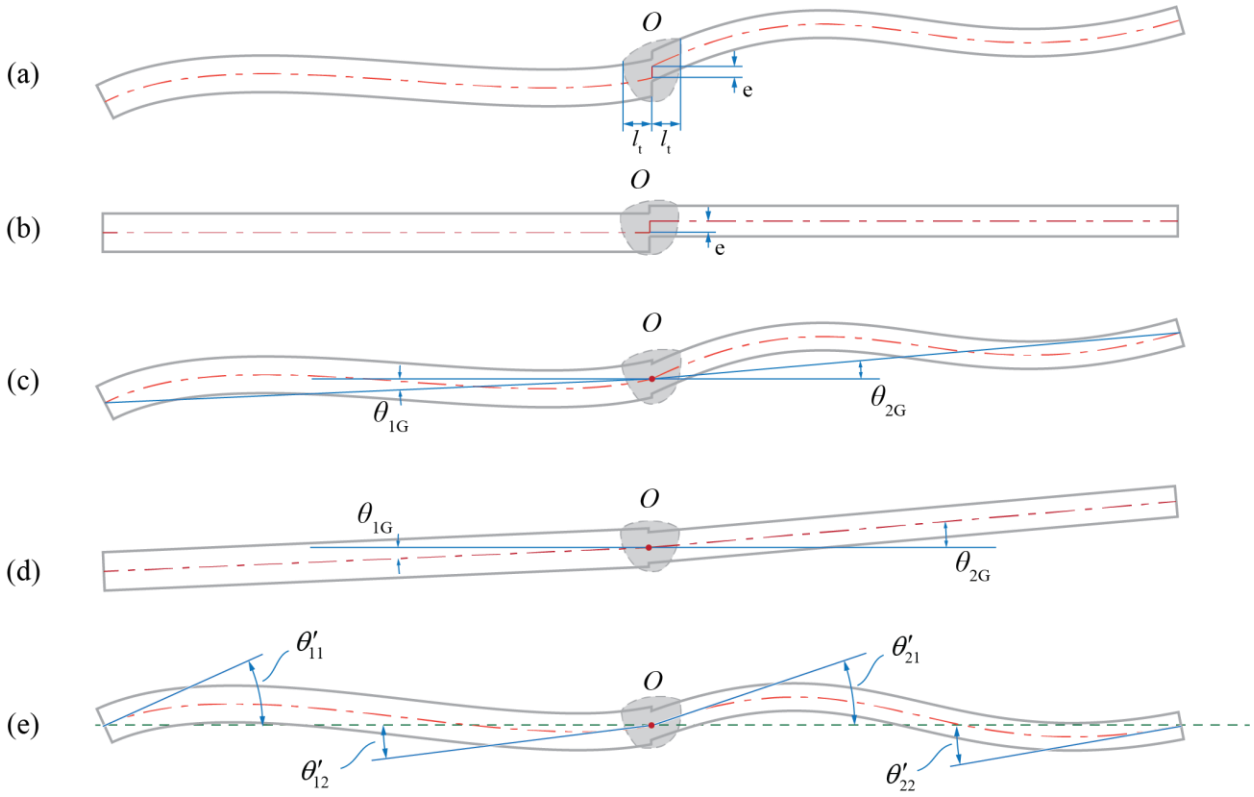

Fig. 4.8 Distortion mode decomposition: (a) complex distortion shape; (b) axial misalignment; (c) distortion after extracting axial misalignment; (d) global angular distortion; (e) local angular distortion.

4.4.2 Assembly of Analytical Solutions

The secondary bending moment of each distortion mode discussed above can be assembled using the principle of superposition. The equation for assembly is simply

$$M_{\text{distortion}}^{(i)} = M_{\text{axial}}^{(i)} + M_{\text{global}}^{(i)} + M_{\text{1,local}}^{(i)} \tag{4.27}$$

where $M_{\text{axial}}^{(i)}, M_{\text{global}}^{(i)}, M_{\text{1,local}}^{(i)}$ are the bending moment in Member i caused by the axial misalignment, the global angular distortion, and the local angular distortion. The following notations will also be used in the following derivation: $M_{\text{0,local}}^{(i)}$ and $V_{\text{0,local}}^{(i)}$ are the bending moment and the shear force in Member i caused by notional loads, $V_{\text{axial}}^{(i)}, V_{\text{global}}^{(i)}, V_{\text{1,local}}^{(i)}$ are the shear force in Member i caused by each distortion mode. $M_{\text{local}}^{(i)} = M_{\text{0,local}}^{(i)} + M_{\text{1,local}}^{(i)}$, $V_{\text{local}}^{(i)} = V_{\text{0,local}}^{(i)} +$

$V_{1,\text{local}}^{(i)}$ are the total bending moment and shear force in Member i with respect to the local angular distortion mode.

The derivation of Eqn. (4.27) is given as follows. We assume the boundary conditions on both ends of the model in Fig. 4.8a is clamped, i.e., restrained translation and rotation, and the model is subject to an axial load P. The total displacement of Member i of each distortion mode is denoted as $v_{\text{axial}}^{(i)}, v_{\text{global}}^{(i)}, v_{\text{local}}^{(i)}$. The governing equations used for all distortion modes considering nonlinear geometry are

$$EI_i \frac{d^4 v_{\text{mode}}^{(i)}}{dx_i^4} - P \frac{d^2 v_{\text{mode}}^{(i)}}{dx_i^2} = 0 \tag{4.28}$$

where $i \in \{1,2\}$ indicates the beam member referred to, and $\text{mode} \in \{\text{axial}, \text{global}, \text{local}\}$ is the distortion mode. The boundary conditions of the axial misalignment mode are given as

$$\begin{aligned} v_{\text{axial}}^{(1)}(0) &= 0 \\ v_{\text{axial}}'^{(1)}(0) &= 0 \\ v_{\text{axial}}^{(2)}(l_2) &= \text{e} \\ v_{\text{axial}}'^{(2)}(l_2) &= 0 \end{aligned} \tag{4.29}$$

The force equilibrium and the geometry relationships about the joint (Position *O*) are

$$\begin{aligned} M_{\text{axial}}^{(1)}(l_1) + P\text{e} &= M_{\text{axial}}^{(2)}(0) \\ V_{\text{axial}}^{(1)}(l_1) &= V_{\text{axial}}^{(2)}(0) \\ v_{\text{axial}}^{(1)}(l_1) + \text{e} &= v_{\text{axial}}^{(2)}(0) \\ v_{\text{axial}}'^{(1)}(l_1) &= v_{\text{axial}}'^{(2)}(0) \end{aligned} \tag{4.30}$$

The boundary conditions of the global angular distortion mode are

$$
\begin{aligned}
v_{\text{global}}^{(1)}(0) &= 0 \\
v_{\text{global}}'^{(1)}(0) &= \theta_{1\text{G}} \\
v_{\text{global}}^{(2)}(l_2) &= \theta_{1\text{G}} l_1 + \theta_{2\text{G}} l_2 \\
v_{\text{global}}'^{(2)}(0) &= \theta_{2\text{G}}
\end{aligned}
\tag{4.31}
$$

The force equilibrium and the geometry relationships about the joint (Position *O*) are

$$
\begin{aligned}
M_{\text{global}}^{(1)}(l_1) &= M_{\text{global}}^{(2)}(0) \\
V_{\text{global}}^{(1)}(l_1) &= V_{\text{global}}^{(2)}(0) \\
v_{\text{global}}^{(1)}(l_1) &= v_{\text{global}}^{(2)}(0) \\
v_{\text{global}}'^{(1)}(l_1) &= v_{\text{global}}'^{(2)}(0) - (\theta_{2\text{G}} - \theta_{1\text{G}})
\end{aligned}
\tag{4.32}
$$

The boundary conditions of the local angular distortion mode are

$$
\begin{aligned}
v_{\text{local}}^{(1)}(0) &= 0 \\
v_{\text{local}}'^{(1)}(0) &= \theta_{11}' \\
v_{\text{local}}^{(2)}(l_2) &= 0 \\
v_{\text{local}}'^{(2)}(0) &= \theta_{22}'
\end{aligned}
\tag{4.33}
$$

The force equilibrium and the geometry relationships about the joint (Position *O*) are

$$
\begin{aligned}
M_{\text{local}}^{(1)}(l_1) &= M_{\text{local}}^{(2)}(0) + m_0 \\
V_{\text{local}}^{(1)}(l_1) &= V_{\text{local}}^{(2)}(0) + F_0 \\
v_{\text{local}}^{(1)}(l_1) &= v_{\text{local}}^{(2)}(0) \\
v_{\text{local}}'^{(1)}(l_1) &= v_{\text{local}}'^{(2)}(0) - (\theta_{21}' - \theta_{12}')
\end{aligned}
\tag{4.34}
$$

Summing up Eqns. (4.29), (4.31), and (4.33) and denoting $v_{\text{total}}^{(i)} = v_{\text{axial}}^{(i)} + v_{\text{global}}^{(i)} + v_{\text{local}}^{(i)}$ yields

$$
\begin{aligned}
v_{\text{total}}^{(1)}(0) &= 0 \\
v_{\text{total}}'^{(1)}(0) &= \theta_{1\text{G}} + \theta_{11}' \\
v_{\text{total}}^{(2)}(l_2) &= \text{e} + \theta_{1\text{G}} l_1 + \theta_{2\text{G}} l_2 \\
v_{\text{total}}'^{(2)}(0) &= \theta_{2\text{G}} + \theta_{22}'
\end{aligned}
\tag{4.35}
$$

Adding up Eqns. (4.30), (4.32), and (4.34) results in

$$
\begin{aligned}
M_{\text{total}}^{(1)}\left(l_1\right)+P\mathrm{e} &= M_{\text{total}}^{(2)}\left(0\right)+m_0 \\
V_{\text{total}}^{(1)}\left(l_1\right) &= V_{\text{total}}^{(2)}\left(0\right)+F_0 \\
v_{\text{total}}^{(1)}\left(l_1\right)+\mathrm{e} &= v_{\text{total}}^{(2)}\left(0\right) \\
v_{\text{total}}'^{(1)}\left(l_1\right) &= v_{\text{total}}'^{(2)}\left(0\right)-\left(\theta_{2\mathrm{G}}-\theta_{1\mathrm{G}}\right)-\left(\theta_{21}'-\theta_{12}'\right)
\end{aligned}
\tag{4.36}
$$

where $M_{\text{total}}^{(i)}=M_{\text{axial}}^{(i)}+M_{\text{global}}^{(i)}+M_{\text{local}}^{(i)}$ and $V_{\text{total}}^{(i)}=V_{\text{axial}}^{(i)}+V_{\text{global}}^{(i)}+V_{\text{local}}^{(i)}$. Eqns. (4.35) and (4.36) are the same as the boundary conditions, force equilibrium and geometry relationships written directly based on the complicated distortion shape in Fig. 4.8a, which validates the claim that the total secondary bending moment caused by the complex distortion is the sum of the secondary bending moment of each distortion mode. As discussed in Sec. 4.3.2.2, the bending moment caused by the notional loads needs to be deducted from $M_{\text{total}}^{(i)}$, and the secondary bending moment caused by distortion is

$$
M_{\text{distortion}}^{(i)}=M_{\text{distortion}}^{(i)}-M_{0,\text{local}}^{(i)} \tag{4.37}
$$

which eventually yields Eqn. (4.27).

4.5 Discussions

4.5.1 Analysis of Distortion Shape Effect

In engineering application, one question of interest is which kinds of initial distortion shape would cause maximum secondary bending and which kinds will have negligible effect. To investigate the effect of distortion shape on secondary bending, we can use the simplified model presented in Sec. 4.3.4 in which both members has the same length l and thickness t. Based on the notional load model in Sec. 4.3.1, the local angular distortion shape is given as

$$v_0^{(1)}(x_1) = \theta'_{11}x_1 + \frac{-2\theta'_{11} - \theta'_{12}}{l}x_1^2 + \frac{\theta'_{11} + \theta'_{12}}{l^2}x_1^3$$
$$v_0^{(2)}(x_2) = \theta'_{21}x_2 + \frac{-2\theta'_{21} - \theta'_{22}}{l}x_2^2 + \frac{\theta'_{21} + \theta'_{22}}{l^2}x_2^3 \quad (4.38)$$

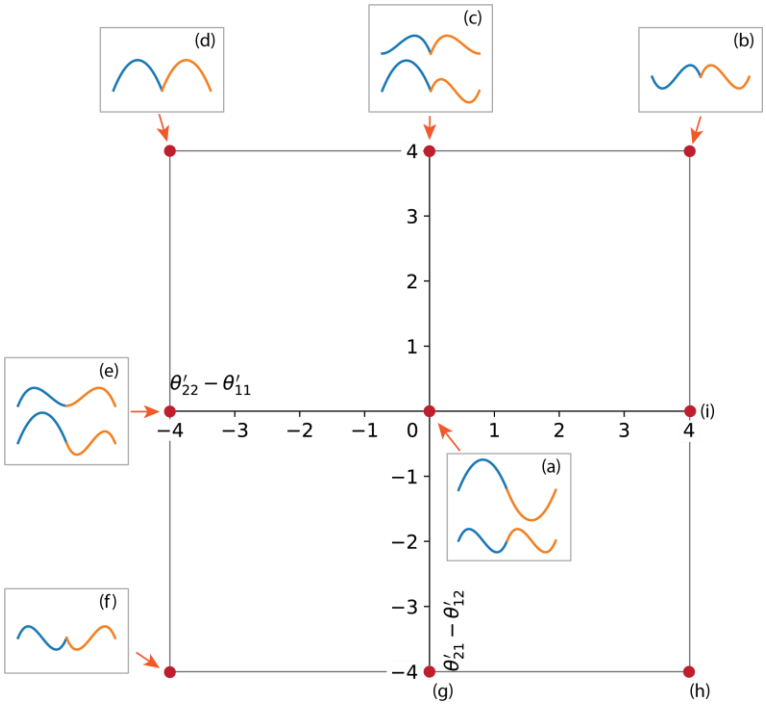

Fig. 4.9 Representative local angular distortion shapes

Since the simplified solution given in Eqn. (4.18) shows its dependency on $\theta'_{21} - \theta'_{12}$ and $\theta'_{22} - \theta'_{11}$, we can plot some representative local angular distortion shapes at eight positions, Point (a)-(i), using Eqn. (4.38) based on different $\theta'_{21} - \theta'_{12}$ and $\theta'_{22} - \theta'_{11}$ (limited to $-2° \leq \theta'_{11}, \theta'_{12}, \theta'_{21}, \theta'_{22} \leq 2°$), as illustrated in Fig. 4.9. The representative distortion shapes corresponding to two points that are symmetrical about the origin, for example, Point (b) and (f), are symmetric about $y = 0$. As such, only distortion shapes corresponding the top-left half plane (Point (a)-(f)) are plotted. Distortion shapes corresponding to Point (g),(h), and (i) are the reflection of the distortion shapes of Point (c), (d), and (e), respectively.

To facilitate a quantitative investigation of the distortion shape's effect on the secondary bending, we denote

$$\Psi_1^{\text{sym}} = \frac{\lambda^2 l^2 \cosh \lambda l - 4\lambda l \sinh \lambda l + 6\cosh \lambda l - 6}{2\lambda^3 l^3 \sinh \lambda l}$$
$$\Psi_2^{\text{sym}} = \frac{-\lambda^2 l^2 - 2\lambda l \sinh \lambda l + 6\cosh \lambda l - 6}{2\lambda^3 l^3 \sinh \lambda l}$$
$$\Theta_1^{\text{sym}} = \frac{-\lambda^2 l^2 \cos \lambda l + 4\lambda l \sin \lambda l + 6\cos \lambda l - 6}{2\lambda^3 l^3 \sin \lambda l} \tag{4.39}$$
$$\Theta_2^{\text{sym}} = \frac{\lambda^2 l^2 + 2\lambda l \sin \lambda l + 6\cos \lambda l - 6}{2\lambda^3 l^3 \sin \lambda l}$$

and we can write Eqn. (4.18) in the following form

$$k_{\text{b,s}} = \begin{cases} 6\dfrac{l}{t}\left[\Psi_1^{\text{sym}}\left(\theta'_{21} - \theta'_{12}\right) + \Psi_2^{\text{sym}}\left(\theta'_{22} - \theta'_{11}\right)\right] & P > 0 \\ 6\dfrac{l}{t}\left[\Theta_1^{\text{sym}}\left(\theta'_{21} - \theta'_{12}\right) + \Theta_2^{\text{sym}}\left(\theta'_{22} - \theta'_{11}\right)\right] & P < 0 \end{cases} \tag{4.40}$$

Clearly, for given l and t, $\Psi_1^{\text{sym}}, \Psi_2^{\text{sym}}, \Theta_1^{\text{sym}}, \Theta_2^{\text{sym}}$ are functions of $\lambda = \sqrt{12|P|/Et^3}$, and they will vary as P changes, exhibiting the straightening effect.

Suppose we are given $l = 200$ mm and $t = 5$ mm. We start from plotting $k_{\text{b,s}}$ when $P \to 0$ (using Eqn. (4.19)) over the same range of $\theta'_{21} - \theta'_{12}$ and $\theta'_{22} - \theta'_{11}$ in Fig. 4.9, as shown in Fig. 4.10a. We can use $|k_{\text{b,s}}|$ as a metric for the secondary bending effect. We can observe that the maximum $|k_{\text{b,s}}|$ occurs at Point (d) where $\theta'_{22} - \theta'_{11} = -4°$, $\theta'_{21} - \theta'_{12} = 4°$ and Point (h) where $\theta'_{22} - \theta'_{11} = 4°$, $\theta'_{21} - \theta'_{12} = -4°$, while the minimum $|k_{\text{b,s}}|$ is zero, which happens along $\theta'_{22} - \theta'_{11} = \theta'_{21} - \theta'_{12}$ (see the dashed line in Fig. 4.10a). Then, we plot $k_{\text{b,s}}$ when $\sigma_{\text{n}} = 100$ MPa in Fig. 4.10b and $\sigma_{\text{n}} = -50$ MPa in Fig. 4.10c. The maximum $|k_{\text{b,s}}|$ still occurs at Point (d) and Point (h), but the dashed line indicating minimum $|k_{\text{b,s}}|$ ($k_{\text{b,s}} = 0$) has rotated (about the origin) clockwise when σ_{n} increases and counter-clockwise when σ_{n} decreases. If we further decrease σ_{n} to -80 MPa (see Fig. 4.10d), we can see the line $k_{\text{b,s}} = 0$ rotated even more such that

its slope is negative. The maximum $|k_{b,s}|$ now occurs at Point (f) where $\theta'_{22} - \theta'_{11} = -4°$, $\theta'_{21} - \theta'_{12} = -4°$ and Point (b) where $\theta'_{22} - \theta'_{11} = 4°$, $\theta'_{21} - \theta'_{12} = 4°$.

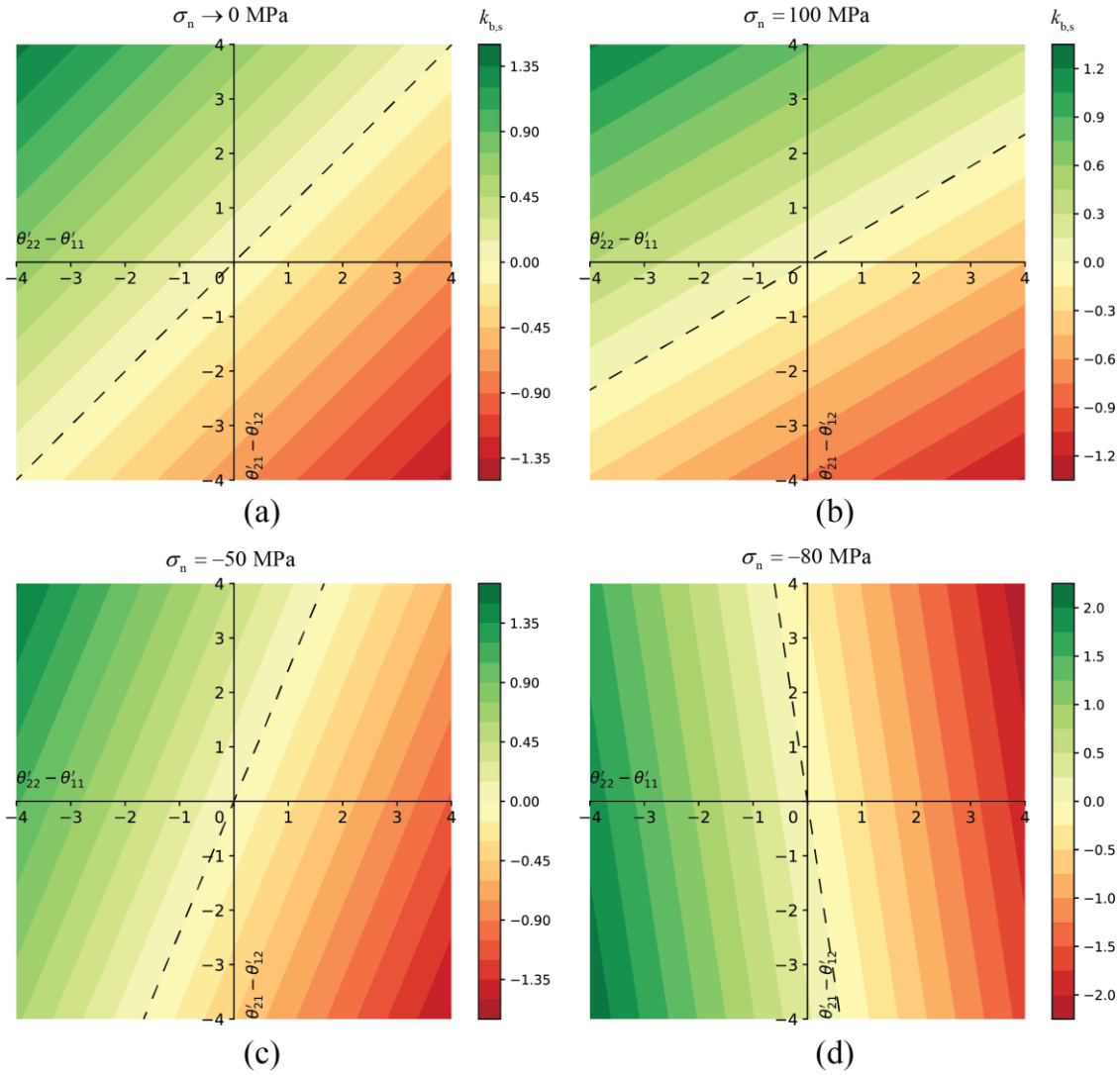

Fig. 4.10 $k_{b,s}$ as a function of $\theta'_{22} - \theta'_{11}$ and $\theta'_{21} - \theta'_{12}$ when: (a) $\sigma_n \to 0$ MPa; (b) $\sigma_n = 100$ MPa; (c) $\sigma_n = -50$ MPa; (d) $\sigma_n = -80$ MPa.

The above phenomenon can be explained with the help of the expression for the dashed line representing the minimum $|k_{b,s}|$, which can be obtained by setting $k_{b,s} = 0$ in Eqn. (4.18) and reorganizing the equation as

$$\left(\theta'_{21}-\theta'_{12}\right)=\begin{cases}-\dfrac{\Psi_2^{\mathrm{sym}}}{\Psi_1^{\mathrm{sym}}}\left(\theta'_{22}-\theta'_{11}\right) & P>0\\ -\dfrac{\Theta_2^{\mathrm{sym}}}{\Theta_1^{\mathrm{sym}}}\left(\theta'_{22}-\theta'_{11}\right) & P<0\end{cases} \tag{4.41}$$

Judging from Eqn. (4.40), we can claim that $k_{\mathrm{b,s}}$ monotonically increases or decreases in the normal direction of the line $k_{\mathrm{b,s}}=0$. Based on the expression of $k_{\mathrm{b,s}}$ (Eqn. (4.40)) and $k_{\mathrm{b,s}}=0$ (Eqn. (4.41)), we can reveal some insights on the initial distortion shapes' influence on $\left|k_{\mathrm{b,s}}\right|$.

(a) Importance of $\theta'_{22}-\theta'_{11}$ and $\theta'_{21}-\theta'_{12}$

When $P\to 0$, we can see that $\theta'_{22}-\theta'_{11}$ has the same effect as $\theta'_{21}-\theta'_{12}$ has on $\left|k_{\mathrm{b,s}}\right|$, as shown in Fig. 4.10a. When $P\to+\infty$, the slope of $k_{\mathrm{b,s}}=0$, $-\Psi_2^{\mathrm{sym}}/\Psi_1^{\mathrm{sym}}$, monotonically decreases and finally reaches

$$\lim_{P\to+\infty}-\frac{\Psi_2^{\mathrm{sym}}}{\Psi_1^{\mathrm{sym}}}=0 \tag{4.42}$$

resulting in the line $k_{\mathrm{b,s}}=0$ being horizontal, which indicates that when the load level is large, $\theta'_{21}-\theta'_{12}$ will have greater influence than $\theta'_{22}-\theta'_{11}$ has on $\left|k_{\mathrm{b,s}}\right|$. For $P<0$, since the line $k_{\mathrm{b,s}}=0$ will continue rotate counterclockwise when P decreases, $\theta'_{22}-\theta'_{11}$ will have greater influence than $\theta'_{21}-\theta'_{12}$ has on $\left|k_{\mathrm{b,s}}\right|$.

(b) Initial distortion shape's effect on $\left|k_{\mathrm{b,s}}\right|$

Based on the $k_{\mathrm{b,s}}$ solution when $P\to 0$, we can establish two parameters that can approximately describe the initial distortion shape's effect without calculating detailed $k_{\mathrm{b,s}}$. The first one is

$$\left|\left(\theta'_{21}-\theta'_{12}\right)-\left(\theta'_{22}-\theta'_{11}\right)\right| \tag{4.43}$$

which comes from Eqn. (4.19). As shown previously, within the axial fatigue load level of interest, $|k_{b,s}|$ mostly increases when $|(\theta'_{22} - \theta'_{11}) - (\theta'_{21} - \theta'_{12})|$ increases, and Eqn. (4.43) can provide a good approximation of the magnitude of $|k_{b,s}|$. The second one is the integral of the initial distortion shape function, given as

$$\left|\int v_0 dx\right| \tag{4.44}$$

For the local angular distortion shape discussed in this section, the integral in the above equation equals to

$$\begin{aligned}\int v_0 dx &= \int_0^l v_0^{(1)} dx + \int_0^l v_0^{(2)} dx \\ &= \frac{l^2}{12}\left(\theta'_{21} - \theta'_{12}\right) - \frac{l^2}{12}\left(\theta'_{22} - \theta'_{11}\right)\end{aligned} \tag{4.45}$$

which is proportional to $k_{b,s}$ given in Eqn. (4.19). As such, $|\int v_0 dx|$ can also provide a good estimation of $|k_{b,s}|$.

By plotting the above metric, e.g., Eqn. (4.44), in Fig. 4.11 and comparing with the representative distortion shapes in Fig. 4.9, we can see that the distortion shapes corresponding to Point (d) and (h), which exhibits an "eagle" shape (see Fig. 4.9d), are subject to the most secondary bending. Meanwhile, the distortion shapes corresponding to Point (b) and (f), each of which contains one sinusoidal-like wave on each side and features a sudden slope change at the joint (see Fig. 4.9b and f), and Point (a), which represents all anti-symmetrical distortion shapes, such as a sine wave with joint in the middle (see Fig. 4.9a), will introduce little secondary bending. Particularly for Point (a), the $k_{b,s}$ caused by its corresponding distortion shape will always be zero regardless of the applied axial load level since $k_{b,s} = 0$ always passes through Point (a).

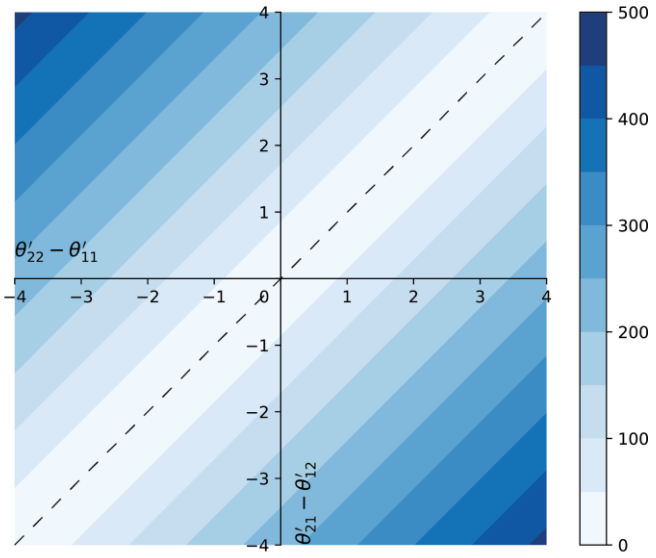

Fig. 4.11 $\left|\int v_0 dx\right|$ plotted as a function of $\theta'_{22} - \theta'_{11}$ and $\theta'_{21} - \theta'_{12}$.

4.5.2 Decomposition of Distortions in Stiffened Panels

The decomposition and assembly procedure developed in Sec. 4.4 can also be applied on the distortions between stiffeners in panel structures. Fig. 4.12a shows a typical initial distortion profile between two stiffener documented in [41], containing displaced stiffeners and distortion curvatures, and the base plate is subject to an axial load P. Since the base plate is continuous, there is no axial misalignment associated with fillet welds at stiffener locations. For simplicity, we also assume that the stiffeners are fixed (i.e., restrained translation and rotation) in the structure, and Position A, B in Fig. 4.12 are the weld toe positions of interest.

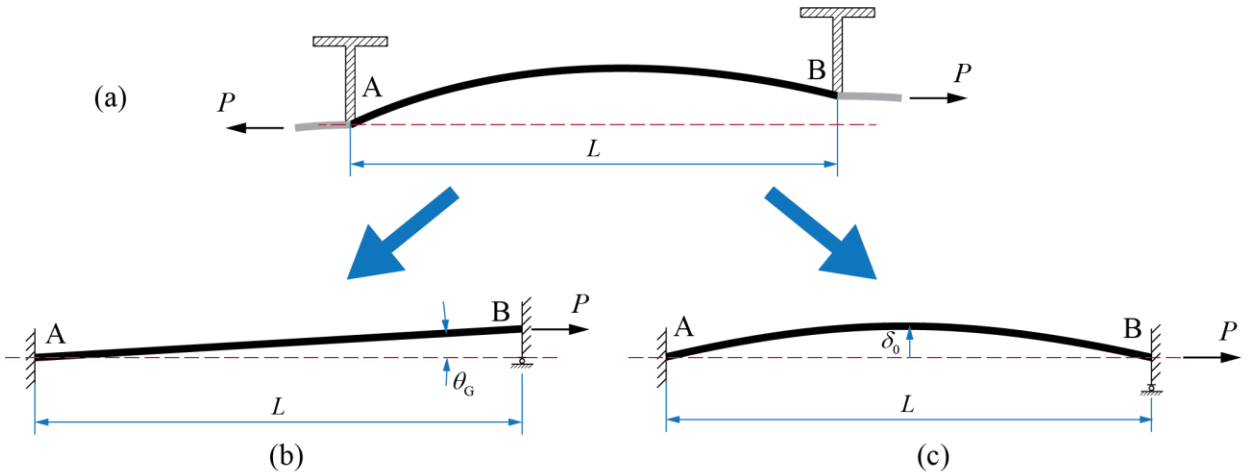

Fig. 4.12 Distortion decomposition of a distortion profile in stiffened panels: (a) original distortion; (b) global angular distortion; (c) local angular distortion.

Before the decomposition, we first expand the definition of the basic distortion modes in the context of stiffened panels to keep terminology consistent. The global angular distortion formed between two stiffeners only involves one member as shown in Fig. 4.12b, characterized by θ_G, and the local angular distortion between the stiffeners contains the curved component of the initial distortion profile only. As such, the buckling distortion mode and the cosine angular distortion mode discussed in Sec.2.3.1 are subtypes of the local angular distortion mode under this definition.

Based on the decomposition rule discussed in Sec. 4.4.1, we can divide the distortion into two basic distortion modes: the global angular distortion in Fig. 4.12b and the local angular distortion in Fig. 4.12c, which can be represented by the buckling distortion mode in Sec. 2.3.1.2. Under the given boundary conditions, we can easily show that the global angular distortion will not introduce any secondary bending stress at Positions A, B, i.e., $k_{\mathrm{b,global}} = 0$. The secondary bending caused by the local angular distortion in Fig. 4.12c, $k_{\mathrm{b,local}}$, can be calculated using Eqn. (2.8) with respect to the buckling distortion mode.

Finally, the secondary bending with respect to the distortion profile in Fig. 4.12a is obtained by superimposing $k_{\mathrm{b,global}}$ and $k_{\mathrm{b,local}}$. In this case, the secondary bending is only related to $k_{\mathrm{b,local}}$.

4.5.3 Substitution of Analytical Solutions

In Sec. 4.4.2, the assembly procedure is derived based on nonlinear geometry, meaning that technically, $M_{\mathrm{axial}}^{(i)}, M_{\mathrm{global}}^{(i)}, M_{\mathrm{1,local}}^{(i)}$ in Eqn. (4.27) needs to be calculated on a nonlinear geometry basis. However, in engineering application, $M_{\mathrm{axial}}^{(i)}, M_{\mathrm{global}}^{(i)}, M_{\mathrm{1,local}}^{(i)}$ based on linear geometry can be used in Eqn. (4.27), partly or wholly, to approximate the total secondary bending caused by distortion. For example, in the calculation of the secondary bending in the lab-scale specimens in Sec. 2.4.1, because the axial misalignments in the specimens are small, linear geometry solution given in [63] is used to calculate $M_{\mathrm{axial}}^{(i)}$; however, $M_{\mathrm{global}}^{(i)}$ and $M_{\mathrm{1,local}}^{(i)}$ are still computed using nonlinear geometry solutions given by Eqn. (2.9) and Eqn. (2.11). Such substitutions can simplify the calculation process but will sacrifice the accuracy. Therefore, they are only preferred when the magnitude of a distortion mode is small, or the nonlinear geometry effect is not significant.

4.6 Chapter Conclusions

This chapter developed a general analytical modeling procedure for misalignment and distortion curvature effects on welded joints. By extending the analytical solution of the local angular distortion to a more general extent based on the notional load method and nonlinear geometry, the superposition of the local angular distortion mode and the misalignments modes discussed in Chapter 3 is enabled. The analytical solution is validated using finite element method. Then, the general modeling procedure is designed based on a divide-and-conquer strategy. First, a complicated distortion effect at a welded joint is decomposed into several basic distortion mode

problems. Next, the analytical solution to each basic distortion mode is obtained using previously developed results. And finally, using the principle of superposition, the solutions are added up together, leading to the complex distortion effect sought.

By examining the analytical solution to the local angular distortion, we found that 1) a linear geometry approximation of the analytical solution can be obtained by taking the limit of the nonlinear analytical solution as P approaches zero; 2) based on the symmetric nominal structure assumption, the "eagle" shaped distortion curvatures would induce the most secondary bending, while distortion shapes that contain a full sine-wave on both members of the joint, or feature anti-symmetry with respect to the joint position will cause little secondary bending.

Moreover, the decomposition and assembly procedure can be easily expanded beyond the scope of a butt-welded joint following the rule presented, so that different types of joint configuration can be covered, such as the distortions in stiffened panel, adding flexibility to the developed procedure. Also, by decomposing the complicated distortion problem into several simple ones, justifiable simplifications can be applied with respect to each distortion mode, thus reducing the difficulty in calculations.

Chapter 5

A Generalized Procedure for Distortion Decomposition and Assembly of Elementary Distortion Mode-Based Solutions

5.1 Chapter Introduction

This chapter first summarizes the analytical solutions developed in each chapter and presents them in tabular form based on engineering application scenarios. A step-by-step distortion mode decomposition and assembly procedure are then provided. Finally, two comprehensive application examples are provided to illustrate how the analytical solutions developed in this research can be used in real engineering problems.

5.2 Decomposition and Assembly for Treatment of Butt-Welded Plates

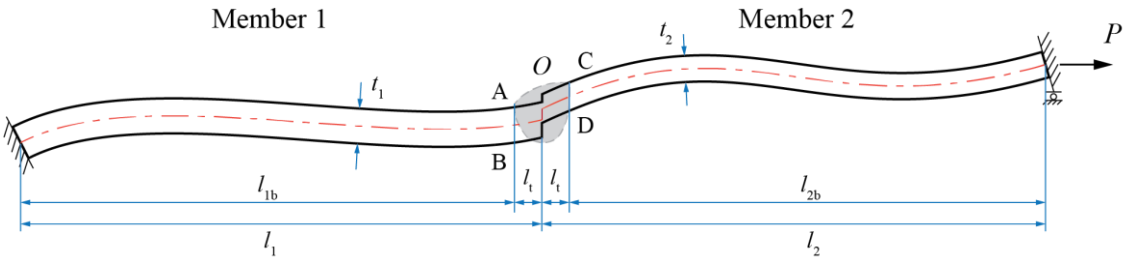

Fig. 5.1 Illustration of a welded joint with complex distortions.

Consider a butt joint with the distortion shown in Fig. 5.1 under clamped boundary condition, the secondary bending moment at Position *O* caused by an axial load *P* on a welded joint subject to complex distortions is obtained by

$$M_{\text{distortion}}^{(i)} = M_{\text{axial}}^{(i)} + M_{\text{global}}^{(i)} + M_{\text{1,local}}^{(i)} \tag{5.1}$$

where $M_{\text{axial}}^{(i)}, M_{\text{global}}^{(i)}, M_{\text{1,local}}^{(i)}$ corresponds to bending moment induced by axial misalignment, global angular distortion, and local angular distortion modes, respectively. The bending stress

caused by all distortion modes corresponding to the four weld toe locations (Positions A, B, C, D) are given as

$$\sigma_{\mathrm{b}}^{\mathrm{A}} = -\sigma_{\mathrm{b}}^{\mathrm{B}} = -\frac{6M_{\mathrm{distortion}}^{(1)}}{t_1^2} \tag{5.2}$$

$$\sigma_{\mathrm{b}}^{\mathrm{C}} = -\sigma_{\mathrm{b}}^{\mathrm{D}} = -\frac{6M_{\mathrm{distortion}}^{(2)}}{t_2^2} \tag{5.3}$$

And the secondary bending induced stress concentration factor, k_{b}, at the four weld toe positions can be calculated as:

$$k_{\mathrm{b}}^{i} = \frac{\sigma_{\mathrm{b}}^{i}}{\sigma_{\mathrm{n}}} \quad i \in \{\mathrm{A, B, C, D}\} \tag{5.4}$$

in which the beam section nominal stress σ_{n} is expressed as P/t_1 by definition, corresponding to the average stress in Member 1 or P/t_2 corresponding to the average stress in Member 2.

$M_{\mathrm{axial}}^{(i)}, M_{\mathrm{global}}^{(i)}, M_{1,\mathrm{local}}^{(i)}$ in Eqn. (5.1) can be calculated using the formulae in the tables in this section. The parameter corresponds to each distortion mode is obtained through the decomposition procedure provided in Sec. 4.4.1. Table 5.1 provides an index for the tables of analytical formulae given in this section. When calculating the secondary bending moments in Eqn. (5.1), one should pick one table for each distortion mode based on the application scenario.

Table 5.1 Index of tables for calculating secondary bending moment caused by each distortion mode.

Deformation	Consider joint representation	$M_{\mathrm{axial}}^{(i)}$	$M_{\mathrm{global}}^{(i)}$	$M_{1,\mathrm{local}}^{(i)}$
Small deformation	Y	Table 5.2	Table 5.5	N/A
	N	Table 5.3	Table 5.6	Table 5.9
Large deformation	Y	Table 5.4	Table 5.7	Table 5.10
	N	Table 5.3*	Table 5.8	Table 5.11

*: same as small deformation condition

5.2.1 Axial Misalignment Mode

This section provides several tables of formulae for calculating the bending moment caused by the axial misalignment, $M_{\text{axial}}^{(i)}$, derived from the analytical solutions developed in Sec. 3.2. Fig. 5.2a shows the analytical model of the axial misalignment distortion. The axial misalignment e is defined as the vertical distance between the center lines of Member 1 and that of Member 2 at the joint center position (Position *O*), with the sign convention given in Fig. 5.2b.

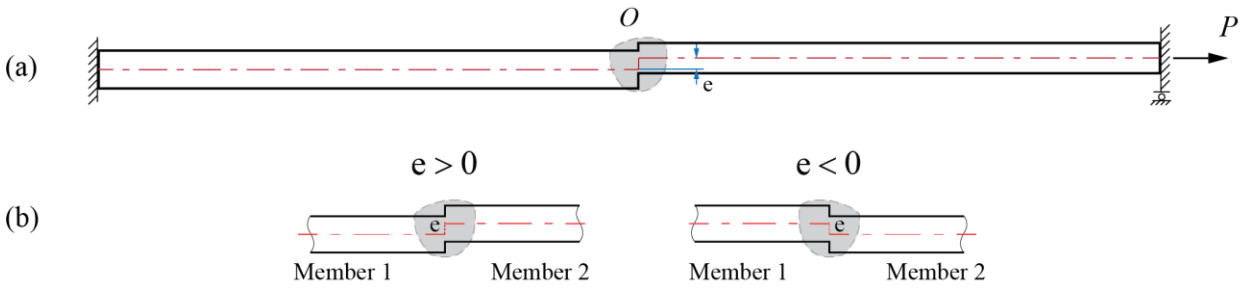

Fig. 5.2 Illustration of axial misalignment (a) analytical model; (b) sign convention.

5.2.1.1 Small Deformation (Linear Geometry) Solutions

Tables provided in this section correspond to small deformation conditions where the analytical solutions are derived based on linear geometry. The derivation of the formulae in this section is documented in Sec. 3.2.3.

(a) With consideration of the joint representation.

The analytical solutions with consideration of the joint representation, which can include the joint size effect, are provided in Table 5.2.

Table 5.2 Formulae for calculating the bending moment due to axial misalignment in butt joints considering joint representation under small deformation condition.

Type	Bending moment $M_{\text{axial}}^{(i)}$
$l_{1\text{b}} = l_{2\text{b}} = l_{\text{b}}$ and $t_1 = t_2 = t$	$M_{\text{axial}}^{(1)} = -\dfrac{Pl_{\text{b}}}{2l_{\text{b}} + 3l_{\text{t}}}\text{e}$ $M_{\text{axial}}^{(2)} = \dfrac{Pl_{\text{b}}}{2l_{\text{b}} + 3l_{\text{t}}}\text{e}$
$l_{1\text{b}} = l_{2\text{b}} = l_{\text{b}}$	$M_{\text{axial}}^{(1)} = -\dfrac{Pt_1^3 l_{\text{b}}\left(7t_2^3 + t_1^3\right)}{l_{\text{b}}t_2^6 + 14l_{\text{b}}t_1^3t_2^3 + 24l_{\text{t}}t_1^3t_2^3 + l_{\text{b}}t_1^6}\text{e}$ $M_{\text{axial}}^{(2)} = \dfrac{Pt_2^3 l_{\text{b}}\left(7t_1^3 + t_2^3\right)}{l_{\text{b}}t_2^6 + 14l_{\text{b}}t_1^3t_2^3 + 24l_{\text{t}}t_1^3t_2^3 + l_{\text{b}}t_1^6}\text{e}$
$t_{1\text{b}} = t_{2\text{b}} = t_{\text{b}}$	$M_{\text{axial}}^{(1)} = -\dfrac{Pl_{2\text{b}}\left(4l_{1\text{b}}^3 + 3l_{1\text{b}}^2l_{2\text{b}} + l_{2\text{b}}^3\right)}{l_{1\text{b}}^4 + 4l_{1\text{b}}^3l_{2\text{b}} + 12l_{1\text{b}}^2l_{\text{t}}l_{2\text{b}} + 6l_{1\text{b}}^2l_{2\text{b}}^2 + 12l_{1\text{b}}l_{\text{t}}l_{2\text{b}}^2 + 4l_{1\text{b}}l_{2\text{b}}^3 + l_{2\text{b}}^4}\text{e}$ $M_{\text{axial}}^{(2)} = \dfrac{Pl_{1\text{b}}\left(4l_{2\text{b}}^3 + 3l_{2\text{b}}^2l_{1\text{b}} + l_{1\text{b}}^3\right)}{l_{1\text{b}}^4 + 4l_{1\text{b}}^3l_{2\text{b}} + 12l_{1\text{b}}^2l_{\text{t}}l_{2\text{b}} + 6l_{1\text{b}}^2l_{2\text{b}}^2 + 12l_{1\text{b}}l_{\text{t}}l_{2\text{b}}^2 + 4l_{1\text{b}}l_{2\text{b}}^3 + l_{2\text{b}}^4}\text{e}$
General l and t	$M_{\text{axial}}^{(1)} = -\dfrac{Pt_1^3 l_{2\text{b}}\left(4l_{1\text{b}}^3t_2^3 + 3l_{1\text{b}}^2l_{2\text{b}}t_2^3 + l_{2\text{b}}^3t_1^3\right)}{l_{1\text{b}}^4t_2^6 + 4l_{1\text{b}}^3l_{2\text{b}}t_1^3t_2^3 + 12l_{1\text{b}}^2l_{\text{t}}l_{2\text{b}}t_1^3t_2^3 + 6l_{1\text{b}}^2l_{2\text{b}}^2t_1^3t_2^3 + 12l_{1\text{b}}l_{\text{t}}l_{2\text{b}}^2t_1^3t_2^3 + 4l_{1\text{b}}l_{2\text{b}}^3t_1^3t_2^3 + l_{2\text{b}}^4t_1^6}\text{e}$ $M_{\text{axial}}^{(2)} = \dfrac{Pt_2^3 l_{1\text{b}}\left(4l_{2\text{b}}^3t_1^3 + 3l_{2\text{b}}^2l_{1\text{b}}t_1^3 + l_{1\text{b}}^3t_2^3\right)}{l_{1\text{b}}^4t_2^6 + 4l_{1\text{b}}^3l_{2\text{b}}t_1^3t_2^3 + 12l_{1\text{b}}^2l_{\text{t}}l_{2\text{b}}t_1^3t_2^3 + 6l_{1\text{b}}^2l_{2\text{b}}^2t_1^3t_2^3 + 12l_{1\text{b}}l_{\text{t}}l_{2\text{b}}^2t_1^3t_2^3 + 4l_{1\text{b}}l_{2\text{b}}^3t_1^3t_2^3 + l_{2\text{b}}^4t_1^6}\text{e}$

(b) Without consideration of the joint representation.

The analytical solution without consideration of the joint representation is provided in Table 5.3. These equations are applicable when the joint size is not known or the joint size effect is of less importance.

Table 5.3 Formulae for calculating the bending moment due to axial misalignment in butt joints without considering joint representation under small deformation conditions.

Type	Bending moment $M_{\text{axial}}^{(i)}$
$l_1 = l_2 = l$ and $t_1 = t_2 = t$	$M_{\text{axial}}^{(1)} = -\frac{P}{2}\text{e}$ $M_{\text{axial}}^{(2)} = \frac{P}{2}\text{e}$
$l_1 = l_2 = l$	$M_{\text{axial}}^{(1)} = -\frac{Pt_1^3\left(7t_2^3 + t_1^3\right)}{t_2^6 + 14t_1^3t_2^3 + t_1^6}\text{e}$ $M_{\text{axial}}^{(2)} = \frac{Pt_2^3\left(7t_1^3 + t_2^3\right)}{t_2^6 + 14t_1^3t_2^3 + t_1^6}\text{e}$
$t_1 = t_2 = t$	$M_{\text{axial}}^{(1)} = -\frac{Pl_2\left(4l_1^3 + 3l_1^2l_2 + l_2^3\right)}{l_1^4 + 4l_1^3l_2 + 6l_1^2l_2^2 + 4l_1l_2^3 + l_2^4}\text{e}$ $M_{\text{axial}}^{(2)} = \frac{Pl_1\left(4l_{2\text{b}}^3 + 3l_2^2l_1 + l_1^3\right)}{l_1^4 + 4l_1^3l_2 + 6l_1^2l_2^2 + 4l_1l_2^3 + l_2^4}\text{e}$
General l and t	$M_{\text{axial}}^{(1)} = -\frac{Pt_1^3l_2\left(4l_1^3t_2^3 + 3l_1^2l_2t_2^3 + l_2^3t_1^3\right)}{l_1^4t_2^6 + 4l_1^3l_2t_1^3t_2^3 + 6l_1^2l_2^2t_1^3t_2^3 + 4l_1l_2^3t_1^3t_2^3 + l_2^4t_1^6}\text{e}$ $M_{\text{axial}}^{(2)} = \frac{Pt_2^3l_1\left(4l_2^3t_1^3 + 3l_2^2l_1t_1^3 + l_1^3t_2^3\right)}{l_1^4t_2^6 + 4l_1^3l_2t_1^3t_2^3 + 6l_1^2l_2^2t_1^3t_2^3 + 4l_1l_2^3t_1^3t_2^3 + l_2^4t_1^6}\text{e}$

5.2.1.2 Large Deformation (Nonlinear Geometry) Solutions

Tables provided in this section correspond to large deformation conditions where the analytical solution are derived based on nonlinear geometry. The derivation of the equations in this section is documented in Sec. 3.2.4.

(a) With consideration of the joint representation.

The analytical solutions with consideration of the joint representation, which can include the joint size effect, are provided in Table 5.4.

Table 5.4 Formulae for calculating the bending moment due to axial misalignment in butt joints considering joint representation under large deformation condition.

Type	Bending moment $M_{\text{axial}}^{(i)}$	Remarks
$l_1 = l_2 = l$ and $t_1 = t_2 = t$	For $P > 0$, $M_{\text{axial}}^{(1)} = \frac{P\text{e}}{2}\left(\frac{\lambda l \sinh \lambda l - \cosh \lambda l + 1}{\lambda l \cosh \lambda l - \sinh \lambda l}\sinh \lambda l_{\text{t}} - \cosh \lambda l_{\text{t}}\right)$ $M_{\text{axial}}^{(2)} = \frac{P\text{e}}{2}\left(-\frac{\lambda l \sinh \lambda l - \cosh \lambda l + 1}{\lambda l \cosh \lambda l - \sinh \lambda l}\sinh \lambda l_{\text{t}} + \cosh \lambda l_{\text{t}}\right)$ For $P < 0$, $M_{\text{axial}}^{(1)} = \frac{P\text{e}}{2}\left(\frac{-\lambda l \sin \lambda l - \cos \lambda l + 1}{\lambda l \cos \lambda l - \sin \lambda l}\sin \lambda l_{\text{t}} - \cos \lambda l_{\text{t}}\right)$ $M_{\text{axial}}^{(2)} = \frac{P\text{e}}{2}\left(-\frac{-\lambda l \sin \lambda l - \cos \lambda l + 1}{\lambda l \cos \lambda l - \sin \lambda l}\sin \lambda l_{\text{t}} + \cos \lambda l_{\text{t}}\right)$	$\lambda = 2\sqrt{\frac{3\lvert P\rvert}{Et^3}}$
General l and t	For $P > 0$, $M_{\text{axial}}^{(1)} = P\text{e}\left(\phi_{\text{e}}^{(1)} \sinh \lambda_1 l_{\text{t}} + \psi_{\text{e}}^{(1)} \cosh \lambda_1 l_{\text{t}}\right)$ $M_{\text{axial}}^{(2)} = P\text{e}\left(\phi_{\text{e}}^{(2)} \sinh \lambda_2 l_{\text{t}} + \psi_{\text{e}}^{(2)} \cosh \lambda_2 l_{\text{t}}\right)$ For $P < 0$, $M_{\text{axial}}^{(1)} = P\text{e}\left(\gamma_{\text{e}}^{(1)} \sin \lambda_1 l_{\text{t}} + \chi_{\text{e}}^{(1)} \cos \lambda_1 l_{\text{t}}\right)$ $M_{\text{axial}}^{(2)} = P\text{e}\left(\gamma_{\text{e}}^{(2)} \sin \lambda_2 l_{\text{t}} + \chi_{\text{e}}^{(2)} \cos \lambda_2 l_{\text{t}}\right)$	$\lambda_1 = 2\sqrt{\frac{3\lvert P\rvert}{Et_1^3}}$ $\lambda_2 = 2\sqrt{\frac{3\lvert P\rvert}{Et_2^3}}$ Refer to Appendix C.2 for $\phi_{\text{e}}^{(1)}, \psi_{\text{e}}^{(1)}, \phi_{\text{e}}^{(2)}, \psi_{\text{e}}^{(2)}$ $\gamma_{\text{e}}^{(1)}, \chi_{\text{e}}^{(1)}, \gamma_{\text{e}}^{(2)}, \chi_{\text{e}}^{(2)}$

(b) Without consideration of the joint representation.

The analytical solutions for the axial misalignment mode without consideration of the joint representation are the same as those provided in Table 5.3 and does not exhibit a nonlinear geometry effect.

5.2.2 Global Angular Distortion Mode (Angular Misalignment)

This section provides several tables of formulae for calculating the bending moment caused by the global angular distortion (also referred to as angular misalignment), $M_{\text{global}}^{(i)}$, derived from the analytical solutions developed in Sec. 3.2. Fig. 5.3a shows the analytical model of the global angular distortion. The global angular distortion α_{G} is defined as the angle formed between the centerlines of Member 1 and Member 2, i.e., $\alpha_{\text{G}} = \theta_{2\text{G}} - \theta_{1\text{G}}$, where $\theta_{1\text{G}}$ and $\theta_{2\text{G}}$ are the slope of each member with respect to a horizontal baseline. The sign convention of $\theta_{1\text{G}}$ and $\theta_{2\text{G}}$ are given in Fig. 5.3b.

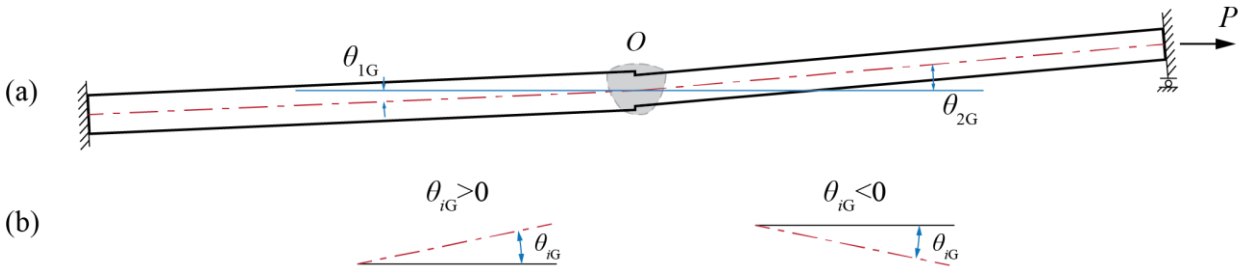

Fig. 5.3 Illustration of global angular distortion: (a) analytical model; (b) sign convention.

5.2.2.1 Small Deformation (Linear Geometry) Solutions

Tables provided in this section correspond to small deformation conditions where the analytical solutions are derived based on linear geometry. The derivation of the formulae in this section is documented in Sec. 3.2.3.

(a) With consideration of the joint representation.

The analytical solutions with consideration of the joint representation, which can include the joint size effect, are provided in Table 5.5.

Table 5.5 Formulae for calculating the bending moment due to global angular distortion in butt joints considering joint representation under small deformation conditions.

Type	Bending moment $M_{\text{global}}^{(i)}$
$l_{1\text{b}} = l_{2\text{b}} = l_{\text{b}}$ and $t_1 = t_2 = t$	$M_{\text{global}}^{(1)} = M_{\text{global}}^{(2)} = -\dfrac{Pl_{\text{b}}}{4}\alpha_{\text{G}}$
$l_{1\text{b}} = l_{2\text{b}} = l_{\text{b}}$	$M_{\text{global}}^{(1)} = -\dfrac{Pt_1^3 l_{\text{b}}\left(7l_{\text{t}}t_2^3 + 4l_{\text{b}}t_2^3 - l_{\text{t}}t_1^3\right)}{l_{\text{b}}t_2^6 + 14l_{\text{b}}t_1^3t_2^3 + 24l_{\text{t}}t_1^3t_2^3 + l_{\text{b}}t_1^6}\alpha_{\text{G}}$ $M_{\text{global}}^{(2)} = -\dfrac{Pt_2^3 l_{\text{b}}\left(7l_{\text{t}}t_1^3 + 4l_{\text{b}}t_1^3 - l_{\text{t}}t_2^3\right)}{l_{\text{b}}t_2^6 + 14l_{\text{b}}t_1^3t_2^3 + 24l_{\text{t}}t_1^3t_2^3 + l_{\text{b}}t_1^6}\alpha_{\text{G}}$
$t_{1\text{b}} = t_{2\text{b}} = t_{\text{b}}$	$M_{\text{global}}^{(1)} = -\dfrac{Pl_{2\text{b}}\left(4l_{1\text{b}}^3 l_{\text{t}} + 2l_{1\text{b}}^3 l_{2\text{b}} + 3l_{1\text{b}}^2 l_{\text{t}} l_{2\text{b}} + 2l_{1\text{b}}^2 l_{2\text{b}}^2 - l_{\text{t}} l_{2\text{b}}^3\right)}{l_{1\text{b}}^4 + 4l_{1\text{b}}^3 l_{2\text{b}} + 12l_{1\text{b}}^2 l_{\text{t}} l_{2\text{b}} + 6l_{1\text{b}}^2 l_{2\text{b}}^2 + 12l_{1\text{b}} l_{\text{t}} l_{2\text{b}}^2 + 4l_{1\text{b}} l_{2\text{b}}^3 + l_{2\text{b}}^4}\alpha_{\text{G}}$ $M_{\text{global}}^{(2)} = -\dfrac{Pl_{1\text{b}}\left(4l_{2\text{b}}^3 l_{\text{t}} + 2l_{2\text{b}}^3 l_{1\text{b}} + 3l_{2\text{b}}^2 l_{\text{t}} l_{1\text{b}} + 2l_{2\text{b}}^2 l_{1\text{b}}^2 - l_{\text{t}} l_{1\text{b}}^3\right)}{l_{1\text{b}}^4 + 4l_{1\text{b}}^3 l_{2\text{b}} + 12l_{1\text{b}}^2 l_{\text{t}} l_{2\text{b}} + 6l_{1\text{b}}^2 l_{2\text{b}}^2 + 12l_{1\text{b}} l_{\text{t}} l_{2\text{b}}^2 + 4l_{1\text{b}} l_{2\text{b}}^3 + l_{2\text{b}}^4}\alpha_{\text{G}}$
General l and t	$M_{\text{global}}^{(1)} = -\dfrac{Pt_1^3 l_{2\text{b}}\left(4l_{1\text{b}}^3 l_{\text{t}} t_2^3 + 2l_{1\text{b}}^3 l_{2\text{b}} t_2^3 + 3l_{1\text{b}}^2 l_{\text{t}} l_{2\text{b}} t_2^3 + 2l_{1\text{b}}^2 l_{2\text{b}}^2 t_2^3 - l_{\text{t}} l_{2\text{b}}^3 t_1^3\right)}{l_{1\text{b}}^4 t_2^6 + 4l_{1\text{b}}^3 l_{2\text{b}} t_1^3 t_2^3 + 12l_{1\text{b}}^2 l_{\text{t}} l_{2\text{b}} t_1^3 t_2^3 + 6l_{1\text{b}}^2 l_{2\text{b}}^2 t_1^3 t_2^3 + 12l_{1\text{b}} l_{\text{t}} l_{2\text{b}}^2 t_1^3 t_2^3 + 4l_{1\text{b}} l_{2\text{b}}^3 t_1^3 t_2^3 + l_{2\text{b}}^4 t_1^6}\alpha_{\text{G}}$ $M_{\text{global}}^{(2)} = -\dfrac{Pt_2^3 l_{1\text{b}}\left(4l_{2\text{b}}^3 l_{\text{t}} t_1^3 + 2l_{2\text{b}}^3 l_{1\text{b}} t_1^3 + 3l_{2\text{b}}^2 l_{\text{t}} l_{1\text{b}} t_1^3 + 2l_{2\text{b}}^2 l_{1\text{b}}^2 t_1^3 - l_{\text{t}} l_{1\text{b}}^3 t_2^3\right)}{l_{1\text{b}}^4 t_2^6 + 4l_{1\text{b}}^3 l_{2\text{b}} t_1^3 t_2^3 + 12l_{1\text{b}}^2 l_{\text{t}} l_{2\text{b}} t_1^3 t_2^3 + 6l_{1\text{b}}^2 l_{2\text{b}}^2 t_1^3 t_2^3 + 12l_{1\text{b}} l_{\text{t}} l_{2\text{b}}^2 t_1^3 t_2^3 + 4l_{1\text{b}} l_{2\text{b}}^3 t_1^3 t_2^3 + l_{2\text{b}}^4 t_1^6}\alpha_{\text{G}}$

(b) Without consideration of the joint representation.

The analytical solution without consideration of the joint representation is provided in Table 5.6.

Table 5.6 Formulae for calculating the bending moment due to global angular distortion in butt joints without considering joint representation under small deformation conditions.

Type	Bending moment $M_{\text{global}}^{(i)}$
$l_1 = l_2 = l$ and $t_1 = t_2 = t$	$M_{\text{global}}^{(1)} = M_{\text{global}}^{(2)} = -\frac{Pl}{4}\alpha_{\text{G}}$
$l_1 = l_2 = l$	$M_{\text{global}}^{(1)} = M_{\text{global}}^{(2)} = -\frac{4Plt_1^3t_2^3}{t_2^6 + 14t_1^3t_2^3 + t_1^6}\alpha_{\text{G}}$
$t_1 = t_2 = t$	$M_{\text{global}}^{(1)} = M_{\text{global}}^{(2)} = -\frac{2P(l_1 + l_2)l_1^2l_2^2}{l_1^4 + 4l_1^3l_2 + 6l_1^2l_2^2 + 4l_1l_2^3 + l_2^4}\alpha_{\text{G}}$
General l and t	$M_{\text{global}}^{(1)} = M_{\text{global}}^{(2)} = -\frac{2P(l_1 + l_2)l_1^2l_2^2t_1^3t_2^3}{l_1^4t_2^6 + 4l_1^3l_2t_1^3t_2^3 + 6l_1^2l_2^2t_1^3t_2^3 + 4l_1l_2^3t_1^3t_2^3 + l_2^4t_1^6}\alpha_{\text{G}}$

5.2.2.2 Large Deformation (Nonlinear Geometry) Solutions

Tables provided in this section correspond to large deformation conditions where the analytical solution are derived based on nonlinear geometry. The derivation of the equations in this section is documented in Sec. 3.2.4.

(a) With consideration of the joint representation.

The analytical solutions with consideration of the joint representation, are provided in Table 5.7.

Table 5.7 Formulae for calculating the bending moment due to global angular distortion in butt joints considering joint representation under large deformation conditions.

Type	Bending moment $M_{\text{global}}^{(i)}$	Remarks
$l_1 = l_2 = l$ and $t_1 = t_2 = t$	For $P > 0$, $M_{\text{axial}}^{(1)} = M_{\text{axial}}^{(2)} = \frac{P\alpha_{\text{G}} l}{2}\left(\frac{1}{\lambda l}\sinh\lambda l_{\text{t}} - \frac{\cosh\lambda l - 1}{\lambda l \sinh\lambda l}\cosh\lambda l_{\text{t}}\right)$ For $P < 0$, $M_{\text{global}}^{(1)} = M_{\text{global}}^{(2)} = \frac{P\alpha_{\text{G}} l}{2}\left(\frac{1}{\lambda l}\sin\lambda l_{\text{t}} + \frac{\cos\lambda l - 1}{\lambda l \sin\lambda l}\cos\lambda l_{\text{t}}\right)$	$\lambda = 2\sqrt{\frac{3\lvert P\rvert}{Et^3}}$
General l and t	For $P > 0$, $M_{\text{global}}^{(1)} = P\alpha_{\text{G}}\left(\phi_{\alpha_{\text{G}}}^{(1)}\sinh\lambda_1 l_{\text{t}} + \psi_{\alpha_{\text{G}}}^{(1)}\cosh\lambda_1 l_{\text{t}}\right)$ $M_{\text{global}}^{(2)} = P\alpha_{\text{G}}\left(\phi_{\alpha_{\text{G}}}^{(2)}\sinh\lambda_2 l_{\text{t}} + \psi_{\alpha_{\text{G}}}^{(2)}\cosh\lambda_2 l_{\text{t}}\right)$ For $P < 0$, $M_{\text{global}}^{(1)} = P\alpha_{\text{G}}\left(\gamma_{\alpha_{\text{G}}}^{(1)}\sin\lambda_1 l_{\text{t}} + \chi_{\alpha_{\text{G}}}^{(1)}\cos\lambda_1 l_{\text{t}}\right)$ $M_{\text{global}}^{(2)} = P\alpha_{\text{G}}\left(\gamma_{\alpha_{\text{G}}}^{(2)}\sin\lambda_2 l_{\text{t}} + \chi_{\alpha_{\text{G}}}^{(2)}\cos\lambda_2 l_{\text{t}}\right)$	$\lambda_1 = 2\sqrt{\frac{3\lvert P\rvert}{Et_1^3}}$ $\lambda_2 = 2\sqrt{\frac{3\lvert P\rvert}{Et_2^3}}$ Refer to Appendix C.3 for $\phi_{\alpha_{\text{G}}}^{(1)}, \psi_{\alpha_{\text{G}}}^{(1)}, \phi_{\alpha_{\text{G}}}^{(2)}, \psi_{\alpha_{\text{G}}}^{(2)}$ $\gamma_{\alpha_{\text{G}}}^{(1)}, \chi_{\alpha_{\text{G}}}^{(1)}, \gamma_{\alpha_{\text{G}}}^{(2)}, \chi_{\alpha_{\text{G}}}^{(2)}$ Also, $\psi_{\alpha_{\text{G}}}^{(1)} = \psi_{\alpha_{\text{G}}}^{(2)}$ $\chi_{\alpha_{\text{G}}}^{(1)} = \chi_{\alpha_{\text{G}}}^{(2)}$

(b) Without consideration of the joint representation.

The analytical solutions without consideration of the joint representation are provided in Table 5.8.

Table 5.8 Formulae for calculating the bending moment due to global angular distortion in butt joints without considering joint representation under large deformation conditions.

Type	Bending moment $M_{\text{global}}^{(i)}$	Remarks
$l_1 = l_2 = l$ and $t_1 = t_2 = t$	For $P > 0$, $M_{\text{global}}^{(1)} = M_{\text{global}}^{(2)} = -\frac{P\alpha_{\text{G}} l}{2}\left(\frac{\cosh \lambda l - 1}{\lambda l \sinh \lambda l}\right)$ For $P < 0$, $M_{\text{global}}^{(1)} = M_{\text{global}}^{(2)} = \frac{P\alpha_{\text{G}} l}{2}\left(\frac{\cos \lambda l - 1}{\lambda l \sin \lambda l}\right)$	$\lambda = 2\sqrt{\frac{3\lvert P\rvert}{Et^3}}$
General l and t	For $P > 0$, $M_{\text{global}}^{(1)} = M_{\text{global}}^{(2)} = P\alpha_{\text{G}}\psi_{\alpha_{\text{G}}}^{(1)}$ For $P < 0$, $M_{\text{global}}^{(1)} = M_{\text{global}}^{(2)} = P\alpha_{\text{G}}\chi_{\alpha_{\text{G}}}^{(1)}$	$\lambda_1 = 2\sqrt{\frac{3\lvert P\rvert}{Et_1^3}}$ $\lambda_2 = 2\sqrt{\frac{3\lvert P\rvert}{Et_2^3}}$ Refer to Appendix C.3 for $\psi_{\alpha_{\text{G}}}^{(1)}, \chi_{\alpha_{\text{G}}}^{(1)}$

5.2.3 Local Angular Distortion Mode

This section provides several tables of formulae for calculating the bending moment caused by the local angular distortion (also referred to as distortion curvature), $M_{1,\text{local}}^{(i)}$, derived from the analytical solutions developed in Sec. 4.3. The local angular distortion is defined as the curvature shape of the distortion without misalignments. It is characterized by the four local angular distortion angles (or the slopes) at the ends of each member, $\theta'_{11}, \theta'_{12}, \theta'_{21}$, and θ'_{22} (see Fig.

5.4a). Fig. 5.4a shows the analytical model of the local angular distortion and the sign convention for the local angular distortion angles θ'_{ij} is given in Fig. 5.4b.

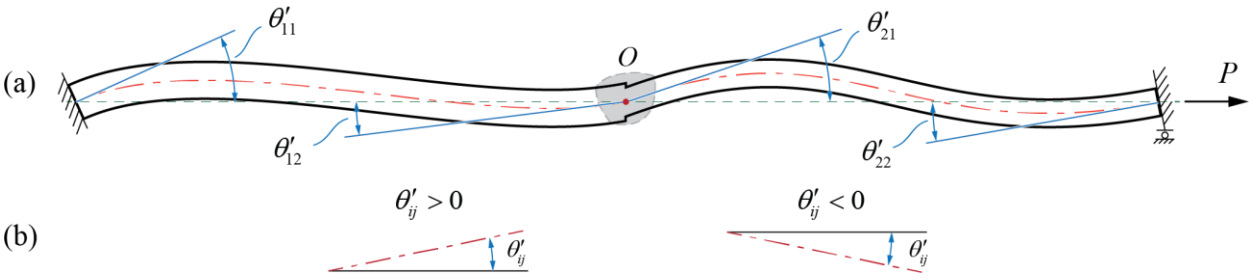

Fig. 5.4 Illustration of local angular distortion: (a) analytical model; (b) sign convention.

5.2.3.1 Small Deformation (Linear Geometry) Solutions

Table 5.9 provided in this section corresponds to small deformation conditions. The derivation of the formulae in this section is documented in Sec. 4.3.3. The solutions for small deformation is only available when the joint representation is not considered.

Table 5.9 Formulae for calculating the bending moment due to local angular distortion in butt joints without considering joint representation under small deformation condition.

Type	Bending moment $M_{1,\text{local}}^{(i)}$
$l_1 = l_2 = l$ and $t_1 = t_2 = t$	$M_{1,\text{local}}^{(1)} = M_{1,\text{local}}^{(2)} = \frac{Pl}{24}\left[\left(\theta'_{22} - \theta'_{11}\right) - \left(\theta'_{21} - \theta'_{12}\right)\right]$
$l_1 = l_2 = l$	$M_{1,\text{local}}^{(1)} = M_{1,\text{local}}^{(2)} = \frac{Pl}{30\left(t_2^6 + 4t_1^3t_2^3 + 6t_1^3t_2^3 + 4t_1^3t_2^3 + t_1^6\right)}\left[-t_2^3\left(t_2^3 + 9t_1^3 + 10t_1^3\right)\theta'_{11} + 2t_2^3\left(2t_2^3 + 3t_1^3 + 5t_1^3\right)\theta'_{12} - 2t_1^3\left(2t_1^3 + 3t_2^3 + 5t_2^3\right)\theta'_{21} + t_1^3\left(t_1^3 + 9t_2^3 + 10t_2^3\right)\theta'_{22}\right]$
$t_1 = t_2 = t$	$M_{1,\text{local}}^{(1)} = M_{1,\text{local}}^{(2)} = \frac{P}{30\left(l_1^4 + 4l_1^3l_2 + 6l_1^2l_2^2 + 4l_1l_2^3 + l_2^4\right)}\left[-l_1^2\left(l_1^3 + 9l_1l_2^2 + 10l_2^3\right)\theta'_{11} + 2l_1^2\left(2l_1^3 + 3l_1l_2^2 + 5l_2^3\right)\theta'_{12} - 2l_2^2\left(2l_2^3 + 3l_2l_1^2 + 5l_1^3\right)\theta'_{21} + l_2^2\left(l_2^3 + 9l_2l_1^2 + 10l_1^3\right)\theta'_{22}\right]$
General l and t	$M_{1,\text{local}}^{(1)} = M_{1,\text{local}}^{(2)} = \frac{P}{30\mathcal{L}}\left[-l_1^2t_2^3\left(l_1^3t_2^3 + 9l_1l_2^2t_1^3 + 10l_2^3t_1^3\right)\theta'_{11} + 2l_1^2t_2^3\left(2l_1^3t_2^3 + 3l_1l_2^2t_1^3 + 5l_2^3t_1^3\right)\theta'_{12} - 2l_2^2t_1^3\left(2l_2^3t_1^3 + 3l_2l_1^2t_2^3 + 5l_1^3t_2^3\right)\theta'_{21} + l_2^2t_1^3\left(l_2^3t_1^3 + 9l_2l_1^2t_2^3 + 10l_1^3t_2^3\right)\theta'_{22}\right]$ Where $\mathcal{L} = l_1^4t_2^6 + 4l_1^3l_2t_1^3t_2^3 + 6l_1^2l_2^2t_1^3t_2^3 + 4l_1l_2^3t_1^3t_2^3 + l_2^4t_1^6$

5.2.3.2 Large Deformation (Nonlinear Geometry) Solutions

Tables provided in this section correspond to large deformation conditions where the analytical solution are derived based on nonlinear geometry. The derivation of the equations in this section is documented in Sec. 4.3.

(a) With consideration of the joint representation.

The analytical solutions with consideration of the joint representation, which can include the joint size effect, are provided in Table 5.7.

Table 5.10 Formulae for calculating the bending moment due to local angular distortion in butt joints considering joint representation under large deformation condition.

Type	Bending moment $M_{1,\text{local}}^{(i)}$	Remarks
$l_1 = l_2 = l$ and $t_1 = t_2 = t$	For $P > 0$, $M_{1,\text{local}}^{(1)} = P\Big[\Big(\phi_{\theta'_{11}}^{(1s)} \sinh \lambda l_t + \psi_{\theta'_{11}}^{(1s)} \cosh \lambda l_t\Big)\theta'_{11}$ $+\Big(\phi_{\theta'_{12}}^{(1s)} \sinh \lambda l_t + \psi_{\theta'_{12}}^{(1s)} \cosh \lambda l_t\Big)\theta'_{12}$ $+\Big(\phi_{\theta'_{21}}^{(1s)} \sinh \lambda l_t + \psi_{\theta'_{21}}^{(1s)} \cosh \lambda l_t\Big)\theta'_{21}$ $+\Big(\phi_{\theta'_{22}}^{(1s)} \sinh \lambda l_t + \psi_{\theta'_{22}}^{(1s)} \cosh \lambda l_t\Big)\theta'_{22}$ $-\Big(\zeta_{\theta'_{11}}^{(1s)} + \kappa_{\theta'_{11}}^{(1s)} l_t\Big)\theta'_{11} - \Big(\zeta_{\theta'_{12}}^{(1s)} + \kappa_{\theta'_{12}}^{(1s)} l_t\Big)\theta'_{12}\Big]$ $M_{1,\text{local}}^{(2)} = P\Big[\Big(\phi_{\theta'_{11}}^{(2s)} \sinh \lambda l_t + \psi_{\theta'_{11}}^{(2)} \cosh \lambda l_t\Big)\theta'_{11}$ $+\Big(\phi_{\theta'_{12}}^{(2s)} \sinh \lambda l_t + \psi_{\theta'_{12}}^{(2s)} \cosh \lambda l_t\Big)\theta'_{12}$ $+\Big(\phi_{\theta'_{21}}^{(2s)} \sinh \lambda l_t + \psi_{\theta'_{21}}^{(2s)} \cosh \lambda l_t\Big)\theta'_{21}$ $+\Big(\phi_{\theta'_{22}}^{(2s)} \sinh \lambda l_t + \psi_{\theta'_{22}}^{(2s)} \cosh \lambda l_t\Big)\theta'_{22}$ $-\Big(\zeta_{\theta'_{21}}^{(2s)} + \kappa_{\theta'_{21}}^{(2s)} l_t\Big)\theta'_{21} - \Big(\zeta_{\theta'_{22}}^{(2s)} + \kappa_{\theta'_{22}}^{(2s)} l_t\Big)\theta'_{22}\Big]$ For $P < 0$, $M_{1,\text{local}}^{(1)} = P\Big[\Big(\gamma_{\theta'_{11}}^{(1s)} \sin \lambda l_t + \chi_{\theta'_{11}}^{(1s)} \cos \lambda l_t\Big)\theta'_{11}$ $+\Big(\gamma_{\theta'_{12}}^{(1s)} \sin \lambda l_{t1} + \chi_{\theta'_{12}}^{(1s)} \cos \lambda l_t\Big)\theta'_{12}$ $+\Big(\gamma_{\theta'_{21}}^{(1s)} \sin \lambda l_t + \chi_{\theta'_{21}}^{(1s)} \cos \lambda l_t\Big)\theta'_{21}$ $+\Big(\gamma_{\theta'_{22}}^{(1s)} \sin \lambda l_t + \chi_{\theta'_{22}}^{(1s)} \cos \lambda l_t\Big)\theta'_{22}$ $-\Big(\upsilon_{\theta'_{11}}^{(1s)} + \mu_{\theta'_{11}}^{(1s)} l_t\Big)\theta'_{11} - \Big(\upsilon_{\theta'_{12}}^{(1s)} + \mu_{\theta'_{12}}^{(1s)} l_t\Big)\theta'_{12}\Big]$ $M_{1,\text{local}}^{(2)} = P\Big[\Big(\gamma_{\theta'_{11}}^{(2s)} \sin \lambda l_t + \chi_{\theta'_{11}}^{(2s)} \cos \lambda l_t\Big)\theta'_{11}$ $+\Big(\gamma_{\theta'_{12}}^{(2s)} \sin \lambda l_t + \chi_{\theta'_{12}}^{(2s)} \cos \lambda l_t\Big)\theta'_{12}$ $+\Big(\gamma_{\theta'_{21}}^{(2s)} \sin \lambda l_t + \chi_{\theta'_{21}}^{(2s)} \cos \lambda l_t\Big)\theta'_{21}$ $+\Big(\gamma_{\theta'_{22}}^{(2s)} \sin \lambda l_t + \chi_{\theta'_{22}}^{(2s)} \cos \lambda l_t\Big)\theta'_{22}$ $-\Big(\upsilon_{\theta'_{21}}^{(2s)} + \mu_{\theta'_{21}}^{(2s)} l_t\Big)\theta'_{21} - \Big(\upsilon_{\theta'_{22}}^{(2s)} + \mu_{\theta'_{22}}^{(2s)} l_t\Big)\theta'_{22}\Big]$	$\lambda = 2\sqrt{\frac{3\lvert P\rvert}{Et^3}}$ Refer to Appendix C.4.3 for $\phi_{\theta'_{11}}^{(1s)}, \psi_{\theta'_{11}}^{(1s)}, \phi_{\theta'_{12}}^{(1s)}, \psi_{\theta'_{12}}^{(1s)},$ $\phi_{\theta'_{21}}^{(1s)}, \psi_{\theta'_{21}}^{(1s)}, \phi_{\theta'_{22}}^{(1s)}, \psi_{\theta'_{22}}^{(1s)},$ $\phi_{\theta'_{11}}^{(2s)}, \psi_{\theta'_{11}}^{(2s)}, \phi_{\theta'_{12}}^{(2s)}, \psi_{\theta'_{12}}^{(2s)},$ $\phi_{\theta'_{21}}^{(2s)}, \psi_{\theta'_{21}}^{(2s)}, \phi_{\theta'_{22}}^{(2s)}, \psi_{\theta'_{22}}^{(2s)},$ $\zeta_{\theta'_{11}}^{(1s)}, \kappa_{\theta'_{11}}^{(1s)}, \zeta_{\theta'_{12}}^{(1s)}, \kappa_{\theta'_{12}}^{(1s)},$ $\zeta_{\theta'_{21}}^{(2s)}, \kappa_{\theta'_{21}}^{(2s)}, \zeta_{\theta'_{22}}^{(2s)}, \kappa_{\theta'_{22}}^{(2s)}$ Refer to Appendix C.4.4 for $\gamma_{\theta'_{11}}^{(1s)}, \chi_{\theta'_{11}}^{(1s)}, \gamma_{\theta'_{12}}^{(1s)}, \chi_{\theta'_{12}}^{(1s)},$ $\gamma_{\theta'_{21}}^{(1s)}, \chi_{\theta'_{21}}^{(1s)}, \gamma_{\theta'_{22}}^{(1s)}, \chi_{\theta'_{22}}^{(1s)},$ $\gamma_{\theta'_{11}}^{(2s)}, \chi_{\theta'_{11}}^{(2s)}, \gamma_{\theta'_{12}}^{(2s)}, \chi_{\theta'_{12}}^{(2s)},$ $\gamma_{\theta'_{21}}^{(2s)}, \chi_{\theta'_{21}}^{(2s)}, \gamma_{\theta'_{22}}^{(2s)}, \chi_{\theta'_{22}}^{(2s)},$ $\upsilon_{\theta'_{11}}^{(1s)}, \mu_{\theta'_{11}}^{(1s)}, \upsilon_{\theta'_{12}}^{(1s)}, \mu_{\theta'_{12}}^{(1s)},$ $\upsilon_{\theta'_{21}}^{(2s)}, \kappa_{\theta'_{21}}^{(2s)}, \upsilon_{\theta'_{22}}^{(2s)}, \mu_{\theta'_{22}}^{(2s)}$

General l and t	For $P > 0$, $M_{1,\text{local}}^{(1)} = P\Big[\Big(\phi_{\theta'_{11}}^{(1)} \sinh\lambda_1 l_t + \psi_{\theta'_{11}}^{(1)} \cosh\lambda_1 l_t\Big)\theta'_{11}$ $+\Big(\phi_{\theta'_{12}}^{(1)} \sinh\lambda_1 l_t + \psi_{\theta'_{12}}^{(1)} \cosh\lambda_1 l_t\Big)\theta'_{12}$ $+\Big(\phi_{\theta'_{21}}^{(1)} \sinh\lambda_1 l_t + \psi_{\theta'_{21}}^{(1)} \cosh\lambda_1 l_t\Big)\theta'_{21}$ $+\Big(\phi_{\theta'_{22}}^{(1)} \sinh\lambda_1 l_t + \psi_{\theta'_{22}}^{(1)} \cosh\lambda_1 l_t\Big)\theta'_{22}$ $-\Big(\zeta_{\theta'_{11}}^{(1)} + \kappa_{\theta'_{11}}^{(1)} l_t\Big)\theta'_{11} - \Big(\zeta_{\theta'_{12}}^{(1)} + \kappa_{\theta'_{12}}^{(1)} l_t\Big)\theta'_{12}\Big]$ $M_{1,\text{local}}^{(2)} = P\Big[\Big(\phi_{\theta'_{11}}^{(2)} \sinh\lambda_2 l_t + \psi_{\theta'_{11}}^{(2)} \cosh\lambda_2 l_t\Big)\theta'_{11}$ $+\Big(\phi_{\theta'_{12}}^{(2)} \sinh\lambda_2 l_t + \psi_{\theta'_{12}}^{(2)} \cosh\lambda_2 l_t\Big)\theta'_{12}$ $+\Big(\phi_{\theta'_{21}}^{(2)} \sinh\lambda_2 l_t + \psi_{\theta'_{21}}^{(2)} \cosh\lambda_2 l_t\Big)\theta'_{21}$ $+\Big(\phi_{\theta'_{22}}^{(2)} \sinh\lambda_2 l_t + \psi_{\theta'_{22}}^{(2)} \cosh\lambda_2 l_t\Big)\theta'_{22}$ $-\Big(\zeta_{\theta'_{21}}^{(2)} + \kappa_{\theta'_{21}}^{(2)} l_t\Big)\theta'_{21} - \Big(\zeta_{\theta'_{22}}^{(2)} + \kappa_{\theta'_{22}}^{(2)} l_t\Big)\theta'_{22}\Big]$ For $P < 0$, $M_{1,\text{local}}^{(1)} = P\Big[\Big(\gamma_{\theta'_{11}}^{(1)} \sin\lambda_1 l_t + \chi_{\theta'_{11}}^{(1)} \cos\lambda_1 l_t\Big)\theta'_{11}$ $+\Big(\gamma_{\theta'_{12}}^{(1)} \sin\lambda_1 l_t + \chi_{\theta'_{12}}^{(1)} \cos\lambda_1 l_t\Big)\theta'_{12}$ $+\Big(\gamma_{\theta'_{21}}^{(1)} \sin\lambda_1 l_t + \chi_{\theta'_{21}}^{(1)} \cos\lambda_1 l_t\Big)\theta'_{21}$ $+\Big(\gamma_{\theta'_{22}}^{(1)} \sin\lambda_1 l_t + \chi_{\theta'_{22}}^{(1)} \cos\lambda_1 l_t\Big)\theta'_{22}$ $-\Big(\upsilon_{\theta'_{11}}^{(1)} + \mu_{\theta'_{11}}^{(1)} l_t\Big)\theta'_{11} - \Big(\upsilon_{\theta'_{12}}^{(1)} + \mu_{\theta'_{12}}^{(1)} l_t\Big)\theta'_{12}\Big]$ $M_{1,\text{local}}^{(2)} = P\Big[\Big(\gamma_{\theta'_{11}}^{(2)} \sin\lambda_2 l_t + \chi_{\theta'_{11}}^{(2)} \cos\lambda_2 l_t\Big)\theta'_{11}$ $+\Big(\gamma_{\theta'_{12}}^{(2)} \sin\lambda_2 l_t + \chi_{\theta'_{12}}^{(2)} \cos\lambda_2 l_t\Big)\theta'_{12}$ $+\Big(\gamma_{\theta'_{21}}^{(2)} \sin\lambda_2 l_t + \chi_{\theta'_{21}}^{(2)} \cos\lambda_2 l_t\Big)\theta'_{21}$ $+\Big(\gamma_{\theta'_{22}}^{(2)} \sin\lambda_2 l_t + \chi_{\theta'_{22}}^{(2)} \cos\lambda_2 l_t\Big)\theta'_{22}$ $-\Big(\upsilon_{\theta'_{21}}^{(2)} + \mu_{\theta'_{21}}^{(2)} l_t\Big)\theta'_{21} - \Big(\upsilon_{\theta'_{22}}^{(2)} + \mu_{\theta'_{22}}^{(2)} l_t\Big)\theta'_{22}\Big]$	$\lambda_1 = 2\sqrt{\frac{3\lvert P\rvert}{Et_1^3}}$ $\lambda_2 = 2\sqrt{\frac{3\lvert P\rvert}{Et_2^3}}$ Refer to Appendix C.4.1 for $\phi_{\theta'_{11}}^{(1)}, \psi_{\theta'_{11}}^{(1)}, \phi_{\theta'_{12}}^{(1)}, \psi_{\theta'_{12}}^{(1)},$ $\phi_{\theta'_{21}}^{(1)}, \psi_{\theta'_{21}}^{(1)}, \phi_{\theta'_{22}}^{(1)}, \psi_{\theta'_{22}}^{(1)},$ $\phi_{\theta'_{11}}^{(2)}, \psi_{\theta'_{11}}^{(2)}, \phi_{\theta'_{12}}^{(2)}, \psi_{\theta'_{12}}^{(2)},$ $\phi_{\theta'_{21}}^{(2)}, \psi_{\theta'_{21}}^{(2)}, \phi_{\theta'_{22}}^{(2)}, \psi_{\theta'_{22}}^{(2)},$ $\zeta_{\theta'_{11}}^{(1)}, \kappa_{\theta'_{11}}^{(1)}, \zeta_{\theta'_{12}}^{(1)}, \kappa_{\theta'_{12}}^{(1)},$ $\zeta_{\theta'_{21}}^{(2)}, \kappa_{\theta'_{21}}^{(2)}, \zeta_{\theta'_{22}}^{(2)}, \kappa_{\theta'_{22}}^{(2)}.$ Refer to Appendix C.4.2 for $\gamma_{\theta'_{11}}^{(1)}, \chi_{\theta'_{11}}^{(1)}, \gamma_{\theta'_{12}}^{(1)}, \chi_{\theta'_{12}}^{(1)},$ $\gamma_{\theta'_{21}}^{(1)}, \chi_{\theta'_{21}}^{(1)}, \gamma_{\theta'_{22}}^{(1)}, \chi_{\theta'_{22}}^{(1)},$ $\gamma_{\theta'_{11}}^{(2)}, \chi_{\theta'_{11}}^{(2)}, \gamma_{\theta'_{12}}^{(2)}, \chi_{\theta'_{12}}^{(2)},$ $\gamma_{\theta'_{21}}^{(2)}, \chi_{\theta'_{21}}^{(2)}, \gamma_{\theta'_{22}}^{(2)}, \chi_{\theta'_{22}}^{(2)},$ $\upsilon_{\theta'_{11}}^{(1)}, \mu_{\theta'_{11}}^{(1)}, \upsilon_{\theta'_{12}}^{(1)}, \mu_{\theta'_{12}}^{(1)},$ $\upsilon_{\theta'_{21}}^{(2)}, \kappa_{\theta'_{21}}^{(2)}, \upsilon_{\theta'_{22}}^{(2)}, \mu_{\theta'_{22}}^{(2)}.$

(b) Without consideration of the joint representation.

The analytical solutions without consideration of the joint representation are provided in Table 5.11.

Table 5.11 Formulae for calculating the bending moment due to local angular distortion in butt joints without considering joint representation under large deformation conditions.

Type	Bending moment $M_{1,\mathrm{local}}^{(i)}$	Remarks
$l_1 = l_2 = l$ and $t_1 = t_2 = t$	For $P > 0$, $M_{1.\mathrm{local}}^{(1)} = M_{1.\mathrm{local}}^{(2)}$ $= -Pl\left[\left(\frac{\lambda^2 l^2 \cosh \lambda l - 4\lambda l \sinh \lambda l + 6\cosh \lambda l - 6}{2\lambda^3 l^3 \sinh \lambda l}\right)\left(\theta'_{21} - \theta'_{12}\right) + \left(\frac{-\lambda^2 l^2 - 2\lambda l \sinh \lambda l + 6\cosh \lambda l - 6}{2\lambda^3 l^3 \sinh \lambda l}\right)\left(\theta'_{22} - \theta'_{11}\right)\right]$ For $P < 0$, $M_{1.\mathrm{local}}^{(1)} = M_{1.\mathrm{local}}^{(2)}$ $= -Pl\left[\left(\frac{-\lambda^2 l^2 \cos \lambda l + 4\lambda l \sin \lambda l + 6\cos \lambda l - 6}{2\lambda^3 l^3 \sin \lambda l}\right)\left(\theta'_{21} - \theta'_{12}\right) + \left(\frac{\lambda^2 l^2 + 2\lambda l \sin \lambda l + 6\cos \lambda l - 6}{2\lambda^3 l^3 \sin \lambda l}\right)\left(\theta'_{22} - \theta'_{11}\right)\right]$	$\lambda = 2\sqrt{\frac{3\lvert P\rvert}{Et^3}}$
General l and t	For $P > 0$, $M_{1,\mathrm{local}}^{(1)} = M_{1,\mathrm{local}}^{(2)} = P\left[\left(\psi_{\theta'_{11}}^{(1)} - \zeta_{\theta'_{11}}^{(1)}\right)\theta'_{11} + \left(\psi_{\theta'_{12}}^{(1)} - \zeta_{\theta'_{12}}^{(1)}\right)\theta'_{12} + \psi_{\theta'_{21}}^{(1)}\theta'_{21} + \psi_{\theta'_{22}}^{(1)}\theta'_{22}\right]$ For $P < 0$, $M_{1,\mathrm{local}}^{(1)} = M_{1,\mathrm{local}}^{(2)} = P\left[\left(\chi_{\theta'_{11}}^{(1)} - \upsilon_{\theta'_{11}}^{(1)}\right)\theta'_{11} + \left(\chi_{\theta'_{12}}^{(1)} - \upsilon_{\theta'_{12}}^{(1)}\right)\theta'_{12} + \chi_{\theta'_{21}}^{(1)}\theta'_{21} + \chi_{\theta'_{22}}^{(1)}\theta'_{22}\right]$	$\lambda_1 = 2\sqrt{\frac{3\lvert P\rvert}{Et_1^3}}$ $\lambda_2 = 2\sqrt{\frac{3\lvert P\rvert}{Et_2^3}}$ Refer to Appendix C.4.1 for $\psi_{\theta'_{11}}^{(1)}, \psi_{\theta'_{12}}^{(1)}, \psi_{\theta'_{21}}^{(1)}, \psi_{\theta'_{22}}^{(1)}, \zeta_{\theta'_{11}}^{(1)}, \zeta_{\theta'_{12}}^{(1)}$. Refer to Appendix C.4.2 for $\chi_{\theta'_{11}}^{(1)}, \chi_{\theta'_{12}}^{(1)}, \chi_{\theta'_{21}}^{(1)}, \chi_{\theta'_{22}}^{(1)}, \upsilon_{\theta'_{11}}^{(1)}, \upsilon_{\theta'_{12}}^{(1)}$

5.3 Decomposition and Assembly for Stiffened Panels

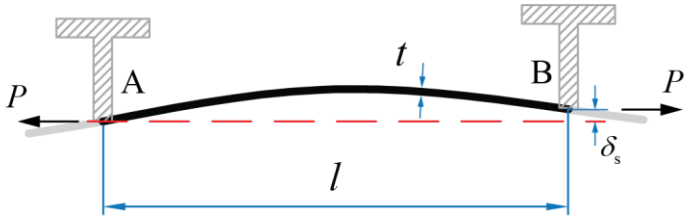

Fig. 5.5 A typical distortion profile in a stiffened panel.

Fig. 5.5 illustrates a typical distortion shape in a stiffened panel between two stiffeners, which contains displaced stiffeners and distortion curvatures. The stiffener spacing is l, and the structure is under an axial loading P as shown in Fig. 5.5. Positions A and B are the weld toe locations of interest on the top surface. Following the decomposition procedure, such distortion is divided into two basic distortion modes: global and local angular distortion. In this research, the stiffeners are assumed to be fixed; therefore, the global angular distortion does not cause any secondary bending, i.e., $M^i_{\text{global}} = 0$ which leads to

$$M^i_{\text{distortion}} = M^i_{1,\text{local}} \quad i \in \{\text{A,B}\} \tag{5.5}$$

Since the thickness is uniform in the model, we can clearly define the stress concentration factor at Positions A and B based on the nominal stress $\sigma_{\text{n}} = P/t$ as

$$k^i_{\text{b}} = -\frac{6M^i_{\text{distortion}}}{Pt} \tag{5.6}$$

Two types of local angular distortion profiles between stiffeners are studied in Sec. 2.3.1, including the buckling distortion mode in Fig. 5.6 and the cosine angular distortion mode in Fig. 5.7. Both distortion modes are characterized by the maximum initial deflection, δ_0. The secondary bending induced stress concentration factor, k_{b}, of these two distortion modes can be calculated using the equations in Table 5.12 and Table 5.13. Based on the symmetrical distortion profile and

boundary conditions, $k_{\mathrm{b}}^{\mathrm{A}} = k_{\mathrm{b}}^{\mathrm{B}} = k_{\mathrm{b}}$. With k_{b} calculated using the formulae in Table 5.12 and Table 5.13, the secondary bending induced stress is eventually obtained by

$$\sigma_{\mathrm{b}} = k_{\mathrm{b}}\sigma_{\mathrm{n}} \tag{5.7}$$

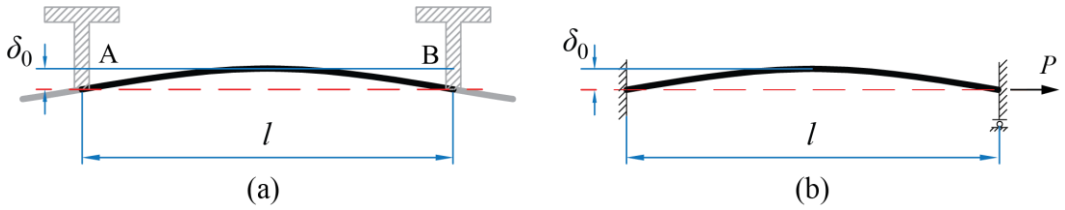

Fig. 5.6 Buckling distortion in stiffened panels: (a) Illustration; (b) analytical model.

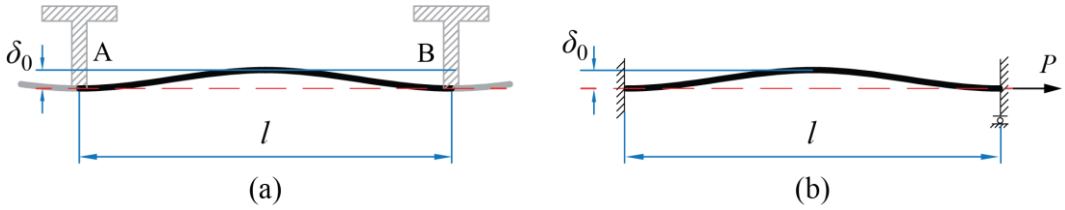

Fig. 5.7 Cosine angular distortion in stiffened panels: (a) Illustration; (b) analytical model.

5.3.1 Small Deformation (Linear Geometry) Solutions

In Table 5.12, k_{b} provided are based on deformation condition, which is obtained by taking the limit of k_{b} in Sec. 2.3.1 as $P \to 0$.

Table 5.12 Formulae for calculating k_{b} due to local angular distortion in stiffened panels under large deformation conditions.

Type	Stress concentration factor k_{b}
Buckling distortion	$k_{\mathrm{b}} = \frac{15}{4}\frac{\delta_0}{t}$
Cosine angular distortion	$k_{\mathrm{b}} = 3\frac{\delta_0}{t}$

5.3.2 Large Deformation (Nonlinear Geometry) Solutions

Tables provided in this section correspond to large deformation conditions where the analytical solution are derived based on nonlinear geometry. The derivation of the equations in this section is documented in Sec. 2.3.1.

Table 5.13 Formulae for calculating k_b due to local angular distortion in stiffened panels under large deformation conditions.

Type	Stress concentration factor k_b	Remarks
Buckling distortion	For $P > 0$, $k_b = 18\frac{\delta_0}{t}\left[\frac{\cosh\frac{\lambda l}{2}}{\lambda l \sinh\frac{\lambda l}{2}} - \frac{8}{(\lambda l)^2}\left(\frac{\cosh\frac{\lambda l}{2}-1}{\lambda l \sinh\frac{\lambda l}{2}}\right)\right]$ For $P < 0$, $k_b = -18\frac{\delta_0}{t}\left[\frac{\cos\frac{\lambda l}{2}}{\lambda l \sin\frac{\lambda l}{2}} + \frac{8}{(\lambda l)^2}\left(\frac{\cos\frac{\lambda l}{2}-1}{\lambda l \sin\frac{\lambda l}{2}}\right)\right]$	$\lambda = 2\sqrt{\frac{3\lvert P\rvert}{Et^3}}$
Cosine angular distortion	For $P > 0$, $k_b = -\frac{144}{(\lambda l)^2}\frac{\delta_0}{t}\left(\frac{4}{\lambda l}\frac{\cosh\frac{\lambda l}{2}-1}{\sinh\frac{\lambda l}{2}} - 1\right)$ For $P < 0$, $k_b = -\frac{144}{(\lambda l)^2}\frac{\delta_0}{t}\left(\frac{4}{\lambda l}\frac{\cos\frac{\lambda l}{2}-1}{\sin\frac{\lambda l}{2}} + 1\right)$	$\lambda = 2\sqrt{\frac{3\lvert P\rvert}{Et^3}}$

5.4 Distortion Data Analysis Procedures

Based on Sec. 4.4, step by step distortion decomposition and assembly procedures for calculating distortions' effect on welded joints in terms of distortion-induced bending stresses at

weld positions are summarized in this section. Fig. 5.9 and Fig. 5.11 show the flow chart of the procedure, and essential remarks and references with respect to each step are given.

5.4.1 Distortion Effects on Butt Joints

Suppose a set of n measurement data points, $\{(x_i, y_i)|i \in \{1, \dots, n\}\}$, of a distortion profile is available along the red line in (dots in Fig. 5.8) for a butt joint in the panel, and the panel is subject to a remote axial load P in the direction shown in Fig. 5.8. Note that, based on the characteristic length scale discussed in Sec. 2.3.1 and Sec.2.4.2, for each side of the butt joint, we only need to consider the distortion within one stiffener spacing (l) range from the butt weld if that side spans more than l. Before treatment of the distortion data, structure dimensions l_1, l_2, t_1, t_2, etc., and Position O (see Fig. 5.1) needs to be determined first.

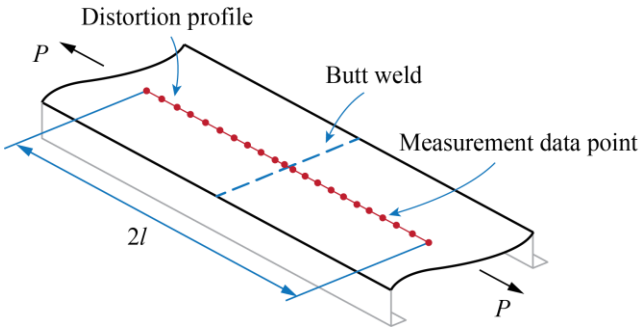

Fig. 5.8 Illustration of a distortion profile and measurements with respect to a butt weld in a panel structure.

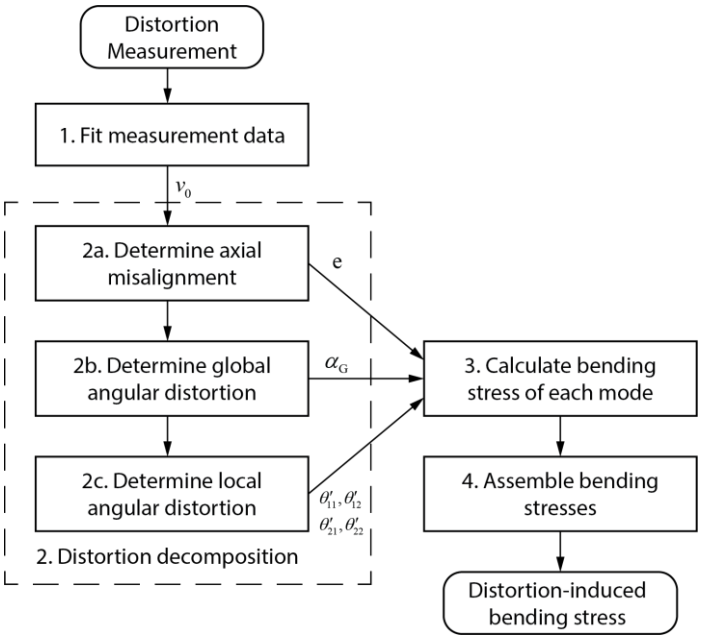

Fig. 5.9 Flow chart of the procedure to calculate distortion-induced bending stress in a butt joint.

1. Fit measurement data

   Perform a 3rd order polynomial fitting for each member.

2. Distortion decomposition

   2a. Determine axial misalignment e

   Refer to Eqn. (4.20) and determine the axial misalignment e. Refer to Eqn. (4.21) for the axial misalignment mode shape $v_{0,\text{axial}}$. Then, remove $v_{0,\text{axial}}$ from v_0, so the remaining distortion is $v_0 - v_{0,\text{axial}}$.

   2b. Determine global angular distortion α_G

   Refer to Eqn. (4.22) to determine the global angular distortion α_G and Eqn. (4.24) for the global angular distortion shape $v_{0,\text{global}}$. Then, remove $v_{0,\text{axial}}$ from v_0, so the remaining distortion is $v_0 - v_{0,\text{axial}} - v_{0,\text{global}}$.

   2c. Determine local angular distortion parameters

The local angular distortion shape is $v_{0,\text{local}} = v_0 - v_{0,\text{axial}} - v_{0,\text{global}}$. The four local angular distortion parameters $(\theta'_{11}, \theta'_{12}, \theta'_{21}, \theta'_{22})$ in Fig. 5.4a are obtained via Eqn. (4.26).

3. Calculate bending moment caused by each distortion mode

   Use Table 5.1 to select the proper table of formulae to calculate $M^{(i)}_{\text{axial}}, M^{(i)}_{\text{global}}, M^{(i)}_{1,\text{local}}$ at the butt joint location.

4. Assemble bending stress of each distortion mode

   Add up the bending moments in Step 3: $M^{(i)}_{\text{distortion}} = M^{(i)}_{\text{axial}} + M^{(i)}_{\text{global}} + M^{(i)}_{1,\text{local}}$. The bending stress is obtained via Eqns. (5.2) or (5.3).

5.4.2 Distortion Effects on Stiffened Panels

Suppose a set of n measurement data, $\{(x_i, y_i) | i \in \{1, \ldots, n\}\}$, of a distortion profile between two stiffeners is available along the red line in Fig. 5.10. The panel is subject to a remote axial load P in the direction shown in Fig. 5.10.

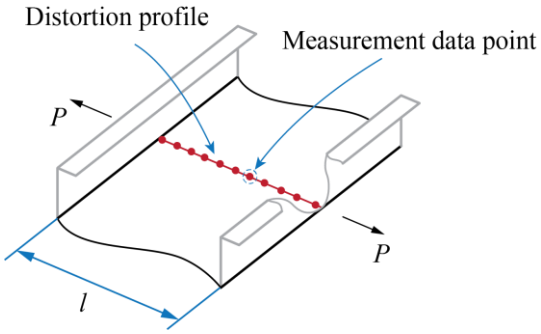

Fig. 5.10 Illustration of a distortion profile and measurements between two stiffeners.

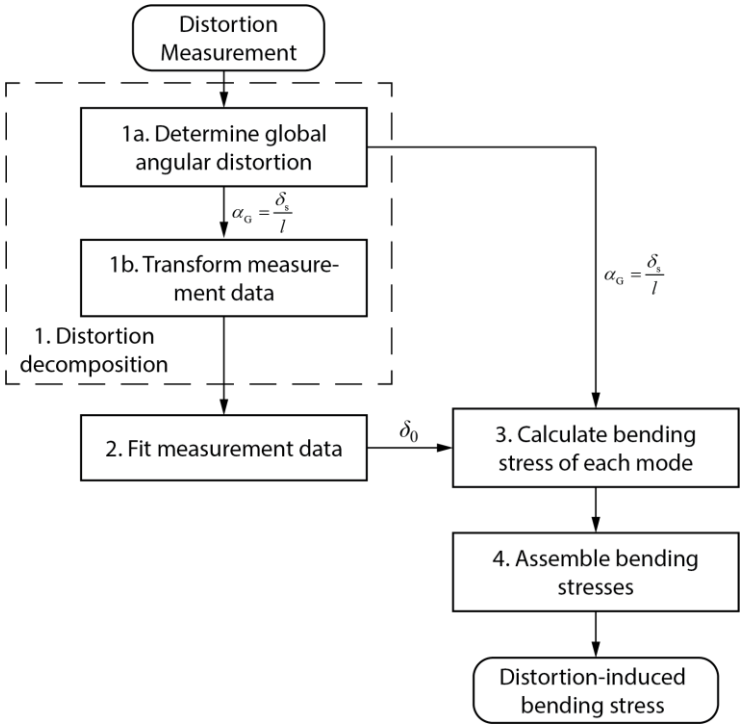

Fig. 5.11 Flow chart of the procedure to calculate distortion-induced bending stress in stiffened panels.

1. Distortion decomposition

   1a. Determine global angular distortion θ_G

   The global angular distortion θ_G can be immediately determined by $\theta_G = \delta_s/l$, as shown in Fig. 5.5. The global angular distortion mode shape is $v_{0,\text{global}} = \delta_s x/l$.

   1b. Transform measurement data

   Transform measurement data by $y_i \leftarrow y_i - \delta_s x_i/l$ to eliminate the global angular distortion component from the measurement. The transformed measurement data corresponds to the local angular distortion.

2. Fit measurement data

   Perform curve-fitting on the transformed measurement data using the model for buckling distortion mode or cosine angular distortion mode (refer to Appendix B.2). The curve-fitting will directly provide the parameter δ_0 for the mode selected.

3. Calculate secondary bending induced bending stress

The global angular distortion θ_{G} in a stiffened panel does not contribute to secondary bending, i.e., $\sigma_{\mathrm{b,global}} = 0$. For the local angular distortion, use Table 5.12 for the small deformation condition or Table 5.13 for the large deformation condition to calculate k_{b} at the fillet weld locations. The bending stress is calculated by$\sigma_{\mathrm{b,local}} = k_{\mathrm{b}}\sigma_{\mathrm{n}}$.

4. Assemble bending stress of each distortion mode

Since the global angular distortion does not introduce bending stress, the total secondary bending stress is $\sigma_{\mathrm{b,distortion}} = \sigma_{\mathrm{b,local}}$ obtained in Step 3.

5.5 Application Examples

5.5.1 Butt Joints in Full-Scale Panels

In this section, we will revisit the distortion profile of Specimen 334 provided in [41], as shown in Fig. 5.12. In this example, a set of 13 distortion measurement data based on the global coordinate is available for each side of the butt joint (see Fig. 5.13), denoted as $\mathcal{M}_1$ and $\mathcal{M}_2$. The two weld toe positions are given as $x_{\mathrm{A}} = -8.43$ mm and $x_{\mathrm{B}} = -1.34$ mm; the stiffener spacing is $l = 400$ mm, and the thickness of the plate is $t = 4$ mm. The Young's modulus of the material is $E = 206000$ MPa. The specimen is subject to a tensile cyclic loading with the nominal stress σ_{n} varying from 0 to 171 MPa. The load direction is shown in Fig. 5.12.

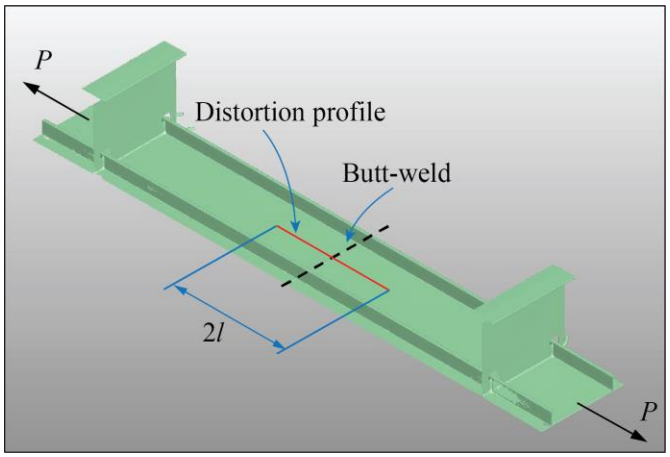

Fig. 5.12 Illustration of full-scale fatigue test Specimen 334 and the distortion profile of interest.

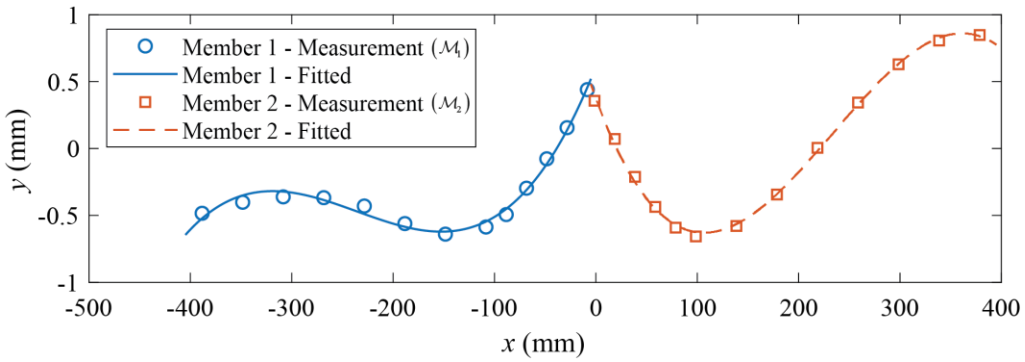

Fig. 5.13 Distortion measurements of Specimen 334 and fitted cubic polynomials.

The x-coordinate of the center of the joint (i.e., Position O in Fig. 5.1) is obtained by

$$x_O = \frac{x_A + x_B}{2} = -4.88 \text{ mm} \tag{5.8}$$

Then, we use the following equation to transform the x-coordinate of the measurement data points, so they follow the local coordinate x_1 (for data points about Member 1) and x_2 (for data points about Member 2) in Fig. 4.1.

$$\begin{aligned} x_{1,i} &= x_i - (x_O - l) \quad i \in \{i \,|\, (x_i, y_i) \in \mathcal{M}_1\} \\ x_{2,i} &= x_i - x_O \qquad\quad i \in \{i \,|\, (x_i, y_i) \in \mathcal{M}_2\} \end{aligned} \tag{5.9}$$

Then, we can perform third-order polynomial fitting with respect to each member, resulting in

$$\begin{aligned} v_0^{(1)} = &\ \ 1.3179\times10^{-7}x_1^3 - 6.6871\times10^{-5}x_1^2 + 8.5784\times10^{-3}x_1 - 0.6457 \\ v_0^{(2)} = &-1.8045\times10^{-7}x_2^3 + 1.2938\times10^{-4}x_2^2 - 2.2143\times10^{-2}x_2 + 0.4814 \end{aligned} \tag{5.10}$$

The fitting result is plotted in Fig. 5.13 based on the global coordinate, and a good agreement is achieved for both sides.

With the initial distortion shape $v_0^{(1)}$ and $v_0^{(2)}$ ready, we can proceed to decompose the distortion. First, the axial misalignment can be calculated by

$$\mathrm{e} = v_0^{(2)}(0) - v_0^{(1)}(l) = -0.0393 \text{ mm} \tag{5.11}$$

By subtracting $v_{0,\text{axial}}^{(1)} = 0$ from $v_0^{(1)}$ and $v_{0,\text{axial}}^{(2)} = \mathrm{e}$ from $v_0^{(2)}$, we get

$$\begin{aligned} v_0^{(1)} - v_{0,\text{axial}}^{(1)} = &\ \ 1.3179\times10^{-7}x_1^3 - 6.6871\times10^{-5}x_1^2 + 8.5784\times10^{-3}x_1 - 0.6457 \\ v_0^{(2)} - v_{0,\text{axial}}^{(2)} = &-1.8045\times10^{-7}x_2^3 + 1.2938\times10^{-4}x_2^2 - 2.2143\times10^{-2}x_2 + 0.5207 \end{aligned} \tag{5.12}$$

Next, the global angular distortion α_G is obtained by

$$\begin{aligned} \theta_{1\mathrm{G}} &= \frac{\left[v_0^{(1)}(l) - v_{0,\text{axial}}^{(1)}(l)\right] - \left[v_0^{(1)}(0) - v_{0,\text{axial}}^{(1)}(0)\right]}{l} = 2.9158\times10^{-3} \text{ rads} \\ \theta_{2\mathrm{G}} &= \frac{\left[v_0^{(2)}(l) - v_{0,\text{axial}}^{(2)}(l)\right] - \left[v_0^{(2)}(0) - v_{0,\text{axial}}^{(2)}(0)\right]}{l} = 0.7356\times10^{-3} \text{ rads} \\ \alpha_\mathrm{G} &= \theta_{2\mathrm{G}} - \theta_{1\mathrm{G}} = -2.1802\times10^{-3} \text{ rads} \end{aligned} \tag{5.13}$$

The shape functions for the global angular distortion, based on Eqn. (4.24), are

$$\begin{aligned} v_{0,\text{global}}^{(1)} &= \theta_{1\mathrm{G}} x_1 = 2.9158\times10^{-3}x_1 \\ v_{0,\text{global}}^{(2)} &= \theta_{2\mathrm{G}} x_2 + \theta_{1\mathrm{G}} l_1 = 0.7356\times10^{-3}x_2 + 1.1663 \end{aligned} \tag{5.14}$$

Further subtracting $v_{0,\text{global}}^{(1)}$ from $v_0^{(1)}$ and $v_{0,\text{global}}^{(2)}$ from $v_0^{(2)}$, we finally obtain the local angular distortion shape functions as

$$
\begin{aligned}
v_{0,\text{local}}^{(1)} &= v_0^{(1)} - v_{0,\text{axial}}^{(1)} - v_{0,\text{global}}^{(1)} \\
&= 1.3179\times10^{-7}\,x_1^3 - 6.6871\times10^{-5}\,x_1^2 + 5.6625\times10^{-3}\,x_1 - 0.6457 \\
v_{0,\text{local}}^{(2)} &= v_0^{(2)} - v_{0,\text{axial}}^{(2)} - v_{0,\text{global}}^{(2)} \\
&= -1.8045\times10^{-7}\,x_2^3 + 1.2938\times10^{-4}\,x_2^2 - 2.2879\times10^{-2}\,x_2 - 0.6457
\end{aligned}
\tag{5.15}
$$

Based on Eqn. (5.15), we can compute the local angular distortion parameters as

$$
\begin{aligned}
\theta'_{11} &= v'^{(1)}_{0,\text{local}}(0) = 5.6625\times10^{-3}\ \text{rads} \\
\theta'_{12} &= v'^{(1)}_{0,\text{local}}(l) = 15.423\times10^{-3}\ \text{rads} \\
\theta'_{21} &= v'^{(2)}_{0,\text{local}}(0) = -22.879\times10^{-3}\ \text{rads} \\
\theta'_{22} &= v'^{(2)}_{0,\text{local}}(l) = -5.9930\times10^{-3}\ \text{rads}
\end{aligned}
\tag{5.16}
$$

With the axial misalignment e in Eqn. (5.11), global angular distortion α_{G} in Eqn. (5.13), and the local angular distortion parameters in Eqn. (5.16), we can then calculate the secondary bending caused by each distortion mode using the tables provided in Sec. 5.2. Because the plate is thin ($t = 4$ mm), we need to consider the large deformation condition; and since the butt joint geometry size is small, the joint size effect can be neglected. Based on Table 5.1, we would use Table 5.3 to calculate $M_{\text{axial}}^{(i)}$, Table 5.8 for $M_{\text{global}}^{(i)}$, and Table 5.11 for $M_{\text{local}}^{(i)}$. Furthermore, the structure in this example satisfies symmetric structure condition (l and t are the same for both members); thus, we would refer to the row corresponding to the $l_1 = l_2 = l$ and $t_1 = t_2 = t$ condition.

In this example, Specimen 334 is subject to a tensile cyclic loading with the nominal stress σ_{n} varying from 0 to 171 MPa. Since the minimum load is always 0, we only need to calculate the distortion induced bending stress when $\sigma_{\text{n}} = 171$ MPa, which corresponds to $P = \sigma_{\text{n}} t = 684$ N. Based on Table 5.3,

$$
M_{\text{axial}}^{(1)} = -M_{\text{axial}}^{(2)} = -\frac{P\text{e}}{2} = 13.441\ \text{N}\cdot\text{mm}
\tag{5.17}
$$

Based on Table 5.8,

$$M_{\text{global}}^{(1)} = M_{\text{global}}^{(2)} = -\frac{P\alpha_{\text{G}} l}{2}\left(\frac{\cosh \lambda l - 1}{\lambda l \sinh \lambda l}\right) = 29.880 \text{ N} \cdot \text{mm} \tag{5.18}$$

And based on Table 5.11,

$$\begin{aligned} M_{1.\text{local}}^{(1)} &= M_{1.\text{local}}^{(2)} \\ &= -Pl\left[\left(\frac{\lambda^2 l^2 \cosh \lambda l - 4\lambda l \sinh \lambda l + 6\cosh \lambda l - 6}{2\lambda^3 l^3 \sinh \lambda l}\right)\left(\theta'_{21} - \theta'_{12}\right)\right. \\ &\qquad \left. + \left(\frac{-\lambda^2 l^2 - 2\lambda l \sinh \lambda l + 6\cosh \lambda l - 6}{2\lambda^3 l^3 \sinh \lambda l}\right)\left(\theta'_{22} - \theta'_{11}\right)\right] \\ &= 323.80 \text{ N} \cdot \text{mm} \end{aligned} \tag{5.19}$$

Using the equation for assembly given in Eqn. (5.1), we can obtain the total bending moment caused by distortion's interaction with the axial load P as

$$\begin{aligned} M_{\text{distortion}}^{(1)} &= M_{\text{axial}}^{(1)} + M_{\text{global}}^{(1)} + M_{1.\text{local}}^{(1)} = 367.12 \text{ N} \cdot \text{mm} \\ M_{\text{distortion}}^{(2)} &= M_{\text{axial}}^{(2)} + M_{\text{global}}^{(2)} + M_{1.\text{local}}^{(2)} = 340.24 \text{ N} \cdot \text{mm} \end{aligned} \tag{5.20}$$

Obviously, the maximum bending stress will occur at Position B (see Fig. 5.1), and the bending stress at Position B can be finally calculated using Eqn. (5.2) as

$$\sigma_{\text{b}}^{\text{B}} = \frac{6M_{\text{distortion}}^{(1)}}{t^2} = 137.67 \text{ MPa} \tag{5.21}$$

As such, we have obtained distortion-induced bending stress. We can then calculate the total structural stress at Position B by

$$\sigma_{\text{s}}^{\text{B}} = \sigma_{\text{m}} + \sigma_{\text{b}}^{\text{B}} = 171 + 137.67 = 308.67 \text{ MPa} \tag{5.22}$$

where $\sigma_{\text{m}} = \sigma_{\text{n}}$ for axially loaded cases in this example. The above structural stress can then be used with the master S-N curve method for fatigue test data interpretation.

5.5.2 Fillet Welds in Stiffened Panels

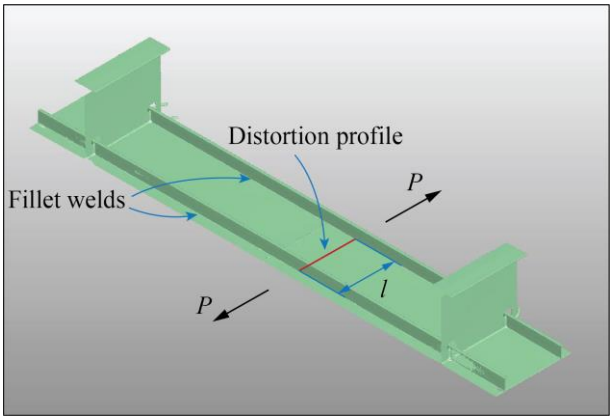

Fig. 5.14 Illustration of the distortion profile of interest between stiffeners in a panel.

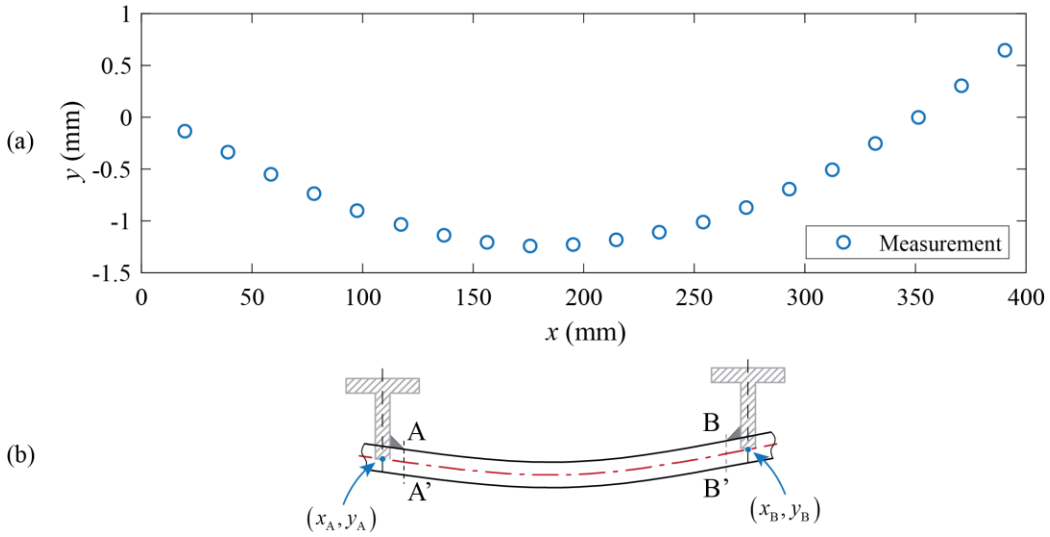

Fig. 5.15 Distortion profile of Specimen 143: (a) distortion measurements; (b) illustration showing the distortion profile and weld toe positions.

In the following example, we will explore the distortion's effect on fillet welds, which connect stiffeners to the plate. Imagine a full panel like the one in Fig. 2.14a, and the distortion between two stiffeners has the same profile as that of Specimen 143 in the transverse direction in [41]. Fig. 5.14 shows the distortion profile of interest. We also assume that the panel is subject to a remote in-plane cyclic fatigue loading, whose direction is also indicated in Fig. 5.14. The nominal stress in this example is assumed to be from 0 to 100 MPa. The stiffener spacing is $l = 400$ mm, and the thickness of the plate is $t = 4$ mm. The Young's modulus of the material is $E = 206000$ MPa.

Suppose a set of 20 distortion measurement data, denoted as $\mathcal{M}$, is available for the aforementioned distortion profile representing the centerline of the plate, as shown in Fig. 5.15a. The root of the two stiffeners (see Fig. 5.15b) are located at $(x_A, y_A) = (0,0)$ and $(x_B, y_B) = (400,0.8996)$.

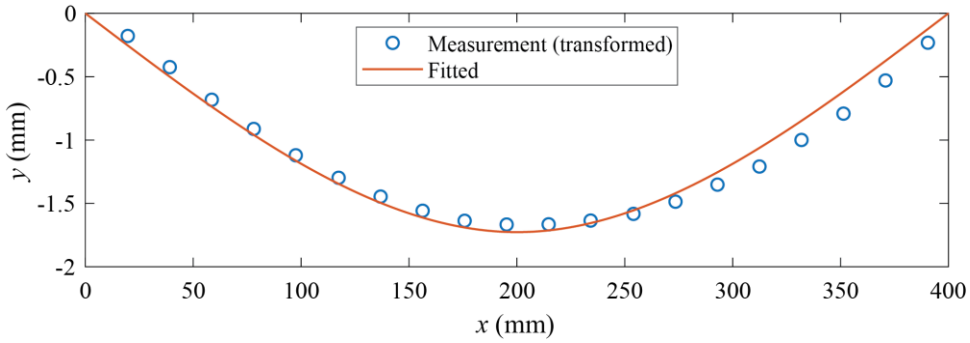

Fig. 5.16 Transformed distortion measurements and fitted curve.

First, the global angular distortion is determined by

$$\theta_G = \frac{\delta_s}{l} = \frac{y_B - y_A}{l} = 2.2489 \times 10^{-3} \text{ rads} \tag{5.23}$$

Then, we can transform the measurement data in $\mathcal{M}$ using the following equation to remove the global angular distortion mode:

$$y_{i,\text{local}} = y_i - \theta_G x_i \tag{5.24}$$

Judging from the transformed measurement in Fig. 5.16, we can see that the local angular distortion shape is similar to the buckling distortion shape. As such, we would fit the transformed measurements using the model for the buckling distortion given in Eqn. (B.14). The resulting δ_0 from the curve-fitting is

$$\delta_0 = -1.7268 \text{ mm} \tag{5.25}$$

The curve fitted is plotted in Fig. 5.16, and a good agreement with the transformed measurement data is achieved.

Since the plate has a small thickness ($t = 4$ mm), we would consider the large deformation condition and refer to Table 5.13 to calculate the k_{b} caused by the buckling distortion mode. Again, we only need to calculate the k_{b} when $\sigma_{\mathrm{n}} = 100$ MPa since the minimum σ_{n} is zero. As such, k_{b} is calculated as

$$k_{\mathrm{b}} = 18\frac{\delta_0}{t}\left[\frac{\cosh\frac{\lambda l}{2}}{\lambda l \sinh\frac{\lambda l}{2}} - \frac{8}{(\lambda l)^2}\left(\frac{\cosh\frac{\lambda l}{2} - 1}{\lambda l \sinh\frac{\lambda l}{2}}\right)\right] = -0.8853 \tag{5.26}$$

The negative k_{b} means that the weld toe position (Position A in Fig. 5.15b) is under compression in this case. Since the global angular distortion does not contribute to the secondary bending, the bending stress caused by distortion at Position A under $\sigma_{\mathrm{n}} = 100$ MPa is given as

$$\sigma_{\mathrm{b}}^{\mathrm{A}} = k_{\mathrm{b}}\sigma_{\mathrm{n}} = -88.53 \text{ MPa} \tag{5.27}$$

And the total structure stress at Position A is

$$\sigma_{\mathrm{s}}^{\mathrm{A}} = \sigma_{\mathrm{m}} + \sigma_{\mathrm{b}}^{\mathrm{A}} = 11.47 \text{ MPa} \tag{5.28}$$

where $\sigma_{\mathrm{m}} = \sigma_{\mathrm{n}}$ for axial loaded condition. For illustration purpose, the bending stress at the bottom surface of the plate (Position A' in Fig. 5.15b), which has the maximum bending stress in Section A-A, is also provided as

$$\sigma_{\mathrm{b}}^{\mathrm{A'}} = -k_{\mathrm{b}}\sigma_{\mathrm{n}} = 88.53 \text{ MPa} \tag{5.29}$$

And the total structure stress at Position A' is

$$\sigma_{\mathrm{b}}^{\mathrm{A'}} = \sigma_{\mathrm{m}} + \sigma_{\mathrm{b}}^{\mathrm{A'}} = 100 + 88.53 = 188.53 \text{ MPa} \tag{5.30}$$

5.6 Chapter Conclusions

In this chapter, we first summarized the analytical solutions developed in Chapter 2 to Chapter 4. By categorizing the analytical solutions based on the distortion mode, the small/large

deformation condition, and consideration of joint representation, we created 12 tables of analytical solution formulae for calculating distortion-induced bending stress. Within each table, specific solution forms corresponding to some common joint configurations are provided for illustrating their applications in typical engineering problems. An index table is also given as a reference for selecting the proper formulae based on the application scenario.

Then, the distortion decomposition and assembly procedure developed in Sec. 4.4 is encapsulated, and step-by-step application procedures are developed for calculating bending stress with respect to distortions in butt-welded plates and stiffened panels. Flow charts for the previously developed procedures are also developed with essential remarks and references as guidance for their application in engineering problems.

Finally, two comprehensive application examples are provided to illustrate how the procedures and analytical formulae developed in this research are used to solve real engineering problems. Based on measurement data documented in the literature, the first example illustrated the calculation of distortion-induced stress on a butt joint in a full-scale panel structure, and the second example showed how the secondary bending-induced stress caused by the distortion between stiffeners is computed. Both examples explained how the complicated distortion is decomposed into basic distortion modes and how the analytical solutions are finally get assembled to get the total secondary bending effect caused by complex distortions.

Chapter 6

Conclusions

6.1 Key Findings

This dissertation presented work on the analytical treatment of the secondary bending effects caused by complex welding-induced distortions on the fatigue behavior of modern lightweight structures. Three elementary distortion modes observed in lightweight structures are studied individually based on strip beam theory under linear and nonlinear geometry, and closed-form analytical solutions are presented for each mode. Furthermore, a comprehensive distortion decomposition-and-assembly procedure is developed to attain the final closed-form solution to a given complex distortion problem. These new solutions, in addition to offering valuable insights on the validity limits of the empirical equations used by the current Codes and Standards, offer a comprehensive suite of tools to engineers and researchers for a consistent and effective treatment of secondary stresses caused by distortion types unique to lightweight shipboard structures in performing fatigue evaluations. Major key findings are summarized as follows:

(1) With the proposed notional load method, closed-form analytical formulae can be developed for analyzing secondary bending stresses caused by nonlinear interactions between distortion curvatures and remotely applied loads.

(2) The notional load method requires only a few distortion measurements for evaluating fatigue performance of welded joints in lightweight structures, significantly reducing the needs for full-field distortion measurements and their mapping onto a structural FE model.

(3) By introducing a rigid body-based joint representation in the analytical model, the force equilibrium and geometry relationships about the joint can be established in such a way that enables the development of the closed-form analytical formulae for calculating secondary bending stress caused by axial and angular misalignments (also called global angular distortion) without curvature.

(4) With the joint definition and the resulting analytical solutions, the interactions between axial and angular misalignment can be properly combined for determining specific secondary bending stress at each of all four weld toe positions.

(5) These new closed-form solutions offer some significant insights not only on what types of distortions are more detrimental to fatigue performance than others but also on the validity limits of the empirical equations stipulated in current Codes and Standards. In addition, a set of parameterized limits can now be clearly stated on conditions when straightening effects should be considered. It is shown that the slenderness ratio l/t can be related to the severity of the nonlinear geometry effect: the higher the l/t becomes, the stronger the nonlinear effect can be seen.

(6) Welding-induced distortions are shown to have significant effects on fatigue behaviors in welded thin-plate structures. Without appropriate treatment for secondary bending stresses, available test data cannot be correlated with existing data that support existing Codes and Standards. The analytical approach presented in this paper proves effective for interpreting fatigue test data obtained in welded thin plate components.

(7) By introducing a consistent reference framework in the general distortion mode decomposition-and-assembly procedure, complex distortions regarding both butt-welded joints and fillet-welded joints in panel structures can be readily decomposed into various

elementary distortion modes with respect to which closed-form solutions have been developed in this dissertation or can be more easily developed.

(8) Based on the distortion mode decomposition-and-assembly procedure, a workflow for evaluating the secondary bending stress effects caused by complex welding-induced distortions on the fatigue performance in lightweight structures can be established. To facilitate real-world engineering applications of the workflow, the closed-form formulae developed are presented in tabular form.

6.2 Recommendations for Future Research Topics

This work has shown the capability of using the notional load method with the strip beam theory based on Föppl-von Kármán equations in the analytical treatment of distortion effects. The analytical models, together with the decomposition-and-assembly procedure, have laid a concrete framework for studying secondary stresses caused by distortion types unique to lightweight shipboard structures in performing fatigue evaluations. Many possible future research topics can be generated based on this framework. These include:

1. *Additional basic distortion modes*: as the awareness of the impact from distortions on the structural integrity of modern lightweight structures increases, more observations of welding-induced distortions will be available in the future. It is possible that we observe new distortion curvatures that could not be well represented by the distortion modes in this dissertation, and additional basic distortion modes could be established by extending the notional load method in this dissertation.
2. *Different boundary conditions*: in this dissertation, only clamped boundary conditions are studied in the analytical model for each distortion mode, which can cover butt-welded joints and fillet-welded joints for connecting stiffeners or frames. There are other forms of

joints that correspond to different boundary conditions, such as fillet-welded cruciform joints. These boundary conditions need to be first defined in the structure context, and then corresponding analytical models can be established and solved.

3. *Plate boundary and three-dimensional distortion effect*: the analytical treatment in this dissertation strictly follows the strip beam theory. Although this assumption is proven applicable in fatigue evaluation of panel structures, the effect of the plate boundary and three-dimensional distortion (i.e., distortion in the direction orthogonal to the loading direction) cannot be revealed and quantified by the analytical solutions in this dissertation. By studying the plate boundary and three-dimensional distortion effect, we could gain more insights on the validity boundary of our strip beam assumption and potential guidance on how our analytical solutions can be simplified. Furthermore, by considering a plate model, we should be able to model the buckling behavior of panel structures more precisely than using beam models.
4. *Distortion tolerance limits*: in engineering applications, it is desired to have a properly defined distortion tolerance limit in Codes and Standards for cost-effectiveness. With the analytical solutions and the methodology leading to them presented in this dissertation, we could analyze the distortion effects mathematically and define a proper parametric description of distortion for establishing distortion tolerance limits.

Appendices

Appendix A

Detailed Solution Processes for Each Distortion Mode

In this appendix, the detailed solution process for each distortion mode is provided, including the cosine angular distortion mode, the buckling distortion mode, the global angular distortion mode based on symmetric geometry, and the local angular distortion mode based on symmetric geometry. The treatment of boundary conflict between the linear beam model and the imperfect beam model is also presented in Appendix A.6. Finally, a simplification technique of the solution process is provided in Appendix A.7.

A.1 Cosine Angular Distortion Mode

Taking advantage of the symmetry condition at $x = l/2$, one can write the boundary conditions with respect to the governing equation given in Eqn. (2.3) corresponding to the linear beam without imperfections (see Fig. 2.3b), as ($V_0 = -EIv'''_0$ is the shear force in the linear beam):

$$\begin{aligned} v_0(0) &= 0 \\ v_0'(0) &= 0 \\ v_0'\left(\frac{l}{2}\right) &= 0 \\ V_0\left(\frac{l}{2}\right) &= \frac{F_0}{2} \\ v_0(x) &= v_0(l-x). \end{aligned} \tag{A.1}$$

Then, the solution that satisfies the above boundary conditions can be found in classical Mechanics of Materials textbooks [90]. By setting $\delta_0 = v_0(l/2)$, the corresponding notional load can be obtained as $F_0 = 192EI\delta_0/l^3$. Next, by a close examination of the nonlinear beam model with the

initial imperfections prescribed by the now known $v_0(x)$ in Fig. 2.3a, its boundary conditions are given as:

$$\begin{aligned} v_1(0) &= 0 \\ v_1'(0) &= 0 \\ v_1'\left(\frac{l}{2}\right) &= 0 \\ V_1\left(\frac{l}{2}\right) &= 0 \\ v_1(x) &= v_1(l-x). \end{aligned} \tag{A.2}$$

In (A.2), V_1 represents the secondary shear force caused by axial load P and has the following form

$$V_1 = -\frac{\partial M_1}{\partial x} + P\frac{\partial\left(v_0+v_1\right)}{\partial x} = -EIv_1''' + P\left(v_0'+v_1'\right). \tag{A.3}$$

Considering the symmetry condition at $x = l/2$, no constraint is applied on the translation degree of freedom and thus V_1 should be zero as given in Eqn. (A.2).

From Eqns. (A.1) and (A.2), it can be see that the boundary conditions in terms of both displacements and rotations are the same between the linear beam and the imperfect beam model. Then, Eqns. (A.1) and (A.2) are combined and form the boundary conditions for $v(x)$ shown in Fig. 2.3c (i.e., an equivalent nonlinear beam without initial imperfections):

$$\begin{aligned} v(0) &= 0 \\ v'(0) &= 0 \\ v'\left(\frac{l}{2}\right) &= 0 \\ V\left(\frac{l}{2}\right) &= \frac{F_0}{2} \\ v(x) &= v(l-x). \end{aligned} \tag{A.4}$$

The final nonlinear beam deflection $v(x)$ can be obtained by solving Eqn. (2.5) with the above boundary conditions given in Eqn. (A.4). By substituting $F_0 = 192EI\delta_0/l^3$ into Eqn. (A.4) , $v(x)$ corresponding to the beam span from $x = 0$ to $x = l/2$ is given as:

$$v(x) = \begin{cases} \dfrac{96\delta_0}{\lambda^3 l^3}\left[-\sinh\lambda x + \dfrac{\cosh\frac{\lambda l}{2} - 1}{\sinh\frac{\lambda l}{2}}\left(\cosh\lambda x - 1\right) + \lambda x\right] & P > 0 \\ \dfrac{96\delta_0}{\lambda^3 l^3}\left[\sin\lambda x + \dfrac{\cos\frac{\lambda l}{2} - 1}{\sin\frac{\lambda l}{2}}\left(\cos\lambda x - 1\right) - \lambda x\right] & P < 0 \end{cases} \tag{A.5}$$

and the expression for the beam span from $x = l/2$ to $x = l$ can be obtained by substituting x with $l - x$ in Eqn. (A.5), as a result of symmetry with respect to $x = l/2$.

The distortion-induced secondary moment at the weld location $M_1(0)$ is found as:

$$M_1(0) = EIv''(0) - EIv_0''(0) = \begin{cases} \dfrac{24P\delta_0}{\lambda^2 l^2}\left(\dfrac{4}{\lambda l}\dfrac{\cosh\frac{\lambda l}{2} - 1}{\sinh\frac{\lambda l}{2}} - 1\right) & P > 0 \\ \dfrac{24P\delta_0}{\lambda^2 l^2}\left(\dfrac{4}{\lambda l}\dfrac{\cos\frac{\lambda l}{2} - 1}{\sin\frac{\lambda l}{2}} + 1\right) & P < 0 \end{cases} \tag{A.6}$$

The resulting k_b at beam the top surface ($y = t/2$) at the weld location ($x = 0$) becomes:

$$k_\mathrm{b} = \frac{\sigma_\mathrm{b}}{\sigma_\mathrm{n}} = \frac{-6M_1(0)/t^2}{P/t} = -\frac{6M_1(0)}{Pt}, \tag{A.7}$$

which yields Eqn. (2.6).

A.2 Buckling Distortion Mode

The boundary conditions in Fig. 2.4b to obtain the buckling distortion shape on a linear beam can be written as:

$$
\begin{aligned}
v_0(0) &= 0 \\
M_0(0) &= 0 \\
v_0'\left(\frac{l}{2}\right) &= 0 \\
V_0\left(\frac{l}{2}\right) &= \frac{F_0}{2} \\
v_0(x) &= v_0(l-x).
\end{aligned}
\tag{A.8}
$$

By setting $\delta_0 = v_0(l/2)$, the corresponding notional load can be obtained as $F_0 = 48EI\delta_0/l^3$. Then, based on constraints on the nonlinear beam model with the initial imperfections prescribed by the now known $v_0(x)$ in Fig. 2.3a, its boundary conditions are given as:

$$
\begin{aligned}
v_1(0) &= 0 \\
v_1'(0) &= 0 \\
v_1'\left(\frac{l}{2}\right) &= 0 \\
V_1\left(\frac{l}{2}\right) &= 0 \\
v_1(x) &= v_1(l-x).
\end{aligned}
\tag{A.9}
$$

The second boundary condition of the imperfect beam in Eqn. (A.9) constrains the rotation while the linear beam model (represented by Eqn. (A.8)) does not. Such conflict needs to be solved before Eqn. (A.8) and (A.9) can be added together to form the nonlinear perfect beam problem in Fig. 2.4c. The rule to resolve such conflicts is given in Appendix A.6. In this case, the rotation degree of freedom at $x = 0$ is constrained in the imperfect beam model but is free in the linear beam model. We can easily know from the solution to Eqn. (A.8) that the rotation at $x = 0$ is $3\delta_0/l$, so we replace the second boundary condition in Eqn. (A.8) with $v'_0(0) = 3\delta_0/l$, and obtain a new set of boundary conditions for the linear beam, given as

$$
\begin{aligned}
v_0(0) &= 0 \\
v_0'(0) &= 3\frac{\delta_0}{l} \\
v_0'\left(\frac{l}{2}\right) &= 0 \\
V_0\left(\frac{l}{2}\right) &= \frac{F_0}{2} \\
v_0(x) &= v_0(l-x).
\end{aligned}
\tag{A.10}
$$

It can be simply proved that using Eqn. (A.10) (together with $\delta_0 = v_0(l/2)$) will yield the same initial distortion obtained by Eqn. (A.8). Then we can proceed to add Eqn. (A.10) and (A.9) together to form the nonlinear perfect beam problem shown in Fig. 2.4c as follows:

$$
\begin{aligned}
v(0) &= 0 \\
v'(0) &= 3\frac{\delta_0}{l} \\
v'\left(\frac{l}{2}\right) &= 0 \\
V\left(\frac{l}{2}\right) &= \frac{F_0}{2} = \frac{24EI\delta_0}{l^3} \\
v(x) &= v(l-x).
\end{aligned}
\tag{A.11}
$$

Again, by solving Eqn. (2.5) with the boundary conditions in Eqn. (A.11), we can obtain the total deflection $v(x)$ as

$$v(x)=\begin{cases} 3\delta_0\left\{\begin{array}{l}\left(\dfrac{1}{\lambda l}-\dfrac{8}{\lambda^3 l^3}\right)\sinh\lambda x+\left[-\dfrac{\cosh\frac{\lambda l}{2}}{\lambda l\sinh\frac{\lambda l}{2}}+\dfrac{8}{\lambda^2 l^2}\left(\dfrac{\cosh\frac{\lambda l}{2}-1}{\lambda l\sinh\frac{\lambda l}{2}}\right)\right]\cosh\lambda x \\ +\dfrac{8}{\lambda^2 l^3}x+\dfrac{\cosh\frac{\lambda l}{2}}{\lambda l\sinh\frac{\lambda l}{2}}-\dfrac{8}{\lambda^2 l^2}\left(\dfrac{\cosh\frac{\lambda l}{2}-1}{\lambda l\sinh\frac{\lambda l}{2}}\right)\end{array}\right\} & P>0 \\ 3\delta_0\left\{\begin{array}{l}\left(\dfrac{1}{\lambda l}+\dfrac{8}{\lambda^3 l^3}\right)\sin\lambda x+\left[\dfrac{\cos\frac{\lambda l}{2}}{\lambda l\sin\frac{\lambda l}{2}}+\dfrac{8}{\lambda^2 l^2}\left(\dfrac{\cos\frac{\lambda l}{2}-1}{\lambda l\sin\frac{\lambda l}{2}}\right)\right]\cos\lambda x \\ -\dfrac{8}{\lambda^2 l^3}x-\dfrac{\cos\frac{\lambda l}{2}}{\lambda l\sin\frac{\lambda l}{2}}-\dfrac{8}{\lambda^2 l^2}\left(\dfrac{\cos\frac{\lambda l}{2}-1}{\lambda l\sin\frac{\lambda l}{2}}\right)\end{array}\right\} & P<0 \end{cases}, \quad \text{(A.12)}$$

and the secondary bending moment caused by distortion can be obtained by

$$M_1(0)=M(0)-M_0(0)=\begin{cases} 3P\delta_0\left[-\dfrac{\cosh\frac{\lambda l}{2}}{\lambda l\sinh\frac{\lambda l}{2}}+\dfrac{8}{\lambda^2 l^2}\left(\dfrac{\cosh\frac{\lambda l}{2}-1}{\lambda l\sinh\frac{\lambda l}{2}}\right)\right] & P>0 \\ 3P\delta_0\left[\dfrac{\cos\frac{\lambda l}{2}}{\lambda l\sin\frac{\lambda l}{2}}+\dfrac{8}{\lambda^2 l^2}\left(\dfrac{\cos\frac{\lambda l}{2}-1}{\lambda l\sin\frac{\lambda l}{2}}\right)\right] & P<0 \end{cases}. \quad \text{(A.13)}$$

Finally, by substituting Eqn. (A.13) into Eqn. (A.7), we obtain the solution in Eqn. (2.8)

A.3 Global Angular Distortion Mode Based on Symmetric Geometry

This section contains the global and local angular distortion based on symmetric geometry assumption as described in Sec. 2.3.2.

The secondary bending caused by global angular distortion can be obtained from the model in Fig. 2.7 directly without using notional loads. The boundary conditions in this model can be written as:

$$\begin{aligned} v(0) &= 0 \\ v'(0) &= \theta_G \\ v'(l) &= \theta_G \\ V(l) &= 0. \end{aligned} \tag{A.14}$$

Solving Eqn. (2.5) with the above boundary conditions, we can get the total deflection as

$$v(x) = \begin{cases} \dfrac{\theta_G}{\lambda}\sinh\lambda x + \dfrac{\theta_G}{\lambda}\dfrac{1-\cosh\lambda l}{\sinh\lambda l}\cosh\lambda x + \dfrac{\theta_G}{\lambda}\dfrac{\cosh\lambda l - 1}{\sinh\lambda l} & P > 0 \\ \dfrac{\theta_G}{\lambda}\sin\lambda x + \dfrac{\theta_G}{\lambda}\dfrac{\cos\lambda l - 1}{\sin\lambda l}\cos\lambda x + \dfrac{\theta_G}{\lambda}\dfrac{1-\cos\lambda l}{\sin\lambda l} & P < 0 \end{cases}, \tag{A.15}$$

and the secondary bending as

$$M_1(x) = M(x) = \begin{cases} P\dfrac{\theta_G}{\lambda}\dfrac{1-\cosh\lambda l}{\sinh\lambda l} & P > 0 \\ -P\dfrac{\theta_G}{\lambda}\dfrac{1-\cos\lambda l}{\sin\lambda l} & P < 0 \end{cases}. \tag{A.16}$$

By substituting Eqn. (A.16) into Eqn. (A.7), we can obtain the solution in Eqn. (2.9).

A.4 Local Angular Distortion Mode Based on Symmetric Geometry

Given local angular distortion angles θ'_1, θ'_2 as shown in Fig. 2.8a, we can use a tilted cantilever beam and apply a notional force F_0 and a notional moment m_0 to achieve the distortion shape. The boundary conditions for the linear beam in Fig. 2.8b is

$$\begin{aligned} v_0(0) &= 0 \\ v_0'(0) &= \theta_1' \\ V_0(l) &= F_0 \\ M_0(l) &= m_0. \end{aligned} \tag{A.17}$$

Together with the displacement at $x = l$,

$$\begin{aligned} v_0(l) &= 0 \\ v_0'(l) &= \theta_2' \end{aligned} \tag{A.18}$$

we can get the notional load in Eqn. (2.10). Then, we need to list the boundary conditions of the imperfect beam model in Fig. 2.8a.

$$\begin{aligned} v_1(0) &= 0 \\ v_1'(0) &= 0 \\ v_1'(l) &= 0 \\ V_1(l) &= 0 \end{aligned} \tag{A.19}$$

In this example, the imperfect beam model has its translational degree of freedom constrained at $x = 0$, and rotational degree of freedom constrained at $x = 0$ and $x = l$. The linear beam model has both translational and rotational degree of freedom constrained at $x = 0$ only. As discussed in Appendix A.6, we would constrain the rotational degree of freedom at $x = l$, giving us the following boundary conditions of the linear beam

$$\begin{aligned} v_0(0) &= 0 \\ v_0'(0) &= \theta_1' \\ v_0'(l) &= \theta_2' \\ V_0(l) &= F_0. \end{aligned} \tag{A.20}$$

Then, the boundary conditions for the nonlinear perfect beam problem would simply be

$$\begin{aligned} v(0) &= 0 \\ v'(0) &= \theta_1' \\ v'(l) &= \theta_2' \\ V(l) &= F_0. \end{aligned} \tag{A.21}$$

With Eqn. (A.21), we can solve Eqn. (2.5) and get

$$v(x)=\begin{cases}\left\{\begin{aligned}&\left[\theta_1'\left(\frac{1}{\lambda}+\frac{6}{\lambda^3 l^2}\right)+\frac{6\theta_2'}{\lambda^3 l^2}\right]\sinh\lambda x\\&+\left[\begin{aligned}&\theta_1'\left(-\frac{6}{\lambda^2 l^2}\frac{\cosh\lambda l-1}{\lambda\sinh\lambda l}-\frac{\cosh\lambda l}{\lambda\sinh\lambda l}\right)\\&+\theta_2'\left(-\frac{6}{\lambda^2 l^2}\frac{\cosh\lambda l-1}{\lambda\sinh\lambda l}+\frac{1}{\lambda\sinh\lambda l}\right)\end{aligned}\right](\cosh\lambda x-1)\\&-\frac{6}{\lambda^2 l^2}(\theta_1'+\theta_2')x\end{aligned}\right\} & P>0\\ \left\{\begin{aligned}&\left[\theta_1'\left(\frac{1}{\lambda}-\frac{6}{\lambda^3 l^2}\right)-\frac{6\theta_2'}{\lambda^3 l^2}\right]\sin\lambda x\\&+\left[\begin{aligned}&\theta_1'\left(-\frac{6}{\lambda^2 l^2}\frac{\cos\lambda l-1}{\lambda\sin\lambda l}+\frac{\cos\lambda l}{\lambda\sin\lambda l}\right)\\&+\theta_2'\left(-\frac{6}{\lambda^2 l^2}\frac{\cos\lambda l-1}{\lambda\sin\lambda l}-\frac{1}{\lambda\sin\lambda l}\right)\end{aligned}\right](\cos\lambda x-1)\\&+\frac{6}{\lambda^2 l^2}(\theta_1'+\theta_2')x\end{aligned}\right\} & P<0\end{cases} \tag{A.22}$$

and the secondary bending moment as

$$M_1(x)=M(x)-M_0(x)=\begin{cases}P\left[\begin{aligned}&\theta_1'\left(-\frac{6}{\lambda^2 l^2}\frac{\cosh\lambda l-1}{\lambda\sinh\lambda l}-\frac{\cosh\lambda l}{\lambda\sinh\lambda l}+\frac{4}{\lambda^2 l}\right)\\&+\theta_2'\left(-\frac{6}{\lambda^2 l^2}\frac{\cosh\lambda l-1}{\lambda\sinh\lambda l}+\frac{1}{\lambda\sinh\lambda l}+\frac{2}{\lambda^2 l}\right)\end{aligned}\right] & P>0\\ P\left[\begin{aligned}&\theta_1'\left(-\frac{6}{\lambda^2 l^2}\frac{\cos\lambda l-1}{\lambda\sin\lambda l}+\frac{\cos\lambda l}{\lambda\sin\lambda l}-\frac{4}{\lambda^2 l}\right)\\&+\theta_2'\left(-\frac{6}{\lambda^2 l^2}\frac{\cos\lambda l-1}{\lambda\sin\lambda l}-\frac{1}{\lambda\sin\lambda l}-\frac{2}{\lambda^2 l}\right)\end{aligned}\right] & P<0\end{cases} \tag{A.23}$$

which can be finally converted into stress concentration factor given in Eqn. (2.11) by substituting Eqn. (A.23) into Eqn. (A.7).

A.5 Local Angular Distortion Mode Based on General Geometry

Given local angular distortion angles $\theta'_{11}, \theta'_{12}, \theta'_{21}, \theta'_{22}$ as shown in Fig. 4.1, we can the notional load model in Sec. 4.3.1, and finally obtain the notional loads shown in Fig. 4.2b given by Eqn. (4.11). The solutions to Eqn. (4.5) for both members take the form of:

For $P > 0$,

$$\begin{aligned} v^{(1)} &= A_1 \sinh \lambda_1 x_1 + B_1 \cosh \lambda_1 x_1 + C_1 x_1 + D_1 \\ v^{(2)} &= A_2 \sinh \lambda_2 x_2 + B_2 \cosh \lambda_2 x_2 + C_2 x_2 + D_2 \end{aligned} \tag{A.24}$$

For $P < 0$,

$$\begin{aligned} v^{(1)} &= A_1 \sin \lambda_1 x_1 + B_1 \cos \lambda_1 x_1 + C_1 x_1 + D_1 \\ v^{(2)} &= A_2 \sin \lambda_2 x_2 + B_2 \cos \lambda_2 x_2 + C_2 x_2 + D_2 \end{aligned} \tag{A.25}$$

where A_i, B_i, C_i, D_i are unknown coefficients. The boundary conditions of the model in Fig. 4.2b correspond to the clamped conditions:

$$\begin{aligned} v^{(1)}(0) &= 0 \\ v'^{(1)}(0) &= \theta'_{11} \\ v^{(2)}(l) &= 0 \\ v'^{(2)}(l_2) &= \theta'_{22} \end{aligned} \tag{A.26}$$

The force equilibrium and geometry relationships are given in Eqns. (4.6) and (4.7). Note that based on von Kármán equation, $M^{(i)}$ and $V^{(i)}$ in Eqn. (4.6) are calculated by

$$\begin{aligned} M^{(i)} &= EI \frac{d^2 v^{(i)}}{dx_i^2} \\ V^{(i)} &= -EI \frac{d^3 v^{(i)}}{dx_i^3} + P \frac{dv^{(i)}}{dx_i^3} = C_i P \end{aligned} \tag{A.27}$$

With Eqns. (A.26), (4.6) and (4.7), unknown coefficients in Eqns. (A.24) and (A.25) can be solved, leading to Eqn. (4.12).

A.6 Treatment of Constraint Conflicts

We refer to the difference in the constrained degrees of freedom between the linear beam model and the imperfect beam model as constraint conflicts.

The principle for resolving such conflicts is to follow the constraint imposed on the imperfect beam. It can be achieved by using equivalent linear beam models. For example, the two linear beam problems in Fig. A.1 are equivalent since they yield same $v_0(x)$.

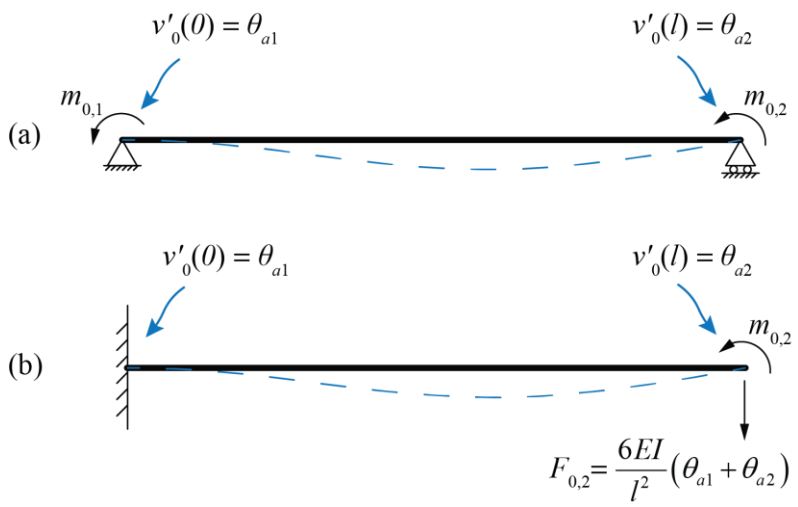

Fig. A.1 Two equivalent linear beam models.

There are two possible scenarios: 1) If a degree of freedom is constrained in the imperfect beam model but not in the linear beam model, we shall replace the corresponding boundary condition with a prescribed displacement constraint. The value of the prescribed displacement is obtained from the solution to the original linear beam problem. 2) If a degree of freedom is free in the imperfect beam model but not in the linear beam model, we shall then release the constraint on that degree of freedom in the linear beam and apply the corresponding reaction force/moment at that location. The reaction force is calculated based on the solution to the original linear beam problem as well. One example for each scenario based on Fig. A.1a are given below.

Example 1: Suppose the rotational degree of freedom at $x = 0$ is free in the original linear beam model, and there is a notional moment acting on $x = 0$ (as in Fig. A.1a),

$$M_0(0) = m_{0,1} \tag{A.28}$$

The same degree of freedom is constrained in the imperfect beam model. The slope of v_0 at $x = 0$ is calculated from the original linear beam as θ_{a1}. In this case, we shall fixate the rotational degree of freedom at $x = 0$ and replace the boundary condition stated by Eqn. (A.28) with a prescribed rotation boundary condition as follows:

$$v_0'(l) = \theta_{a1}. \tag{A.29}$$

Example 2: Suppose the translational degree of freedom at $x = l$ is constrained in the original linear beam model (see Fig. A.1a). The corresponding boundary condition is given as

$$v_0(l) = 0. \tag{A.30}$$

And the reaction force corresponding to this degree of freedom is calculated based on the original linear beam model as $V_0(l) = -\frac{6EI}{l^2}(\theta_{a1} + \theta_{a2})$. Suppose in the imperfect beam, the translational degree of freedom at $x = l$ is free. In this situation, we should release the constraint on this degree of freedom and replace it with a notional load $F_{0,2}$ equal to the shear reaction force at $x = l$ in the original linear beam. The corresponding boundary condition on the translational degree of freedom at $x = l$ then becomes

$$V_0(l) = -F_{0,2} = -\frac{6EI}{l^2}(\theta_{a1} + \theta_{a2}). \tag{A.31}$$

A.7 Simplifications of the Solution Process

Based on Eqn. (A.2) in Appendix A.1, Eqn. (A.9) in Appendix A.2, and Eqn. (A.19) above, we can see that the values in these boundary conditions are always zero (i.e., either no prescribed values for v_1 or no force/moment applied on the imperfect beam), but provides important information on what degree of freedom is constrained in the imperfect beam. Therefore, we can skip listing out the complete boundary condition equations on the imperfect beam but just note the constraint conditions on each degree of freedom. After applying the rule mentioned in Appendix

A.6 to constrain/release certain degrees of freedom on the linear beam, we can then acquire the boundary conditions for the nonlinear perfect beam problem by simply replacing v_0, V_0, M_0 with v, V, M, respectively. For example, after we obtain Eqn.(A.20), we can directly write Eqn. (A.21) by replacing v_0 with v, and V_0 with V.

Appendix B

Distortion Measurement Data Process Procedure

In this appendix, a systematic distortion measurement data process procedure for notional load modeling of the initial distortion is presented. Using a cubic Hermite spline model and ordinary least squares method, we can obtain the distortion shape and its corresponding notional load model in a mathematical way.

B.1 Distortion Measurements

In the notional load method, the characteristics required to describe the distortion shape are the displacement and rotations at where notional loads are applied. However, in reality these parameters are hard to measure at those exact locations: for translational displacement, the surface condition of the plate will greatly affect the measurement, especially around welded joints; for rotation angle, there is no direct way to measure the local angular rotation of a plate with distortion curvature.

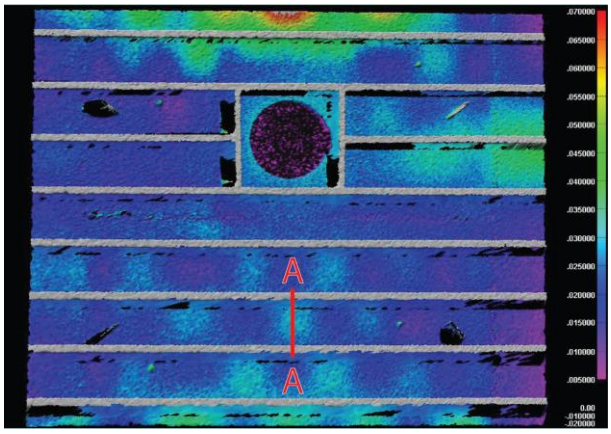

Fig. B.1 Distortion displacement measurement using LIDAR [72].

The most common distortion measurement used in literature is the displacement measurement using LIDAR or similar technology, as shown in Fig. B.1. The measurement at a sampling point is its distance to a prescribed reference plane. In this research, we only need to consider the distortion profile along a cross-section cut of interest, say A-A in Fig. B.1, so only the distortion measurements along A-A will be extracted and processed.

B.2 Curve Fitting using Cubic Hermite Spline and Ordinary Least Squares

B.2.1 Cubic Hermite Spline

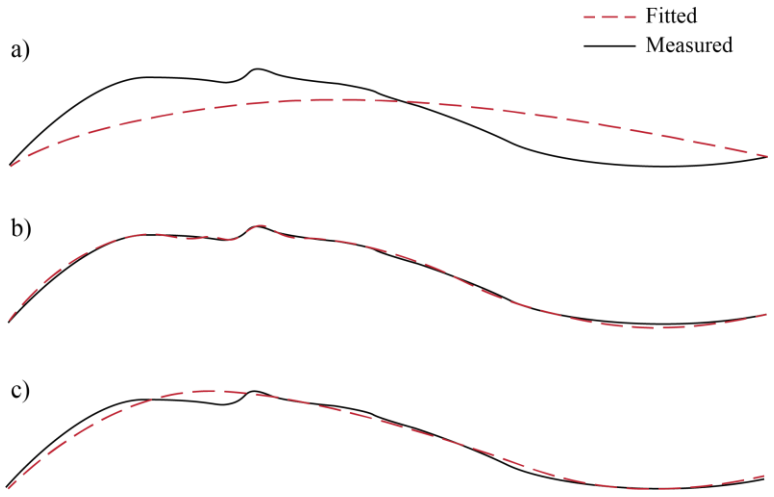

Fig. B.2 Illustration of fitting results: (a) underfitting; (b) overfitting; (c) good fitting with no overfitting or underfitting.

Having the distortion displacement measurements, the best way to obtain the displacement and rotation sought at notional load application location is to perform a curve fitting of the measurements. Considering the application in this research, the fitted curve shall satisfy the following requirements:

- No overfitting or underfitting: higher-order fluctuations (e.g. surface conditions) in the measurements should be smoothed out, and general distortion shape should be captured, see Fig. B.2.
- Compatible with notional load method, i.e., the fitted curve can be recreated by applying certain notional loads onto a linear beam.

The deflection of a linear beam, which is governed by Eqn. (2.3), is a piecewise cubic polynomial and is continuous in itself and its first derivative (not necessary for second and third derivative because of applied concentrated force/moment). Therefore, the distortion shape modeled by the notional load method is, by definition in [91], a cubic Hermite spline (all notional loads applied on knots of the spline). Furthermore, the spline fitting has the advantage of smoothness and less local influence [92], satisfying the first requirement listed above. Thus, the best model to be used for fitting the distortion data is the cubic Hermite spline, which is also called a C^1-spline in mathematics.

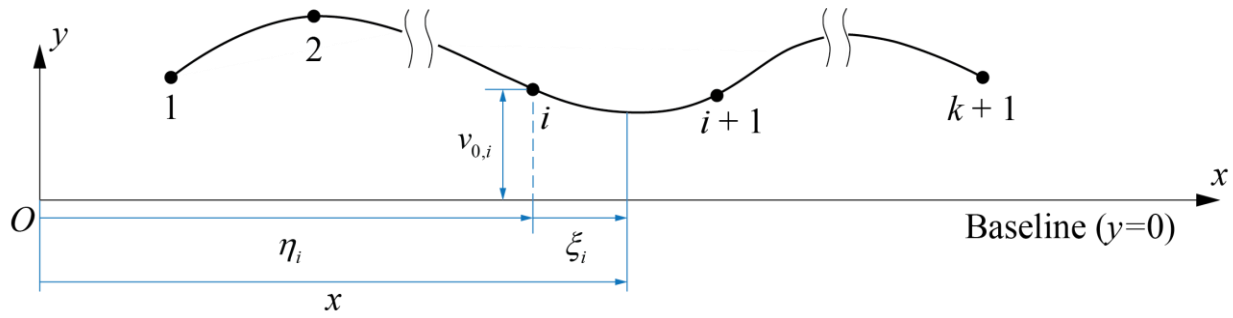

Fig. B.3 Illustration of a spline with *k*+1 nodes.

Fig. B.3 shows a spline with $k+1$ knots. The x-coordinate of the knot i is η_i, and the displacement and rotation at knot i is $v_{0,i}$ and $v'_{0,i}$, respectively. The expression for the piece of spline between knot i and knot $i+1$, or the i-th interval, $\Psi_{0,i}(\xi_i)$ is given as

$$\Psi_{0,i}(\xi_i)=\begin{cases} v_{0,i}\left(1-\frac{3}{l_i^2}\xi_i^2+\frac{2}{l_i^3}\xi_i^3\right)+v_{0,i+1}\left(\frac{3}{l_i^2}\xi_i^2-\frac{2}{l_i^3}\xi_i^3\right) & \\ +v'_{0,i}\left(\xi_i-\frac{2}{l_i}\xi_i^2+\frac{1}{l_i^2}\xi_i^3\right)+v'_{0,i+1}\left(-\frac{1}{l_i}\xi_i^2+\frac{1}{l_i^2}\xi_i^3\right) & \xi_i\in[\eta_i,\eta_{i+1}) \\ 0 & \text{otherwise} \end{cases} \tag{B.1}$$

where $\xi_i = x-\eta_i$ is the local x-coordinate of the i-th interval as shown in Fig. B.3; $l_i=\eta_{i+1}-\eta_i$ is the length of i-th interval. The non-zero expression in Eqn. (B.1) can also be written in the following form

$$\Psi_{0,i}(\xi_i)=\left[1-\frac{3}{l_i^2}\xi_i^2+\frac{2}{l_i^3}\xi_i^3 \quad \xi_i-\frac{2}{l_i}\xi_i^2+\frac{1}{l_i^2}\xi_i^3 \quad \frac{3}{l_i^2}\xi_i^2-\frac{2}{l_i^3}\xi_i^3 \quad -\frac{1}{l_i}\xi_i^2+\frac{1}{l_i^2}\xi_i^3\right]\begin{Bmatrix} v_{0,i} \\ v'_{0,i} \\ v_{0,i+1} \\ v'_{0,i+1}\end{Bmatrix}$$
$$=\begin{bmatrix} N_{i,1}(\xi_i) & N_{i,2}(\xi_i) & N_{i,3}(\xi_i) & N_{i,4}(\xi_i)\end{bmatrix}\begin{Bmatrix} v_{0,i} \\ v'_{0,i} \\ v_{0,i+1} \\ v'_{0,i+1}\end{Bmatrix} \qquad \xi_i\in[\eta_i,\eta_{i+1}) \tag{B.2}$$

And the entire spline can be written in the following form:

$$\Psi_0(x)=\sum_{i\in\{1,2,\ldots,k\}}\Psi_{0,i}(x-\eta_i) \tag{B.3}$$

Suppose that we have a set of n distortion measurement points, $\{(x_j,y_j)|j\in\{1,2,\ldots,n\}\}$, with respect to the same global x-y coordinates in Fig. B.3 (an example of a distortion measurement data point is shown in Fig. B.4) and we decide to fit them using the C^1-spline model, we need to first provide the number of knots $(k+1)$ and the x-coordinates (i.e., $\{\eta_1,\eta_2\ldots,\eta_{k+1}\}$) of each knot as the basic characteristics of the spline. They will determine the flexibility of the spline. Regarding the application in this research, which is curve fitting for the purpose of notional load modeling, usually a 2- or 3-node spline with evenly distributed knots is enough, or the problem would become too big. Also, if too many nodes are used, it would cause overfitting problem as well.

B.2.2 Fitting using Ordinary Least Squares

Assume that we would like to fit a $(k+1)$-node C^1-spline from the given set of n distortion measurements (called observations in statistics), we can use the ordinary least squares (OLS) method from statistics. Despite that $\Psi_0(x)$ is a piecewise function, it is a linear combination of unknown parameters and therefore the OLS is applicable. The regression model for the $(k+1)$-node C^1-spline based on n measurements would be

$$\mathbf{y} = \Psi_0(\mathbf{x}) + \boldsymbol{\varepsilon} \tag{B.4}$$

where $\mathbf{y} = (y_1, y_2, \dots, y_n)^{\mathrm{T}}$ is the vector of observed distortion $y_j, j \in \{1,2, \dots, n\}$ (dependent variable), $\mathbf{x} = (x_1, x_2, \dots, x_n)^{\mathrm{T}}$ is the vector of x-coordinate $x_j, j \in \{1,2, \dots, n\}$ of each observation (independent variable), and $\boldsymbol{\varepsilon} = (\varepsilon_1, \varepsilon_2, \dots, \varepsilon_n)^{\mathrm{T}}$ is the error vector. The unknown parameters in this model are $v_{0,i}$ and $v'_{0,i}$ at each node, which will be obtained through the OLS process. Since we use a $(k+1)$-node spline for the regression model, we would have a total of $2(k+1)$ unknown parameters. We can write these unknown parameters in the following vector form, denoted by $\boldsymbol{\beta}$:

$$\boldsymbol{\beta} = \begin{pmatrix} v_{0,1} \\ v'_{0,1} \\ v_{0,2} \\ v'_{0,2} \\ \vdots \\ v_{0,k+1} \\ v'_{0,k+1} \end{pmatrix} \tag{B.5}$$

To use the ordinary least squares, we need to write the model in the following form:

$$\mathbf{y} = \mathbf{X}\boldsymbol{\beta} + \boldsymbol{\varepsilon} \tag{B.6}$$

where $\mathbf{X}$ is the regressor matrix. Each row in $\mathbf{X}$ corresponds to an observation. In the $(k+1)$-node C^1-spline regression, each row in $\mathbf{X}$ depend on which interval the corresponding observation falls into. We can start from a row in $\mathbf{X}$, for example, row j, which corresponds to distortion measurement data point (x_j, y_j). We assume that x_j falls between knot i and knot $i+1$ (or falls in the i-th interval), as shown in Fig. B.4, i.e., $x_j \in [\eta_i, \eta_{i+1})$. Based on Eqn. (B.2) and Eqn. (B.3) , we can obtain $\Psi_0(x_j)$ as

$$\Psi\left(x_j\right)=\begin{bmatrix}0 & \cdots & 0 & N_{i,1}\left(x_j-\eta_i\right) & N_{i,2}\left(x_j-\eta_i\right) & N_{i,3}\left(x_j-\eta_i\right) & N_{i,4}\left(x_j-\eta_i\right) & 0 & \cdots & 0\end{bmatrix}\begin{Bmatrix}v_{0,1}\\ v'_{0,1}\\ \vdots\\ v_{0,i}\\ v'_{0,i}\\ v_{0,i+1}\\ v'_{0,i+1}\\ \vdots\\ v_{0,k+1}\\ v'_{0,k+1}\end{Bmatrix} \quad \text{(B.7)}$$

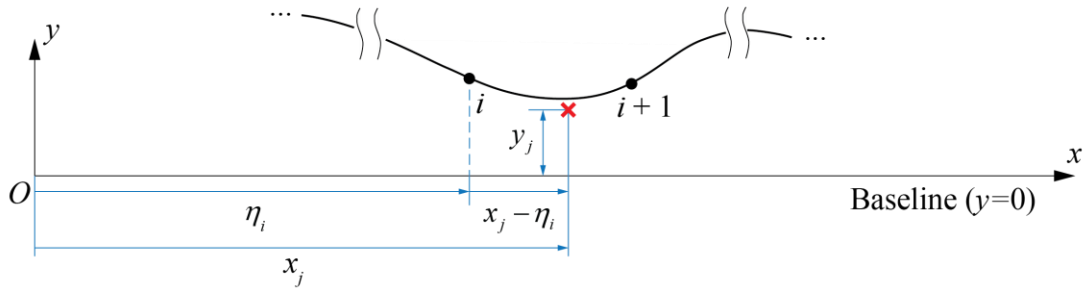

Fig. B.4 Illustration of a distortion measurement data point.

In the row vector, the terms related to the i-th interval are those given in Eqn. (B.2), while the rest terms are all zero. We can write $\Psi_0(x_j)$ in this form for every observation. The only exception happens when x_j equals to the x-coordinate of the last knot, i.e., x_j=η_{k+1}. In this case, we consider this data point falls in the k-th interval because there is no $(k+1)$-th interval. We can give out the general form of the row vector in Eqn. (B.7) for each data point, denoted as $\mathbf{x}_j$:

$$\mathbf{x}_j=\begin{cases}\begin{bmatrix}0_{1\times 2(i-1)} & N_{i,1}\left(x_j-\eta_i\right) & N_{i,2}\left(x_j-\eta_i\right) & N_{i,3}\left(x_j-\eta_i\right) & N_{i,4}\left(x_j-\eta_i\right) & 0_{1\times 2(k-i)}\end{bmatrix} & \forall x_j\in[\eta_i,\eta_{i+1})\wedge(i<k)\\ \begin{bmatrix}0_{1\times 2(k-1)} & N_{k,1}\left(x_j-\eta_k\right) & N_{k,2}\left(x_j-\eta_k\right) & N_{k,3}\left(x_j-\eta_k\right) & N_{k,4}\left(x_j-\eta_k\right)\end{bmatrix} & \forall x_j\in[\eta_k,\eta_{k+1}]\end{cases} \quad \text{(B.8)}$$

where $0_{1\times 2(i-1)}$ represents a $1\times 2(i-1)$ zero row vector. With Eqn. (B.8), we can obtain $\mathbf{x}_j$ for each observation and the regressor matrix $\mathbf{X}$ can be written as

$$\mathbf{X} = \begin{bmatrix} \mathbf{x}_1 \\ \mathbf{x}_2 \\ \vdots \\ \mathbf{x}_n \end{bmatrix} \tag{B.9}$$

Finally, the best estimate of unknown parameters $\boldsymbol{\beta}$ is given by [92]

$$\hat{\boldsymbol{\beta}} = \left(\mathbf{X}^\top \mathbf{X}\right)^{-1} \mathbf{X}^\top \mathbf{y} \tag{B.10}$$

which gives us the fitted translation and rotation values at each knot.

B.2.3 Treatment of Restrained Degrees of Freedom

If a degree of freedom (one of the paremeters in $\boldsymbol{\beta}$) is prescribed in the curve fitting, the terms in $\mathbf{y}$, $\mathbf{x}_j$, and $\boldsymbol{\beta}$ corresponds to or affected by that degree of freedom needs to be modified. For example, we prescribe the rotation at knot i by $v'_{0,i} = \theta$. The first modification would be to remove $v'_{0,i}$ from $\boldsymbol{\beta}$ since it is now a known parameter. The new vector of unknown parameters, $\boldsymbol{\beta}'$, is

$$\boldsymbol{\beta}' = \begin{pmatrix} v_{0,1} \\ v'_{0,1} \\ \vdots \\ v_{0,i} \\ v_{0,i+1} \\ \vdots \\ v_{0,k+1} \\ v'_{0,k+1} \end{pmatrix} \tag{B.11}$$

Then, for any measurement whose corresponding x-coordinate falls in the intervals (one or two, depending on if the restrained degree of freedom is on the ends or not) associated with this degree of freedom (i.e., $x_j \in [\eta_{i-1}, \eta_{i+1})$) , the corresponding rows in the $\mathbf{y}$ vector would become

$$y'_j = \begin{cases} y_j - N_{i-1,4}\theta & \forall x_j \in \left[\eta_{i-1}, \eta_i\right) \\ y_j - N_{i,2}\theta & \forall x_j \in \left[\eta_i, \eta_{i+1}\right) \end{cases} \tag{B.12}$$

Finally, we remove the column corresponding to the restrained degree of freedom from the regressor matrix $\mathbf{X}$ and obtain a new regressor matrix $\mathbf{X_r}$. In this case, we would remove the $2i$-th column which corresponds to $v'_{0,i}$. We can then plug the updated $\mathbf{y}'$, $\mathbf{X_r}$, into Eqn.(B.10) to obtain the best estimate ($\widehat{\boldsymbol{\beta}}'$) for the updated $\boldsymbol{\beta}'$.

B.2.4 Calculate Notional Load From Curve Fitting Result

As discussed previously, the cubic Hermite spline is the deflection shape of a linear beam subject to concentrated force and moments applied at the spline's knot positions. With the fitted spline, the next objective would be to calculate value of the notional loads.

The basic way would be taking derivatives of the spline and derive results with respect to each knot based on beam theory to obtain the notional loads on the knots. Here, we present an alternative way for calculating the notional loads: by taking advantage of the vector $\widehat{\boldsymbol{\beta}}$ and use the matrix-displacement method to calculate the notional loads. From the matrix-displacement method, we know the following equation [93]

$$\mathbf{K}\boldsymbol{\delta} = \mathbf{F} \tag{B.13}$$

where $\mathbf{K}$ is the stiffness matrix of the structure, $\boldsymbol{\delta}$ is the nodal displacement vector, and $\mathbf{F}$ is the vector of force applied on the nodes. We can immediately see that, with a proper stiffness matrix $\mathbf{K}$, we can directly substitute $\boldsymbol{\delta}$ with $\widehat{\boldsymbol{\beta}}$ from the curve fitting result and obtain the force vector $\mathbf{F}$, which would be the notional load sought. The stiffness $\mathbf{K}$ for the notional load model can be easily obtained with a straight horizontal beam bending model with $k+1$ nodes located at $x = \eta_1, \eta_2, \dots, \eta_{k+1}$ (corresponds to knots of the spline). The formation of the stiffness matrix is classic and can be found in [93]. For analytical approaches in this research, it is preferred that the stiffness matrix is kept symbolic during the calculation.

B.3 Curve Fitting Models for Distortions in Stiffened Panels

The local angular distortion in stiffened panels studied in Sec. 2.3.1 can be fitted using a cubic Hermite spline with three knots. However, based on the simple notional load models used for the buckling distortion mode and the cosine angular distortion mode, we can directly write down the expression of the model to be used for curve fitting these two distortion modes. For the buckling distortion mode, the curve fitting model is

$$y \sim \begin{cases} \delta_0 \left[-4\dfrac{x^3}{l^3} + 3\dfrac{x}{l} \right] & 0 < x < \dfrac{l}{2} \\ \delta_0 \left[-4\dfrac{(l-x)^3}{l^3} + 3\dfrac{l-x}{l} \right] & \dfrac{l}{2} \le x \le l \\ 0 & \text{otherwise} \end{cases} \tag{B.14}$$

where δ_0 is the only parameter to be determined. For the cosine angular distortion mode, the model is

$$y \sim \begin{cases} \delta_0 \left[-16\dfrac{x^3}{l^3} + 12\dfrac{x^2}{l^2} \right] & 0 < x < \dfrac{l}{2} \\ \delta_0 \left[-16\dfrac{(l-x)^3}{l^3} + 12\dfrac{(l-x)^2}{l^2} \right] & \dfrac{l}{2} \le x \le l \\ 0 & \text{otherwise} \end{cases} \tag{B.15}$$

where δ_0 is the only parameter to be determined. These two models represents specific subsets of cubic Hermite splines.

Appendix C

Detailed Expression of the Analytical Solutions

C.1 Auxiliary Variables

The following two auxiliary variables, Φ_t and Φ_c, are used to simplify the expression corresponding to tensile axial loading cases and compressive axial loading cases.

$$\begin{aligned}\Phi_t = {} & \lambda_1^2\lambda_2\left(l_1+l_2\right)\sinh\lambda_1 l_1\cosh\lambda_2 l_2+\lambda_1\lambda_2^2\left(l_1+l_2\right)\cosh\lambda_1 l_1\sinh\lambda_2 l_2 \\ & -2\lambda_1\lambda_2\left(\cosh\lambda_1 l_1\cosh\lambda_2 l_2-1\right)-\left(\lambda_1^2+\lambda_2^2\right)\sinh\lambda_1 l_1\sinh\lambda_2 l_2\end{aligned} \tag{C.1}$$

$$\begin{aligned}\Phi_c = {} & \lambda_1^2\lambda_2\left(l_1+l_2\right)\sin\lambda_1 l_1\cos\lambda_2 l_2+\lambda_1\lambda_2^2\left(l_1+l_2\right)\cos\lambda_1 l_1\sin\lambda_2 l_2 \\ & +2\lambda_1\lambda_2\left(\cos\lambda_1 l_1\cos\lambda_2 l_2-1\right)-\left(\lambda_1^2+\lambda_2^2\right)\sin\lambda_1 l_1\sin\lambda_2 l_2\end{aligned} \tag{C.2}$$

where

$$\lambda_i=\sqrt{\frac{|P|}{EI_i}} \tag{C.3}$$

C.2 Axial Misalignment

C.2.1 Coefficients for $P > 0$

$$\begin{aligned}M^{(1)}\left(x_1''\right) &= P\mathrm{e}\left(\phi_{\mathrm{e}}^{(1)}\sinh\lambda_1 x_1''+\psi_{\mathrm{e}}^{(1)}\cosh\lambda_1 x_1''\right) \\ M^{(2)}\left(x_2'\right) &= P\mathrm{e}\left(\phi_{\mathrm{e}}^{(2)}\sinh\lambda_2 x_2'+\psi_{\mathrm{e}}^{(2)}\cosh\lambda_2 x_2'\right)\end{aligned} \tag{C.4}$$

where

$$\begin{aligned}\phi_{\mathrm{e}}^{(1)} = {} & -\frac{1}{\Phi_t}\left\{\lambda_1\lambda_2\sinh\lambda_1 l_1\left(\cosh\lambda_2 l_2-1\right)+\lambda_2^2\left(\cosh\lambda_1 l_1-1\right)\sinh\lambda_2 l_2\right. \\ & \left.-\lambda_1\lambda_2^2\left(l_1+l_2\right)\sinh\lambda_1 l_1\sinh\lambda_2 l_2\right\}\end{aligned} \tag{C.5}$$

$$\psi_{\mathrm{e}}^{(1)} = -\frac{1}{\Phi_{\mathrm{t}}}\left\{\lambda_1\lambda_2^2\left(l_1+l_2\right)\cosh\lambda_1 l_1\sinh\lambda_2 l_2 - \lambda_2^2\sinh\lambda_1 l_1\sinh\lambda_2 l_2 \right.$$
$$\left. -\lambda_1\lambda_2\left(\cosh\lambda_1 l_1+1\right)\left(\cosh\lambda_2 l_2-1\right)\right\} \tag{C.6}$$

$$\phi_{\mathrm{e}}^{(2)} = -\frac{1}{\Phi_{\mathrm{t}}}\left\{-\lambda_1\lambda_2\left(\cosh\lambda_1 l_1-1\right)\sinh\lambda_2 l_2 - \lambda_1^2\sinh\lambda_1 l_1\left(\cosh\lambda_2 l_2-1\right)\right.$$
$$\left. +\lambda_1^2\lambda_2\left(l_1+l_2\right)\sinh\lambda_1 l_1\sinh\lambda_2 l_2\right\} \tag{C.7}$$

$$\psi_{\mathrm{e}}^{(2)} = -\frac{1}{\Phi_{\mathrm{t}}}\left\{-\lambda_1^2\lambda_2\left(l_1+l_2\right)\sinh\lambda_1 l_1\cosh\lambda_2 l_2 + \lambda_1^2\sinh\lambda_1 l_1\sinh\lambda_2 l_2\right.$$
$$\left. +\lambda_1\lambda_2\left(\cosh\lambda_1 l_1-1\right)\left(\cosh\lambda_2 l_2+1\right)\right\} \tag{C.8}$$

C.2.2 Coefficients for $P < 0$

$$M_1\left(x_1''\right) = P\mathrm{e}\left(\gamma_{\mathrm{e}}^{(1)}\sin\lambda_1 x_1'' + \chi_{\mathrm{e}}^{(1)}\cos\lambda_1 x_1''\right)$$
$$M_2\left(x_2'\right) = P\mathrm{e}\left(\gamma_{\mathrm{e}}^{(2)}\sin\lambda_2 x_2' + \chi_{\mathrm{e}}^{(2)}\cos\lambda_2 x_2'\right) \tag{C.9}$$

where

$$\gamma_{\mathrm{e}}^{(1)} = -\frac{1}{\Phi_{\mathrm{c}}}\left\{\lambda_1\lambda_2\sin\lambda_1 l_1\left(\cos\lambda_2 l_2-1\right)+\lambda_2^2\left(\cos\lambda_1 l_1-1\right)\sin\lambda_2 l_2\right.$$
$$\left. +\lambda_1\lambda_2^2\left(l_1+l_2\right)\sin\lambda_1 l_1\sin\lambda_2 l_2\right\} \tag{C.10}$$

$$\chi_{\mathrm{e}}^{(1)} = -\frac{1}{\Phi_{\mathrm{c}}}\left\{\lambda_1\lambda_2^2\left(l_1+l_2\right)\cos\lambda_1 l_1\sin\lambda_2 l_2 - \lambda_2^2\sin\lambda_1 l_1\sin\lambda_2 l_2\right.$$
$$\left. +\lambda_1\lambda_2\left(\cos\lambda_1 l_1+1\right)\left(\cos\lambda_2 l_2-1\right)\right\} \tag{C.11}$$

$$\gamma_{\mathrm{e}}^{(2)} = -\frac{1}{\Phi_{\mathrm{c}}}\left\{-\lambda_1\lambda_2\left(\cos\lambda_1 l_1-1\right)\sin\lambda_2 l_2 - \lambda_1^2\sin\lambda_1 l_1\left(\cos\lambda_2 l_2-1\right)\right.$$
$$\left. -\lambda_1^2\lambda_2\left(l_1+l_2\right)\sin\lambda_1 l_1\sin\lambda_2 l_2\right\} \tag{C.12}$$

$$\chi_{\mathrm{e}}^{(2)} = -\frac{1}{\Phi_{\mathrm{c}}}\left\{-\lambda_1^2\lambda_2\left(l_1+l_2\right)\sin\lambda_1 l_1\cos\lambda_2 l_2 + \lambda_1^2\sin\lambda_1 l_1\sin\lambda_2 l_2\right.$$
$$\left. -\lambda_1\lambda_2\left(\cos\lambda_1 l_1-1\right)\left(\cos\lambda_2 l_2+1\right)\right\} \tag{C.13}$$

C.3 Global Angular Distortion/Angular Misalignment

C.3.1 Coefficients for $P > 0$

$$\begin{aligned} M^{(1)} &= P\alpha_{\mathrm{G}}\left(\phi_{\alpha_{\mathrm{G}}}^{(1)}\sinh\lambda_1 x_1'' + \psi_{\alpha_{\mathrm{G}}}^{(1)}\cosh\lambda_1 x_1''\right) \\ M^{(2)} &= P\alpha_{\mathrm{G}}\left(\phi_{\alpha_{\mathrm{G}}}^{(2)}\sinh\lambda_2 x_2' + \psi_{\alpha_{\mathrm{G}}}^{(2)}\cosh\lambda_2 x_2'\right) \end{aligned} \tag{C.14}$$

where

$$\begin{aligned} \phi_{\alpha_{\mathrm{G}}}^{(1)} = -\frac{1}{\Phi_{\mathrm{t}}}\Big\{&-\lambda_1\lambda_2\left(l_1+l_2\right)\sinh\lambda_1 l_1\cosh\lambda_2 l_2 + \lambda_1\lambda_2 l_1\sinh\lambda_1 l_1 - \lambda_2^2 l_2\sinh\lambda_2 l_2 \\ &+\lambda_1\sinh\lambda_1 l_1\sinh\lambda_2 l_2 + \lambda_2\left(\cosh\lambda_1 l_1+1\right)\left(\cosh\lambda_2 l_2-1\right)\Big\} \end{aligned} \tag{C.15}$$

$$\begin{aligned} \psi_{\alpha_{\mathrm{G}}}^{(1)} = -\frac{1}{\Phi_{\mathrm{t}}}\Big\{&\lambda_1\lambda_2 l_1\cosh\lambda_1 l_1\left(\cosh\lambda_2 l_2-1\right) + \lambda_1\lambda_2 l_2\left(\cosh\lambda_1 l_1-1\right)\cosh\lambda_2 l_2 \\ &-\lambda_2\sinh\lambda_1 l_1\left(\cosh\lambda_2 l_2-1\right) - \lambda_1\left(\cosh\lambda_1 l_1-1\right)\sinh\lambda_2 l_2\Big\} \end{aligned} \tag{C.16}$$

$$\begin{aligned} \phi_{\alpha_{\mathrm{G}}}^{(2)} = -\frac{1}{\Phi_{\mathrm{t}}}\Big\{&-\lambda_1\lambda_2\left(l_1+l_2\right)\cosh\lambda_1 l_1\sinh\lambda_2 l_2 + \lambda_1\lambda_2 l_2\sinh\lambda_2 l_2 - \lambda_1^2 l_1\sinh\lambda_1 l_1 \\ &+\lambda_2\sinh\lambda_1 l_1\sinh\lambda_2 l_2 + \lambda_1\left(\cosh\lambda_1 l_1-1\right)\left(\cosh\lambda_2 l_2+1\right)\Big\} \end{aligned} \tag{C.17}$$

$$\begin{aligned} \psi_{\alpha_{\mathrm{G}}}^{(2)} = -\frac{1}{\Phi_{\mathrm{t}}}\Big\{&\lambda_1\lambda_2 l_1\cosh\lambda_1 l_1\left(\cosh\lambda_2 l_2-1\right) + \lambda_1\lambda_2 l_2\left(\cosh\lambda_1 l_1-1\right)\cosh\lambda_2 l_2 \\ &-\lambda_2\sinh\lambda_1 l_1\left(\cosh\lambda_2 l_2-1\right) - \lambda_1\left(\cosh\lambda_1 l_1-1\right)\sinh\lambda_2 l_2\Big\} \end{aligned} \tag{C.18}$$

C.3.2 Coefficients for $P < 0$

$$\begin{aligned} M_1\left(x_1''\right) &= P\alpha_{\mathrm{G}}\left(\gamma_{\alpha_{\mathrm{G}}}^{(1)}\sin\lambda_1 x_1'' + \chi_{\alpha_{\mathrm{G}}}^{(1)}\cos\lambda_1 x_1''\right) \\ M_2\left(x_2'\right) &= P\alpha_{\mathrm{G}}\left(\gamma_{\alpha_{\mathrm{G}}}^{(2)}\sin\lambda_2 x_2' + \chi_{\alpha_{\mathrm{G}}}^{(2)}\cos\lambda_2 x_2'\right) \end{aligned} \tag{C.19}$$

where

$$\begin{aligned} \gamma_{\alpha_{\mathrm{G}}}^{(1)} = -\frac{1}{\Phi_{\mathrm{c}}}\Big\{&-\lambda_1\lambda_2\left(l_1+l_2\right)\sin\lambda_1 l_1\cos\lambda_2 l_2 + \lambda_1\lambda_2 l_1\sin\lambda_1 l_1 - \lambda_2^2 l_2\sin\lambda_2 l_2 \\ &+\lambda_1\sin\lambda_1 l_1\sin\lambda_2 l_2 - \lambda_2\left(\cos\lambda_1 l_1+1\right)\left(\cos\lambda_2 l_2-1\right)\Big\} \end{aligned} \tag{C.20}$$

$$\chi_{\alpha_G}^{(1)} = -\frac{1}{\Phi_c}\left\{-\lambda_1\lambda_2 l_1 \cos\lambda_1 l_1\left(\cos\lambda_2 l_2 - 1\right) - \lambda_1\lambda_2 l_2\left(\cos\lambda_1 l_1 - 1\right)\cos\lambda_2 l_2 \right. \\ \left. + \lambda_2 \sin\lambda_1 l_1\left(\cos\lambda_2 l_2 - 1\right) + \lambda_1\left(\cos\lambda_1 l_1 - 1\right)\sin\lambda_2 l_2\right\} \tag{C.21}$$

$$\gamma_{\alpha_G}^{(2)} = -\frac{1}{\Phi_c}\left\{-\lambda_1\lambda_2\left(l_1 + l_2\right)\cos\lambda_1 l_1 \sin\lambda_2 l_2 + \lambda_1\lambda_2 l_2 \sin\lambda_2 l_2 - \lambda_1^2 l_1 \sin\lambda_1 l_1 \right. \\ \left. + \lambda_2 \sin\lambda_1 l_1 \sin\lambda_2 l_2 - \lambda_1\left(\cos\lambda_1 l_1 - 1\right)\left(\cos\lambda_2 l_2 + 1\right)\right\} \tag{C.22}$$

$$\chi_{\alpha_G}^{(2)} = -\frac{1}{\Phi_c}\left\{-\lambda_1\lambda_2 l_1 \cos\lambda_1 l_1\left(\cos\lambda_2 l_2 - 1\right) - \lambda_1\lambda_2 l_2\left(\cos\lambda_1 l_1 - 1\right)\cos\lambda_2 l_2 \right. \\ \left. + \lambda_2 \sin\lambda_1 l_1\left(\cos\lambda_2 l_2 - 1\right) + \lambda_1\left(\cos\lambda_1 l_1 - 1\right)\sin\lambda_2 l_2\right\} \tag{C.23}$$

C.4 Local Angular Distortion

C.4.1 Coefficients for $P > 0$

$$
\begin{aligned}
M_1^{(1)}(x_1') &= P\left(\phi_{\theta_{11}'}^{(1)}\sinh\lambda_1 x_1' + \psi_{\theta_{11}'}^{(1)}\cosh\lambda_1 x_1'\right)\theta_{11}' + P\left(\phi_{\theta_{12}'}^{(1)}\sinh\lambda_1 x_1' + \psi_{\theta_{12}'}^{(1)}\cosh\lambda_1 x_1'\right)\theta_{12}' \\
&\quad + P\left(\phi_{\theta_{21}'}^{(1)}\sinh\lambda_1 x_1' + \psi_{\theta_{21}'}^{(1)}\cosh\lambda_1 x_1'\right)\theta_{21}' + P\left(\phi_{\theta_{22}'}^{(1)}\sinh\lambda_1 x_1' + \psi_{\theta_{22}'}^{(1)}\cosh\lambda_1 x_1'\right)\theta_{22}' \\
&\quad - P\left(\zeta_{\theta_{11}'}^{(1)} + \kappa_{\theta_{11}'}^{(1)} x_1'\right)\theta_{11}' - P\left(\zeta_{\theta_{12}'}^{(1)} + \kappa_{\theta_{12}'}^{(1)} x_1'\right)\theta_{12}' \\
M_1^{(2)}(x_2) &= P\left(\phi_{\theta_{11}'}^{(2)}\sinh\lambda_2 x_2 + \psi_{\theta_{11}'}^{(2)}\cosh\lambda_2 x_2\right)\theta_{11}' + P\left(\phi_{\theta_{12}'}^{(2)}\sinh\lambda_2 x_2 + \psi_{\theta_{12}'}^{(2)}\cosh\lambda_2 x_2\right)\theta_{12}' \\
&\quad + P\left(\phi_{\theta_{21}'}^{(2)}\sinh\lambda_2 x_2 + \psi_{\theta_{21}'}^{(2)}\cosh\lambda_2 x_2\right)\theta_{21}' + P\left(\phi_{\theta_{22}'}^{(2)}\sinh\lambda_2 x_2 + \psi_{\theta_{22}'}^{(2)}\cosh\lambda_2 x_2\right)\theta_{22}' \\
&\quad - P\left(\zeta_{\theta_{21}'}^{(2)} + \kappa_{\theta_{21}'}^{(2)} x_2\right)\theta_{21}' - P\left(\zeta_{\theta_{22}'}^{(2)} + \kappa_{\theta_{22}'}^{(2)} x_2\right)\theta_{22}'
\end{aligned}
\tag{C.24}
$$

where

$$
\begin{aligned}
\phi_{\theta_{11}'}^{(1)} &= -\frac{1}{\Phi_t\lambda_1^2 l_1^2}\Big\{2\lambda_1\left[\lambda_2^2 l_1(l_1+l_2)-3\right]\sinh\lambda_1 l_1\sinh\lambda_2 l_2 + 2\lambda_1\lambda_2(2l_1+3l_2)\sinh\lambda_1 l_1\cosh\lambda_2 l_2 - 2\lambda_2^2 l_1\cosh\lambda_1 l_1\sinh\lambda_2 l_2 \\
&\quad -6\lambda_2\cosh\lambda_1 l_1\cosh\lambda_2 l_2 - 4\lambda_1\lambda_2 l_1\sinh\lambda_1 l_1 + \lambda_2^2\left[\lambda_1^2 l_1^2(l_1+l_2)+2l_1+6l_2\right]\sinh\lambda_2 l_2 + \lambda_2\left(\lambda_1^2 l_1^2+6\right)\cosh\lambda_1 l_1 \\
&\quad -\lambda_2\left(\lambda_1^2 l_1^2+6\right)\cosh\lambda_2 l_2 + 6\lambda_2\Big\}
\end{aligned}
\tag{C.25}
$$

$$
\begin{aligned}
\psi_{\theta_{11}'}^{(1)} &= -\frac{1}{\Phi_t\lambda_1^2 l_1^2}\Big\{2\lambda_2^2 l_1\sinh\lambda_1 l_1\sinh\lambda_2 l_2 + 6\lambda_2\sinh\lambda_1 l_1\cosh\lambda_2 l_2 - 2\lambda_1\left[\lambda_2^2 l_1(l_1+l_2)-3\right]\cosh\lambda_1 l_1\sinh\lambda_2 l_2 \\
&\quad -2\lambda_1\lambda_2(2l_1+3l_2)\cosh\lambda_1 l_1\cosh\lambda_2 l_2 - \lambda_2\left(\lambda_1^2 l_1^2+6\right)\sinh\lambda_1 l_1 - \lambda_1\left(\lambda_1^2 l_1^2+6\right)\sinh\lambda_2 l_2 \\
&\quad +4\lambda_1\lambda_2 l_1\cosh\lambda_1 l_1 + \lambda_1\lambda_2\left[\lambda_1^2 l_1^2(l_1+l_2)+2l_1+6l_2\right]\cosh\lambda_2 l_2 - 2\lambda_1\lambda_2 l_1\Big\}
\end{aligned}
\tag{C.26}
$$

$$\phi_{\theta'_{12}}^{(1)} = -\frac{1}{\Phi_t \lambda_1^2 l_1^2}\Big\{-\lambda_1\left[\lambda_1^2 l_1^2 - 4\lambda_2^2 l_1\left(l_1+l_2\right)+6\right]\sinh\lambda_1 l_1 \sinh\lambda_2 l_2 + \lambda_1\lambda_2\left[\lambda_1^2 l_1^2\left(l_1+l_2\right)+2l_1+6l_2\right]\sinh\lambda_1 l_1\cosh\lambda_2 l_2$$
$$-4\lambda_2^2 l_1\cosh\lambda_1 l_1\sinh\lambda_2 l_2 - \lambda_2\left(\lambda_1^2 l_1^2+6\right)\cosh\lambda_1 l_1\cosh\lambda_2 l_2 - 2\lambda_1\lambda_2 l_1\sinh\lambda_1 l_1 \quad \text{(C.27)}$$
$$+2\lambda_2^2\left(2l_1+3l_2\right)\sinh\lambda_2 l_2 + 6\lambda_2\cosh\lambda_1 l_1 - 6\lambda_2\cosh\lambda_2 l_2 + \lambda_2\left(\lambda_1^2 l_1^2+6\right)\Big\}$$

$$\psi_{\theta'_{12}}^{(1)} = -\frac{1}{\Phi_t \lambda_1^2 l_1^2}\Big\{4\lambda_2^2 l_1\sinh\lambda_1 l_1\sinh\lambda_2 l_2 + \lambda_2\left(\lambda_1^2 l_1^2+6\right)\sinh\lambda_1 l_1\cosh\lambda_2 l_2 + \lambda_1\left[\lambda_1^2 l_1^2 - 4\lambda_2^2 l_1\left(l_1+l_2\right)+6\right]\cosh\lambda_1 l_1\sinh\lambda_2 l_2$$
$$-\lambda_1\lambda_2\left[\lambda_1^2 l_1^2\left(l_1+l_2\right)+2l_1+6l_2\right]\cosh\lambda_1 l_1\cosh\lambda_2 l_2 - 6\lambda_2\sinh\lambda_1 l_1 - 6\lambda_1\sinh\lambda_2 l_2 \quad \text{(C.28)}$$
$$+2\lambda_1\lambda_2 l_1\cosh\lambda_1 l_1 + 2\lambda_1\lambda_2\left(2l_1+3l_2\right)\cosh\lambda_2 l_2 - 4\lambda_1\lambda_2 l_1\Big\}$$

$$\phi_{\theta'_{21}}^{(1)} = -\frac{1}{\Phi_t \lambda_2^2 l_2^2}\Big\{\lambda_1\left[4\lambda_2^2 l_2\left(l_1+l_2\right)+\lambda_2^2 l_2^2+6\right]\sinh\lambda_1 l_1\sinh\lambda_2 l_2 - \lambda_1\lambda_2\left[\lambda_2^2 l_2^2\left(l_1+l_2\right)+6l_1+10l_2\right]\sinh\lambda_1 l_1\cosh\lambda_2 l_2$$
$$-4\lambda_2^2 l_2\cosh\lambda_1 l_1\sinh\lambda_2 l_2 + \lambda_2\left(\lambda_2^2 l_2^2+6\right)\cosh\lambda_1 l_1\cosh\lambda_2 l_2 + 2\lambda_1\lambda_2\left(3l_1+2l_2\right)\sinh\lambda_1 l_1 \quad \text{(C.29)}$$
$$-2\lambda_2^2 l_2\sinh\lambda_2 l_2 - 6\lambda_2\cosh\lambda_1 l_1 + 6\lambda_2\cosh\lambda_2 l_2 - \lambda_2\left(\lambda_2^2 l_2^2+6\right)\Big\}$$

$$\psi_{\theta'_{21}}^{(1)} = -\frac{1}{\Phi_t \lambda_2^2 l_2^2}\Big\{4\lambda_2^2 l_2\sinh\lambda_1 l_1\sinh\lambda_2 l_2 - \lambda_2\left(\lambda_2^2 l_2^2+6\right)\sinh\lambda_1 l_1\cosh\lambda_2 l_2 - \lambda_1\left[4\lambda_2^2 l_2\left(l_1+l_2\right)+\lambda_2^2 l_2^2+6\right]\cosh\lambda_1 l_1\sinh\lambda_2 l_2$$
$$+\lambda_1\lambda_2\left[\lambda_2^2 l_2^2\left(l_1+l_2\right)+6l_1+10l_2\right]\cosh\lambda_1 l_1\cosh\lambda_2 l_2 + 6\lambda_2\sinh\lambda_1 l_1 + 6\lambda_1\sinh\lambda_2 l_2 \quad \text{(C.30)}$$
$$-2\lambda_1\lambda_2\left(3l_1+2l_2\right)\cosh\lambda_1 l_1 - 2\lambda_1\lambda_2 l_2\cosh\lambda_2 l_2 - 4\lambda_1\lambda_2 l_2\Big\}$$

$$\phi_{\theta'_{22}}^{(1)} = -\frac{1}{\Phi_t \lambda_2^2 l_2^2}\Big\{2\lambda_1\left[\lambda_2^2 l_2\left(l_1+l_2\right)+3\right]\sinh\lambda_1 l_1\sinh\lambda_2 l_2 - 2\lambda_1\lambda_2\left(3l_1+4l_2\right)\sinh\lambda_1 l_1\cosh\lambda_2 l_2 - 2\lambda_2^2 l_2\cosh\lambda_1 l_1\sinh\lambda_2 l_2$$
$$+6\lambda_2\cosh\lambda_1 l_1\cosh\lambda_2 l_2 + \lambda_1\lambda_2\left[\lambda_2^2 l_2^2\left(l_1+l_2\right)+6l_1+2l_2\right]\sinh\lambda_1 l_1 - 4\lambda_2^2 l_2\sinh\lambda_2 l_2 \quad \text{(C.31)}$$
$$-\lambda_2\left(\lambda_2^2 l_2^2+6\right)\cosh\lambda_1 l_1 + \lambda_2\left(\lambda_2^2 l_2^2+6\right)\cosh\lambda_2 l_2 - 6\lambda_2\Big\}$$

$$\psi^{(1)}_{\theta'_{22}} = -\frac{1}{\Phi_t \lambda_2^2 l_2^2}\Big\{2\lambda_2^2 l_2 \sinh\lambda_1 l_1 \sinh\lambda_2 l_2 - 6\lambda_2 \sinh\lambda_1 l_1 \cosh\lambda_2 l_2 - 2\lambda_1\Big[\lambda_2^2 l_2\left(l_1+l_2\right)+3\Big]\cosh\lambda_1 l_1 \sinh\lambda_2 l_2$$
$$+2\lambda_1\lambda_2\left(3l_1+4l_2\right)\cosh\lambda_1 l_1 \cosh\lambda_2 l_2 + \lambda_2\left(\lambda_2^2 l_2^2+6\right)\sinh\lambda_1 l_1 + \lambda_1\left(\lambda_2^2 l_2^2+6\right)\sinh\lambda_2 l_2 \tag{C.32}$$
$$-\lambda_1\lambda_2\Big[\lambda_2^2 l_2^2\left(l_1+l_2\right)+6l_1+2l_2\Big]\cosh\lambda_1 l_1 - 4\lambda_1\lambda_2 l_2 \cosh\lambda_2 l_2 - 2\lambda_1\lambda_2 l_2\Big\}$$

$$\phi^{(2)}_{\theta'_{11}} = -\frac{1}{\Phi_t \lambda_1^2 l_1^2}\Big\{-2\lambda_2\Big[\lambda_1^2 l_1\left(l_1+l_2\right)+3\Big]\sinh\lambda_1 l_1 \sinh\lambda_2 l_2 + 2\lambda_1^2 l_1 \sinh\lambda_1 l_1 \cosh\lambda_2 l_2 + 2\lambda_1\lambda_2\left(4l_1+3l_2\right)\cosh\lambda_1 l_1 \sinh\lambda_2 l_2$$
$$-6\lambda_1 \cosh\lambda_1 l_1 \cosh\lambda_2 l_2 + 4\lambda_1^2 l_1 \sinh\lambda_1 l_1 - \lambda_1\lambda_2\Big[\lambda_1^2 l_1^2\left(l_1+l_2\right)+2l_1+6l_2\Big]\sinh\lambda_2 l_2 \tag{C.33}$$
$$-\lambda_1\left(\lambda_1^2 l_1^2+6\right)\cosh\lambda_1 l_1 + \lambda_1\left(\lambda_1^2 l_1^2+6\right)\cosh\lambda_2 l_2 + 6\lambda_1\Big\}$$

$$\psi^{(2)}_{\theta'_{11}} = -\frac{1}{\Phi_t \lambda_1^2 l_1^2}\Big\{-2\lambda_1^2 l_1 \sinh\lambda_1 l_1 \sinh\lambda_2 l_2 + 2\lambda_2\Big[\lambda_1^2 l_1\left(l_1+l_2\right)+3\Big]\sinh\lambda_1 l_1 \cosh\lambda_2 l_2 + 6\lambda_1 \cosh\lambda_1 l_1 \sinh\lambda_2 l_2$$
$$-2\lambda_1\lambda_2\left(4l_1+3l_2\right)\cosh\lambda_1 l_1 \cosh\lambda_2 l_2 - \lambda_2\left(\lambda_1^2 l_1^2+6\right)\sinh\lambda_1 l_1 - \lambda_1\left(\lambda_1^2 l_1^2+6\right)\sinh\lambda_2 l_2 \tag{C.34}$$
$$+4\lambda_1\lambda_2 l_1 \cosh\lambda_1 l_1 + \lambda_1\lambda_2\Big[\lambda_1^2 l_1^2\left(l_1+l_2\right)+2l_1+6l_2\Big]\cosh\lambda_2 l_2 + 2\lambda_1\lambda_2 l_1\Big\}$$

$$\phi^{(2)}_{\theta'_{12}} = -\frac{1}{\Phi_t \lambda_1^2 l_1^2}\Big\{-\lambda_2\Big[\lambda_1^2 l_1^2 + 4\lambda_1^2 l_1\left(l_1+l_2\right)+6\Big]\sinh\lambda_1 l_1 \sinh\lambda_2 l_2 + 4\lambda_1^2 l_1 \sinh\lambda_1 l_1 \cosh\lambda_2 l_2$$
$$+\lambda_1\lambda_2\Big[\lambda_1^2 l_1^2\left(l_1+l_2\right)+10l_1+6l_2\Big]\cosh\lambda_1 l_1 \sinh\lambda_2 l_2 - \lambda_1\left(\lambda_1^2 l_1^2+6\right)\cosh\lambda_1 l_1 \cosh\lambda_2 l_2 + 2\lambda_1^2 l_1 \sinh\lambda_1 l_1 \tag{C.35}$$
$$-2\lambda_1\lambda_2\left(2l_1+3l_2\right)\sinh\lambda_2 l_2 - 6\lambda_1 \cosh\lambda_1 l_1 + 6\lambda_1 \cosh\lambda_2 l_2 + \lambda_1\left(\lambda_1^2 l_1^2+6\right)\Big\}$$

$$\psi^{(2)}_{\theta'_{12}} = -\frac{1}{\Phi_t \lambda_1^2 l_1^2}\Big\{-4\lambda_1^2 l_1 \sinh\lambda_1 l_1 \sinh\lambda_2 l_2 + \lambda_2\Big[\lambda_1^2 l_1^2 + 4\lambda_1^2 l_1\left(l_1+l_2\right)+6\Big]\sinh\lambda_1 l_1 \cosh\lambda_2 l_2 + \lambda_1\left(\lambda_1^2 l_1^2+6\right)\cosh\lambda_1 l_1 \sinh\lambda_2 l_2$$
$$-\lambda_1\lambda_2\Big[\lambda_1^2 l_1^2\left(l_1+l_2\right)+10l_1+6l_2\Big]\cosh\lambda_1 l_1 \cosh\lambda_2 l_2 - 6\lambda_2 \sinh\lambda_1 l_1 - 6\lambda_1 \sinh\lambda_2 l_2 + 2\lambda_1\lambda_2 l_1 \cosh\lambda_1 l_1 \tag{C.36}$$
$$+2\lambda_1\lambda_2\left(2l_1+3l_2\right)\cosh\lambda_2 l_2 + 4\lambda_1\lambda_2 l_1\Big\}$$

$$\phi_{\theta'_{21}}^{(2)} = -\frac{1}{\Phi_t \lambda_2^2 l_2^2}\Big\{\lambda_2\left[-4\lambda_1^2 l_2\left(l_1+l_2\right)+\lambda_2^2 l_2^2+6\right]\sinh\lambda_1 l_1\sinh\lambda_2 l_2+4\lambda_1^2 l_2\sinh\lambda_1 l_1\cosh\lambda_2 l_2$$
$$-\lambda_1\lambda_2\left[\lambda_2^2 l_2^2\left(l_1+l_2\right)+6l_1+2l_2\right]\cosh\lambda_1 l_1\sinh\lambda_2 l_2+\lambda_1\left(\lambda_2^2 l_2^2+6\right)\cosh\lambda_1 l_1\cosh\lambda_2 l_2 \quad \text{(C.37)}$$
$$-2\lambda_1^2\left(3l_1+2l_2\right)\sinh\lambda_1 l_1+2\lambda_1\lambda_2 l_2\sinh\lambda_2 l_2+6\lambda_1\cosh\lambda_1 l_1-6\lambda_1\cosh\lambda_2 l_2-\lambda_1\left(\lambda_2^2 l_2^2+6\right)\Big\}$$

$$\psi_{\theta'_{21}}^{(2)} = -\frac{1}{\Phi_t \lambda_2^2 l_2^2}\Big\{-4\lambda_1^2 l_2\sinh\lambda_1 l_1\sinh\lambda_2 l_2-\lambda_2\left[-4\lambda_1^2 l_2\left(l_1+l_2\right)+\lambda_2^2 l_2^2+6\right]\sinh\lambda_1 l_1\cosh\lambda_2 l_2-\lambda_1\left(\lambda_2^2 l_2^2+6\right)\cosh\lambda_1 l_1\sinh\lambda_2 l_2$$
$$+\lambda_1\lambda_2\left[\lambda_2^2 l_2^2\left(l_1+l_2\right)+6l_1+2l_2\right]\cosh\lambda_1 l_1\cosh\lambda_2 l_2+6\lambda_2\sinh\lambda_1 l_1+6\lambda_1\sinh\lambda_2 l_2-2\lambda_1\lambda_2\left(3l_1+2l_2\right)\cosh\lambda_1 l_1 \quad \text{(C.38)}$$
$$-2\lambda_1\lambda_2 l_2\cosh\lambda_2 l_2+4\lambda_1\lambda_2 l_2\Big\}$$

$$\phi_{\theta'_{22}}^{(2)} = -\frac{1}{\Phi_t \lambda_2^2 l_2^2}\Big\{2\lambda_2\left[-\lambda_1^2 l_2\left(l_1+l_2\right)+3\right]\sinh\lambda_1 l_1\sinh\lambda_2 l_2+2\lambda_1^2 l_2\sinh\lambda_1 l_1\cosh\lambda_2 l_2-2\lambda_1\lambda_2\left(3l_1+2l_2\right)\cosh\lambda_1 l_1\sinh\lambda_2 l_2$$
$$+6\lambda_1\cosh\lambda_1 l_1\cosh\lambda_2 l_2-\lambda_1^2\left[\lambda_2^2 l_2^2\left(l_1+l_2\right)+6l_1+2l_2\right]\sinh\lambda_1 l_1+4\lambda_1\lambda_2 l_2\sinh\lambda_2 l_2 \quad \text{(C.39)}$$
$$+\lambda_1\left(\lambda_2^2 l_2^2+6\right)\cosh\lambda_1 l_1-\lambda_1\left(\lambda_2^2 l_2^2+6\right)\cosh\lambda_2 l_2-6\lambda_1\Big\}$$

$$\psi_{\theta'_{22}}^{(2)} = -\frac{1}{\Phi_t \lambda_2^2 l_2^2}\Big\{-2\lambda_1^2 l_2\sinh\lambda_1 l_1\sinh\lambda_2 l_2+2\lambda_2\left[\lambda_1^2 l_2\left(l_1+l_2\right)-3\right]\sinh\lambda_1 l_1\cosh\lambda_2 l_2-6\lambda_1\cosh\lambda_1 l_1\sinh\lambda_2 l_2$$
$$+2\lambda_1\lambda_2\left(3l_1+2l_2\right)\cosh\lambda_1 l_1\cosh\lambda_2 l_2+\lambda_2\left(\lambda_2^2 l_2^2+6\right)\sinh\lambda_1 l_1+\lambda_1\left(\lambda_2^2 l_2^2+6\right)\sinh\lambda_2 l_2 \quad \text{(C.40)}$$
$$-\lambda_1\lambda_2\left[\lambda_2^2 l_2^2\left(l_1+l_2\right)+6l_1+2l_2\right]\cosh\lambda_1 l_1-4\lambda_1\lambda_2 l_2\cosh\lambda_2 l_2+2\lambda_1\lambda_2 l_2\Big\}$$

By taking advantage of

$$\lambda_i^2 = \frac{|P|}{EI_i} \quad \text{(C.41)}$$

we can obtain the following coefficients based on Eqn. (4.9)

$$\zeta_{\theta'_{11}}^{(1)} = \frac{2}{\lambda_1^2 l_1} \tag{C.42}$$

$$\zeta_{\theta'_{12}}^{(1)} = \frac{4}{\lambda_1^2 l_1} \tag{C.43}$$

$$\zeta_{\theta'_{21}}^{(2)} = -\frac{4}{\lambda_2^2 l_2} \tag{C.44}$$

$$\zeta_{\theta'_{22}}^{(2)} = -\frac{2}{\lambda_2^2 l_2} \tag{C.45}$$

$$\boldsymbol{\kappa}_{\theta'_{11}}^{(1)} = \boldsymbol{\kappa}_{\theta'_{12}}^{(1)} = -\frac{6}{\lambda_1^2 l_1^2} \tag{C.46}$$

$$\boldsymbol{\kappa}_{\theta'_{21}}^{(2)} = \boldsymbol{\kappa}_{\theta'_{22}}^{(2)} = \frac{6}{\lambda_2^2 l_2^2} \tag{C.47}$$

C.4.2 Coefficients for $P < 0$

$$
\begin{aligned}
M_1^{(1)}(x_1') &= P\left(\gamma_{\theta_{11}'}^{(1)} \sin\lambda_1 x_1' + \chi_{\theta_{11}'}^{(1)} \cos\lambda_1 x_1'\right)\theta_{11}' + P\left(\gamma_{\theta_{12}'}^{(1)} \sin\lambda_1 x_1' + \chi_{\theta_{12}'}^{(1)} \cos\lambda_1 x_1'\right)\theta_{12}' \\
&\quad + P\left(\gamma_{\theta_{21}'}^{(1)} \sin\lambda_1 x_1' + \chi_{\theta_{21}'}^{(1)} \cos\lambda_1 x_1'\right)\theta_{21}' + P\left(\gamma_{\theta_{22}'}^{(1)} \sin\lambda_1 x_1' + \chi_{\theta_{22}'}^{(1)} \cos\lambda_1 x_1'\right)\theta_{22}' \\
&\quad - P\left(\upsilon_{\theta_{11}'}^{(1)} + \mu_{\theta_{11}'}^{(1)} x_1'\right)\theta_{11}' - P\left(\upsilon_{\theta_{12}'}^{(1)} + \mu_{\theta_{12}'}^{(1)} x_1'\right)\theta_{12}' \\
M_1^{(2)}(x_2) &= P\left(\gamma_{\theta_{11}'}^{(2)} \sin\lambda_2 x_2 + \chi_{\theta_{11}'}^{(2)} \cos\lambda_2 x_2\right)\theta_{11}' + P\left(\gamma_{\theta_{12}'}^{(2)} \sin\lambda_2 x_2 + \chi_{\theta_{12}'}^{(2)} \cos\lambda_2 x_2\right)\theta_{12}' \\
&\quad + P\left(\gamma_{\theta_{21}'}^{(2)} \sin\lambda_2 x_2 + \chi_{\theta_{21}'}^{(2)} \cos\lambda_2 x_2\right)\theta_{21}' + P\left(\gamma_{\theta_{22}'}^{(2)} \sin\lambda_2 x_2 + \chi_{\theta_{22}'}^{(2)} \cos\lambda_2 x_2\right)\theta_{22}' \\
&\quad - P\left(\upsilon_{\theta_{21}'}^{(2)} + \mu_{\theta_{21}'}^{(2)} x_2\right)\theta_{21}' - P\left(\upsilon_{\theta_{22}'}^{(2)} + \mu_{\theta_{22}'}^{(2)} x_2\right)\theta_{22}'
\end{aligned}
\tag{C.48}
$$

where

$$
\begin{aligned}
\gamma_{\theta_{11}'}^{(1)} = -\frac{1}{\Phi_c \lambda_1^2 l_1^2}\Big\{ & 2\lambda_1\left[\lambda_2^2 l_1\left(l_1+l_2\right)+3\right]\sin\lambda_2 l_2 \sin\lambda_1 l_1 - 2\lambda_1\lambda_2\left(2l_1+3l_2\right)\sin\lambda_1 l_1 \cos\lambda_2 l_2 + 2\lambda_2^2 l_1 \cos\lambda_1 l_1 \sin\lambda_2 l_2 \\
& -6\lambda_2 \cos\lambda_2 l_2 \cos\lambda_1 l_1 + 4\lambda_1\lambda_2 l_1 \sin\lambda_1 l_1 + \lambda_2^2\left[\lambda_1^2 l_1^2\left(l_1+l_2\right)-2l_1-6l_2\right]\sin\lambda_2 l_2 - \lambda_2\left(\lambda_1^2 l_1^2-6\right)\cos\lambda_1 l_1 \\
& +\lambda_2\left(\lambda_1^2 l_1^2-6\right)\cos\lambda_2 l_2 + 6\lambda_2\Big\}
\end{aligned}
\tag{C.49}
$$

$$
\begin{aligned}
\chi_{\theta_{11}'}^{(1)} = -\frac{1}{\Phi_c \lambda_1^2 l_1^2}\Big\{ & -2\lambda_2^2 l_1 \sin\lambda_1 l_1 \sin\lambda_2 l_2 + 6\lambda_2 \sin\lambda_1 l_1 \cos\lambda_2 l_2 + 2\lambda_1\left[\lambda_2^2 l_1\left(l_1+l_2\right)+3\right]\cos\lambda_1 l_1 \sin\lambda_2 l_2 \\
& -2\lambda_1\lambda_2\left(2l_1+3l_2\right)\cos\lambda_1 l_1 \cos\lambda_2 l_2 + \lambda_2\left(\lambda_1^2 l_1^2-6\right)\sin\lambda_1 l_1 + \lambda_1\left(\lambda_1^2 l_1^2-6\right)\sin\lambda_2 l_2 \\
& +4\lambda_1\lambda_2 l_1 \cos\lambda_1 l_1 - \lambda_1\lambda_2\left[\lambda_1^2 l_1^2\left(l_1+l_2\right)-2l_1-6l_2\right]\cos\lambda_2 l_2 - 2\lambda_1\lambda_2 l_1\Big\}
\end{aligned}
\tag{C.50}
$$

$$\gamma_{\theta'_{12}}^{(1)} = -\frac{1}{\Phi_c \lambda_1^2 l_1^2}\Big\{-\lambda_1\left[\lambda_1^2 l_1^2 - 4\lambda_2^2 l_1\left(l_1+l_2\right)-6\right]\sin\lambda_1 l_1 \sin\lambda_2 l_2 + \lambda_1\lambda_2\left[\lambda_1^2 l_1^2\left(l_1+l_2\right)-2l_1-6l_2\right]\sin\lambda_1 l_1\cos\lambda_2 l_2$$
$$+4\lambda_2^2 l_1\cos\lambda_1 l_1\sin\lambda_2 l_2 + \lambda_2\left(\lambda_1^2 l_1^2-6\right)\cos\lambda_1 l_1\cos\lambda_2 l_2 + 2\lambda_1\lambda_2 l_1\sin\lambda_1 l_1 \quad \text{(C.51)}$$
$$-2\lambda_2^2\left(2l_1+3l_2\right)\sin\lambda_2 l_2 + 6\lambda_2\cos\lambda_1 l_1 - 6\lambda_2\cos\lambda_2 l_2 - \lambda_2\left(\lambda_1^2 l_1^2-6\right)\Big\}$$

$$\chi_{\theta'_{12}}^{(1)} = -\frac{1}{\Phi_c \lambda_1^2 l_1^2}\Big\{-4\lambda_2^2 l_1\sin\lambda_2 l_2\sin\lambda_1 l_1 - \lambda_2\left(\lambda_1^2 l_1^2-6\right)\sin\lambda_1 l_1\cos\lambda_2 l_2 - \lambda_1\left[\lambda_1^2 l_1^2 - 4\lambda_2^2 l_1\left(l_1+l_2\right)-6\right]\cos\lambda_1 l_1\sin\lambda_2 l_2$$
$$+\lambda_1\lambda_2\left[\lambda_1^2 l_1^2\left(l_1+l_2\right)-2l_1-6l_2\right]\cos\lambda_1 l_1\cos\lambda_2 l_2 - 6\lambda_2\sin\lambda_1 l_1 - 6\lambda_1\sin\lambda_2 l_2 \quad \text{(C.52)}$$
$$+2\lambda_1\lambda_2 l_1\cos\lambda_1 l_1 + 2\lambda_1\lambda_2\left(2l_1+3l_2\right)\cos\lambda_2 l_2 - 4\lambda_1\lambda_2 l_1\Big\}$$

$$\gamma_{\theta'_{21}}^{(1)} = -\frac{1}{\Phi_c \lambda_2^2 l_2^2}\Big\{\lambda_1\left[4\lambda_2^2 l_2\left(l_1+l_2\right)+\lambda_2^2 l_2^2-6\right]\sin\lambda_1 l_1\sin\lambda_2 l_2 - \lambda_1\lambda_2\left[\lambda_2^2 l_2^2\left(l_1+l_2\right)-6l_1-10l_2\right]\sin\lambda_1 l_1\cos\lambda_2 l_2$$
$$+4\lambda_2^2 l_2\cos\lambda_1 l_1\sin\lambda_2 l_2 - \lambda_2\left(\lambda_2^2 l_2^2-6\right)\cos\lambda_2 l_2\cos\lambda_1 l_1 - 2\lambda_1\lambda_2\left(3l_1+2l_2\right)\sin\lambda_1 l_1 \quad \text{(C.53)}$$
$$+2\lambda_2^2 l_2\sin\lambda_2 l_2 - 6\lambda_2\cos\lambda_1 l_1 + 6\lambda_2\cos\lambda_2 l_2 + \lambda_2\left(\lambda_2^2 l_2^2-6\right)\Big\}$$

$$\chi_{\theta'_{21}}^{(1)} = -\frac{1}{\Phi_c \lambda_2^2 l_2^2}\Big\{-4\lambda_2^2 l_2\sin\lambda_1 l_1\sin\lambda_2 l_2 + \lambda_2\left(\lambda_2^2 l_2^2-6\right)\sin\lambda_1 l_1\cos\lambda_2 l_2 + \lambda_1\left[4\lambda_2^2 l_2\left(l_1+l_2\right)+\lambda_2^2 l_2^2-6\right]\cos\lambda_1 l_1\sin\lambda_2 l_2$$
$$-\lambda_1\lambda_2\left[\lambda_2^2 l_2^2\left(l_1+l_2\right)-6l_1-10l_2\right]\cos\lambda_1 l_1\cos\lambda_2 l_2 + 6\lambda_2\sin\lambda_1 l_1 + 6\lambda_1\sin\lambda_2 l_2 \quad \text{(C.54)}$$
$$-2\lambda_1\lambda_2\left(3l_1+l_2\right)\cos\lambda_1 l_1 - 2\lambda_1\lambda_2 l_2\cos\lambda_2 l_2 - 4\lambda_1\lambda_2 l_2\Big\}$$

$$\gamma_{\theta'_{22}}^{(1)} = -\frac{1}{\Phi_c \lambda_2^2 l_2^2}\Big\{2\lambda_1\left[\lambda_2^2 l_2\left(l_1+l_2\right)-3\right]\sin\lambda_2 l_2\sin\lambda_1 l_1 + 2\lambda_1\lambda_2\left(3l_1+4l_2\right)\sin\lambda_1 l_1\cos\lambda_2 l_2 + 2\lambda_2^2 l_2\cos\lambda_1 l_1\sin\lambda_2 l_2$$
$$+6\lambda_2\cos\lambda_1 l_1\cos\lambda_2 l_2 + \lambda_1\lambda_2\left[\lambda_2^2 l_2^2\left(l_1+l_2\right)-6l_1-2l_2\right]\sin\lambda_1 l_1 + 4\lambda_2^2 l_2\sin\lambda_2 l_2 \quad \text{(C.55)}$$
$$+\lambda_2\left(\lambda_2^2 l_2^2-6\right)\cos\lambda_1 l_1 - \lambda_2\left(\lambda_2^2 l_2^2-6\right)\cos\lambda_2 l_2 - 6\lambda_2\Big\}$$

$$\chi^{(1)}_{\theta'_{22}} = -\frac{1}{\Phi_c \lambda_2^2 l_2^2}\Big\{-2\lambda_2^2 l_2 \sin\lambda_2 l_2 \sin\lambda_1 l_1 - 6\lambda_2 \sin\lambda_1 l_1 \cos\lambda_2 l_2 + 2\lambda_1\left[\lambda_2^2 l_2\left(l_1+l_2\right)-3\right]\cos\lambda_1 l_1 \sin\lambda_2 l_2$$
$$+2\lambda_1\lambda_2\left(3l_1+4l_2\right)\cos\lambda_1 l_1 \cos\lambda_2 l_2 - \lambda_2\left(\lambda_2^2 l_2^2-6\right)\sin\lambda_1 l_1 - \lambda_1\left(\lambda_2^2 l_2^2-6\right)\sin\lambda_2 l_2 \tag{C.56}$$
$$+\lambda_1\lambda_2\left[\lambda_2^2 l_2^2\left(l_1+l_2\right)-6l_1-2l_2\right]\cos\lambda_1 l_1 - 4\lambda_1\lambda_2 l_2 \cos\lambda_2 l_2 - 2\lambda_1\lambda_2 l_2\Big\}$$

$$\gamma^{(2)}_{\theta'_{11}} = -\frac{1}{\Phi_c \lambda_1^2 l_1^2}\Big\{-2\lambda_2\left[\lambda_1^2 l_1\left(l_1+l_2\right)-3\right]\sin\lambda_2 l_2 \sin\lambda_1 l_1 - 2\lambda_1^2 l_1 \sin\lambda_1 l_1 \cos\lambda_2 l_2 - 2\lambda_1\lambda_2\left(4l_1+3l_2\right)\cos\lambda_1 l_1 \sin\lambda_2 l_2$$
$$-6\lambda_1 \cos\lambda_1 l_1 \cos\lambda_2 l_2 - 4\lambda_1^2 l_1 \sin\lambda_1 l_1 - \lambda_1\lambda_2\left[\lambda_1^2 l_1^2\left(l_1+l_2\right)-2l_1-6l_2\right]\sin\lambda_2 l_2 \tag{C.57}$$
$$+\lambda_1\left(\lambda_1^2 l_1^2-6\right)\cos\lambda_1 l_1 - \lambda_1\left(\lambda_1^2 l_1^2-6\right)\cos\lambda_2 l_2 + 6\lambda_1\Big\}$$

$$\chi^{(2)}_{\theta'_{11}} = -\frac{1}{\Phi_c \lambda_1^2 l_1^2}\Big\{2\lambda_1^2 l_1 \sin\lambda_2 l_2 \sin\lambda_1 l_1 - 2\lambda_2\left[\lambda_1^2 l_1\left(l_1+l_2\right)-3\right]\cos\lambda_2 l_2 \sin\lambda_1 l_1 + 6\lambda_1 \cos\lambda_1 l_1 \sin\lambda_2 l_2$$
$$-2\lambda_1\lambda_2\left(4l_1+3l_2\right)\cos\lambda_1 l_1 \cos\lambda_2 l_2 + \lambda_2\left(\lambda_1^2 l_1^2-6\right)\sin\lambda_1 l_1 + \lambda_1\left(\lambda_1^2 l_1^2-6\right)\sin\lambda_2 l_2 \tag{C.58}$$
$$+4\lambda_1\lambda_2 l_1 \cos\lambda_1 l_1 - \lambda_1\lambda_2\left[\lambda_1^2 l_1^2\left(l_1+l_2\right)-2l_1-6l_2\right]\cos\lambda_2 l_2 + 2\lambda_1\lambda_2 l_1\Big\}$$

$$\gamma^{(2)}_{\theta'_{12}} = -\frac{1}{\Phi_c \lambda_1^2 l_1^2}\Big\{-\lambda_2\left[\lambda_1^2 l_1^2 + 4\lambda_1^2 l_1\left(l_1+l_2\right)-6\right]\sin\lambda_1 l_1 \sin\lambda_2 l_2 - 4\lambda_1^2 l_1 \sin\lambda_1 l_1 \cos\lambda_2 l_2$$
$$+\lambda_1\lambda_2\left[\lambda_1^2 l_1^2\left(l_1+l_2\right)-10l_1-6l_2\right]\cos\lambda_1 l_1 \sin\lambda_2 l_2 + \lambda_1\left(\lambda_1^2 l_1^2-6\right)\cos\lambda_1 l_1 \cos\lambda_2 l_2 - 2\lambda_1^2 l_1 \sin\lambda_1 l_1 \tag{C.59}$$
$$+2\lambda_1\lambda_2\left(2l_1+3l_2\right)\sin\lambda_2 l_2 - 6\lambda_1 \cos\lambda_1 l_1 + 6\lambda_1 \cos\lambda_2 l_2 - \lambda_1\left(\lambda_1^2 l_1^2-6\right)\Big\}$$

$$\chi^{(2)}_{\theta'_{12}} = -\frac{1}{\Phi_c \lambda_1^2 l_1^2}\Big\{4\lambda_1^2 l_1 \sin\lambda_1 l_1 \sin\lambda_2 l_2 - \lambda_2\left[\lambda_1^2 l_1^2 + 4\lambda_1^2 l_1\left(l_1+l_2\right)-6\right]\sin\lambda_1 l_1 \cos\lambda_2 l_2 - \lambda_1\left(\lambda_1^2 l_1^2-6\right)\cos\lambda_1 l_1 \sin\lambda_2 l_2$$
$$+\lambda_1\lambda_2\left[\lambda_1^2 l_1^2\left(l_1+l_2\right)-10l_1-6l_2\right]\cos\lambda_1 l_1 \cos\lambda_2 l_2 - 6\lambda_2 \sin\lambda_1 l_1 - 6\lambda_1 \sin\lambda_2 l_2 + 2\lambda_1\lambda_2 l_1 \cos\lambda_1 l_1 \tag{C.60}$$
$$+2\lambda_1\lambda_2\left(2l_1+3l_2\right)\cos\lambda_2 l_2 + 4\lambda_1\lambda_2 l_1\Big\}$$

$$\gamma_{\theta'_{21}}^{(2)} = -\frac{1}{\Phi_c \lambda_2^2 l_2^2}\Big\{-\lambda_2\left[4\lambda_1^2 l_2\left(l_1+l_2\right)-\lambda_2^2 l_2^2+6\right]\sin\lambda_1 l_1 \sin\lambda_2 l_2 - 4\lambda_1^2 l_2 \sin\lambda_1 l_1 \cos\lambda_2 l_2$$
$$-\lambda_1\lambda_2\left[\lambda_2^2 l_2^2\left(l_1+l_2\right)-6l_1-2l_2\right]\cos\lambda_1 l_1 \sin\lambda_2 l_2 - \lambda_1\left(\lambda_2^2 l_2^2-6\right)\cos\lambda_1 l_1 \cos\lambda_2 l_2 \qquad \text{(C.61)}$$
$$+2\lambda_1^2\left(3l_1+2l_2\right)\sin\lambda_1 l_1 - 2\lambda_1\lambda_2 l_2 \sin\lambda_2 l_2 + 6\lambda_1 \cos\lambda_1 l_1 - 6\lambda_1 \cos\lambda_2 l_2 + \lambda_1\left(\lambda_2^2 l_2^2-6\right)\Big\}$$

$$\chi_{\theta'_{21}}^{(2)} = -\frac{1}{\Phi_c \lambda_2^2 l_2^2}\Big\{4\lambda_1^2 l_2 \sin\lambda_1 l_1 \sin\lambda_2 l_2 - \lambda_2\left[4\lambda_1^2 l_2\left(l_1+l_2\right)-\lambda_2^2 l_2^2+6\right]\sin\lambda_1 l_1 \cos\lambda_2 l_2 + \lambda_1\left(\lambda_2^2 l_2^2-6\right)\cos\lambda_1 l_1 \sin\lambda_2 l_2$$
$$-\lambda_1\lambda_2\left[\lambda_2^2 l_2^2\left(l_1+l_2\right)-6l_1-2l_2\right]\cos\lambda_1 l_1 \cos\lambda_2 l_2 + 6\lambda_2 \sin\lambda_1 l_1 + 6\lambda_1 \sin\lambda_2 l_2 - 2\lambda_1\lambda_2\left(3l_1+2l_2\right)\cos\lambda_1 l_1 \qquad \text{(C.62)}$$
$$-2\lambda_1\lambda_2 l_2 \cos\lambda_2 l_2 + 4\lambda_1\lambda_2 l_2\Big\}$$

$$\gamma_{\theta'_{22}}^{(2)} = -\frac{1}{\Phi_c \lambda_2^2 l_2^2}\Big\{-2\lambda_2\left[\lambda_1^2 l_2\left(l_1+l_2\right)+3\right]\sin\lambda_2 l_2 \sin\lambda_1 l_1 - 2\lambda_1^2 l_2 \sin\lambda_1 l_1 \cos\lambda_2 l_2 + 2\lambda_1\lambda_2\left(3l_1+2l_2\right)\cos\lambda_1 l_1 \sin\lambda_2 l_2$$
$$+6\lambda_1 \cos\lambda_1 l_1 \cos\lambda_2 l_2 - \lambda_1^2\left[\lambda_2^2 l_2^2\left(l_1+l_2\right)-6l_1-2l_2\right]\sin\lambda_1 l_1 - 4\lambda_1\lambda_2 l_2 \sin\lambda_2 l_2 \qquad \text{(C.63)}$$
$$-\lambda_1\left(\lambda_2^2 l_2^2-6\right)\cos\lambda_1 l_1 + \lambda_1\left(\lambda_2^2 l_2^2-6\right)\cos\lambda_2 l_2 - 6\lambda_1\Big\}$$

$$\chi_{\theta'_{22}}^{(2)} = -\frac{1}{\Phi_c \lambda_2^2 l_2^2}\Big\{2\lambda_1^2 l_2 \sin\lambda_2 l_2 \sin\lambda_1 l_1 - 2\lambda_2\left[\lambda_1^2 l_2\left(l_1+l_2\right)+3\right]\sin\lambda_1 l_1 \cos\lambda_2 l_2 - 6\lambda_1 \cos\lambda_1 l_1 \sin\lambda_2 l_2$$
$$+2\lambda_1\lambda_2\left(3l_1+2l_2\right)\cos\lambda_1 l_1 \cos\lambda_2 l_2 - \lambda_2\left(\lambda_2^2 l_2^2-6\right)\sin\lambda_1 l_1 - \lambda_1\left(\lambda_2^2 l_2^2-6\right)\sin\lambda_2 l_2 \qquad \text{(C.64)}$$
$$+\lambda_1\lambda_2\left[\lambda_2^2 l_2^2\left(l_1+l_2\right)-6l_1-2l_2\right]\cos\lambda_1 l_1 - 4\lambda_1\lambda_2 l_2 \cos\lambda_2 l_2 + 2\lambda_1\lambda_2 l_2\Big\}$$

And also,

$$\upsilon_{\theta''_{11}}^{(1)} = -\frac{2}{\lambda_1^2 l_1} \qquad \text{(C.65)}$$

$$\upsilon_{\theta'_{12}}^{(1)} = -\frac{4}{\lambda_1^2 l_1} \tag{C.66}$$

$$\upsilon_{\theta'_{21}}^{(2)} = \frac{4}{\lambda_2^2 l_2} \tag{C.67}$$

$$\upsilon_{\theta'_{22}}^{(2)} = \frac{2}{\lambda_2^2 l_2} \tag{C.68}$$

$$\mu_{\theta'_{11}}^{(1)} = \mu_{\theta'_{12}}^{(1)} = \frac{6}{\lambda_1^2 l_1^2} \tag{C.69}$$

$$\mu_{\theta'_{21}}^{(2)} = \mu_{\theta'_{22}}^{(2)} = -\frac{6}{\lambda_2^2 l_2^2} \tag{C.70}$$

C.4.3 Coefficients for Symmetric Structure, $P > 0$

$$
\begin{aligned}
M_1^{(1s)}(x_1') &= P\left(\phi_{\theta_{11}'}^{(1s)}\sinh\lambda x_1' + \psi_{\theta_{11}'}^{(1s)}\cosh\lambda x_1'\right)\theta_{11}' + P\left(\phi_{\theta_{12}'}^{(1s)}\sinh\lambda x_1' + \psi_{\theta_{12}'}^{(1s)}\cosh\lambda x_1'\right)\theta_{12}' \\
&\quad + P\left(\phi_{\theta_{21}'}^{(1s)}\sinh\lambda x_1' + \psi_{\theta_{21}'}^{(1s)}\cosh\lambda x_1'\right)\theta_{21}' + P\left(\phi_{\theta_{22}'}^{(1s)}\sinh\lambda x_1' + \psi_{\theta_{22}'}^{(1s)}\cosh\lambda x_1'\right)\theta_{22}' \\
&\quad - P\left(\zeta_{\theta_{11}'}^{(1s)} + \kappa_{\theta_{11}'}^{(1s)}x_1'\right)\theta_{11}' - P\left(\zeta_{\theta_{12}'}^{(1s)} + \kappa_{\theta_{12}'}^{(1s)}x_1'\right)\theta_{12}' \\
M_1^{(2s)}(x_2) &= P\left(\phi_{\theta_{11}'}^{(2s)}\sinh\lambda x_2 + \psi_{\theta_{11}'}^{(2)}\cosh\lambda_2 x_2\right)\theta_{11}' + P\left(\phi_{\theta_{12}'}^{(2s)}\sinh\lambda x_2 + \psi_{\theta_{12}'}^{(2s)}\cosh\lambda x_2\right)\theta_{12}' \\
&\quad + P\left(\phi_{\theta_{21}'}^{(2s)}\sinh\lambda x_2 + \psi_{\theta_{21}'}^{(2s)}\cosh\lambda_2 x_2\right)\theta_{21}' + P\left(\phi_{\theta_{22}'}^{(2s)}\sinh\lambda x_2 + \psi_{\theta_{22}'}^{(2s)}\cosh\lambda x_2\right)\theta_{22}' \\
&\quad - P\left(\zeta_{\theta_{21}'}^{(2s)} + \kappa_{\theta_{21}'}^{(2s)}x_2\right)\theta_{21}' - P\left(\zeta_{\theta_{22}'}^{(2s)} + \kappa_{\theta_{22}'}^{(2s)}x_2\right)\theta_{22}'
\end{aligned}
\tag{C.71}
$$

where

$$
\phi_{\theta_{11}'}^{(1s)} = -\phi_{\theta_{22}'}^{(2s)} = -\frac{\lambda^3 l^3 + 2\lambda^2 l^2\sinh\lambda l + 4\lambda l\cosh\lambda l + 2\lambda l - 6\sinh\lambda l}{2\lambda^3 l^2\left(\lambda l\cosh\lambda l - \sinh\lambda l\right)} \tag{C.72}
$$

$$
\psi_{\theta_{11}'}^{(1s)} = -\psi_{\theta_{22}'}^{(2s)} = -\frac{\lambda^2 l^2 - 2\lambda l\sinh\lambda l - 6\cosh\lambda l + 6}{2\lambda^3 l^2\sinh\lambda l} \tag{C.73}
$$

$$
\phi_{\theta_{12}'}^{(1s)} = -\phi_{\theta_{21}'}^{(2s)} = -\frac{\lambda^3 l^3\cosh\lambda l + 3\lambda^2 l^2\sinh\lambda l + 2\lambda l\cosh\lambda l + 4\lambda l - 6\sinh\lambda l}{2\lambda^3 l^2\left(\lambda l\cosh\lambda l - \sinh\lambda l\right)} \tag{C.74}
$$

$$
\psi_{\theta_{12}'}^{(1s)} = -\psi_{\theta_{21}'}^{(2s)} = -\frac{-\lambda^2 l^2\cosh\lambda l - 4\lambda l\sinh\lambda l - 6\cosh\lambda l + 6}{2\lambda^3 l^2\sinh\lambda l} \tag{C.75}
$$

$$
\phi_{\theta_{21}'}^{(1s)} = -\phi_{\theta_{12}'}^{(2s)} = \frac{\lambda^3 l^3\cosh\lambda l - 5\lambda^2 l^2\sinh\lambda l + 10\lambda l\cosh\lambda l - 4\lambda l - 6\sinh\lambda l}{2\lambda^3 l^2\left(\lambda l\cosh\lambda l - \sinh\lambda l\right)} \tag{C.76}
$$

$$
\psi_{\theta_{21}'}^{(1s)} = -\psi_{\theta_{12}'}^{(2s)} = -\frac{\lambda^2 l^2\cosh\lambda l - 4\lambda l\sinh\lambda l + 6\cosh\lambda l - 6}{2\lambda^3 l^2\sinh\lambda l} \tag{C.77}
$$

$$
\phi_{\theta_{22}'}^{(1s)} = -\phi_{\theta_{11}'}^{(2s)} = -\frac{\lambda^3 l^3 + 2\lambda^2 l^2\sinh\lambda l - 8\lambda l\cosh\lambda l + 2\lambda l + 6\sinh\lambda l}{2\lambda^3 l^2\left(\lambda l\cosh\lambda l - \sinh\lambda l\right)} \tag{C.78}
$$

$$
\psi_{\theta_{22}'}^{(1s)} = -\psi_{\theta_{11}'}^{(2s)} = -\frac{-\lambda^2 l^2 - 2\lambda l\sinh\lambda l + 6\cosh\lambda l - 6}{2\lambda^3 l^2\sinh\lambda l} \tag{C.79}
$$

$$
\zeta_{\theta_{11}'}^{(1s)} = -\zeta_{\theta_{22}'}^{(2s)} = \frac{2}{\lambda^2 l} \tag{C.80}
$$

$$\zeta_{\theta'_{12}}^{(1s)} = -\zeta_{\theta'_{21}}^{(2s)} = \frac{4}{\lambda^2 l} \tag{C.81}$$

$$\kappa_{\theta'_{11}}^{(1s)} = \kappa_{\theta'_{12}}^{(1s)} = -\kappa_{\theta'_{21}}^{(2s)} = -\kappa_{\theta'_{22}}^{(2s)} = -\frac{6}{\lambda^2 l^2} \tag{C.82}$$

C.4.4 Coefficients for Symmetric Structure, $P < 0$

$$\begin{aligned}
M_1^{(1s)}(x_1') &= P\left(\gamma_{\theta'_{11}}^{(1s)} \sin\lambda x_1' + \chi_{\theta'_{11}}^{(1s)} \cos\lambda x_1'\right)\theta'_{11} + P\left(\gamma_{\theta'_{12}}^{(1s)} \sin\lambda x_1' + \chi_{\theta'_{12}}^{(1s)} \cos\lambda x_1'\right)\theta'_{12} \\
&\quad + P\left(\gamma_{\theta'_{21}}^{(1s)} \sin\lambda x_1' + \chi_{\theta'_{21}}^{(1s)} \cos\lambda x_1'\right)\theta'_{21} + P\left(\gamma_{\theta'_{22}}^{(1s)} \sin\lambda x_1' + \chi_{\theta'_{22}}^{(1s)} \cos\lambda x_1'\right)\theta'_{22} \\
&\quad - P\left(\upsilon_{\theta'_{11}}^{(1s)} + \mu_{\theta'_{11}}^{(1s)} x_1'\right)\theta'_{11} - P\left(\upsilon_{\theta'_{12}}^{(1s)} + \mu_{\theta'_{12}}^{(1s)} x_1'\right)\theta'_{12} \\
M_1^{(2s)}(x_2) &= P\left(\gamma_{\theta'_{11}}^{(2s)} \sin\lambda x_2 + \chi_{\theta'_{11}}^{(2s)} \cos\lambda x_2\right)\theta'_{11} + P\left(\gamma_{\theta'_{12}}^{(2s)} \sin\lambda x_2 + \chi_{\theta'_{12}}^{(2s)} \cos\lambda x_2\right)\theta'_{12} \\
&\quad + P\left(\gamma_{\theta'_{21}}^{(2s)} \sin\lambda x_2 + \chi_{\theta'_{21}}^{(2s)} \cos\lambda x_2\right)\theta'_{21} + P\left(\gamma_{\theta'_{22}}^{(2s)} \sin\lambda x_2 + \chi_{\theta'_{22}}^{(2s)} \cos\lambda x_2\right)\theta'_{22} \\
&\quad - P\left(\upsilon_{\theta'_{21}}^{(2s)} + \mu_{\theta'_{21}}^{(2s)} x_2\right)\theta'_{21} - P\left(\upsilon_{\theta'_{22}}^{(2s)} + \mu_{\theta'_{22}}^{(2s)} x_2\right)\theta'_{22}
\end{aligned} \tag{C.83}$$

where

$$\gamma_{\theta'_{11}}^{(1s)} = -\gamma_{\theta'_{22}}^{(2s)} = -\frac{\lambda^3 l^3 + 2\lambda^2 l^2 \sin\lambda l - 4\lambda l \cos\lambda l - 2\lambda l + 6\sin\lambda l}{2\lambda^3 l^2 (\lambda l \cos\lambda l - \sin\lambda l)} \tag{C.84}$$

$$\chi_{\theta'_{11}}^{(1s)} = -\chi_{\theta'_{22}}^{(2s)} = -\frac{-\lambda^2 l^2 + 2\lambda l \sin\lambda l - 6\cos\lambda l + 6}{2\lambda^3 l^2 \sin\lambda l} \tag{C.85}$$

$$\gamma_{\theta'_{12}}^{(1s)} = -\gamma_{\theta'_{21}}^{(2s)} = -\frac{\lambda^3 l^3 \cos\lambda l + 3\lambda^2 l^2 \sin\lambda l - 2\lambda l \cos\lambda l - 4\lambda l + 6\sin\lambda l}{2\lambda^3 l^2 (\lambda l \cos\lambda l - \sin\lambda l)} \tag{C.86}$$

$$\chi_{\theta'_{12}}^{(1s)} = -\chi_{\theta'_{21}}^{(2s)} = -\frac{\lambda^2 l^2 \cos\lambda l + 4\lambda l \sin\lambda l - 6\cos\lambda l + 6}{2\lambda^3 l^2 \sin\lambda l} \tag{C.87}$$

$$\gamma_{\theta'_{21}}^{(1s)} = -\gamma_{\theta'_{12}}^{(2s)} = \frac{\lambda^3 l^3 \cos\lambda l - 5\lambda^2 l^2 \sin\lambda l - 10\lambda l \cos\lambda l + 4\lambda l + 6\sin\lambda l}{2\lambda^3 l^2 (\lambda l \cos\lambda l - \sin\lambda l)} \tag{C.88}$$

$$\chi_{\theta'_{21}}^{(1s)} = -\chi_{\theta'_{12}}^{(2s)} = -\frac{-\lambda^2 l^2 \cos\lambda l + 4\lambda l \sin\lambda l + 6\cos\lambda l - 6}{2\lambda^3 l^2 \sin\lambda l} \tag{C.89}$$

$$\gamma_{\theta'_{22}}^{(1s)} = -\gamma_{\theta'_{11}}^{(2s)} = -\frac{\lambda^3 l^3 + 2\lambda^2 l^2 \sin\lambda l + 8\lambda l \cos\lambda l - 2\lambda l - 6\sin\lambda l}{2\lambda^3 l^2 (\lambda l \cos\lambda l - \sin\lambda l)} \tag{C.90}$$

$$\chi_{\theta'_{22}}^{(1s)} = -\chi_{\theta'_{11}}^{(2s)} = -\frac{\lambda^2 l^2 + 2\lambda l \sin \lambda l + 6\cos \lambda l - 6}{2\lambda^3 l^2 \sin \lambda l} \tag{C.91}$$

$$\upsilon_{\theta'_{11}}^{(1s)} = -\upsilon_{\theta'_{22}}^{(2s)} = -\frac{2}{\lambda^2 l} \tag{C.92}$$

$$\upsilon_{\theta'_{12}}^{(1s)} = -\upsilon_{\theta'_{21}}^{(2s)} = -\frac{4}{\lambda^2 l} \tag{C.93}$$

$$\mu_{\theta'_{11}}^{(1s)} = \mu_{\theta'_{12}}^{(1s)} = -\mu_{\theta'_{21}}^{(2s)} = -\mu_{\theta'_{22}}^{(2s)} = \frac{6}{\lambda^2 l^2} \tag{C.94}$$

Appendix D

Evaluation of magnesium weldment fatigue data using traction and notch stress methods

This appendix contains an investigation of a set of magnesium weldment fatigue test data in literature using finite element-based methods. Within the study, the secondary bending caused by axial misalignments is considered using the analytical solution developed in this dissertation, illustrating how the distortion effect can be included without explicitly FE modeling by using these analytical solutions.

D.1 Appendix Introduction

Magnesium alloys have recently gained increasing attention for achieving structural lightweighting in the transportation systems, such as magnesium-intensive autobody structures, due to their high strength-to-weight ratio, good manufacturability (e.g., weldability), and reasonable raw material cost [94–99]. One of the important design criteria in adopting magnesium-intensive structures is to ensure adequate fatigue capacity of welded joints subjected to time-varying or cyclic loading conditions in service.

Unlike conventional structural materials such as structural steels and mainstream aluminum alloys for which well-recognized fatigue evaluation procedures are available, e.g. [24,74,100], built upon a large amount of experimental test data over decades, magnesium weldment test data have only become available more recently. These include experimental testing efforts by Tsujikawa et al. [94], Jordon et al. [101], Chowdhury et al. [102] and Shen et al. [103] and more recently by Karakas et al. [104]. These investigations have shown that fatigue behaviors of welded joints are rather different from those in non-welded components in a similar way to

those in other conventional structural metal weldments [21]. However, in terms of how to effectively generalize these magnesium weldment test data for use in a structural CAE model for fatigue evaluation, there seems no general consensus to date. There exist numerous methods that are being considered. These are nominal stress method [24], hot-spot stress method (e.g., [26]), local notch stress method [27–29,104], traction structural stress [30–32] and structural strain method [105,106], including crack initiation life based theory of critical distance (TCD) and averaged strain energy density (A-SED) methods [107–109]. These methods all aim to determine a relevant stress or strain parameter that can be shown capable of correlating available test data from various joint geometries into a narrow scatter so that such a parameter can be used in CAE based fatigue evaluation of complex structures. Since this paper is focused on applications in dealing with complex joint types, the mesh-insensitive traction stress and equivalent notch stress methods are selected for further evaluation of magnesium weldment data. The former offers the simplicity for modeling a complex structure without explicitly representing weld toe or weld root notch geometry while the latter can be used as a reference solution for comparison purpose, in which notch geometry is modeled in detail.

One particular set of magnesium weldment test data of interest in this regard is those recently published by Sonsino et al. [110] and Karakas et al. [104] on fatigue behaviors of three different joint types [104,107,111,112] for which an equivalent notch stress (defined with 1 mm notch radius) method was used for correlating the test data and showed promising results. As a continuation of that study, it would be useful to examine if the detailed modeling requirements, e.g., imposing a 1 mm notch radius, can be relaxed for achieving a similar data correlation. This is important in that a complex CAE structural model may not be capable of incorporating such a small notch radius in practice. For this purpose, the traction-based structural stress method will be

considered here for investigating how the same fatigue test data can be effectively correlated and compared with the equivalent notch stress method used in [104]. Furthermore, another question to be addressed is if the structural strain based master E-N curve method [106] is applicable for representing the test data collected from magnesium weldments. If confirmed, scatter bands obtained from other structural metal weldments, e.g., structural steel and aluminum alloys, can be used as an approximation for determining confidence levels in structural fatigue evaluation before a large amount of data become available for magnesium weldments.

With the above discussions, the aim of this work to examine if the traction stress method is effective in correlating magnesium weldment fatigue test data and how such a correlation can be compared with other structural joint data such as aluminum alloy and steel weldments. In this paper, we start with a brief description of the fatigue test data obtained on magnesium weldments by Karakas [104] for the purpose of providing essential information to be used for performing further analysis by using the traction structural stress method. Due to the simple joint types and loading mode involved, a two-dimensional (2D) traction stress analysis is then adopted for computing traction-based stress concentration factors for each of the three joint types. Next, a traction stress-based fatigue parameter is introduced by adapting an earlier development on fracture mechanics-based treatment of applied stress ratio. Finally, the proposed fatigue parameter is used to demonstrate how all the magnesium weld fatigue data from [104] can be effectively correlated into a narrow band. Furthermore, this study shows that the treatment of the applied stress ratio can be used in conjunction with the effective notch stress method used by Karakas [104] to achieve a similar beneficial effect on data correlation. The implications from weld toe and weld throat failure modes will also be discussed in light of the key findings resulted from this investigation.

D.2 Fatigue Test Data

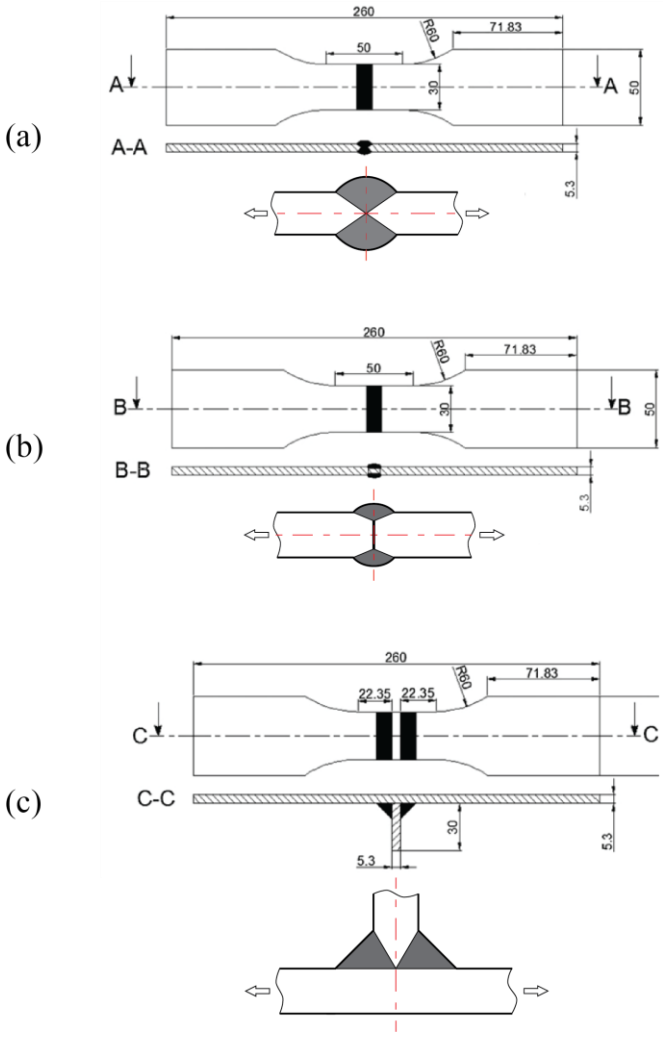

Fig. D.1 Illustration of three joint types tested [111]: (a) full penetration butt joint; (b) partial penetration butt joint; (c) T-joint.

Fatigue tests on magnesium alloy weldments were carried out by Karakas et al., as reported in [104]. Three typical types of joints were investigated: full penetration butt joint, partial penetration butt joint and T-joint, as shown in Fig. D.1. Detailed specimen dimensions including local joint profiles are also shown in Fig. D.1. The full penetration butt joint, and T-joint specimens were manufactured using a MIG welding process, and the partial penetration butt joint specimens were made using a TIG welding process. The base material is AZ31 (ISO-MgAl3Zn1) in an extruded plate form, and the filler wire is AZ61A type. The thickness of the plate is 5.3 mm. Three

different load ratios were used in fatigue testing, i.e., fully-reversed loading ($R = -1$), pulsating loading ($R = 0$), and high tensile mean loading ($R = 0.5$). All tests were performed under load-controlled conditions with frequency $f = 15{\sim}30$Hz at room temperature. Further details of the tests and specimen details can be found in [104,107,111].

Fig. D.2 shows the typical failure modes associated with three types of test specimens. The failure mode in all full penetration butt joint and T-joint specimens is weld toe cracking, and the failure mode for partial penetration butt joint specimens is weld root or weld throat cracking.

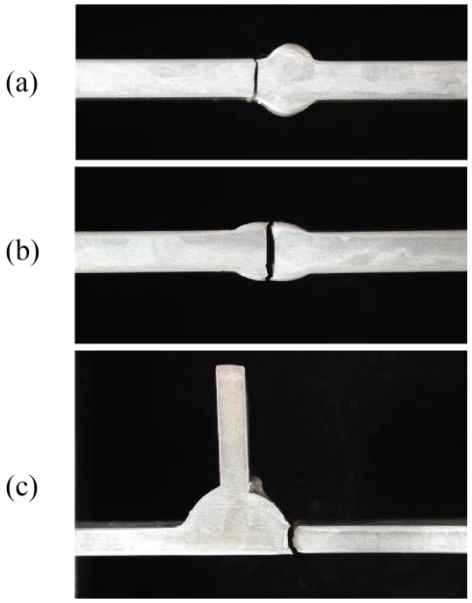

Fig. D.2 Failure modes of the tested specimens [104]: (a) full penetration butt joint; (b) partial penetration butt joint; (c) T-joints.

All test data are summarized in Fig. D.3 using nominal stress range, $\Delta\sigma_n$, calculated based on base plate cross-section area. As a result, it is not surprising that partial penetration butt joint data (weld root failure mode) are situated at the lower side of the plot than other weld toe cracking data. Another trend observable in Fig. D.3 is that the applied stress ratio R seems to have a significant effect, particularly at $R = -1$, regardless of joint types. As expected, the test data from three joint types to a large extent form their own scatter bands, which necessitates the weld classification approach [24]. For the sake of easy reference in later sections, a standard deviation

(STD) of 0.469 represents a scatter measure for all test data in Fig. D.3. Karakas et al. [104] performed their analysis of the test data in Fig. D.3 using a local equivalent notch stress method with the fictitious notch radius of $r_f = 1.0$ mm and the results are shown in Fig. D.4. It is worth pointing out that the use of the local equivalent notch stress range parameter reduces the scatter band from 0.469 to 0.368 in terms of STD.

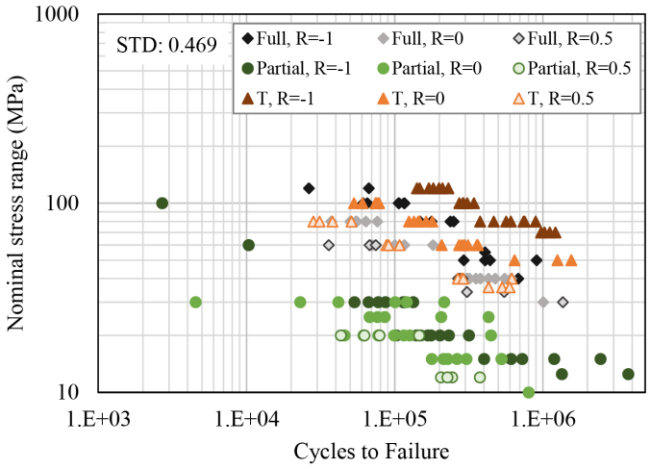

Fig. D.3 All test data obtained from three joint types plotted using plate nominal stress range

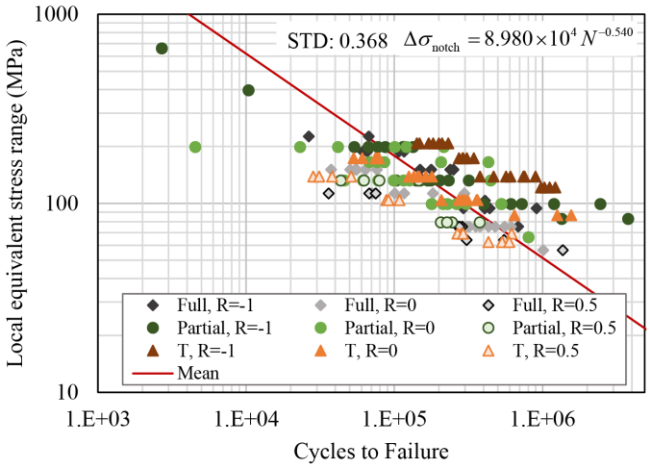

Fig. D.4 All test data obtained from three joint types plotted using local equivalent notch stress range with $r_f = 1$ mm [104]

D.3 Data Analysis using Traction Stress Method

D.3.1 Traction Structural Stress Determination

The traction structural stress method was originally developed by Dong et al. [30–32] and has been used in a number of recent studies [36,37] for dealing with both weld toe and weld root cracking fatigue failure modes. In this study, only 2D structural stress definition and implementation are needed, given the three joint configurations and simple cyclic tension loading conditions shown in Fig. D.1. Further details of the traction stress method and its 3D implementation for complex structures can be found in some previous publications, e.g., [30].

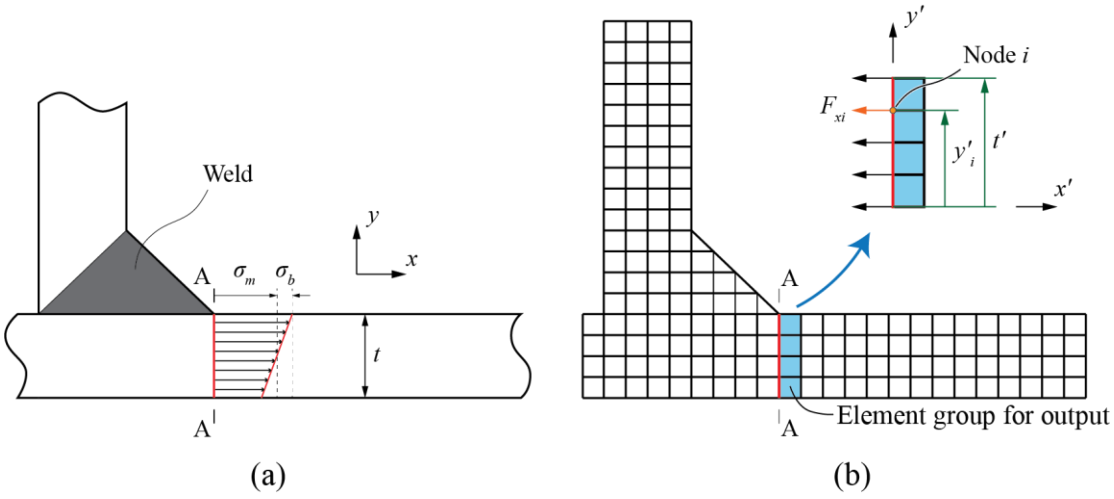

Fig. D.5 Traction structural stress method: (a) traction structural stress definition; (b) implementation in 2D finite element analysis

The normal traction structural stress σ_s is defined as the sum of the membrane and bending traction stress components, σ_m and σ_b, as defined in Fig. D.5a.

$$\sigma_s = \sigma_m + \sigma_b \tag{D.1}$$

In 2D analysis, we first create a 2D finite element (FE) model, as shown in Fig. D.5b; then, we define the hypothetical crack path of interest, for example, section A-A in Fig. D.5b. Next, we identify the element group for nodal force extraction, which includes all elements next to the hypothetical crack path (A-A) on one side, shown as highlighted elements in Fig. D.5b. We define a node set N = {i | Node i being on the crack path A-A} which contains the nodes used for nodal

force extraction. Finally, we extract the nodal forces from nodes in the set N defined earlier, and σ_m and σ_b can be calculated from the finite element results by

$$\sigma_m = \frac{1}{t'}\sum_{i\in N} F_{x'i}$$
$$\sigma_b = -\frac{6}{t'^2}\sum_{i\in N} F_{x'i}\left(y'_i - \frac{t'}{2}\right) \quad \text{(D.2)}$$

where x', y' are the local coordinate system with x' being the normal direction of the crack path; t' is the length of the crack path A-A, $F_{x'i}$ is the total nodal force in x'-direction on node *i* of the output element group, y'_i is the y'-coordinate of node *i*, as depicted in Fig. D.5b. The required nodal force output can be obtained directly with most commercial finite element software, for example, "NFORC" in ABAQUS, "NLOAD" in ANSYS, and "GPFORCE" in NASTRAN. A good mesh-insensitivity of the traction structural stresses has been demonstrated in previous publications [30–32,37], as long as overall joint geometry is correctly represented.

It should be noted that any joint misalignment present in fatigue specimens can be directly treated as a contribution to σ_b in Eqn. (D.1). This can be done either by building a misalignment into the FE model or calculated separately if a closed-form solution is available. Since the test specimens (Fig. D.1) of interest in this study did not have any documented misalignments [104], we assume a near-negligibly small amount of misalignment (e) of 0.1t, where t is the base plate thickness. This misalignment amount (e/t =0.1) is uniformly applied for all butt-welded joint types. Note that allowable joint misalignments for developing design fatigue S-N curve is e/t =0.25 for offshore structures as stipulated by DNV-RP-C203 [33] and e/t =0.5 for thin gauge shipboard panels in military ships as discussed by Huang et al. [76]. As recently investigated by Xing et al. [63,89], the misalignment induced stress concentration factor (SCF) only contributes to weld toe cracking in a noticeable manner and has a negligible effect on weld throat cracking in

partial penetration butt welds or fillet welds. For simple butt joint specimens involved in this study, the axial misalignment induced SCF for weld toe failure mode simply becomes [63,89] $SCF_e = 3 \times (e/t) = 0.3$.

D.3.2 Equivalent Traction Stress

In addition to the traction stress in range given in Eqn. (D.1), an equivalent traction structural stress parameter adopted by the 2007 ASME B&PV Code [32,74] contains a number of correction parameters derived based on fracture mechanics principles. For the present purpose, the only relevant parameter is the load ratio correction parameter. The load ratio is defined as the ratio of applied minimum traction stress to maximum traction stress

$$R = \frac{\sigma_{\min}}{\sigma_{\max}} \tag{D.3}$$

which can affect the fatigue life of welded joints. As given in [32], by introducing an equivalent stress intensity in the form of $\sqrt{\Delta K^{+} K_{\max}}$ proposed by Kujawski [113], the load ratio correction against the traction stress range in Eqn. (D.1) can be written as:

$$\begin{cases} (1-R)^{1/m} & R \geq 0 \\ (1-R)^{2/m} & R < 0 \end{cases} \tag{D.4}$$

where *m* takes a value 3.6 obtained from a unified representation of both short and long fatigue crack growth data [114]. Then the equivalent traction stress parameter for fatigue data correlation purpose to be used in this study becomes:

$$\Delta\sigma_{\mathrm{Es}} = \begin{cases} \dfrac{\Delta\sigma_s}{(1-R)^{1/m}} & R \geq 0 \\ \dfrac{\Delta\sigma_s}{(1-R)^{2/m}} & R < 0 \end{cases} \tag{D.5}$$

D.3.3 Traction Stress Analysis of Test Specimens

Quarter symmetry conditions are used for modeling the butt-welded specimens (both full and partial penetrations) in Fig. D.1a and Fig. D.1b. Similarly, one half-symmetry condition is used for modeling the T-joint specimens shown in Fig. D.1c, as shown in Fig. D.6. The global view of the FE model used for the T-joint specimen is illustrated in Fig. D.6, including modeling details involving loading grip representation, remote loading application using element face pressure. Fig. D.7 provides the local views showing the elements (highlighted), for which nodal forces from FE results are to be extracted for use in Eqn. (D.2) for computing σ_s through Eqn. (D.1), corresponding to weld toe cracking in full penetration butt weld (Fig. D.7a), weld root cracking in partial penetration butt weld (Fig. D.7b), and weld toe cracking in T-joint (Fig. D.7c). By taking advantage of the mesh-insensitivity of the traction stress method, the FE meshes used (Fig. D.7) are considered more than adequate [32]. ABAQUS "CPS4" plane stress elements were used for modeling all three joint types and linear elastic behavior, based on Young's modulus ($E = 43000$ MPa) and Poisson's ratio ($\nu = 0.35$) given in [111], were also used. A unit pressure load (1 MPa) as shown in Fig. D.6 was used for computing SCF at respective failure locations as shown in Fig. D.7.

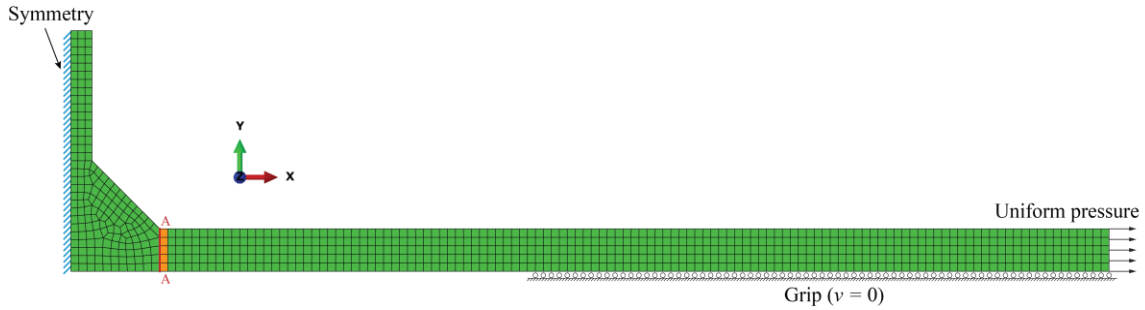

Fig. D.6 Global view of T-joint FE model

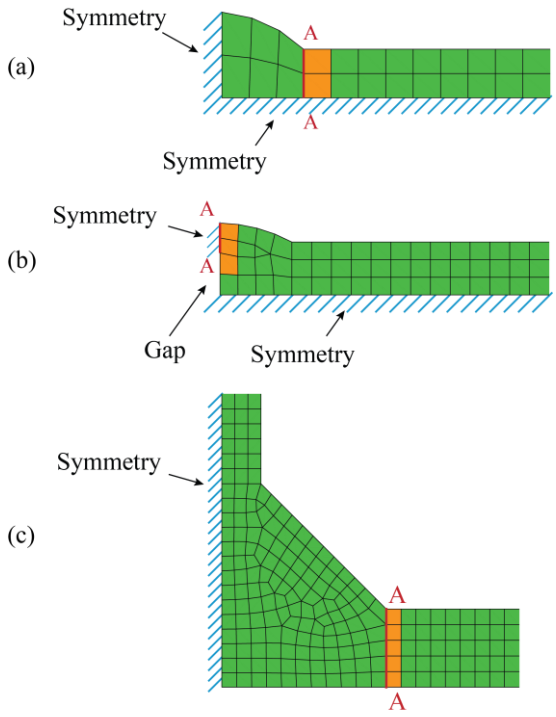

Fig. D.7 Local views of FE models: (a) full penetration butt joint; (b) partial penetration butt joint; (c) T-joint

Based on the failure mode discussed with respect to each joint type, the corresponding membrane and bending based SCF can be calculated simply by $SCF_m = \sigma_m/\sigma_n$ and $SCF_b = \sigma_b/\sigma_n$ under unit nominal stress, i.e., $\sigma_n = 1$ MPa. The results are summarized in Table D.1. The total structural stress concentration factor, $SCF_s = \sigma_s/\sigma_n = SCF_m + SCF_b$, is also given in Table D.1.

Table D.1 Calculated structural stress SCF at critical location of interest

Joint type	SCF_m	SCF_b	SCF_s
Full penetration butt joint	1	0.6436	1.6436
Partial penetration butt joint	1.7667	3.0163	4.7830
T-joint	1	0.0654	1.0654

D.3.4 Data Correlation

All test data are first plotted in Fig. D.8 in terms of structural stress range $\Delta\sigma_s = SCF_s \cdot \Delta\sigma_n$, where SCF_s is given in Table D.1. As can be seen, all three types of joints show an improved correlation over the one plotted in terms of the plate nominal stress range, shown in Fig. D.3. The standard deviation or STD as a measure of the scatter band is 0.356. It is also interesting to note that the STD value is similar to that when the effective notch stress range is used (see Fig. D.4). In recognition of the strong R ratio effects on the data behavior discussed in Sec. D.2, the equivalent traction stress parameter given in Eqn. (D.5) should be used for data correlation purposes. The results are shown in Fig. D.9. A significant improvement in data correlation can be seen over that shown in Fig. D.8 when the structural stress range is used and in Fig. D.4 when equivalent notch stress range is used. The resulting STD value is now at 0.241. In addition, it is important to note that all test data from three joint types no longer exhibits their own respective trends in Fig. D.9, indicating the effectiveness of Eqn. (D.4), which was developed for steel and aluminum weldments [32].

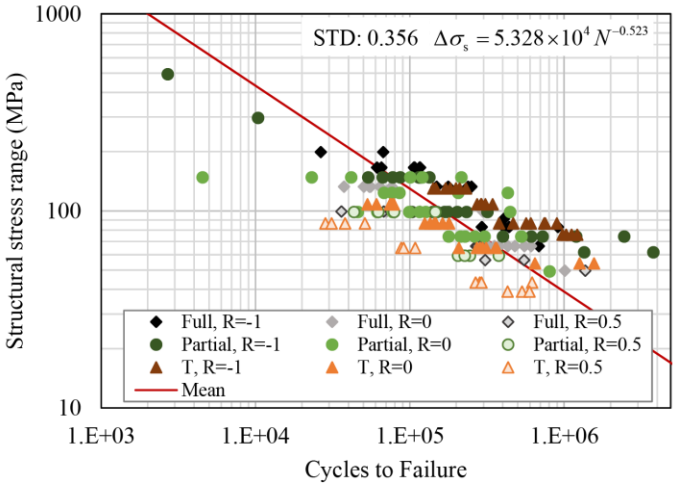

Fig. D.8 Test data correlation using structural stress range.

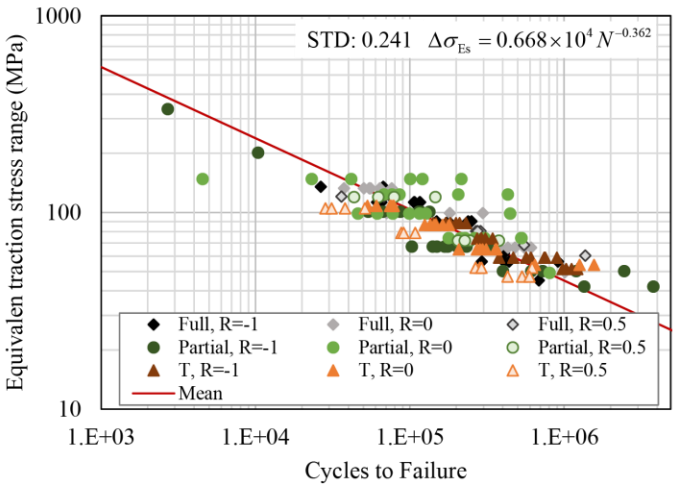

Fig. D.9 Test data correlation using equivalent traction stress.

D.4 Discussions

D.4.1 Weld Toe Failure vs. Weld Root Failure

It can be seen from Fig. D.9 that the partial penetration butt joint data corresponding to weld root failures exhibit a more scatter than the other two joint types corresponding to weld toe failures. In practice, e.g., in BS 7609 [24] or the 2007 ASME B&PV Code [74], weld toe fatigue failures are treated separately from those corresponding to weld root failures. After separating the two failure modes, the results are shown in Fig. D.10. The data corresponding to weld toe failure mode (full penetration butt joint and T-joint) now show a rather narrow scatter band of 0.194 in standard deviation in Fig. D.10a, while data corresponding to weld root failure mode shows a significantly wider scatter band of 0.313 in standard deviation. Such discrepancy validates the observations that the weld root failure mode tends to be more significantly influenced by variations in weld quality, penetration amount, etc., as described in [36,115,116].

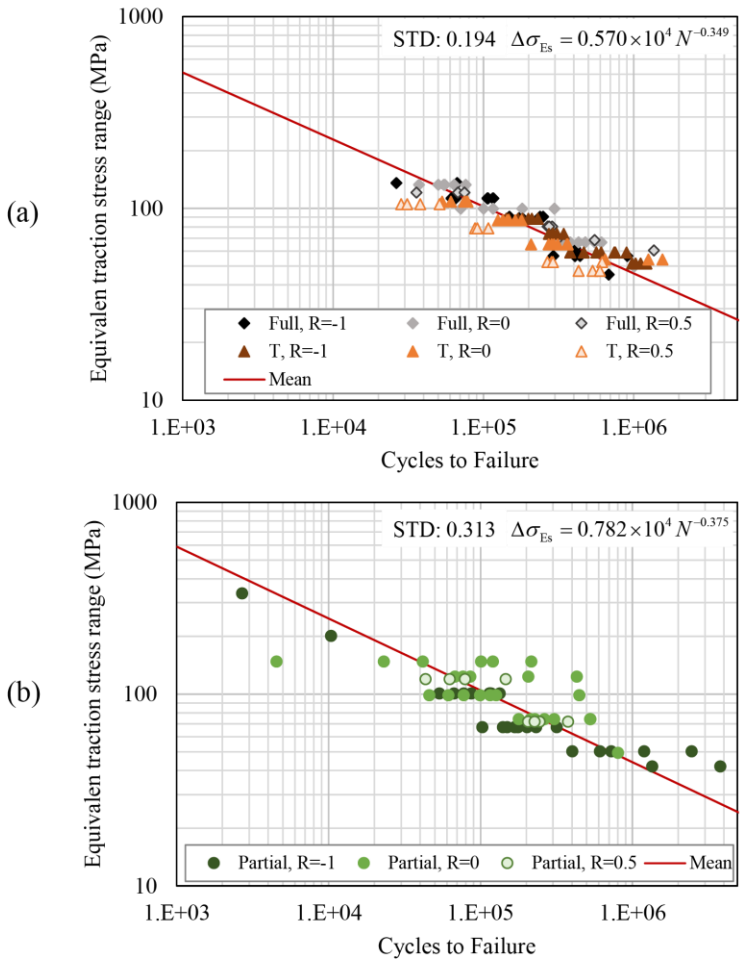

Fig. D.10 Test data correlation using equivalent traction stress range: (a) weld toe failure mode; (b) weld root failure mode.

D.4.2 Equivalent Notch Stress with Load Ratio Correction

By comparing Fig. D.4 with Fig. D.8, both equivalent notch stress range and traction structural stress range seem to show similar effectiveness in correlating the same test data. Then, it should be useful to examine if the load ratio correction term given in Eqn. (D.4) can be applied in conjunction with the equivalent notch stress range. To do so, the equivalent notch stress values used in Fig. D.4 are substituted into Eqn. (D.5) in place of $\Delta\sigma_s$. The results are shown in Fig. D.11. For all test data plotted together in Fig. D.11a, an improved data correlation can be seen, with a standard deviation of 0.267 versus 0.368 before applying the R ratio correction (see Fig. D.4).

Once weld toe and weld throat failure modes are separated, Fig. D.11b shows a standard deviation of 0.242 for weld toe failure modes and Fig. D.11c shows a standard derivation of 0.313. The results in Fig. D.11 clearly shows that the load ratio correction given in Eqn. (D.4) is effective and should be considered in conjunction with the equivalent notch stress method.

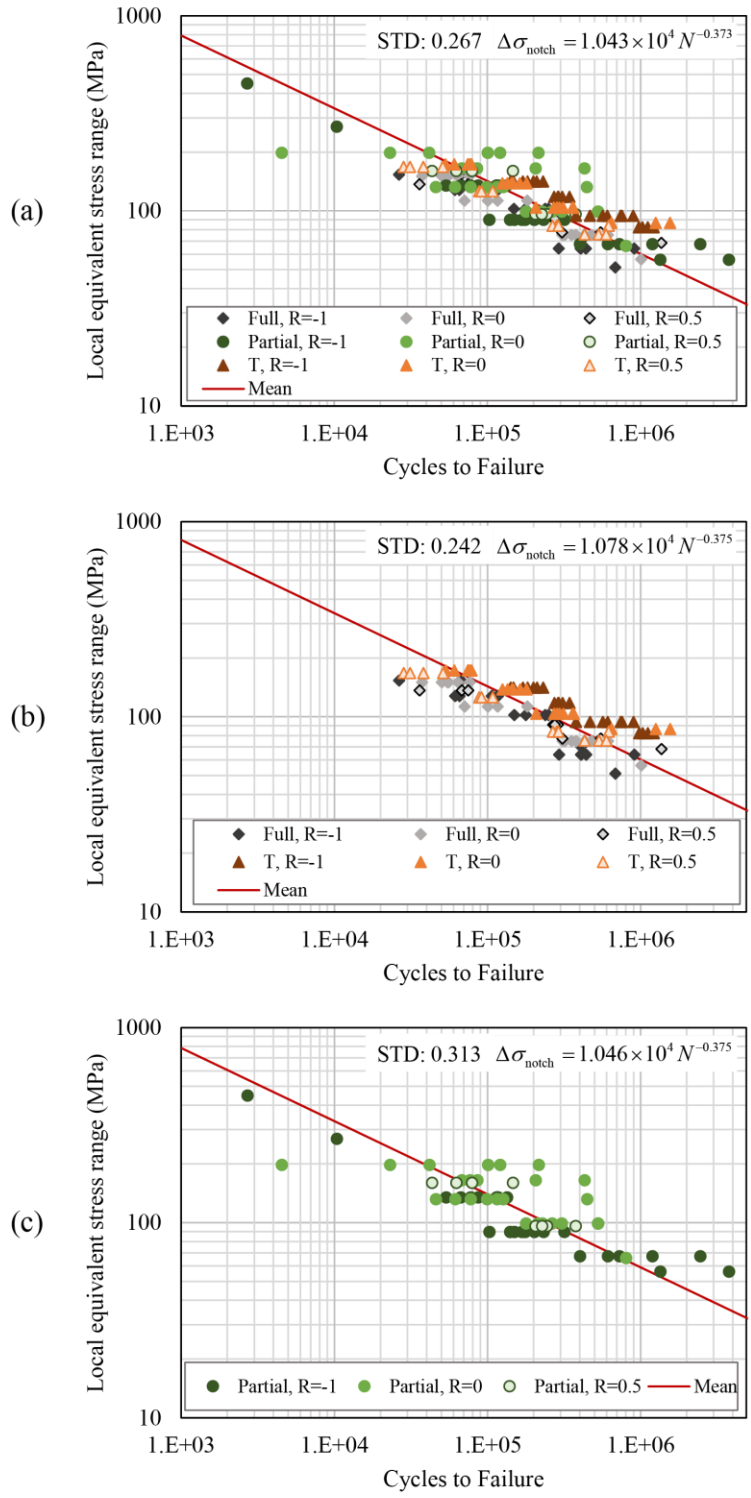

Fig. D.11 Test data correlation using local equivalent notch stress with $r_f = 1$ mm with *R*-ratio correction: (a) all data; (b) weld toe failure; (c) weld root failure.

D.4.3 Further Validation of Load Ratio Correction

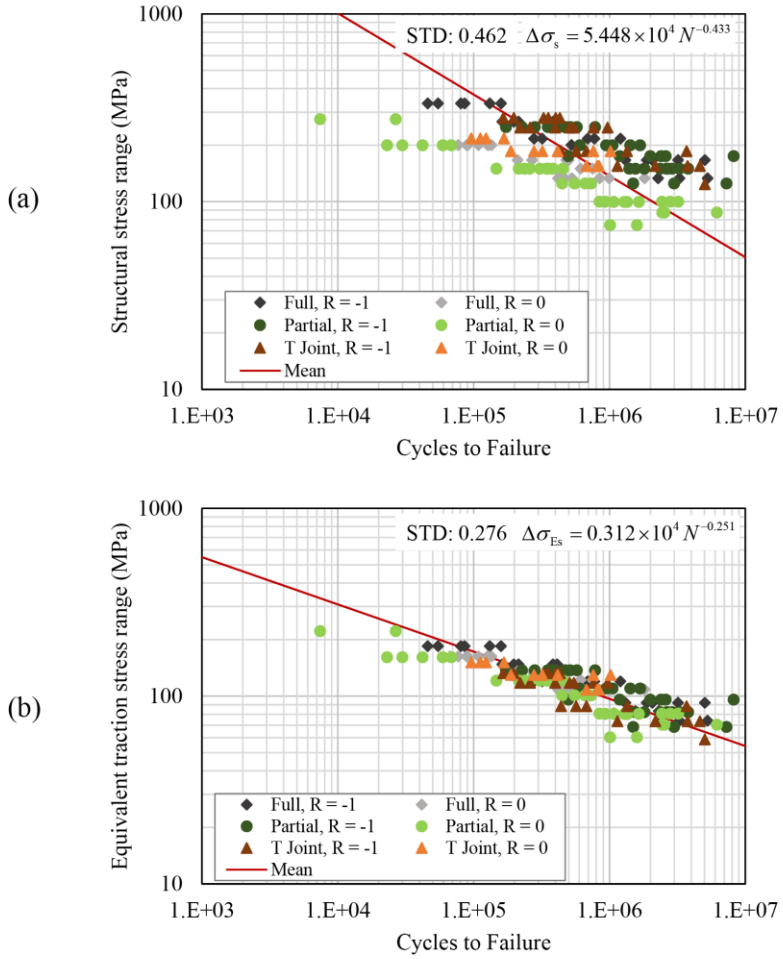

Fig. D.12 Correlation of aluminum test data in [27] using: (a) structural stress range; (b) equivalent traction stress range

Morgenstern et al. [27] conducted aluminum weldment fatigue tests using the same three types of joint types, as shown in Fig. D.1. In these tests, the base plate thickness is at 5 mm and of AW-5083 type. The fatigue test results also displayed a clear load ratio effect. Since the test specimens and loading conditions are almost the same as those shown in Fig. D.1, the same traction stress-based SCFs in Table D.1 for full penetration butt weld and T-joint specimens are directly adopted here. For the partial penetration butt joint specimens used in [27], the traction stress based SCF is calculated using a separate FE model due to its narrower root gap than the one shown in Fig. D.1. The resulting SCF becomes $SCF_s = SCF_m + SCF_b = 1.026 + 0.991 = 2.017$. Fig. D.12

shows the aluminum weldment fatigue results in terms of the traction structural stress range $\Delta\sigma_s$ (Eqn. (D.1)) and equivalent structural stress range (Eqn. (D.5)). It can be clearly seen in Fig. D.12a that the test data with a higher R ratio (or higher mean stress) are mostly situated at the bottom of the scatter band. Once R ratio is considered according to Eqn. (D.5), the standard derivation is reduced from 0.462 to 0.276. The very fact that Eqn. (D.5) is capable of correlating all test data over a wide range of R from magnesium weldments in [104] to aluminum weldment data in [27] validates the effectiveness of the R ratio correction term given in Eqn. (D.4).

D.4.4 Comparison with Master E-N Curve Scatter Band

To examine if the S-N behaviors observed on the magnesium weldments are in some way consistent with those already established for other structural metal weldments, all fatigue test data from different structural metal weldments can be converted to a structural strain based E-N curve plot, referred to as the master E-N curve method [106]. The master E-N curve method, as an extension of the traction stress-based master S-N curve method, has already been shown to provide an effective correlation of a large amount of fatigue test data from weldments made of structural steels, titanium alloys, and aluminum alloys.

For high cycle fatigue regime of interest in this paper, the master E-N curve [106] can be simply obtained by converting the master S-N curve given in ASME Div. 2 Code (since 2007) [32] by Young's modulus E of steel, as briefly described as follows. The master S-N curve in [32] is expressed in terms of equivalent structural stress, defined as,

$$\Delta S_s = \frac{\Delta\sigma_s}{t^{*(2-m)/2m} \cdot I\left(r\right)^{1/m}} \tag{D.6}$$

where $\Delta\sigma_s$ is the traction structural stress range; $t^* = t/1\,mm$ is a dimensionless thickness; $I(r)^{1/m}$ is a dimensionless polynomial function of bending ratio $r = \Delta\sigma_b/(\Delta\sigma_m + \Delta\sigma_b)$, and $m =$

3.6 (same as that in Eqn. (D.5)). The thickness correction term $t^{*(2-m)/2m}$ and bending ratio term $I(r)^{1/m}$ were both derived based on fracture mechanics principles. The structural strain given [106] is simply expressed as $\Delta\varepsilon_s = \Delta\sigma_s/E$, which represents a through-thickness linear strain definition that satisfies the "plane-remaining-plane" condition [106]. By substituting $\Delta\sigma_{\mathrm{Es}}$ defined in Eqn. (D.5) in place of $\Delta\sigma_s$ and dividing it by material Young's modulus E , Eqn. (D.6) then becomes:

$$\Delta E_s = \frac{\Delta\sigma_{\mathrm{Es}}/E}{t^{*(2-m)/2m} \cdot I(r)^{1/m}} \tag{D.7}$$

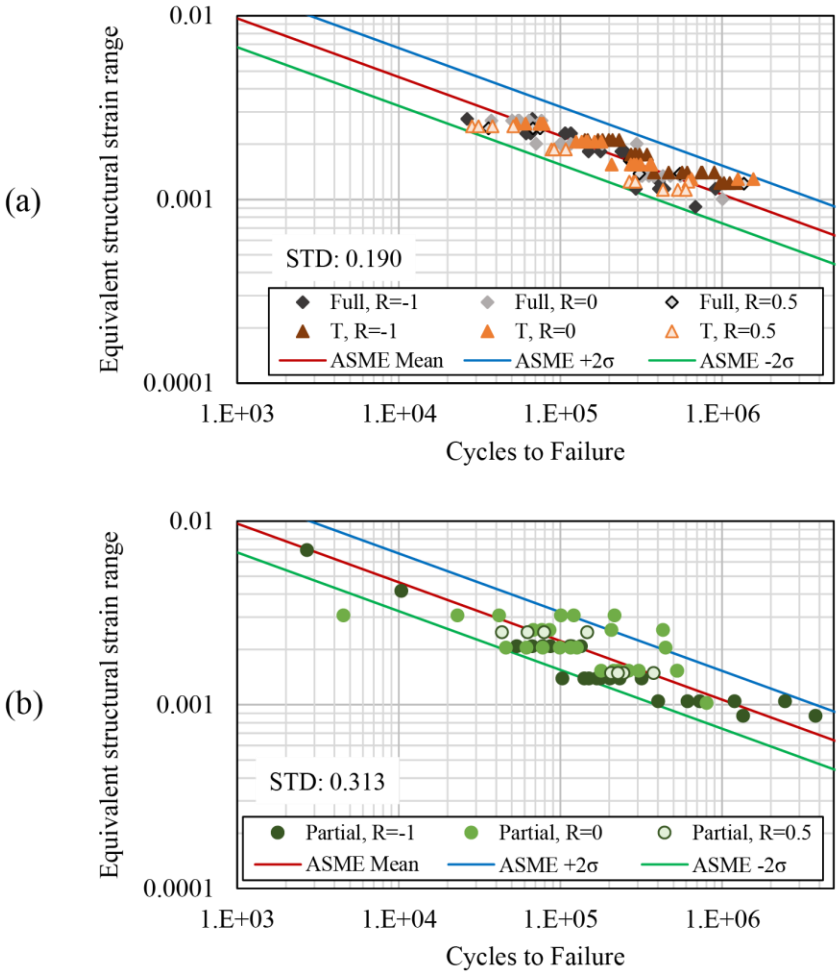

Fig. D.13 Comparison of magnesium weldment fatigue data with master E-N curve scatter band derived from ASME S-N curve: (a) weld toe failure mode; (b) weld root failure mode.

The resulting master E-N curve representation has the same scatter band (STD = 0.240) as that associated with the master S-N curve in [32], as shown as lines (mean$\pm 2STD$) in Fig. D.13. Then, the magnesium test data corresponding to the weld toe failure mode are replotted in Fig. D.13a by using Eqn. (D.7). It is worth noting that the magnesium weldment test data are situated within ASME's mean $\pm 2STD$ scatter band, suggesting the similarity of the fatigue characteristic of magnesium weldments to those of steel and aluminum alloys, as well as the general applicability of these test data provided in [104]. The magnesium weld root failure data (see Fig. D.10b) are plotted in Fig. D.13b by using Eqn. (D.7). It is interesting to note that the mean line (not shown) seem to be approximately aligned with the mean line of the master S-N curve of the magnesium weld root failure data, which is consistent with findings for steel weldment weld root cracking test data discussed in Xing et al. [36].

D.5 Appendix Conclusions

In this appendix, some recent magnesium weldment fatigue test data have been analyzed using both traction structural stress and equivalent notch stress methods. An equivalent traction stress parameter is formulated by incorporating an applied load ratio correction parameter that was formulated in an earlier study. This investigation shows that all the test data from three different joint types can be correlated into a single scatter band, proving the effectiveness of the equivalent traction stress parameter proposed. Furthermore, the load ratio correction parameter can also be used in conjunction with the equivalent notch stress parameter for achieving similar effectiveness. The similarity of the fatigue characteristic of magnesium alloys and that of steel and aluminum alloys and the general applicability of the magnesium weldment test data is further demonstrated by their consistency with the master E-N curve scatter band derived from ASME master S-N curve. Specifically, the following findings are worth noting:

(1) For the thin-gauge magnesium specimens studied, applied load ratio R (or mean stress) shows a significant effect on fatigue performance. The proposed R ratio correction is effective for use in conjunction with both the traction stress and equivalent notch stress methods.

(2) Weld toe failure modes exhibit a much smaller band that weld root failure modes, which is shown to be consistent with that of master S-N curve stipulated in ASME Div. 2 Code based on over 1000 fatigue tests.

(3) The large S-N scatter band in S-N curve form associated with weld throat cracking is similar to what has been seen in structural steel and aluminum alloy weldments and can be attributed to variations in weld penetration from specimen to specimen.

Bibliography

[1] Noury P, Hayman B, McGeorge D, Weitzenböck JR. Lightweight construction for advanced shipbuilding - recent development. 37th WEGEMT Summer Sch 2002:1–23.

[2] Taub A, De Moor E, Luo A, Matlock DK, Speer JG, Vaidya U. Materials for Automotive Lightweighting. Annu Rev Mater Res 2019;49:327–59. https://doi.org/10.1146/annurev-matsci-070218-010134.

[3] Ulbricht A. Rail Vehicle in CFRP-intensive Design. Light Des Worldw 2019;12:36–41. https://doi.org/10.1007/s41777-019-0009-4.

[4] Isenstadt A, German J, Bubna P, Wiseman M, Venkatakrishnan U, Abbasov L, et al. Lightweighting technology development and trends in U.S. passenger vehicles. Int Counc Clean Transp 2016:24.

[5] Bullis K. Automakers Shed the Pounds to Meet Fuel Efficiency Standards. MIT Technol Rev 2013:4. https://www.technologyreview.com/s/510611/automakers-shed-the-pounds-to-meet-fuel-efficiency-standards/.

[6] Skszek T, Conklin J, Zaluzec M, Wagner D. Multi-Material Lightweight Vehicles : Mach-II Design. 2014.

[7] Molavitabrizi D. Design and Analysis of Novel Metallic Structural Concepts for Lightweight Freight Railcars by A thesis submitted to the Faculty of Graduate and Postdoctoral Affairs in partial fulfillment of the requirements for the degree of Master of Applied Science. Carleton University, 2018.

[8] Wennberg D. Light-weighting Methodology in Rail Vehicle Design through Introduction of Load Carrying Sandwich Panels. 2011.

[9] Huang TD, Dong P, DeCan L, Harwig D, Kumar R. Fabrication and engineering technology for lightweight ship structures, Part 1: Distortions and residual stresses in panel fabrication. J Sh Prod 2004;20:43–59.

[10] Song SP, Paradowska AM, Dong PS. Investigation of residual stresses distribution in titanium weldments. Mater Sci Forum 2014;777:171–5. https://doi.org/10.4028/www.scientific.net/MSF.777.171.

[11] Lillemäe I, Remes H, Romanoff J. Influence of initial distortion of 3mm thin superstructure decks on hull girder response for fatigue assessment. Mar Struct 2014;37:203–18. https://doi.org/10.1016/j.marstruc.2014.04.001.

[12] McKinsey & Company. Lightweight, heavy impact 2012.

[13] Liu FC, Dong P, Pei X. A high-speed metal-to-polymer direct joining technique and underlying bonding mechanisms. J Mater Process Technol 2020;280:116610. https://doi.org/10.1016/j.jmatprotec.2020.116610.

[14] Huang TD, Conrardy C, Dong P, Keene P, Kvidahl L, Decan L. Engineering and production technology for lightweight ship structures, Part II: Distortion mitigation technique and implementation. J Sh Prod 2007;23:82–93.

[15] Dong P. Residual stresses and distortions in welded structures: A perspective for

engineering applications. Sci Technol Weld Join 2005;10:389–98. https://doi.org/10.1179/174329305X29465.
[16] Jung G, Huang TD, Dong P, Dull RM, Conrardy CC, Porter NC. Numerical prediction of buckling in ship panel structures. J Sh Prod 2007;23:171–9.
[17] Yang YP, Dong P. Buckling distortions and mitigation techniques for thin-section structures. J Mater Eng Perform 2012;21:153–60. https://doi.org/10.1007/s11665-011-9928-x.
[18] Dong P, Brust FW. Welding residual stresses and effects on fracture in pressure vessel and piping components: a millennium review and beyond. J Press Vessel Technol Trans ASME 2000;122:329–38. https://doi.org/10.1115/1.556189.
[19] Chaithanya PP, Das PK, Crow A, Hunt S. The effect of distortion on the buckling strength of stiffened panels. Ships Offshore Struct 2010;5:141–53. https://doi.org/10.1080/17445300903331818.
[20] Dong P. Residual stresses and distortions in modern manufacturing. NA 515 Coursepack 2020.
[21] Gurney TR. Fatigue of welded structures. 2nd ed. Cambridge University Press; 1979.
[22] Fuchs HO, Fatem, Stephens RI. Metal Fatigue in Engineering. 2nd ed. 2000.
[23] Maddox SJ. Significant features of welds in relation to fatigue. Fatigue Strength Welded Struct., 2002, p. 19–29. https://doi.org/10.1016/b978-1-85573-013-7.50005-7.
[24] British Standards Institution. BS 7608:2014 Guide to fatigue design and assessment of steel products. British Standard Institution; 2014.
[25] Hobbacher AF. Recommendations for Fatigue Design of Welded Joints and Components. 2nd ed. 2019. https://doi.org/10.1007/978-3-319-23757-2_8.
[26] Hobbacher AF. The new IIW recommendations for fatigue assessment of welded joints and components - A comprehensive code recently updated. Int J Fatigue 2009;31:50–8. https://doi.org/10.1016/j.ijfatigue.2008.04.002.
[27] Morgenstern C, Sonsino CM, Hobbacher A, Sorbo F. Fatigue design of aluminium welded joints by the local stress concept with the fictitious notch radius of rf=1 mm. Int J Fatigue 2006;28:881–90. https://doi.org/10.1016/j.ijfatigue.2005.10.006.
[28] Radaj D, Sonsino CM, Fricke W. Fatigue assessment of welded joints by local approaches. Woolhead Publishing; 2006.
[29] Sonsino CM. A consideration of allowable equivalent stresses for fatigue design of welded joints according to the notch stress concept with the reference radii rref = 1.00 and 0.05 mm. Weld World 2009;53:64–75. https://doi.org/10.1007/BF03266705.
[30] Dong P. A structural stress definition and numerical implementation for fatigue analysis of welded joints. Int J Fatigue 2001;23:865–76. https://doi.org/10.1016/S0142-1123(01)00055-X.
[31] Dong P. A robust structural stress method for fatigue analysis of offshore/marine structures. J Offshore Mech Arct Eng 2005;127:68–74. https://doi.org/10.1115/1.1854698.
[32] Dong P, Hong JK, Osage DA, Dewees DJ, Prager M. The master S-N curve method an implementation for fatigue evaluation of welded components in the ASME B&PV Code, Section VIII, Division 2 and API 579-1/ASME FFS-1. Weld Research Council Bulletin 2010;523.
[33] Det Norske Veritas. DNV-RP-C203 Fatigue design of offshore steel structures. Det Norske Veritas; 2011.
[34] Fricke W. Recommended hot-spot analysis procedure for structural details of ships and

FPSOs based on round-robin FE analyses. Int J Offshore Polar Eng 2002;12:40–7.
[35] Dong P, Hong JK. The master S-N curve approach to fatigue evaluation of offshore and marine structures. Proc. Int. Conf. Offshore Mech. Arct. Eng. - OMAE, vol. 2, 2004, p. 847–55. https://doi.org/10.1115/OMAE2004-51324.
[36] Xing S, Dong P, Wang P. A quantitative weld sizing criterion for fatigue design of load-carrying fillet-welded connections. Int J Fatigue 2017;101:448–58. https://doi.org/10.1016/j.ijfatigue.2017.01.003.
[37] Wang P, Pei X, Dong P, Song S. Traction structural stress analysis of fatigue behaviors of rib-to-deck joints in orthotropic bridge deck. Int J Fatigue 2019;125:11–22. https://doi.org/10.1016/j.ijfatigue.2019.03.038.
[38] Lu H, Dong P. An Analytical Shear Strength Model for Load-Carrying Fillet-Welded Connections Incorporating Nonlinear Effects. J Struct Eng 2020;146:04019224. https://doi.org/10.1061/(asce)st.1943-541x.0002532.
[39] Lu H, Dong P, Boppudi S. Strength analysis of fillet welds under longitudinal and transverse shear conditions. Mar Struct 2015;43:87–106. https://doi.org/10.1016/j.marstruc.2015.06.003.
[40] Nie C, Dong P. A traction stress based shear strength definition for fillet welds. J Strain Anal Eng Des 2012;47:562–75. https://doi.org/10.1177/0309324712456646.
[41] Lillemäe I, Liinalampi S, Remes H, Itävuo A, Niemelä A. Fatigue strength of thin laser-hybrid welded full-scale deck structure. Int J Fatigue 2017;95:282–92. https://doi.org/10.1016/j.ijfatigue.2016.11.012.
[42] Michaleris P. Introduction to welding residual stress and distortion. Woodhead Publishing Limited; 2011. https://doi.org/10.1533/9780857092908.1.3.
[43] Baruah M, Bag S. Influence of heat input in microwelding of titanium alloy by micro plasma arc. J Mater Process Technol 2016;231:100–12. https://doi.org/10.1016/j.jmatprotec.2015.12.014.
[44] Deng D, Murakawa H, Liang W. Numerical simulation of welding distortion in large structures. Comput Methods Appl Mech Eng 2007;196:4613–27. https://doi.org/10.1016/j.cma.2007.05.023.
[45] Deng D, Murakawa H. FEM prediction of buckling distortion induced by welding in thin plate panel structures. Comput Mater Sci 2008;43:591–607. https://doi.org/10.1016/j.commatsci.2008.01.003.
[46] Deng D, Zhou Y, Bi T, Liu X. Experimental and numerical investigations of welding distortion induced by CO2 gas arc welding in thin-plate bead-on joints. Mater Des 2013;52:720–9. https://doi.org/10.1016/j.matdes.2013.06.013.
[47] Chen Z, Chen Z, Shenoi RA. Influence of welding sequence on welding deformation and residual stress of a stiffened plate structure. Ocean Eng 2015;106:271–80. https://doi.org/10.1016/j.oceaneng.2015.07.013.
[48] Zhang J, Dong P, Brust FW. A 3-D composite shell element model for residual stress analysis of multi-pass welds. Proc SMiRT 14 1997;1:335–44.
[49] Lillemäe I, Lammi H, Molter L, Remes H. Fatigue strength of welded butt joints in thin and slender specimens. Int J Fatigue 2012;44:98–106. https://doi.org/10.1016/j.ijfatigue.2012.05.009.
[50] Shen W, Qiu Y, Xu L, Song L. Stress concentration effect of thin plate joints considering welding defects. Ocean Eng 2019;184:273–88. https://doi.org/10.1016/j.oceaneng.2019.05.019.

[51] Dong P, Song S, Zhang J, Kim MH. On residual stress prescriptions for fitness for service assessment of pipe girth welds. Int J Press Vessel Pip 2014;123:19–29. https://doi.org/10.1016/j.ijpvp.2014.07.006.
[52] Song S, Dong P. Residual stresses at weld repairs and effects of repair geometry. Sci Technol Weld Join 2017;22:265–77. https://doi.org/10.1080/13621718.2016.1224544.
[53] Dong P. Length scale of secondary stresses in fracture and fatigue. Int J Press Vessel Pip 2008;85:128–43. https://doi.org/10.1016/j.ijpvp.2007.10.005.
[54] Bouchard PJ. Validated residual stress profiles for fracture assessments of stainless steel pipe girth welds. Int J Press Vessel Pip 2007;84:195–222. https://doi.org/10.1016/j.ijpvp.2006.10.006.
[55] Francis JA, Bhadeshia HKDH, Withers PJ. Welding residual stresses in ferritic power plant steels. Mater Sci Technol 2007;23:1009–20. https://doi.org/10.1179/174328407X213116.
[56] Edwards L, Smith MC, Turski M, Fitzpatrick ME, Bouchard PJ. Advances in residual stress modeling and measurement for the structural integrity assessment of welded thermal power plant. Adv. Mater. Res., vol. 41–42, 2008, p. 391–400. https://doi.org/10.4028/www.scientific.net/amr.41-42.391.
[57] Antoniou AC. On the Maximum Deflection of Plating in Newly Built Ships. J Sh Res 1980;24:31–9.
[58] Carlsen CA, Czujko J. The specification of post-welding distortion tolerances for stiffened plates in compression. Struct Eng 1978;56 A:133–41.
[59] British Standards Institution. BS 7910:2013 Guide to methods for assessing the acceptability of flaws in metallic structures. British Standards Institution; 2015.
[60] American Bureau of Shipping. Guide for shipbuilding and repair quality standard for hull structures during construction. 2007.
[61] Department of Defense. MIL-STD-1689A: Fabrication, welding, and inspection of ships structure. 1990.
[62] Dong P, Xing S, Zhou W. Analytical treatment of welding distortion effects on fatigue in thin panels: Part i—closed-form solutions and implications. Marit. Transp. Harvest. Sea Resour., vol. 1, 2016.
[63] Xing S, Dong P. An analytical SCF solution method for joint misalignments and application in fatigue test data interpretation. Mar Struct 2016;50:143–61. https://doi.org/10.1016/j.marstruc.2016.07.006.
[64] Xing S, Dong P, Threstha A. Analysis of fatigue failure mode transition in load-carrying fillet-welded connections. Mar Struct 2016;46:102–26. https://doi.org/10.1016/j.marstruc.2016.01.001.
[65] Lillemäe-Avi I, Remes H, Dong Y, Garbatov Y, Quemener Y, Eggert L, et al. Benchmark study on considering welding-induced distortion in structural stress analysis of thin-plate structures. Prog Anal Des Mar Struct - Proc 6th Int Conf Mar Struct MARSTRUCT 2017 2017:387–94. https://doi.org/10.1201/9781315157368-45.
[66] Eggert L, Fricke W, Paetzold H. Fatigue strength of thin- plated block joints with typical shipbuilding imperfections. Weld World 2012;56:119–28. https://doi.org/10.1007/BF03321402.
[67] Lillemäe I, Remes H, Romanoff J. Influence of initial distortion on the structural stress in 3 mm thick stiffened panels. Thin-Walled Struct 2013;72:121–7. https://doi.org/10.1016/j.tws.2013.07.001.

[68] Chan SL, Zhou ZH. Second-Order elastic analysis of frames using single imperfect element per member. J Struct Eng (United States) 1995;121:939–45. https://doi.org/10.1061/(ASCE)0733-9445(1995)121:6(939).
[69] Chan SL, Gu JX. Exact tangent stiffness for imperfect beam-column members. J Struct Eng (United States) 2000;126:1094–102. https://doi.org/10.1061/(ASCE)0733-9445(2000)126:9(1094).
[70] Gu JX, Chan SL. Second-order analysis and design of steel structures allowing for member and frame imperfections. Int J Numer Methods Eng 2005;62:601–15. https://doi.org/10.1002/nme.1182.
[71] Liew JYR, White DW, Chen WF. Notional-load plastic-hinge method for frame design. J Struct Eng (United States) 1994;120:1434–54. https://doi.org/10.1061/(ASCE)0733-9445(1994)120:5(1434).
[72] Dong P, Zhou W, Xing S. Analytical treatment of welding distortion effects on fatigue in thin panels: Part ii—applications in test data analysis. Marit. Transp. Harvest. Sea Resour., vol. 1, 2016.
[73] Timoshenko SP, Gere JM. Theory of elastic stability. 1961.
[74] American Society of Mechanical Engineers. ASME Boiler and Pressure Vessel Code, Section VIII, Division 2. American Society of Mechanical Engineers; 2007.
[75] Kang HT, Dong P, Hong JK. Fatigue analysis of spot welds using a mesh-insensitive structural stress approach. Int J Fatigue 2007;29:1546–53. https://doi.org/10.1016/j.ijfatigue.2006.10.025.
[76] Huang TD, Harbison M, Kvidahl L, Niolet D, Walks J, Stefanick K, et al. Reduction of overwelding and distortion for naval surface combatants. Part 1: Optimized weld sizing for lightweight ship structures. J Sh Prod Des 2014;30:184–93. https://doi.org/10.5957/JSPD.30.4.130028.
[77] Saunders FI, Wagoner RH. Forming of tailor-welded blanks. Metall Mater Trans A Phys Metall Mater Sci 1996;27:2605–16. https://doi.org/10.1007/BF02652354.
[78] Berge S, Myhre H. Fatigue strength of misaligned cruciform and butt joints. Nor Marit Res 1977;5:29–39.
[79] Andrews RM. The effect of misalignment on the fatigue strength of welded cruciform joints. Fatigue Fract Eng Mater Struct 1996;19:755–68. https://doi.org/10.1111/j.1460-2695.1996.tb01320.x.
[80] Jakubczak H, Glinka G. Fatigue analysis of manufacturing defects in weldments. Int J Fatigue 1986;8:51–7. https://doi.org/10.1016/0142-1123(86)90053-8.
[81] Wylde JG, Maddox SJ. Effect of misalignment on fatigue strength of transverse butt welded joints. Inst. Mech. Eng. Conf. Publ., 1979, p. 37–51.
[82] Iwata T, Matsuoka K. Misalignment Effect on Fatigue Strength of CP Titanium Butt-welded Joints 2007:1637–9.
[83] Pachoud AJ, Manso PA, Schleiss AJ. New parametric equations to estimate notch stress concentration factors at butt welded joints modeling the weld profile with splines. Eng Fail Anal 2017;72:11–24. https://doi.org/10.1016/j.engfailanal.2016.11.006.
[84] Ottersböck MJ, Leitner M, Stoschka M, Maurer W. Analysis of fatigue notch effect due to axial misalignment for ultra high-strength steel butt joints. Weld World 2019;63:851–65. https://doi.org/10.1007/s40194-019-00713-4.
[85] Lotsberg I. Stress concentrations due to misalignment at butt welds in plated structures and at girth welds in tubulars. Int J Fatigue 2009;31:1337–45.

https://doi.org/10.1016/j.ijfatigue.2009.03.005.
[86] Liu X, Song W, Yan Z, Qiang W, Pan H. Misalignment effect on stress concentration of thickness mismatched plate structures. Procedia Struct Integr 2016;2:2038–45. https://doi.org/10.1016/j.prostr.2016.06.256.
[87] Maddox SJ. Fitness-for-purpose assessment of misalignment in transverse butt welds subject to fatigue loading. Welding Institute; 1985.
[88] Zhou W, Dong P, Lillemae I, Remes H. A 2nd−order SCF solution for modeling distortion effects on fatigue of lightweight structures. Weld World 2019;63:1695–705. https://doi.org/10.1007/s40194-019-00772-7.
[89] Zhou W, Dong P, Lillemäe I, Remes H. Analytical treatment of distortion effects on fatigue behaviors of lightweight shipboard structures. Int J Fatigue 2020;130. https://doi.org/10.1016/j.ijfatigue.2019.105286.
[90] Gere JM. Mechanics of materials. 6th ed. Belmont:Thomson Brooks/Cole; 2006.
[91] Kreyszig E. Advanced Engineering Mathematics. 10th ed. John Wiley & Sons, Inc.; 2011.
[92] Faraway JJ. Linear Models with R. 2nd ed. New York: Chapman and Hall/CRC; 2014. https://doi.org/10.1201/b17144.
[93] Livesley RK. Matrix Methods of Structural Analysis. 2nd ed. 1975.
[94] Tsujikawa M, Somekawa H, Higashi K, Iwasaki H, Hasegawa T, Mizuta A. Fatigue of Welded Magnesium Alloy Joints. Mater Trans 2004;45:419–22. https://doi.org/10.2320/matertrans.45.419.
[95] Easton M, Beer A, Barnett M, Davies C, Dunlop G, Durandet Y, et al. Magnesium alloy applications in automative structures. Jom 2008;60:57–62. https://doi.org/10.1007/s11837-008-0150-8.
[96] Commin L, Dumont M, Masse JE, Barrallier L. Friction stir welding of AZ31 magnesium alloy rolled sheets: Influence of processing parameters. Acta Mater 2009;57:326–34. https://doi.org/10.1016/j.actamat.2008.09.011.
[97] Chowdhury SH, Chen DL, Bhole SD, Cao X, Wanjara P. Lap shear strength and fatigue life of friction stir spot welded AZ31 magnesium and 5754 aluminum alloys. Mater Sci Eng A 2012;556:500–9. https://doi.org/10.1016/j.msea.2012.07.019.
[98] Esmaily M, Svensson JE, Fajardo S, Birbilis N, Frankel GS, Virtanen S, et al. Fundamentals and advances in magnesium alloy corrosion. Prog Mater Sci 2017;89:92–193. https://doi.org/10.1016/j.pmatsci.2017.04.011.
[99] Dong P. Quantitative Weld Quality Acceptance Criteria: An Enabler for Structural Lightweighting and Additive Manufacturing. Weld J 2020;99:39–51. https://doi.org/10.29391/2020.99.004.
[100] CEN. EN 1999: Design of aluminium structures. European Committee for Standardization; 2007.
[101] Jordon JB, Horstemeyer MF, Daniewicz SR, Badarinarayan H, Grantham J. Fatigue characterization and modeling of friction stir spot welds in magnesium AZ31 alloy. J Eng Mater Technol Trans ASME 2010;132:1–10. https://doi.org/10.1115/1.4002330.
[102] Chowdhury SM, Chen DL, Bhole SD, Powidajko E, Weckman DC, Zhou Y. Microstructure and mechanical properties of fiber-laser-welded and diode-laser-welded AZ31 magnesium alloy. Metall Mater Trans A Phys Metall Mater Sci 2011;42:1974–89. https://doi.org/10.1007/s11661-010-0574-y.
[103] Shen Z, Ding Y, Chen J, Gerlich AP. Comparison of fatigue behavior in Mg/Mg similar and Mg/steel dissimilar refill friction stir spot welds. Int J Fatigue 2016;92:78–86.

https://doi.org/10.1016/j.ijfatigue.2016.06.033.
[104] Karakas Ö, Morgenstern C, Sonsino CM. Fatigue design of welded joints from the wrought magnesium alloy AZ31 by the local stress concept with the fictitious notch radii of rf = 1.0 and 0.05 mm. Int J Fatigue 2008;30:2210–9. https://doi.org/10.1016/j.ijfatigue.2008.05.017.
[105] Dong P, Pei X, Xing S, Kim MH. A structural strain method for low-cycle fatigue evaluation of welded components. Int J Press Vessel Pip 2014;119:39–51. https://doi.org/10.1016/j.ijpvp.2014.03.003.
[106] Pei X, Dong P, Xing S. A structural strain parameter for a unified treatment of fatigue behaviors of welded components. Int J Fatigue 2019;124:444–60. https://doi.org/10.1016/j.ijfatigue.2019.03.010.
[107] Karakaş, Zhang G, Sonsino CM. Critical distance approach for the fatigue strength assessment of magnesium welded joints in contrast to Neuber's effective stress method. Int J Fatigue 2018;112:21–35. https://doi.org/10.1016/j.ijfatigue.2018.03.004.
[108] Taylor D. The Theory of Critical Distances. Elsevier Science Ltd; 2007.
[109] Mei J, Xing S, Vasu A, Chung J, Desai R, Dong P. The fatigue limit prediction of notched components – A critical review and modified stress gradient based approach. Int J Fatigue 2020;135:105531. https://doi.org/10.1016/j.ijfatigue.2020.105531.
[110] Sonsino CM, Hanselka H, Karakas Ö, Gülsöz A, Vogt M, Dilger K. Fatigue design values for welded joints of the wrought magnesium alloy AZ31 (ISO-MgAl3Zn1) according to the nominal, structural and notch stress concepts in comparison to welded steel and aluminium connections. Weld World 2008;52:79–94. https://doi.org/10.1007/BF03266643.
[111] Karakas Ö. Consideration of mean-stress effects on fatigue life of welded magnesium joints by the application of the Smith-Watson-Topper and reference radius concepts. Int J Fatigue 2013;49:1–17. https://doi.org/10.1016/j.ijfatigue.2012.11.007.
[112] Karakaş Ö. Application of Neuber's effective stress method for the evaluation of the fatigue behaviour of magnesium welds. Int J Fatigue 2017;101:115–26. https://doi.org/10.1016/j.ijfatigue.2016.10.023.
[113] Daniel Kujawski. A new (_K+ Kmax) 0.5 driving force parameter for crack growth in aluminum alloys. Int J Fatigue 2001;23:733–40.
[114] Dong P, Hong JK, Cao Z. Stresses and stress intensities at notches: "Anomalous crack growth" revisited. Int J Fatigue 2003;25:811–25. https://doi.org/10.1016/S0142-1123(03)00130-0.
[115] Kainuma S, Mori T. A fatigue strength evaluation method for load-carrying fillet welded cruciform joints. Int J Fatigue 2006;28:864–72. https://doi.org/10.1016/j.ijfatigue.2005.10.004.
[116] Kainuma S, Mori T. A study on fatigue crack initiation point of load-carrying fillet welded cruciform joints. Int J Fatigue 2008;30:1669–77. https://doi.org/10.1016/j.ijfatigue.2007.11.003.